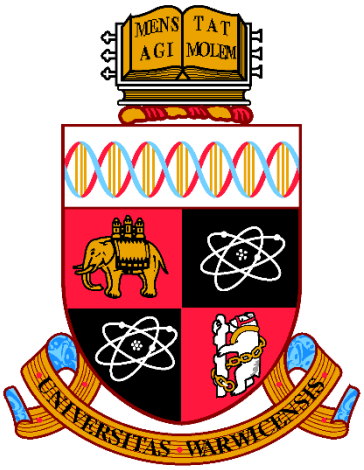

Temperature-Driven Anomaly Detection Methods for Structural Health Monitoring

By

Yanjie ZHU

A thesis submitted to University of Warwick

for the degree of

Doctor of Philosophy

School of Engineering

September 2018

Acknowledgements

I would like to express my heartfelt gratitude to my supervisor, Dr Irwanda Laory, for his excellent supervision, valuable support and precious guidance for my research during last four years.

I would like to extend my deepest gratitude to my co-supervisor, Professor Toby Mottram, for his precious advice and guidance for my research.

I would like to thank my colleagues and staff in School of Engineering, Dr Andre Jesus, Dr Mohammad Reza Salami, Dr Xiaojun Wei, Dr Xueyu Geng and Dr Mike Jennings, who have given me many useful suggestions and guidances in my research work.

Many thanks also go to Mr Neil Gillespie (Civil Engineering Technician), Mr Taylor Arnett (Civil Engineering Technician), Mr Paul Hedley (Supervisory Technician) and Mr Iain Brown (Carpentry Technician) for their efficient supports and professional advice during experimental work.

I am grateful to the financial support from University of Warwick and Chinese Scholar Council.

Many thanks are indebted to my friends in University of Warwick for their companionship during the last four years.

Finally, my special thanks to my beloved parents, Mr Yi Zhu and Mrs Ping Zhang, for their support and encouragement throughout my whole life.

Declaration

This thesis is submitted to the University of Warwick in support of my application for the degree of Doctor of Philosophy. It has been composed by the author and has not been submitted in any previous application for any degree.

This thesis is based upon materials from the following publications.

Zhu, Y., Ni, Y., Jin, H., Inaudi, D., & Laory, I. 2018. A Temperature-driven MPCA Method for Structural Anomaly Detection. *Engineering Structures*. (*Under review*)

Zhu, Y., Ni, Y., Jesus, A., Laory, I., & Liu, J. 2018. Thermal Strain Extraction Methodologies for Bridge Structural Condition Assessment. *Smart Materials and Structures*. **27** 105051. DOI: 10.1088/1361-665X/aad5fb

Zhu, Y., Jesus, A. & Laory, I. 2017. Thermal Effect Identification and Bridge Damage Disclosure by using Blind Source Separation Method. *Structural Health Monitoring 2017*. DOI: 10.12783/shm2017/13907

Zhu, Y., Jesus, A. H. & Laory, I. 2016. Predicting thermal response for structural health monitoring using blind source separation method. *8th European Workshop on Structural Health Monitoring*. Available: http://www.ndt.net/?id=20035

List of publications

Journal paper

Zhu, Y., Ni, Y., Jin, H., Inaudi, D., & Laory, I. 2018. A Temperature-driven MPCA Method for Structural Anomaly Detection. *Engineering Structures*. (*Under review*)

Zhu, Y., Ni, Y., Jesus, A., Laory, I., & Liu, J. 2018. Thermal Strain Extraction Methodologies for Bridge Structural Condition Assessment. *Smart Materials and Structures*. **27** 105051. DOI: 10.1088/1361-665X/aad5fb

Liu, J., Wei, X., Qiu, R., Zheng, J., **Zhu, Y.** & Laory, I. 2018. Instantaneous Frequency Extraction in Time-varying Structures using a Maximum Gradient Method. *Smart Structures and Systems*. **22**(3): 359-368. DOI: 10.12989/sss.2018.22.3.359

Wu, W., Wang, H., **Zhu, Y.**, Yu, J., Zhao, H., & Zhang, H. 2018. New Hanger Design Approach of Tied-Arch Bridge to Enhance Its Robustness. *KSCE Journal of Civil Engineering*, 1-8. DOI: 10.1007/s12205-018-1835-3

Jesus, A., Brommer, P., **Zhu, Y.**, & Laory, I. 2017. Comprehensive Bayesian structural identification using temperature variation. *Engineering Structures*, 141, 75-82. DOI: 10.1016/j.engstruct.2017.01.060

Chao, Z., Ma, G., Zhang, Y., **Zhu, Y.** & Hu, H. 2018. The Application of Artificial Neural Network in Geotechnical Engineering. *IOP Conference Series: Earth and Environmental Science*. 189(2): 022054. DOI: 10.1088/1755-1315/189/2/022054

Ma, G., Chao, Z., Zhang, Y., **Zhu, Y.** & Hu, H. 2018. The Application of Support Vector Machine in Geotechnical Engineering. *IOP Conference Series: Earth and Environmental Science*. 189(2): 022055. DOI: 10.1088/1755-1315/189/2/022055

Conference paper

Zhu, Y., Jesus, A. & Laory, I. 2017. Thermal Effect Identification and Bridge Damage Disclosure by using Blind Source Separation Method. *Structural Health Monitoring 2017*.

Jesus, A., **Zhu, Y.** & Laory, I. 2017. Identifiability based sensor configuration analysis for Bayesian structural identification. *Structural Health Monitoring of Intelligent Infrastructure 2017*. **(Best paper award)**

Zhu, Y., Jesus, A. H. & Laory, I. 2016. Predicting thermal response for structural health monitoring using blind source separation method. *8th European Workshop on Structural Health Monitoring*.

Jesus, A., **Zhu, Y.** & Laory, I. 2016. Comprehensive Bayesian structural identification using temperature expansion of a scale aluminium bridge. *8th European Workshop on Structural Health Monitoring*.

Abstract

Reported in this thesis is a data-driven anomaly detection method for structural health monitoring which is based on the utilization of temperature-induced variations.

Structural anomaly detection should be able to identify meaningful changes in measurements which are due to structural abnormal behaviour. Because, the temperature-induced variations and structural abnormalities may produce significant misinterpretations, the development of solutions to identify a structural anomaly, accounting for temperature influence, from measurements, is a critical procedure to support structural maintenance.

A temperature-driven anomaly detection method is proposed, that introduces the idea of blind source separation for extracting thermal response and for further anomaly detection. Two thermal feature extraction methods are employed corresponding to the classification of underdetermined and overdetermined methods. The underdetermined method has the three phases of: (a) mode decomposition by utilising Empirical Mode Decomposition or Ensemble Empirical Mode Decomposition; (b) data reduction by performing Principal Component Analysis (PCA); (c) blind separation by applying Independent Component Analysis (ICA). The overdetermined method has the two stages of the pre-indication according to PCA and the blind separation by the devotion of ICA. Based on the extracted thermal response, the temperature-driven anomaly detection method is later developed in combination with the four methodologies of: Moving Principal Component Analysis (MPCA); Robust Regression Analysis (RRA); One-Class Support Vector Machine (OCSVM); Artificial Neural Network (ANN). Therefore, the proposed temperature-driven anomaly detection methods are designed as Td-MPCA, Td-RRA, Td-OCSVM, and Td-ANN.

The proposed thermal feature extraction methods and temperature-driven anomaly detection methods have been investigated in the context of three case studies. The first case is a numerical truss bridge with simulated material stiffness reduction to create levels of damage. The second case is a purpose constructed truss bridge in the Structures Lab at the University of Warwick. The third case study is Ricciolo curved viaduct in Switzerland. Two primary findings can be confirmed from the evaluation results of these three case studies. Firstly, temperature-induced variations can conceal damage information in measurements. Secondly, the detection abilities of temperature-driven methods, which are Td-MPCA, Td-RRA, Td-OCSVM, and Td-ANN, for disclosing slight anomalies in time are more efficient when compared with the current anomaly detection method, which are MPCA, RRA, OCSVM, and ANN.

The unique features of the author's proposed temperature-driven anomaly detection method can be highlighted as follows: (a) it is a data-driven method for extracting features from an unknown structural system. In another word, the prior knowledge of the structural in-service conditions and physical models are not necessary; (b) it is the first time that blind source separation approaches and relative algorithms have been successfully employed for extracting temperature-induced responses; (c) it is a new approach to reliably assess the capability of using temperature-induced responses for anomaly detection.

Table of Contents

List of figures

List of tables

Notations and Abbreviations

Acronyms		Terms in full
ANN	-	Artificial Neural Network
BP	-	Back Propagation
BSS	-	Blind Source Separation / Blind Signal Separation
EEMD	-	Ensemble Empirical Mode Decomposition
EEPI		EEMD+PCA+ICA
EMD	-	Empirical Mode Decomposition
EPI	-	EMD+PCA+ICA
ICA	-	Independent Component Analysis
MPCA	-	Moving Principal Component Analysis
OCSVM	-	One-Class Support Vector Machine
PCA	-	Principal Component Analysis
RRA	-	Robust Regression Analysis
SHM	-	Structural Health Monitoring
SVM	-	Support Vector Machine
Td-ANN	-	Temperature-driven Artificial Neural Network
Td-MPCA	-	Temperature-driven Moving Principal Component Analysis
Td-OCSVM	-	Temperature-driven One-Class Support Vector Machine
Td-RRA	-	Temperature-driven Robust Regression Analysis

CHAPTER 1 INTRODUCTION

The safety and serviceability of engineered structures, e.g., bridges, buildings, and tunnels, consistently attracts multi-disciplinary attention because of its crucial importance for civilized society. The health monitoring of infrastructures has therefore become the ultimate goals of academic and engineering societies (Xu & Xia, 2012). Structural Health Monitoring (SHM) has subsequently been developed and implemented to provide an in-time and long-term monitoring solution. This chapter first introduces the concept of Structural Health Monitoring with its objectives and applications in engineering disciplines. The research motivation and objectives are subsequently provided, followed by a short description of the thesis scope, as shown in Figure 1.1.

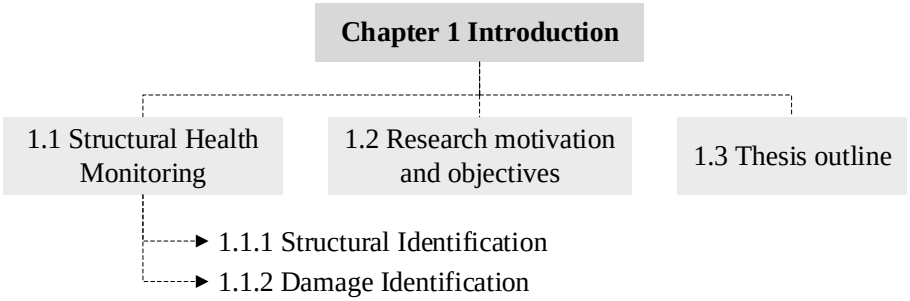

Figure 1.1. Organization of Chapter 1.

1.1 Structural Health Monitoring

The definition of Structural Health Monitoring (SHM) can vary, but the most accepted definition is that SHM is the process of employing advanced computer-aided techniques for the implementation of structural identification and damage identification (Worden & Dulieu-Barton, 2004; Brownjohn, 2007; Farrar & Worden,

2007). The implicit concept of SHM is different from traditional monitoring techniques, for example, Non-Destructive Testing (NDT). NDT, also known as Non-Destructive Evaluation (NDE), is a highly effective tool for damage detection and severity check (Worden & Dulieu-Barton, 2004; Dwivedi *et al.*, 2018), while SHM identifies damage based on monitoring continuously signals from installed sensors (Farrar & Worden, 2007). The widely known hierarchical scheme of an SHM system includes three sub-systems, which are described in Figure 1.2.

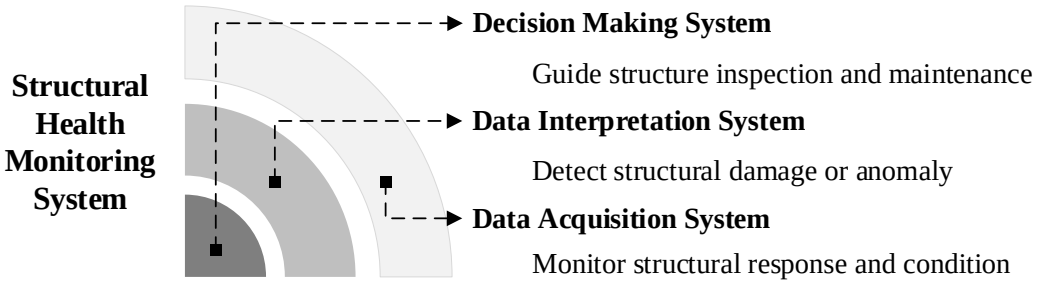

Figure 1.2. Strategy of Structural Health Monitoring System

According to the American Society of Civil Engineers estimation in 2005, approximately 40% of in-service structures in the US are defective, and an investment of over $1.6 trillion is required for maintenance and imperative actions (Xu & Xia, 2012). According to a most recent report conducted by the ASCE, 9.1% of bridges in the US are structurally deficient, and bridges' average lives are 8 years less than designed expectation (American Society of Civil Engineers, 2017). Moreover, the civil structures can be compromised during their service lives by various degradations, for example, concrete cracking, steel fatigue, and environmental corrosion, etc.

To provide a better understanding of mechanical characteristics and better support to the design and construction period, the SHM system is designed as a sufficient tool to track structural conditions and to assess in-service performance. Four main purposes of SHM are summarized as to: (a) provide an update on bridge condition during the construction stage; (b) monitor structural operational performance under real loading conditions; (c) detect damage or deterioration; (d) give guidelines for management of maintenance activities. Moreover, with a SHM system installed and performing successfully, economic benefits can be achieved in the long term. For example, Comisu *et al.* (2017) described an integrated bridge monitoring system and its potential economic benefits in Romania in 2016. These researchers concluded that the

inspection and maintenance cost can be reduced by 25%, and the overall lifetime cost of the bridges could be reduced by 10%.

Proved as a dependable technique, SHM has been implemented in numerous disciplines, for example, aircraft (Diamanti & Soutis, 2010; Malere & Santos, 2013; Qiu *et al.*, 2017; Medeiros *et al.*, 2018; Sun *et al.*, 2018), buildings (Ivorra & Pallarés, 2006; Li *et al.*, 2016; Valinejadshoubi *et al.*, 2016; Su *et al.*, 2017; Tsogka *et al.*, 2017; Ubertini *et al.*, 2017; Azzara *et al.*, 2018), and bridges (Ko & Ni, 2005; Wong, 2007; Koo *et al.*, 2013; Yarnold *et al.*, 2015; Comisu *et al.*, 2017; Huang *et al.*, 2017; Yang *et al.*, 2018). For applications of SHM in the twentieth century, the reader can refer to the contributions of Sohn *et al.* (2003) and Brownjohn (2007).

(a). Aircraft reprinted from (Diamanti & Soutis, 2010)

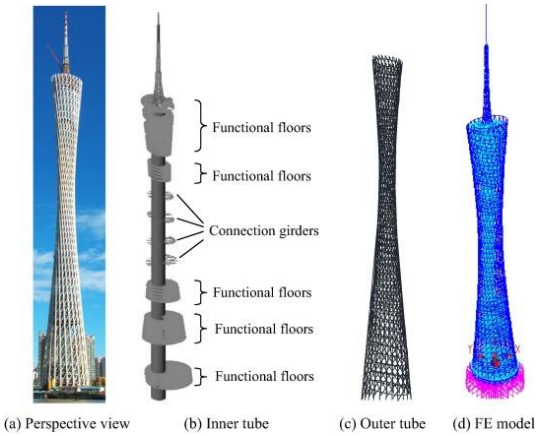

(b). Canton tower reprinted from (Su *et al.*, 2017)

(c). Tamar Bridge reprinted from (Cross *et al.*, 2013)

(d). Aged building reprinted from (Azzara *et al.*, 2018)

Figure 1.3. Examples of SHM implementations

1.1.1 Structural Identification (St-Id)

Another parallel concept is Structural Identification (St-Id), which can be treated as the specific application of SHM in civil structures. According to American Society of Civil Engineers (ASCE) (2013), St-Id uses measured responses to create/update a structural physics-based model for the purpose of performance assessment and decision-making. Figure 1.4 displays the systematic strategy of St-Id, which was summarized by ASCE (2013) and contains six stages of: (1) objectives, observation and conceptualization; (a) measurement, visualization and a priori modelling; (3) controlled experimentation; (4) data processing and feature extraction; (5) selection and calibration of physics-based models; (6) utilization of models for decision-making.

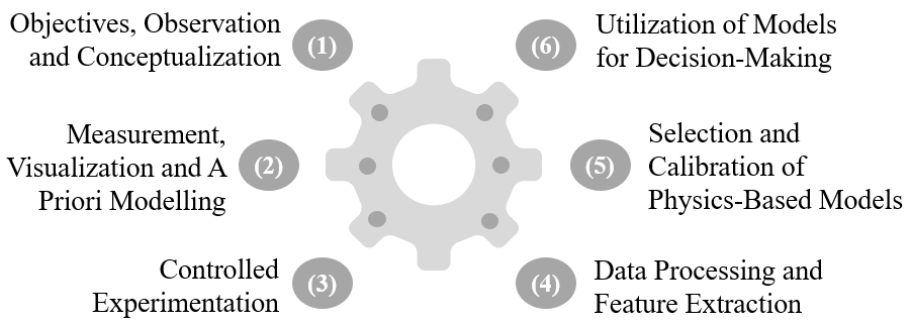

Figure 1.4. Six steps of St-Id

Comparing with the SHM scheme that is displayed in Figure 1.2, the first three steps, i.e. (1)-(3), of St-Id correspond to the data acquisition system of SHM, while steps (4) and (5) are the data interpretation system in SHM. The step (6) of St-Id is same as the last stage of SHM, which is the decision-making step.

This Ph.D. research is focusing on the data interpretation stage of SHM or the data processing and feature extraction, i.e. step (4), of St-Id.

1.1.2 Damage Identification

In civil-structural engineering, the term ‘damage’ can be defined as the appearance of changes in an infrastructure that affect its structural performance adversely (Farrar & Worden, 2007). Therefore, the task of damage identification is to recognise the abnormal data, which is different in some respect from the data collected during the reference period. The reference period is defined as a certain database that the target

structure assumes as an initial or undamaged state. The initial hierarchical structure of damage identification was first proposed by Rytter (1993), as shown in Figure 1.5. This includes four stages of damage detection to identify the existence of anomalies, damage localisation to locate the damage position, damage prediction to evaluate the damage conditions, and damage assessment to predicate the damage influence. Later, Worden and Dulieu-Barton (2004) suggested the addition of one more level, damage classification, to identify the type of the damage, after damage localisation and before damage assessment.

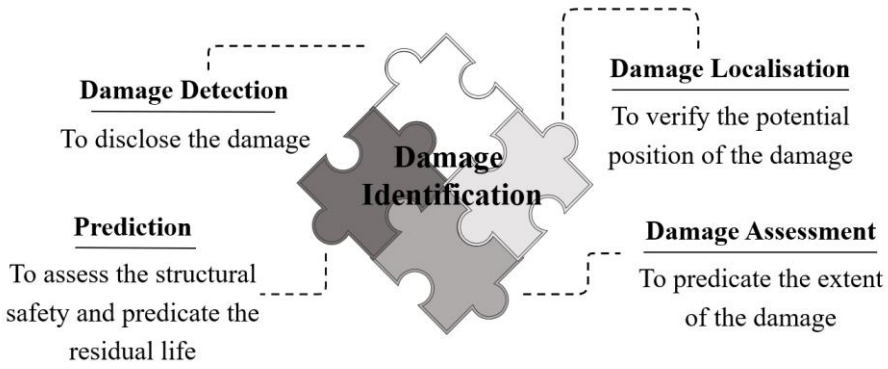

Figure 1.5. Scheme of structural identification

1.2 Research motivation and objectives

To assess the structural condition and damage detection, the SHM system has to analyse the structural response of interest. However, structures are exposed to complex actions that are time varying. Thermal loadings, together with structural loadings and other loading types, can also change the structural characteristics. For example, Sohn (2007) has offered a comprehensive summary of previous findings to show that temperature does affect structural properties, such as material properties (Wood, 1992), structural boundary conditions (Moorty & Roeder, 1992), modal properties (Peeters & De Roeck, 2001; Deraemaeker *et al.*, 2008), and natural frequencies (Ubertini *et al.*, 2017).

The inevitable challenges introduced by environmental parameters cannot be ignored in the real-life SHM applications (Hu *et al.*, 2017), because the damage-induced variations can sometimes be masked by changes due to environmental or operating conditions (Zhao, 2015; Nguyen *et al.*, 2016). To identify the real abnormal variations by considering temperature effects, numerous studies were conducted for

this Ph.D. thesis. The main aim of the research is to develop a temperature-driven anomaly detection method for SHM, which is described in Figure 1.6 with several core scientific concerns.

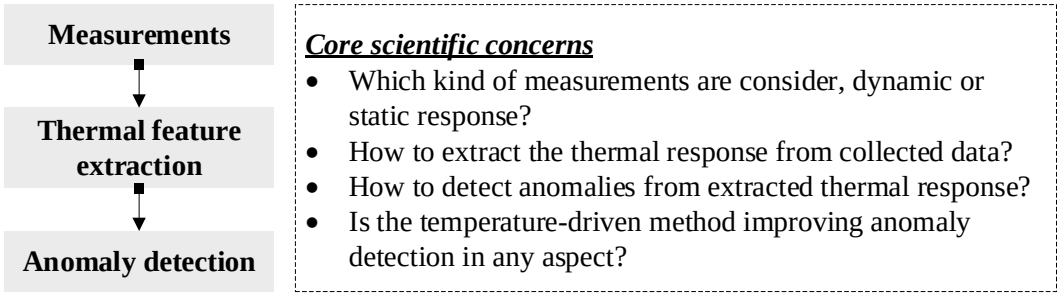

Figure 1.6. Temperature-driven method paradigm with scientific concerns

Considering the scientific concerns and main aim, the following tasks are summarized for this work:

- Benchmark and provide a state-of-the-art research report for the anomaly detection that focuses on cases considering temperature variations.
- Propose thermal feature extraction methods based on Blind Source Separation (BSS) and utilize the extracted thermal responses for damage detection.
- Validate the proposed temperature-driven anomaly detection method with a simulated truss bridge case study, an experimental truss bridge case study, and an in-situ bridge case study.

1.3 Thesis outline

This thesis is divided into seven chapters, as follows:

Chapter 2 presents a literature review on data interpretation methods in the form of a review of current researches on temperature variations.

Chapter 3 elucidates the proposed thermal feature extraction methods, designated as underdetermined and overdetermined methods. The essential core idea, Blind Source Separation (BSS), is introduced in this chapter, followed by a description of the algorithms involved.

Chapter 4 investigates the proposed thermal feature extraction methods using results from a numerical truss model and a laboratory truss experiment.

Chapter 5 outlines the theories behind temperature-driven anomaly detection methods, including Temperature-driven Moving Principal Component Analysis (Td-MPCA), Temperature-driven Robust Regression Analysis (Td-RRA), Temperature-driven One-class Support Vector Machine (Td-OCSVM), and Temperature-driven Artificial Neural Network (Td-ANN).

Chapter 6 presents three case studies, including a numerical truss model, the laboratory truss bridge, and Ricciolo curved viaduct in Switzerland, for evaluating the potential capability of temperature-driven methods to detect anomalies. The performance of the temperature-driven methods, i.e. Td-MPCA, Td-RRA, Td-OCSVM, and Td-ANN, are also evaluated against the performance of methods without temperature-driven process, i.e. MPCA, RRA, SVM, and ANN.

Chapter 7 is for the Concluding Remarks with an explanation of the new contributions' limitations and the author's recommendations for future research in this area.

CHAPTER 2 LITERATURE REVIEW

The purpose of this research is to develop a data-driven anomaly detection method accounting for temperature effects. Therefore, this chapter firstly review the data interpretation methods for the purpose of feature extraction and the novelty detection for Structural Health Monitoring (SHM) or Structural Identification (St-Id), including physics-based and non-physics-based methods. After that, the effect of temperature variations in a SHM system is reviewed with previous solutions dealing with temperature-induced variations. Those solutions can be classified into two clusters, elimination and utilization. The proposed temperature-driven anomaly detection method is based on the idea of utilization, but the novelty factor is this research is extracting thermal response directly and blindly from measurements. Therefore, the last part of this chapter is reviewing all adopted methodologies involved in the proposed methods, which are based on non-physics-based technologies. The temperature-driven anomaly detection method is consisted by two major parts, which are thermal feature extraction and anomalous behaviours detection. The thermal feature extraction employs Blind Source Separation (BSS), Independent Component Analysis (ICA), Empirical Mode Decomposition (EMD), Ensemble Empirical Mode Decomposition (EEMD), and Principal Component Analysis (PCA), while anomaly detection employs Moving Principal Component Analysis (MPCA), RRA, One-Class Support Vector Machine (OCSVM), and Artificial Neural Network (ANN). The organization of this chapter can be found in Figure 2.1.

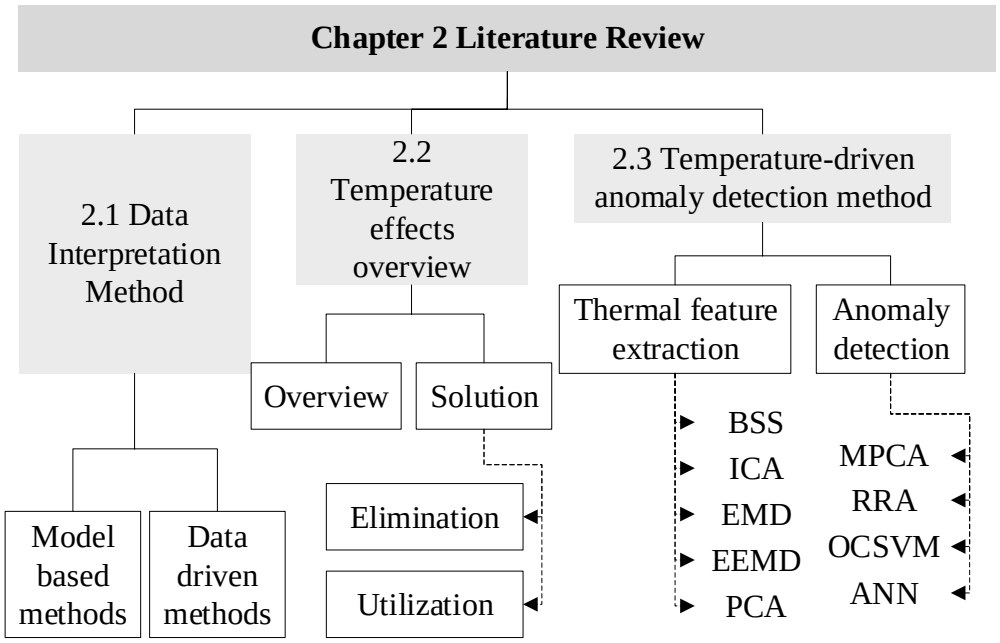

Figure 2.1. Organization of Chapter 2

2.1 Data interpretation of SHM

Variations in structural responses reflect an adverse effect on structural integrity (Van Buren *et al.*, 2017). Commonly, the structural condition is inferred and assessed from changes between physical measurements and numerical predictions from finite element (FE) model (Chang *et al.*, 2003). However, FE models are not compulsory for damage detection. Hence, the method for anomaly detection can be divided into the two streams of physics-based models and direct data interpretation. The detailed distinction can refer to American Society of Civil Engineers (2013). For physics-based structural identification to succeed, an accurate FE model of the real problem is the key in the whole process. This approach has the weakness that the model uncertainty arises at any time from any procedure. For example, an FE model constructed from engineering drawings cannot truly reflect the actual structure's performance. One difference is that the assumed constant mechanical properties cannot be implemented and guaranteed for the in-situ structure due to geometrical uncertainties and inherent material uncertainties. A second difference is that the perfect modelled joints and connections from design drawings cannot simulate the real physical situation. Furthermore, the discrepancy between the real structure and the one designed is inevitable, owing to the practicalities of on-site construction (Chang *et al.*, 2003). To

add to the complexity of solving the problem, it is a major research challenge to predict with confidence all of the evolving patterns of real actions that might happen once the bridge is in use (Inaudi, 2010).

The dynamic test and static test are normally employed to investigate the structural condition as complementary parts (Doebling *et al.*, 1996; Ni *et al.*, 2011). Marefat *et al.* (2004) proposed the load rating factor to assess the plain concrete arch bridge strength, according to the collecting data from the dynamic and static test. Ozden Caglayan *et al.* (2012) then utilized this dynamic and static test results during service condition to refine the bridge model and to assess the bridge strength by utilizing the load rating factor, which is proposed by Marefat *et al.* (2004). Dynamic properties, i.e. modal frequencies, modal damping and mode shapes, have received considerable attention in damage or fault detection (Doebling *et al.*, 1996; MAIA *et al.*, 2003; Sazonov & Klinkhachorn, 2005; Jin, Cho, *et al.*, 2015). The static test has a long tradition in civil engineering, as well as the static structural response, which is the easiest access type of data, i.e. strain and displacement. Inaudi (2010) describes a complete static structural health system with detailed steps and things that engineers should take into account while designing a SHM system for a bridge. Ni *et al.* (2011) used the in-service monitored strain response to evaluate the bridge deck condition of Tsing Ma Bridge. Nguyen *et al.* (2016) used the monitoring displacement data to detect cutting damage on concrete and utilized the first and second derivative of displacement to locate the cutting place on the concrete, as the cutting position supposed to be the point with maximum slope variation. However, the limitation is manifest, firstly, the location is just a rough location, as it is not the exact location of the cutting place. Secondly, if the damage occurred in a symmetrical position along the bridge or there have some uniformly distributed small cracks, it is difficult to use a deflection line or their derivatives to detect or locate the damage. Li *et al.* (2015) proposed to use strain gauges constructed as a Wheatstone bridge to measure the relative displacement between two locations. This idea is then used to measure the relative movements between the concrete deck and steel grid in a concrete-steel composite bridge (Li & Hao, 2015). Li and Hao then used continuous wavelet transform and Hilbert-Huang Transform to investigate relative displacement data, and

they compare the capability of relative displacement as the damage indicator with the normal structural response, i.e. acceleration and displacement.

2.2 Temperature effects overview

As previously introduced in CHAPTER 1, the impact of environmental parameters can strongly affect the results of damage identification, because environmental variations can induce significant cyclic features in measurements (Sohn, 2007; Cross *et al.*, 2012; Xia *et al.*, 2013; Su *et al.*, 2017) and distinctly influence system reliability (Catbas *et al.*, 2008).

Numerous research papers and reports have demonstrated the inevitable impact due to temperature variations in structural response. For example, Helmicki *et al.* (1999) reported that temperature drives many more stresses than traffic. Meanwhile, Catbas *et al.* (2008) observed from one year of monitoring data that the temperature-induced strain can be ten times the traffic-induced strain. Moreover, Cross *et al.* (2013) analysed the temperature and train loads effect on modal properties in both daily and seasonal aspects, while Guo *et al.* (2015) evaluated their dominant contributions to the cumulative displacement of a bridge's expansion joints. For buildings, the research on the large-span gymnasium in China also demonstrated that the environmental influence, especially temperature, obstacles for structural reliability assessment and highly efficient long-term health monitoring (Li *et al.*, 2016). Ubertini *et al.* (2017) and Azzara *et al.* (2018) also assessed the environmental influences on the modal characteristics of aged masonry constructions. For bridges, Westgate (2012) studied the temperature effect on structural natural frequencies of Tsing Ma Bridge. Nguyen *et al.* (2016) pointed out that the stiffness of asphalt and bearings can be influenced by solar irradiation which then affects static test results. From the observation of Hu *et al.* (2017), the crack and inclination of a monitored bridge are heavily affected by seasonal temperature parameters. Moreover, the performance of ultrasound, as an efficient Non-Destructive Testing (NDT) tool to detect damage, is also strongly influenced by the temperature parameter, because the thermal feature can change propagation speed and transducer performance heavily (Herdovics & Cegla, 2018).

Ideally, detecting changes in structural response can refer to an abnormal condition in the structural. However, the temperature variations can induce a distinct thermal

effect, which may be much more evident than the structural damage's effect (Chang *et al.*, 2003; Yarnold *et al.*, 2012). Therefore, in real-life application, the temperature-induced consequence should be considered and interpreted first to reliably identify structural conditions. To cope with the thermal impact issues, the principal efforts have been devoted to the following two solutions, elimination or utilization.

2.2.1 Elimination of temperature effect

Cluster analysis is an efficient solution to eliminate the temperature effect on dynamic responses. The basic idea is to separate the measurements into short sequences to ignore temperature's short-period influence. The theoretical background is that the frequency of temperature variations is much lower than structural modal properties. During each segment, the structural behaviour system is time-invariant. For example, Chen *et al.* analysed the transient alterations in vibration characteristics for a concrete deck with cracks (Chen *et al.*, 1999). The deviation due to cracks reflected in the observed data sufficiently manifests within several minutes. Therefore, the temperature effects can be eliminated in this short-lived data interpretation. Yang *et al.* eliminated the temperature effect indirectly by separating monitoring data, i.e., frequency, into various clusters with the same probability distribution. The subsequent detection is carried out on each independent cluster, in which temperature has a similar effect on structural properties. Therefore, the temperature effects can be eliminated indirectly for short-period data (Yang, Liu, *et al.*, 2016).

Singling out the damage-only-sensitive feature is another solution to eliminate temperature variations. The previous attempt was conducted by Sohn *et al.* (Sohn *et al.*, 2002). They proposed to extract the damage-sensitive feature from the structural system responses that contain a wild range of environmental conditions. The selected feature will be used as input for an auto-associative neural network, while the unmeasured environmental conditions were treated as hidden intrinsic parameters. The other attempt has conducted by Yan *et al.*, who leveraged principal component analysis to eliminate environmental effects on vibration features (Yan *et al.*, 2005a). Cross *et al.* compared three solutions, including cointegration, outlier analysis, and Principal Component Analysis methods, for singling out features that are damage-

sensitive but environment-insensitive (Cross *et al.*, 2012), thereby allowing the environmental effect to be removed.

In other cases, temperature-induced fluctuation is treated as substantial noise in observed signals. Increasing the signal-to-noise ratio by operating Wavelet and Hilbert-Huang transforms can easily avoid temperature effects (Chang *et al.*, 2003). However, the non-negligible conditions are the noise level, i.e., temperature-induced deviation, which must be within 20% of the signal, and the damage should occur during the monitoring period. Herdovics and Cegla proposed a compensation method to interpret ultrasonic signals directly to eliminate the temperature effect without considering transducer type (Herdovics & Cegla, 2018). Other research studies regarding the thermal effect on ultrasound detection can be found in (Konstantinidis *et al.*, 2006; Dan *et al.*, 2014).

2.2.2 Utilization of temperature effect

In recent years, increasing attention regarding direct utilization of temperature related to structural responses for structural identification has been drawn in several papers. Correlating temperature with the structural properties of interest is the most popular way to compensate for temperature effects. The statistical regression analysis and machine learning methods are popular and trustworthy methods for establishing temperature influence models.

However, to utilize the temperature effect, the first crucial step is to identify it. This task motivates the valuable topic of identifying the temperature distribution of structures, especially for long-span bridges (Guo *et al.*, 2015) because the temperature is a critical form of loading condition for long-span bridges (Zhou *et al.*, 2016). The early investigation of temperature distribution in bridges only considered the depth and vertical direction (Zuk, 1965; Emanuel & Hulsey, 1978; Dilger *et al.*, 1983; Kennedy & Soliman, 1987). Since then, more parameters have been considered, including location, material, geometry, and orientation (Tong *et al.*, 2001; Lucas *et al.*, 2003). Recently, Zhou *et al.* (2016)proposed the utilization of transient heat-transfer analysis to simulate temperature in different locations, while Deng *et al.* (2018) mapped the linear correlation pattern between air temperature and the effective temperature inside the box girder according to one year of monitoring data. The

transverse and vertical thermal characteristics have also been investigated by Zhou *et al.* (2016) and Deng *et al.* (2018).

With trustworthy temperature data, the second step is to build a relation model. For example, Peeters and De Roeck (2001) established an eigenfrequency-temperature relation model. This model is based on Auto-regressive and Exogenous (ARX) model from healthy bridge monitoring data. Then this ARX-based model can estimate confidence intervals for eigenfrequency. If a newly recorded eigenfrequency exceeds the estimated confidence intervals, which is simulated by ARX-based model, then the damage can be detected. However, the application on Z-24 Bridge in Switzerland did not consider temperature under freezing point, which makes ARX-based model unable to successfully detect damage below zero degree centigrade. Ni *et al.* (2005) utilized support vector machine (SVM) to identify the correlation pattern of temperature with modal frequencies and indicated the further potential of anomaly detection if the temperature effect can be separated from the measurements. Later, Ni *et al.* (2007) employed linear regression method to predicate the correlation pattern between the expansion joints behaviour, i.e. displacement, and temperature. Similarly, Xu *et al.* (2010) established the statistical model between displacement and effective temperature of Tsing Ma Bridge. After that, Ding and Li (2011) proposed a polynomial regression model to study the relationship between modal frequency and temperature, considering daily and seasonal temperature variation individually. This model was then employed on Runyang Suspension Bridge in China for removing daily temperature effects on frequency.

In recent years, Kromanis and Kripakaran (2014) utilized the measurable structural responses and temperature distributions to develop a regression-based thermal response prediction model, termed as RBTRP methodology. The predicting model is subsequently coupled with anomaly detection methodologies to characterize the response changes by comparing measured and predicted bridge behaviour, named as Temperature-based Measurement Interpretation (TB-MI) (Kromanis & Kripakaran, 2016). Jin *et al.* (2015) combined statistical regression method with the neural network algorithm on a US highway bridge. The dependency of structural natural frequency upon temperature variable was studied by time series analysis method based on the one-year monitoring data. Nguyen *et al.* (2016) adopting the curving fitting method

to find out the linear relation between displacement and temperature. The temperature compensation is subsequently completed by setting a reference temperature and re-calculating all the displacement values into a fixed temperature condition according to the linear relation they have (Nguyen *et al.*, 2016). The uncertainty, in this case, is that the reliability of baseline data, which has to be the health condition. However, this cannot be guaranteed. Yarnold *et al.* proposed to find a three-dimensional best-fit plane among the local strain, global displacements and local temperature, which is a reliable response surface as the representation of the structural condition (Yarnold *et al.*, 2012; Yarnold, 2013; Yarnold & Moon, 2015). This unique correlation can be employed for model calibration and behaviour prediction, and by comparing this correlation every evening, the error due to property changes can be detected. The apparent limitation is ignoring the temperature distribution among the structural cross-section.

However, understanding the temperature distribution and to identifying the relation pattern is a complicated procedure, especially in a long-span bridge, because of the various thermal characteristics of the structural elements, e.g. deck and cable (Zhou *et al.*, 2016). In addition, there are some cases in which temperature measurement is unavailable. In this situation, directly distinguish or extract temperature-induced changes from the mixed structural response is a critical issue.

Therefore, this Ph.D. contributions is proposing a temperature-driven anomaly detection method, which means temperature-induced variations will be extracted first and then employed for damage detection. Following section will introduce the methodologies that utilized in author proposed method.

2.3 Thermal feature extraction

The proposed temperature-driven anomaly detection method is based on the idea of utilizing thermal responses for anomaly detection. Different from previous research efforts, the special attention is devoted to separating temperature-induced response from the measurements. Therefore, the first stage is thermal feature extraction, followed by damage detection stage. The methodologies that are employed in thermal feature extraction is given in this subsection, while the following subsection introduce the methodologies for anomaly detection.

2.3.1 Blind Source Separation (BSS)

Research on information theory and signal processing has recently witnessed tremendous efforts for developing the theory of Blind Source Separation (BSS). BSS represents the problem that recovering unknown sources from a set of observed sources (Cardoso, 1998; Antoni, 2005). The sensor records are the mixture of unknown sources and the mixing information is also unknown (Cardoso, 1998).

To understand the concept of BSS, a footbridge in the University of Warwick is taken as a demonstrator, as shown in Figure 2.2. The inputs for BSS is the measurement databases that recorded from the data acquisition system. However, the input streams, i.e. the static or dynamic responses, are the mixed respond due to the complex loading conditions, which is unknown or with limited knowledge. Therefore, the BSS solution is to find out the decomposing matrix to un-mixing the measurements and separate into the individual structural response, i.e. the structural response due to temperature and the structural response due to human beings' interactions.

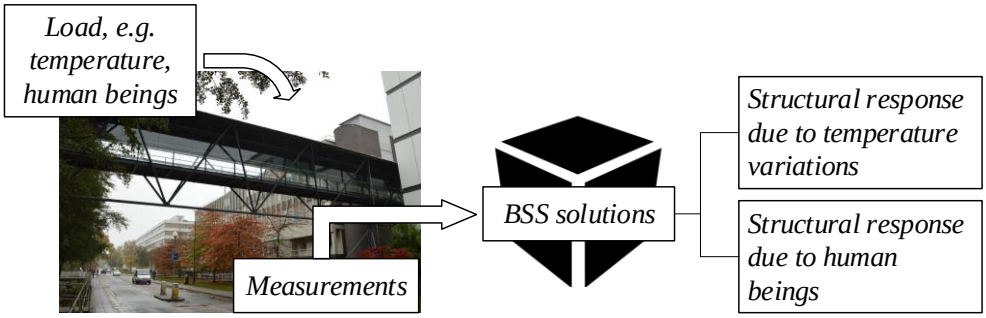

Figure 2.2. The illustrating diagrams of Blind Source Separation

The application of BSS techniques is various, including speech separation, radar signal processing, sonar signal processing, and also biomedical signal processing. Bell and Sejnowski (1995) proposed information maximisation technique for blind separation problem. And Roan *et al.* (2002) then utilized this information maximisation technique to detect damage of gearbox. Later on, Antoni *et al.* (2005) addressed some hinders and challenges while using BSS for vibration signals and proposed a robust separation method based on the short-time Fourier transform. Guo and Kareem (2016) proposed to utilize spatial time-frequency distribution to enhance the blind modal separation for non-stationary data.

BSS is the problem or issue of interest, which is handled by various methodologies. A comprehensive review of BSS algorithms was reviewed by Cichocki (Cichocki, 2002). Antoni *et al.* (2004) also provided a cursory review of BSS approaches as follows:

- Approaches based on periodogram statistics
- High resolution techniques
- Stochastic subspace identification and stabilisation diagrams
- Spectral matrix factorisation
- Approach based on amplitude distributions
- Approach based on 'families of spectra'

Recently, Sadhu *et al.* (2017) reviewed the BSS problem again and summarized them into two clusters: the instantaneous mixing model or the convoluting mixing model. The difference between the above models is the absence consideration of time delay. Basically, blind separation problem is to separate the sources that are linearly mixed, while blind deconvolution is trying to de-convolving signals that were convolved with a delay-line filter effect.

The approaches are also reviewed by Sadhu *et al.* (2017) and this time they classified into two classes, overdetermined and underdetermined. The definition of over- or under- determined is comparing the number of observations channels with the number of original sources.

The detailed classification of the overdetermined solutions are as follows:

- Higher-order statistics, 'the sources are assumed to be statistically independent and therefore various measures of non-Gaussianity (e.g. kurtosis) or information-theoretic measure (e.g. mutual information or negentropy) have been utilized for source separation.' For example, Independent Component Analysis (ICA).
- Second-order statistics, relevant applications can be found in (Tong *et al.*, 1990; Poncelet *et al.*, 2007; Mokhtari *et al.*, 2014; Chen *et al.*, 2015; Seppänen *et al.*, 2015). The auto-correlation structure of the signal is analysed in the second-order statistics without delving into its probabilistic structure.

- Complexity pursuit method. The principle of complexity pursuit can be found in (Hyvärinen, 2001; Stone, 2001). The relative application can be found in (Yang & Nagarajaiah, 2014, 2015; Yang, Nagarajaiah, *et al.*, 2016; Antoni *et al.*, 2017)

The detailed classification of the underdetermined solutions are listed as follows:

- Sparsity representation method. Bofill and Zibulevsky (2001) proposed to utilize sparsity for underdetermined cases. Assistant techniques are time-frequency transformations to achieve sparsity, such as wavelet transform (Kisilev *et al.*, 2004) and short-time Fourier transform (Abrard & Deville, 2005; Aissa-El-Bey *et al.*, 2007).
- Tensor decomposition methods. A tensor is formulated by the covariance matrices of measurements and subsequently is decomposed into covariances by using alternating least squares (Mokios *et al.*, 2006; Sadhu *et al.*, 2017).

2.3.2 Independent Component Analysis (ICA)

The independent component analysis, or known as ICA, is the most popular solution for blind separation problem which is used in this thesis. ICA is to separate a set of non-Gaussian data into a new collection of variables, which are statistically independent. The original idea of ICA was first proposed by Comon (1994), which expressed as the operation of ICA is to maximize the statistical independence among its separated components by performing a linear transformation on the target data.

There are some applications that leverage ICA along with other techniques for structural identification or damage detection. For instance, Early application of ICA can be found in (Chaumette *et al.*, 1993). In the early 1990s, Jutten and Herault proposed sources separation method, combing Independent Component Analysis and a recursive interconnected neural network (Comon *et al.*, 1991; Jutten & Herault, 1991). The method used high-order statistical moments and been tested in several simple single processing and image processing cases. ICA, as a powerful tool for blind separation or blind deconvolution, can also be addressed in (Bell & Sejnowski, 1995). In the recent decade, ICA was employed with the artificial neural network for detecting damage diagnosis (Zang *et al.*, 2004). The authors decomposed time history records into a set of independent components and the mixing matrix. And treat the

mixing matrix as the representation of structural vibration features. The two parts of ICA output are subsequently utilized to build a neural network model, as an indicator for detecting damage. Poncelet *et al.* (2007) applied ICA to estimate the damping ratios and modal frequencies in mechanical systems. The applications mentioned above do not take temperature influence in consideration. In this study, the ICA will be leveraged for extracting mechanical strain induced by seasonal and daily temperature respectively. Yang and Nagarajaiah (2013) combined wavelet transform with ICA to obtain the recovered mixing matrix, which contains interesting damage information. More applications of ICA for modal identification based on dynamic characteristics can be found in researchers conducted by Chang *et al.* and Yang and Nagarajaiah (Yang & Nagarajaiah, 2013; Chang *et al.*, 2016).

2.3.3 EMD/EEMD

The mode decomposition can be viewed as an expansion of the single-channel target data. The empirical mode decomposition (EMD), proposed by Huang et al in 1998 (Huang *et al.*, 1998), is used to decompose a single-channel data, while the ensemble empirical mode decomposition (EEMD), developed by Wu and Huang in 2009 (Wu & Huang, 2009), is the noise-assisted version of EMD, which will be considered as an adaptive mode decomposition method in this research. The essence of both empirical mode decomposition (EMD) and ensemble empirical mode decomposition (EEMD) is to directly extract intrinsic mode functions (IMFs) with various intrinsic time scales, which is based on local characteristics of target data. Since the intrinsic mode function can reveal the oscillation mode that is embedded in the target data, the EMD and EEMD are employed in this study to identify the intrinsic oscillatory modes in mixed structural response recorded by each sensor. Hence, the data can be decomposed subsequently according to their characteristic timescales for further blind separation.

Empirical mode decomposition (EMD) and ensemble empirical mode decomposition (EEMD) have been widely employed in vibration-based structural health monitoring, but not considering temperature effects. Such as, Yang *et al.* demonstrated that EMD is capable of detecting damage, reflected as sudden spikes in first intrinsic mode function separated by EMD (Yang, *et al.*, 2004). However, the

successful applications are based on the following assumptions: the structural acceleration is not polluted by noise and damage induces an abrupt change in stiffness value. Those hypotheses are really difficult to achieve in practice.

O'Brien *et al.* (2017) proposed to apply EMD to decompose vehicle driven responses for damage detection and location. As previous research has demonstrated that a passing vehicle loading can activate three main components in mixed responses, which are vehicle frequency, bridge natural frequency and the vehicle-induced frequency (Yang, *et al.*, 2004). Among those components, the vehicle-induced frequency is more sensitive to damage and has the potential to locating the damage (He & Zhu, 2016). Other applications of EMD and EEMD for damage detection have been summarized in (Amezquita-Sanchez & Adeli, 2016).

2.3.4 Principal Component Analysis (PCA)

According to Lanata and Del Grosso (2006) and Jolliffe (2011), PCA was first formulated by Peason in 1901 and Hotelling (1933). The substantial descriptions of PCA can be found in (Jolliffe, 2011) and mathematical background information related to this research will be introduced in the next chapter.

According to Pimentel *et al.* (Pimentel *et al.*, 2014), the principal component analysis is one of the spectral methods (Chandola *et al.*, 2009). As described by Chandola *et al.*, the spectral methods assume that data can be projected or embedded into a lower dimensional subspace in which 'normal' data can be better distinguished from 'abnormal' data. As one of the proper orthogonal decomposition algorithm, the analysis of the behaviour in terms of eigenvalues and eigenfunctions of the covariance matrix of the data set gives a good indication of the damage initiation and provides information about the severity of the damage (Lanata & Del Grosso, 2006).

As one of the proper orthogonal decomposition (POD) techniques (Liang, Lee, Lim, Lin, Lee & Wu, 2002; Liang, Lee, Lim, Lin, Lee & Ww, 2002), the utilization of PCA in Structural Health Monitoring is mainly divided in the following three parts: (a) data pattern recognition, (b) data enhancing, and (c) data reduction (Figueiredo *et al.*, 2009).

For the purpose of data pattern recognition, generally, researchers are using a certain reference period data obtained from health structure to construct a statistical model to represent the structure's normal condition. For example, Mujica *et al.* (2014) utilized PCA to obtain a baseline pattern of the structure as an undamaged state and then combined with hypothesis testing for damage detection. To obtain the reference model, they collected structural dynamic responses from several sensors of several experiments and applied PCA on all responses. In this way, the dynamics with essential effects can be distinguished from those are redundant in the new coordinates by applying PCA. For the new inspect test, PCA has applied again, and damage can be discerned by comparing those essential dynamics with those in the baseline model. Relevant research can be found in (Mujica *et al.*, 2011). Moreover, PCA has also been examined by Cross *et al.* (2012) for the purpose to create features that are sensitive to damage but insensitive to the environment. The data of interest is mapped by applying PCA, however, the components with less variance in the original data are of interested, called minor components. The minor components are the environment-insensitive features. However, this solution has its shadow zone. For example, if the damage information manifests as one of the principal components, then it will be ignored. One more concern addressed in their paper is that minor components may not be sufficient enough for removing environmental trends, due to the orthogonality constriction among all principal components. Other researches can be found in (Yan *et al.*, 2005b,a). However, there are still reports consider above works' limitation, for example, a certain reference period data cannot represent the structural normal condition if a structure or system has non-stationary and time-invariant characteristic (Moser & Moaveni, 2011; Jin, Cho, *et al.*, 2015). The detailed explanation of this limitation and solutions are provided by Jin *et al.* as well (Jin, Cho, *et al.*, 2015).

For the purpose of data reduction, PCA is representing the target sources into a different space to find a low-dimensional representation. Loh *et al.* (2017) applied PCA to compress frequency response function data collected from a twin-tower steel structure. Datteo *et al.* (2017) combined PCA with Auto Regression model techniques to represent the structural representation in a concise way. In this study, the main function of PCA is data dimension reduction.

There are some other applications, for example, PCA-based anomaly detection approach has been proposed by Shyu *et al.* (2003) proposed and applied in intrusion area. An application of using approximate principal components was given by Dutta *et al.* in astronomy catalogs (Dutta *et al.*, 2007). Moreover, an application on a wooden bridge model was conducted by Toivola *et al.* (2010). For other application can refer to (Timusk *et al.*, 2008; Lämsä & Raiko, 2010; McBain & Timusk, 2011; Chen *et al.*, 2012). Cavadas *et al.* (2013) used PCA to enhance the discrimination of features after damage affected the structure. Mojtahedi *et al.* (2013) used PCA to discern the nonlinearity of measured data of offshore structure.

2.4 Anomaly detection

2.4.1 Moving Principal Component Analysis (MPCA)

MPCA is the abbreviation of moving principal component analysis (Lanata & Posenato, 2007; Lanata *et al.*, 2007; Posenato *et al.*, 2008) which is based on the classical principal component analysis, also known as PCA (Jolliffe, 2011). The description of PCA can be found in the Section 2.3.4.

The algorithm MPCA is designed to figure out the characteristics of a certain time series measurements. This certain period record is named as the initialization phase, in which the structure is supposed to be in healthy condition. After that, anomalous behaviours can be identified according to this initial phase. This certain period is also denominated as window size. The covariance matrix of data inside an active window is calculated and then moving in time; more details can be found in (Posenato *et al.*, 2010; Laory *et al.*, 2011). Cavadas *et al.* (2013) examined the performance of MPCA and found the MPCA could give an early detection of anomalous behaviours.

With the moving window, the computational cost is lower for each step and detection of the presence of new situations is timelier because old measurements do not buffer results. The window size should be sufficiently large, so that the periodic variability, i.e. the seasonal temperature cycles, can be exposed, while rapidity of computation can be guaranteed at the same time. Therefore, the window size should be theoretically multiple of periodic variability. In the following numerical simulation, the one-year window is chosen in the study considering lower computational cost,

instead of two-year window size in (Posenato *et al.*, 2008), because integrated and continuous measurements can be obtained. After selecting the window size, the first principal component, i.e. the eigenvector related to the main eigenvalues, is analysed at each step. The standard deviation of eigenvectors from the first set of data within the fixed window is recorded as σ, which is subsequently used for threshold definition. According to previous researches (Posenato *et al.*, 2008, 2010), the confidence interval is defined as 3σ off the initial data's eigenvectors.

2.4.2 Robust Regression Analysis (RRA)

Outlier detection has attracted considerable interest in various areas. The core idea of Robust Regression Analysis (RRA) is to investigate the correlation among all sensors during the reference period. The thresholds of confidence intervals are also defined based on this reference period. After that, the focus in the practical phase is on the anomalous behaviours among those correlated pairs of sensors, or in another word the behaviour exceeds the thresholds when compared with the previous state during the reference period.

There is one limitation that has to be highlighted here, the selection of proper threshold parameters will affect the success of robust regression methods. Unfortunately, the proper choice is based on experience (Yuen & Ortiz, 2017).

The performance of RRA has been investigated in several papers (Posenato *et al.*, 2008; Laory *et al.*, 2011; Cavadas *et al.*, 2013; Dervilis *et al.*, 2015).

2.4.3 One-Class Support Vector Machine (OCSVM)

In contrast to traditional SVMs, one-class SVMs attempt to learn a decision boundary that achieves the maximum separation between the points and the origin. (Amer *et al.*, 2013)

The one class SVM was first proposed by Schölkopf *et al.* (Schölkopf *et al.*, 2001). The general SVM classification can be addressed as the multi-class classification problem. The one-class SVM (OCSVM) can also be viewed as the traditional two-class problem. But the training dataset should only contain normal data set, or with several data points from the other class, but the number of data from the normal dataset

is far more than data from another class. Hence, the OCSVM is to find the hyperplane or decision boundary to separate the training data from the origin with the maximum margin.

2.4.4 Artificial Neural Network (ANN)

The artificial neural network approaches are the most common learning machines that used for pattern recognition and novelty detection (Markou & Singh, 2003; Hernandez-Garcia & Sanchez-Silva, 2007). Because in the engineering discipline, the ANN model can learn a latent relation between excitation signal (i.e. input) and structural response (output data), even the data are fuzzy or incomplete (Nazarko & Ziemiański, 2011). There are several popular network types that used in damage detection, which are the Multi-Layer Perceptron (MLP) (Moya *et al.*, 1993), self-organising maps (Kohonen, 1998), Radial Basis Function networks (RBF) (Lange *et al.*, 1997), Hopfield networks (Chandola *et al.*, 2009) and oscillatory networks (Tuong Vinh Ho & Rouat, 1998). The review of the above networks can be found in (Markou & Singh, 2003; Pimentel *et al.*, 2014).

The transfer function, also known as activation function, is utilized to transfer or map the activating nodes into an output signal (Sibi *et al.*, 2013), as shown in Figure 2.3. The 'weighted sum' of the inputs with initially settled weight coefficient and bias is computed are transferred to the activation function. The transfer function is inside the hidden layers and is defined by the ANN architecture, which is also utilized to define the confidence interval (Hernandez-Garcia & Sanchez-Silva, 2007). The proper selection of the activation function will certainly affect the accuracy and performance of the neural network (Chiba *et al.*, 2018) and also have an evident effect on the convergence of BP learning algorithms (Chandra & Singh, 2004). According to Sibi *et al.* (2013) and Chiba *et al.* (2018), there are several common activation functions as follows: linear (identify function); sigmoid (logistic function); binary step; sigmoid symmetric; sigmoid stepwise; Gaussian symmetric etc. The Back Propagation (BP) network, a multi-layer perceptron network, is the most common model that has been widely used (Huang, 2010; Nazarko & Ziemiański, 2011; Nazarko & Ziemianski, 2016). The feed-forward BP network is adopted in this research.

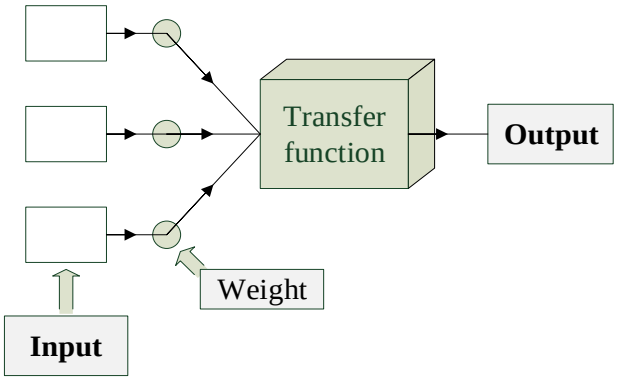

Figure 2.3. The transfer function in the neural network

2.5 Concluding remarks

The contribution of this Ph.D. work is to develop model-free methods for thermal feature extraction and anomaly detection considering temperature effects. Therefore, the Section 2.1 of this literature review has first reviewed the model-based and model-free data interpretation methods After that, the Section 2.2 has conducted the review work on previous research work considering temperature effects. The novelty of this work is extracting temperature-induced structural responses directly and blindly from the measurements. The proposed method in author's PhD work for thermal feature extraction is based on blind source separation, which is reviewed in Section 2.3. After that the extracted thermal features are utilized for anomaly detection. The methodologies adopted are all introduced in Section 2.4. The following CHAPTER 3 will describe the mathematical background of involved methodologies.

CHAPTER 3 THERMAL FEATURES EXTRACTION: METHODOLOGY

This chapter presents the thermal features extraction method that inspired from Blind Source Separation (BSS) applications, which is organized as follows. The overview of thermal features extraction is first presented, which can be classified into under- or over-determined cases. The BSS is introduced next since this is the core idea of proposed thermal extraction method. The last three sections in the chapter are the introduction of all involved algorithms, e.g. Empirical Mode Decomposition (EMD), Ensemble Empirical Mode Decomposition (EEMD), Principal Component Analysis (PCA) and Independent Component Analysis (ICA).

3.1 Overview of thermal features extraction

First of all, the definition of underdetermined and overdetermined is given, as the extraction methods are clustered into these two approaches. For example, in this study, the underdetermined approaches are suitable for limited measurements, i.e. single-channel case will be considered and discussed, while the overdetermined approaches are proposed for multi-channel observations. The original classification of under/over-determination is reposed on the correlation of outputs versus inputs, referring to Figure 3.1. For example, if the number of outputs is over the number of inputs, this condition

is classified into overdetermined case, whose complementary situation, i.e. the channels of outputs are equal or less than the inputs, is called underdetermined.

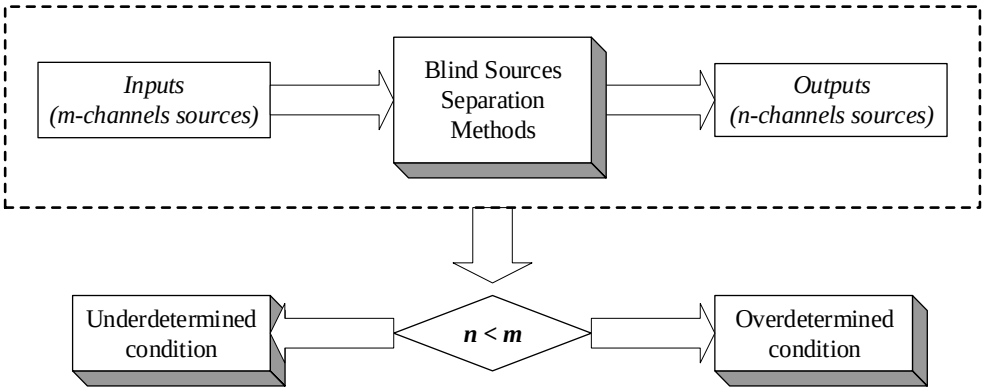

Figure 3.1. Classification of under/over-determined conditions

The process overview of the whole thermal feature extraction idea can be found in Figure 3.2. For the underdetermined approaches, three steps are included, which are mode decomposition, data reduction and blind separation. For the overdetermined approaches, the measurements are first pre-indicated before going through blind separation procedure. The core idea is the blind separation, which is also known as Blind Source Separation (BSS). The next section will cover more details of BSS.

In some cases, only limited number of sensors are available in a place of interest. Therefore, the underdetermined solutions are designed and proposed to use those limited measurements as much as possible, or in another word, individually.

There have some other cases that more than one sensor records are available. The approaches for BSS problem can interpret on the target sources directly, which are clustered into overdetermined solutions. However, the Principal Component Analysis (PCA) is proposed to pre-interpret on the database before the blind separation to provide a pre-indication for blind separation.

Two potential methods, designated as EPI and EEPI, have been proposed in this study. The general framework of EPI and EEPI can be found in Figure 3.3, while detailed descriptions are presented in the following subsections. The feature extraction method is a combination of mode decomposition, data reduction and blind separation. The methodologies included are Empirical Mode Decomposition (EMD), Ensemble Empirical Mode Decomposition (EEMD), Principal Component Analysis (PCA) and

Independent Component Analysis (ICA), which will be described in detail in the follow-up subsections.

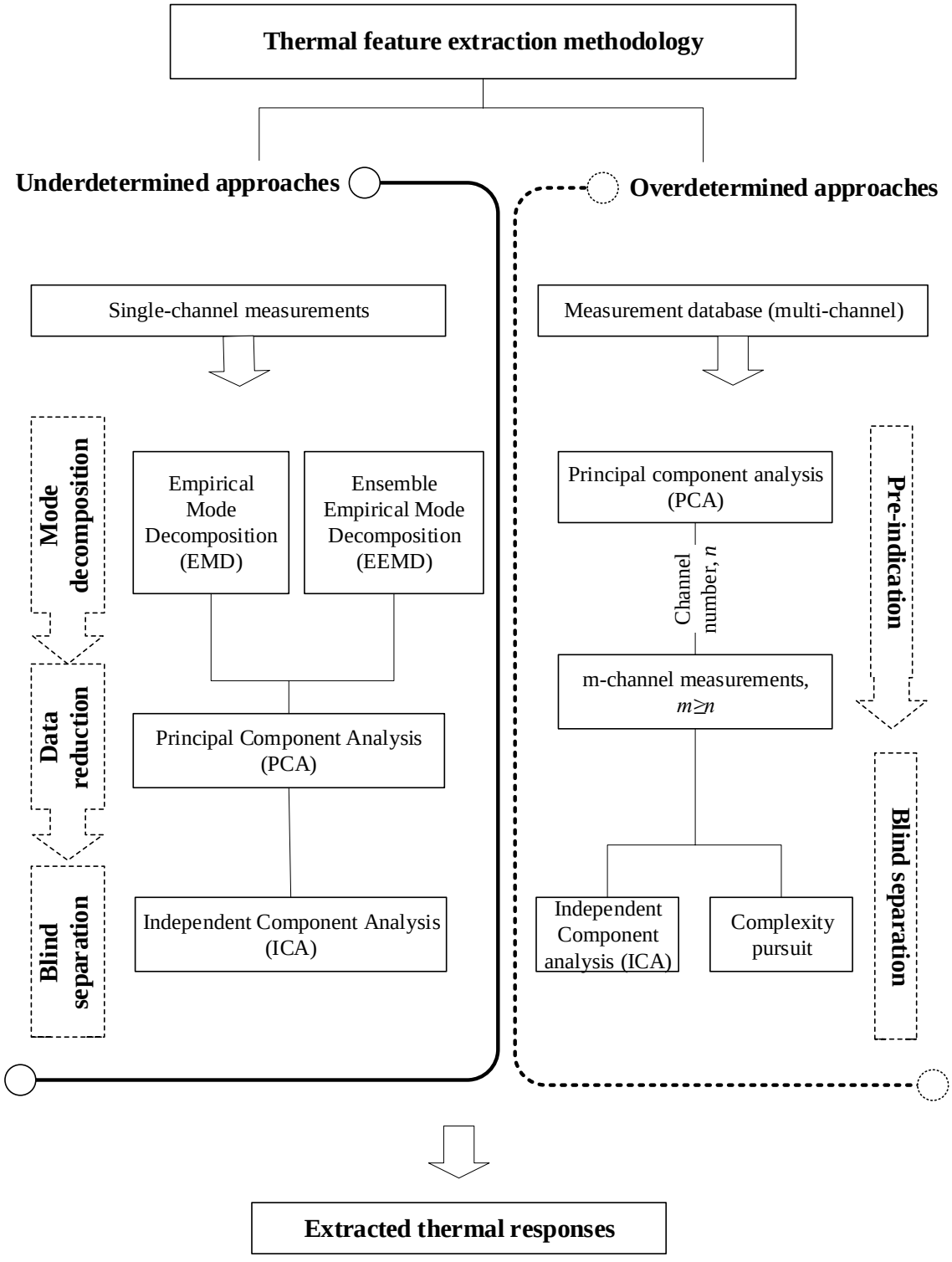

Figure 3.2. Overview of thermal extraction method

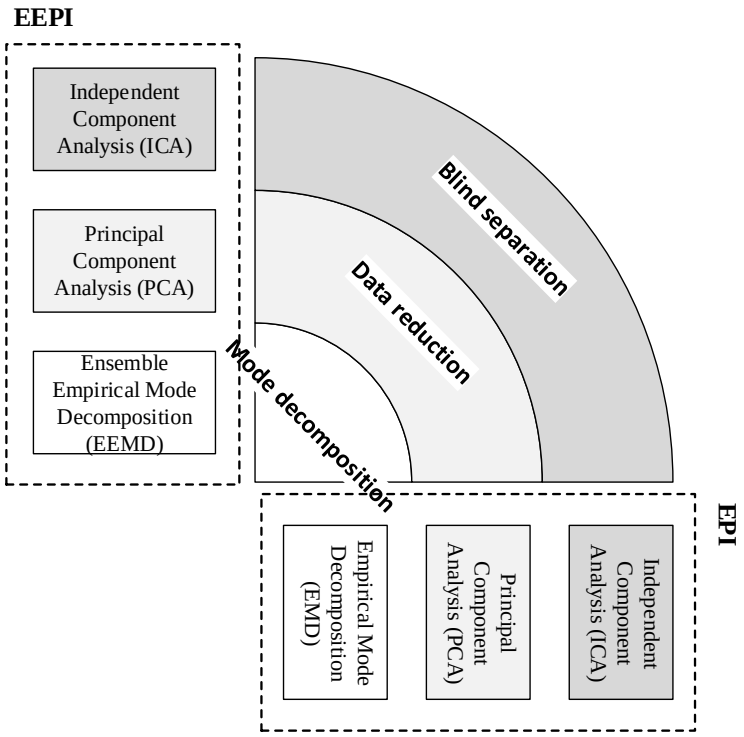

Figure 3.3. General process of underdetermined solutions (EEPI & EPI)

3.2 Blind Source Separation (BSS)

The core idea of the proposed method is the application of Blind Source Separation, also known as BSS. The cursory background information of BSS has been introduced in CHAPTER 2, including its definition, background, development and applications. In this chapter, the fundamental principles of BSS are described briefly. More detailed information can be found in following references (Cardoso, 1998; Cichocki, 2002; Choi *et al.*, 2005).

For the sake of brief and simplicity, the following Eq. 3-1 will be taken as an illustration to explain BSS theory.

$$\begin{cases} x_1(t) = a_{11}s_1(t) + a_{12}s_2(t) \\ x_2(t) = a_{21}s_1(t) + a_{22}s_2(t) \end{cases}$$

Eq. 3-1

Where x_1 and x_2 are observed signals, usually recorded by sensors attached in different place. Therefore, they contain mixture responses of the original sources, s_1 and s_2, with various weights. Those mixing weights, a_{11}, a_{12}, a_{21} and a_{22}, are constant coefficients and assumed as unknown parameters. Hence the aim of blind

source separation is to reveal unrecorded sources, i.e. s_1 and s_2, with limited prior knowledge, for example, only x_1 and x_2 are available.

BSS is to recover original signals from mixed sources, without knowledge of the mixing process and original sources themselves. Most of BSS algorithms tackle the separation problem when the channel number of the mixtures, $\boldsymbol{X}$, is larger than or equal to the channel number of original sources, $\boldsymbol{S}$.

3.3 EMD/EEMD

The algorithms employed for mode decomposition are Empirical Mode Decomposition (EMD) and Ensemble Empirical Mode Decomposition (EEMD). The matrix S in Eq. 3-2 contains all sensor measurements, where the indices n_s and n_t represent the number of sensors and data points in the time domain, respectively. Each column records, $S_i(t)$, can be decomposed into a collection of intrinsic mode functions (IMFs), designated as $\sum_{k=1}^{K} C_k$ in Eq. 3-3, by utilizing EMD/EEMD.

$$S = \begin{bmatrix} S_1(t_1) & \cdots & S_{n_s}(t_1) \\ \vdots & \ddots & \vdots \\ S_1(t_{n_t}) & \cdots & S_{n_s}(t_{n_t}) \end{bmatrix}$$

Eq. 3-2

$$S_i(t) = \sum_{k=1}^{K} C_k \, , i = 1,2, \dots , n_s$$

Eq. 3-3

The flowchart of EEMD can be found in Figure 3.4. The ensemble sifting time is designated as N_{trial}.The final collection of IMFs, C_{Ntrial}, is the ensemble mean of total trails, shown in Figure 3.4 (a), while Figure 3.4 (b) lists the sifting processes of each trail. As a noise-assisted method, the added white noise strength is defined by noise signal ratio, designated as *NSR*, which is the ratio of standard deviation between added noise (σ_{noise}) and target signal (σ_{signal}), given in Eq. 3-4. The recommended *NSR* value is 0.2 (Wu & Huang, 2009), which means the assisted noise has the 0.2 times standard deviation as target signal. However, the recommended *NSR* value will be validated in this research. Therefore, the EMD process is without noise, i.e. $NSR = 0$ and with only one trail.

$$NSR = \frac{\sigma_{noise}}{\sigma_{signal}}$$

Eq. 3-4

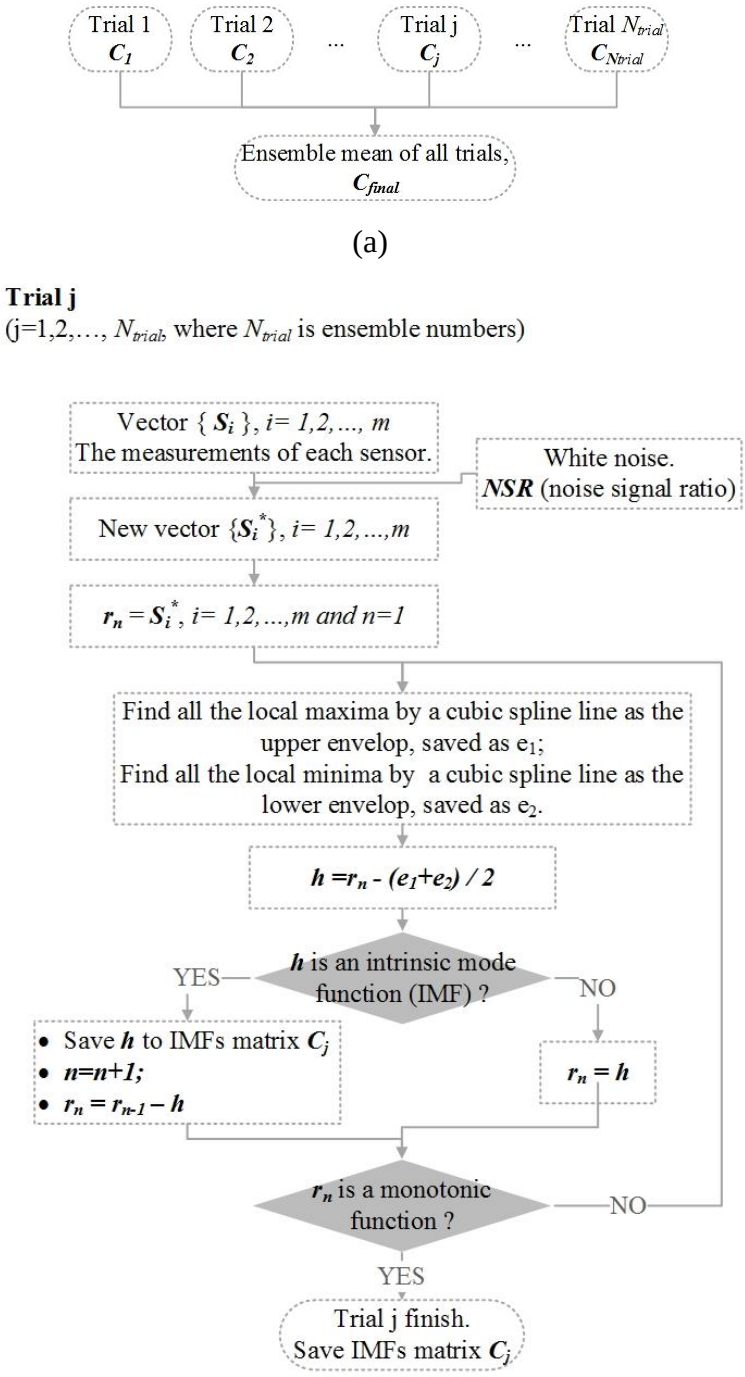

Figure 3.4. Ensemble empirical mode decomposition theoretical model: (a) final ensemble mean trial; (b) single trial

As mentioned, the purpose of deposing target signal into a group intrinsic mode functions (IMFs) is to provide components whose instantaneous frequencies have physical meaning. Therefore, a satisfactory IMF should meet the necessary conditions

when defining a meaningful instantaneous frequency. Hence, two essential conditions should be satisfied by a qualified intrinsic mode function of sensor measurements, as the first judgement process shown in Figure 3.4 (b). The first condition is the difference of extrema points number and zero crossings number should less than or equal to one in the whole sifted data set, designated as ***h*** in Figure 3.4 (b). The second rule is the mean value of the upper envelop, e_1, and the lower envelop, e_2, is zero. To stop the sifting process, the residue, r_n should be a monotonic function, which means no more IMF can be extracted from r_n. Readers who are interested in further theoretical background of EMD and EEMD may refer to the papers (Huang *et al.*, 1998; Wu & Huang, 2009).

The results of mode decomposition, no matter employing EMD or EEMD, are a collection of IMFs, C_{final}, which will be dimensionally reduced by PCA before applying blind separation method.

3.4 Principal Component Analysis

To compress the size of the finial group of intrinsic mode functions, the matrix C_{final} is interpreted by Principal Component Analysis (PCA). PCA is a statistic data interpretation method for compressing the size of a dataset by transforming it to a principal component space. The reformed new variables are called principal components. There are some specific features of those principal components, such as:

- All the principal components are uncorrelated and orthogonal to each other;
- All the principal components are ordered, which means the 1st principal component has the largest possible variance, while the last one has the smallest variance.

The data to be analysed by PCA function is the final collection of intrinsic mode functions, matrix C_{final}, which is the output from mode decomposition. Each column in C_{final} represents an intrinsic mode function, and overall component number is recorded as n_c. For the sake of simplicity, the set of C_{final} is modified into a vector of IMFs, abbreviated as a vector-matrix notation c.

The principal component analysis is firstly calculating the covariance matrix of c. The variance of this covariance matrix is of interest. Its eigenvectors are subsequently obtained and sorted in the descending order of their corresponding eigenvalues. Thus, the original data set, c, can be reconstructed into a smaller data set, designated as the principal components.

The covariance matrix of the original data c can be termed as matrix V, and the eigenvector of V is abbreviated as matrix D ,whose columns are rearranged according to V 's eigenvalues, from the highest eigenvalue to the lowest. Then, the first m columns of D, which can account for over 95% of the variance, will be saved as the transform matrix A and the original data c will be transformed to the new principal components matrix, P, which contains m orthogonal principal components, often abbreviated as PCs. Those PCs will then be used for blind separation.

As a quantitatively rigorous method for data dimensionality reduction, the core conversion of PCA is the orthogonal decomposition of the covariance matrix of the target variables, which can generate a new and smaller set of uncorrelated variables, called principal components, from the target variables. Those principal components are the linear combination of the original variables and orthogonal to each other without any redundant information. The basic procedures of PCA are summarized in Figure 3.5, where a matrix **X** contains all structural measurements from all sensors. Each column represents an individual sensor's time series record, while each row shows the collected data from all sensors at a specific time step, seeing Figure 3.5.

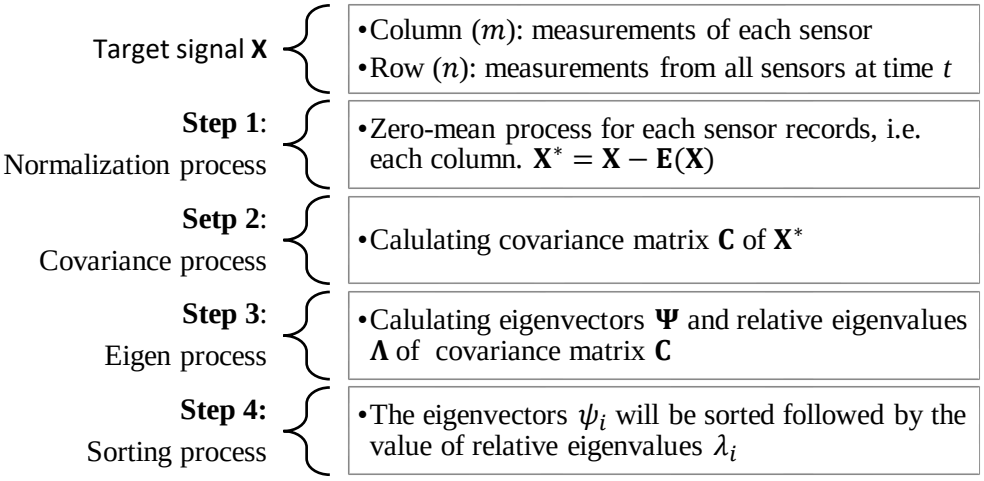

Figure 3.5. Basic theory of Principal Component Analysis

In this study, the step 2 and 3 in Figure 3.5 is achieved by using singular value decomposition (SVD), since Jolliffe (2002) suggested that SVD might be the most computationally efficient solution to find principal components for PCA. The basic algebraic theory of SVD is decomposing $\mathbf{X}^*$ (step 1 in Figure 3.5) as in Eq. 3-5.

$$\mathbf{X}^* = \mathbf{ULA^T}$$

Eq. 3-5

$$x_{ij}^* = \sum_{k=1}^{r} u_{ik} l_k^{1/2} a_{jk}$$

Eq. 3-6

The $\mathbf{X}^*$matrix contains m sensor channels with n independent observations. The $m \times r$ orthonormal matrix $\mathbf{A}$ is eigenvectors of $(\mathbf{X}^*)^{\boldsymbol{T}}\boldsymbol{X}^*$, and $\mathbf{L}$ is a $r \times r$ diagonal matrix that contains square roots of eigenvalues of $(\mathbf{X}^*)^{\boldsymbol{T}}\boldsymbol{X}^*$, which means its elements l_k is the kth eigenvalue of $(\mathbf{X}^*)^{\boldsymbol{T}}\boldsymbol{X}^*$. The extra information from SVD separation is the $n \times r$ orthonormal matrix $\mathbf{U}$ which relates with PC scores. The PC scores represents the $\mathbf{X}^*$ in new principal component space, i.e. each independent observation on each principal component space. The definition of PC scores, notated as $\mathbf{Z}$ in Eq. 3-7, is given by Jolliffe (2002), whose *k*th column represents the *k*th PC scores.

$$\mathbf{Z} = \mathbf{X}^*\mathbf{A} = \mathbf{ULA^TA} = \mathbf{UL}$$

Eq. 3-7

Therefore, the eigenvalues of the *k*th PC score is $l_k/(m-1)$, where $k = 1,2,\dots,m$, since the l_k is the kth eigenvalue of $(\mathbf{X}^*)^{\boldsymbol{T}}\boldsymbol{X}^*$, consequently the kth eigenvalue of covariance matrix $\mathbf{C}$ is $l_k/(m-1)$ $(\mathbf{X}^*)^{\boldsymbol{T}}\boldsymbol{X}^*$. Hence, the variance of matrix $\mathbf{U}$ is $1/(m-1)$.

The target of SVD is to find out a new $m \times n$ matrix, $\boldsymbol{X_{new}}$, with the first p PCs ($p < r$) can minimize the Euclidean norm of difference between $\boldsymbol{X}^*$ and $\boldsymbol{X_{new}}$, $\|\mathbf{X_{new}} - \mathbf{X}^*\|$.

$$\left\|x_{new,ij} - x_{ij}^*\right\| = \sum_{i=1}^{m}\sum_{j=1}^{n}\left(x_{new,ij} - x_{ij}\right)^2$$

Eq. 3-8

Therefore, the information that SVD can provide is not only the coefficients and variances for the PCs, but also the PC scores, which will be used for visualized biplot construction (Gabriel, 1971).

The first principal component is the eigenvector with the largest eigenvalue, which means when the projected original variables on this direction have the maximum variances among all eigenvector-eigenvalue choices (Hubert *et al.*, 2005; Jolliffe, 2011). Therefore, the first few principal components contain most characteristics of the whole observations since their variance together can exceed 80% or 90% of the total variances of observations. In this study, the cumulative percentage of selected principal components should be over 95% of total variation.

In this study, PCA is employed as a tool to indicate the intrinsic variables of the observations, or in another word, the number of main driving forces that contribute the overall strains. This is utilized as a guide for fast ICA separation. As mentioned, the bioplots are based on the singular value decomposition (SVD). As a graphical representation, it is utilized in case study section to visualize the correlation between target signals and principal components, i.e. the magnitude and sign of target signal's contribution to the components.

3.5 Independent Component Analysis

The collection of observations, matrix *S*, in Eq. 3-1 can be given as an example to explain ICA. Eq. 3-9 shows the transposition process of matrix *S*, where the indices *t* is the sample index that equals to $1,2,\dots,n_t$.

$$S^T = \begin{bmatrix} S_1(t_1) & \cdots & S_1(t_{n_t}) \\ \vdots & \ddots & \vdots \\ S_{n_s}(t_1) & \cdots & S_{n_s}(t_{n_t}) \end{bmatrix} = \begin{pmatrix} S_1(t) \\ \vdots \\ S_{n_s}(t) \end{pmatrix}$$

Eq. 3-9

The observations can be assumed as the linear mixture of independent components S^*, abbreviated as ICs, which are shown in Eq. 3-10.

$$\begin{pmatrix} S_1(t) \\ \vdots \\ S_{n_s}(t) \end{pmatrix} = M \begin{pmatrix} S_1^*(t) \\ \vdots \\ S_{n_s}^*(t) \end{pmatrix}$$

Eq. 3-10

Where M is some unknown mixing matrix and n_s^* is the number of latent independent components, which might not be equal to observed mixtures. To simplify ICA estimation, centring and whitening the observable variables are the two necessary pre-processing steps; details can be find in (Hyvärinen *et al.*, 2004). Since independent component analysis is a mature algorithm, more details can be found in Hyvärinen's work. However, two ambiguities of ICA must be mentioned as it will be used in next numerical model analysis section. The first is that the independent components (ICs) may have different magnitude when compared with observable data. This is because the scalar change can somehow cancel between $s_i^*(t)$ and the corresponding column m_i in mixing matrix M. For example, Equation 5 is simplified by vector-matrix notation, see Eq. 3-11. If $s_i^*(t)$ is multiplied by Δ_i, the effect can be offset by dividing m_i with the same scalar, as showing in Eq. 3-12.

$$S = MS^* = \sum_{i=1}^{n} m_i S_i^*$$

Eq. 3-11

$$S = \sum_{i=1}^{n} m_i S_i^* = \sum_i \left(\frac{1}{\Delta_i} m_i\right)(s_i^* \Delta_i)$$

Eq. 3-12

Therefore, the variances and magnitude of the ICs cannot be guaranteed and determined. The solution for this restriction is to fix the magnitudes of ICs with unit variance, which means $E(s_i^*, s_i^*) = 1$. However, an inevitable sign of this ambiguity is the ICs which might be opposite to the corresponding latent variables, i.e. multiplied by -1, which fortunately is insignificant in most applications (Hyvärinen *et al.*, 2004). Another restriction is the order of independent components that cannot be controlled as the elements in the sum in Equation 6, which can be arrayed freely.

The fast ICA algorithm is using the criteria of maximizing nongaussianity to estimate the independent components, where the nongaussianity is measured by kurtosis.

Taking two independent components as an example as follows. Matrix $\mathbf{X}$ is consist by two vectors, $\mathbf{x_1}$ and $\mathbf{x_2}$, which are time-history measurements. Vector $\mathbf{x_1}$ and $\mathbf{x_2}$ are linear combination of $\mathbf{s_1}$ and $\mathbf{s_2}$ with mixing matrix $\mathbf{A}$, containing weight factor a_{11}, a_{12}, a_{21} and a_{22}, as given in Eq. 3-13

$$\mathbf{X} = \mathbf{AS} \rightarrow \mathbf{x_i} = \sum_{j=1}^{2} a_{ij}\mathbf{s_j}, i = 1,2$$

Eq. 3-13

Theoretically, the estimator of independent components, $\mathbf{s_1}$ and $\mathbf{s_2}$, can be obtained by finding the decomposing matrix $\mathbf{B^T}$, to let Eq. 3-14 hold.

$$\mathbf{S_{est}} = \mathbf{B^T X}$$

Eq. 3-14

The decomposing matrix $\mathbf{B^T}$ should be the inverse of matrix of **A**. However, in blind source separation case, the mixing matrix **A** is unknown, therefore the challenge is to find the unknown decomposing matrix **B** to separate observed sources, $\mathbf{x_1}$ and $\mathbf{x_2}$, into independent components, $\mathbf{s_{est2}}$ and $\mathbf{s_{est1}}$.

Because both matrix **A** and **S** are unknown, one assumption in ICA estimation must be mentioned, which is the ICA estimating components, i.e. $\mathbf{S_{est}}$, have the unit variance. This is due to the ambiguity of magnitudes of ICA estimation is inevitable. In other word, the magnitudes of independent components cannot be estimated exactly since the scalar multiplier or division in **s** and **a** can cancel each other. Taking following Eq. 3-15 as an example, the scalar α and β in $\mathbf{s_1}$ and $\mathbf{s_2}$ can be canceled due to the same division in mixing weights a_{11} and a_{12} respectively.

$$\mathbf{x_1} = \frac{1}{\alpha} a_{11} \alpha \mathbf{s_1} + \frac{1}{\beta} a_{12} \beta \mathbf{s_2}$$

Eq. 3-15

To simplify ICA estimation, the pre-processing contains centring and whitening procedure. The vector **x** in Eq. 1 is the zero-mean vector obtained from its original sensor measurements, $\mathbf{x_{org}}$, by subtracting their row mean, $\mathbf{x} = \mathbf{x_{org}} - \mathrm{E}\{\mathbf{x_{org}}\}$. This centring process will result in the zero mean of independent components too, that's why all the estimators in case study are zero-mean sources. The second necessary process is whitening the records, as shown in Eq. 3-16. The purpose of whitening target signals is to reduce the estimated parameters in the mixing matrix by half. The proof process can be found in previous paper (Zhu *et al.*, 2017).

$$\mathbf{X_w} = \Lambda \mathbf{X}$$

Eq. 3-16

$$\Lambda = \mathbf{U}\boldsymbol{\Sigma}^{-1/2}\mathbf{U}^{\mathbf{T}}$$

Eq. 3-17

The matrix $\boldsymbol{\Lambda}$ is the whitening matrix, which can be decomposed into a diagonal matrix $\boldsymbol{\Sigma} = diag(\sigma_1 \dots \sigma_n)$ and an orthogonal matrix $\mathbf{U}$ as shown in Eq. 3-17. Apparently, this is the process of singular value decomposition (SVD), which will be explained in detail in next subsection. It is also well-known that the covariance matrix $\mathbf{C_x}$ of target signals $\mathbf{X}$, can be separated by SVD as shown in Eq. 3-18.

$$\mathbf{C_x} = \mathbf{U}\boldsymbol{\Sigma}\mathbf{U}^{\mathbf{T}}$$

Eq. 3-18

The eigenvalues of $\mathbf{C_x}$ is organized as a diagonal matrix $\boldsymbol{\Sigma} = diag(\sigma_1 \dots \sigma_n)$ and $\mathbf{U}$ is the orthogonal matrix consists the unit-norm eigenvectors $(\mathbf{u_1} \dots \mathbf{u_n})$ of the $\mathbf{C_x}$. Consequently, the following Eq. 3-19 is hold.

$$\mathbf{C_{x_w}} = \mathrm{E}\{(\boldsymbol{\Lambda}\mathbf{X})(\boldsymbol{\Lambda}\mathbf{X})^{\mathbf{T}}\} = \boldsymbol{\Lambda}\mathbf{C_x}\boldsymbol{\Lambda}^{\mathbf{T}} = \left(\mathbf{U}\mathbf{D}^{-\frac{\mathbf{1}}{\mathbf{2}}}\mathbf{U}^{\mathbf{T}}\right)(\mathbf{U}\mathbf{D}\mathbf{U}^{\mathbf{T}})\left(\mathbf{U}\mathbf{D}^{-\frac{\mathbf{1}}{\mathbf{2}}}\mathbf{U}^{\mathbf{T}}\right) = \mathbf{I}$$

Eq. 3-19

Where $\mathbf{C_{x_w}}$ is the covariance matrix of matrix $\mathbf{X_w}$. Since $\mathbf{C_{x_w}}$ is unit matrix, $\mathbf{X_w}$ is white and Eq. 3-20 is the whiten process. The $\mathbf{X_w}$ will be utilized for next ICA estimating procedure and previous Eq. 3-15 can be updated to Eq. 3-20 as follows.

$$\mathbf{X_w} = \Lambda\mathbf{A}\mathbf{S}$$

Eq. 3-20

According to the central limit theorem, 'the distribution of a sum of independent random variables tends toward a Gaussian distribution, under certain conditions', which means any vector $\mathbf{x_w}$ is closer to Gaussian distribution than vector $\mathbf{s}$.

The main body of fast fixed-point algorithm is then employed here as an iteration scheme to find a unit vector $\mathbf{b}$ that maximizes the nongaussianity of $\mathbf{b}^{\mathbf{T}}\mathbf{x_w}$, which is the estimated sources of $\mathbf{s}$, as shown in Eq. 3-21 updated from Eq. 3-14.

$$\mathbf{S_{est}} = \mathbf{B}^{\mathbf{T}}\mathbf{X_w}$$

Eq. 3-21

The nongaussianity of $\mathbf{b}^{\mathbf{T}}\mathbf{x_w}$ for ICA estimation can be measured by minimizing or maximizing kurtosis, which is also known as fourth-order cumulant and is a classic

measurement of nongaussianity. The kurtosis values is defined in Eq. 3-22 for zero-mean variables (Hyvärinen *et al.*, 2004).

$$\mathrm{kurt}(\mathbf{b^T x_w}) = \mathrm{E}\{(\mathbf{b^T x_w})^4\} - 3(\mathrm{E}\{(\mathbf{b^T x_w})^2\})^2$$

Eq. 3-22

For a Gaussian variable $\mathbf{y}$ as an example, the kurtosis is zero, because the fourth moment of a Gaussian variable equals to $3(\mathrm{E}\{\mathbf{y^2}\})^2$. Thus, a non-Gaussian random variable should have a nonzero kurtosis. As mentioned, the independent components are assumed with unit convenience, hence, the above Eq. 3-23 can be simplified as follows and the absolute value of kurtosis is chosen since it can be positive or negative.

$$\mathrm{kurt}(\mathbf{b^T x_w}) = \mathrm{E}\{(\mathbf{b^T x_w})^4\} - 3$$

Eq. 3-23

The weight vector $\mathbf{b^T}$ with unit norm starts from a random vector. The iteration of this compotation is to find the direction where the gradient of kurtosis of $\mathbf{b^T x_w}$ is the extrema.

In this study, the Eq. 3-24 is utilized for fixed point iteration in fast ICA, followed by the normalization (unit norms) in Eq. 3-25 (Hyvärinen & Oja, 2000).

$$\mathbf{b} \leftarrow E\{\mathbf{x_w} f(\mathbf{b^T x_w})\} - E\{f'(\mathbf{b^T x_w})\}\mathbf{b}$$

Eq. 3-24

$$\mathbf{b} \leftarrow \frac{\mathbf{b}}{||\mathbf{b}||} = \frac{\mathbf{b}}{\sqrt{\sum_i \mathbf{b_i^2}}}$$

Eq. 3-25

Where the functions f and f' of $\mathbf{b^T x_w}$ are defined in Eq. 3-26 and Eq. 3-27.

$$f = 4 \times (\mathbf{b^T x_w})^3$$

Eq. 3-26

$$f' = 12 \times (\mathbf{b^T x_w})^2$$

Eq. 3-27

The iteration will be stopped if the absolute value of previous and new weight vector $\mathbf{b}$ shows convergence tend, as the value should close to 1.

In consequence, the decomposing matrix, $\mathbf{B^T}$, can be obtained and estimated independent components, $\mathbf{S_{est}}$, can be calculated according to Eq. 3-21. It has to be

noticed that the ICA estimator strain is all normalized strain with zero-mean and unit norms.

3.6 Concluding Remarks

This chapter has presented the mathematic background of the proposed thermal feature extraction methods. The novelty of this Ph.D. research is the utilization of blind source separation (BSS) to separate the thermal features from the measurements collected from sensor system. Therefore, the theoretical background of BSS has been presented in section 3.2, just following the overview section 3.1, which is the overview section to introduce the proposed thermal feature methods.

According to the availability of measurements, the proposed thermal feature extraction methods have been classified into the underdetermined approach for the case of single-channel records and the overdetermined approach for the case of multi-channel measurements. The overall framework of both underdetermined and overdetermined thermal feature extraction methods has been introduced in Section 3.1.

Regarding to the underdetermined cases, the methods are designated as EPI and EEPI for the sake of simplicity. As a reminder, EPI represents for the combination of Empirical Mode Decomposition (EMD), Principal Component Analysis (PCA), and Independent Component Analysis (ICA), while EEPI stands for the combination of Ensemble Empirical Mode Decomposition (EEMD), PCA, and ICA. Three procedures are involved in EPI and EEPI, which are mode decomposition, data reduction, and blind separation. The single-channel measurements are first decomposed into a group of intrinsic mode functions (IMFs) by employing EMD or EEMD. After that, the PCA is occupied as the indicator to select the number of IMFs for the final step of blind separation by employing ICA.

Regarding to the overdetermined cases, the multi-channel input measurements are investigated by PCA directly to indicate the number of sources for blind separation. The method of ICA is proposed for blind separation as well.

In Section 3.2, the fundamental idea of proposed thermal feature extraction, blind source separation (BSS), has been presented. It is the first time to employ BSS for separating thermal features directly and blindly from the structural responses. The

afterwards Section 3.3 to 3.5 are organized to introduce the mathematical background of adopted methodologies, which are EMD/EEMD, PCA, ICA individually.

Both underdetermined solutions and overdetermined approaches will be evaluated in the following CHAPTER 4 by utilizing a numerical truss bridge and an experimental case study.

CHAPTER 4 THERMAL FEATURES EXTRACTION: CASE STUDY

This chapter investigates the performance of thermal feature extraction methods that have been presented in the previous CHAPTER 3. The methods have been classified into underdetermined solutions and overdetermined solutions. The evaluation study of proposed methods takes the form of numerical case study and experimental case study based on the truss model in the Section 4.1 and 4.2 respectively. Both Section 4.1 and 4.2 are divided into four parts. The first parts of two case studies are gives a brief overview of the truss model, including the model or experimental setup. The second parts, Section 4.1.2 and 4.2.2, deal with the investigation process of proposed underdetermined methods, while the third parts, Section 4.1.3 and 4.2.3, concern with the overdetermined methods. The evaluation findings of numerical and experimental case studies are summarized in the fourth subsections, Section 4.1.4 and 4.2.4. The concluding remarks are conducted at the end of this chapter in 4.3.

4.1 Numerical case study

In this section, the case study is conducted on the finite element model of a truss bridge. The brief introduction of this truss model is first given in Section 4.1.1, followed by two independent Sections 4.1.2 and 4.1.3 the evaluate the underdetermined decomposition methods and overdetermined decomposition method respectively.

4.1.1 Model introduction

A down-scaled aluminium bridge for simulation is modelled in ANSYS. Figure 4.1 gives the 3D geometry with three various length of chords. The length of the short, medium, and long chord are 203.47 mm, 375.92mm, and 524.60 mm respectively. More detailed geometry information can be found in Appendix B. The chords are simulated by using link model in ANSYS and fixed at the all four ends. The bridge is built with aluminium materials. The Young's modulus of aluminium is 70 GPa, its density is $2.7g \cdot cm^{-3}$, Poisson's ratio is 0.35, and its thermal expansion is 23.1 $\mu m \cdot m^{-1} \cdot K^{-1}$, as displayed in Table 4.1.

In this case study, the bridge is in healthy condition (i.e. no damage) and exposed to two loading conditions, as shown in Figure 4.2. The first is temperature loadings, given in Figure 4.2(a). The key values are as follows: (1) the average temperature is 9.7℃; (2) maximum daily fluctuation is 4℃ and maximum annual fluctuation is 7℃; (3) every load step represents 2.5 hours, as three days are selected from each month and 36 days cycles are simulated among 365 load steps.

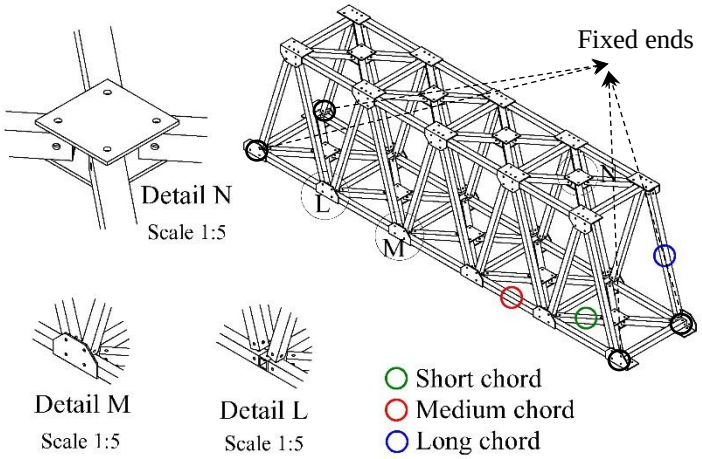

Figure 4.1 Down-scaled aluminium truss bridge dimension overview

Table 4.1. Principal material properties of aluminium bridge

Young's modulus	Density	Poisson's ratio	Thermal expansion
70 GPa	$2.7g \cdot cm^{-3}$	0.35	23.1 $\mu m \cdot m^{-1} \cdot K^{-1}$

A time-varying traffic load is then shown in Figure 4.2(b) and applied at all bottom nodes of the bridge model. The 24-hour traffic load variation conforms to a normal distribution with double peaks, with maximum 5 kN on each bottom node. Since every load step simulates as 2.5 hours, 10 data points are simulated as one daily cycle (i.e. 24-hour traffic load variation).

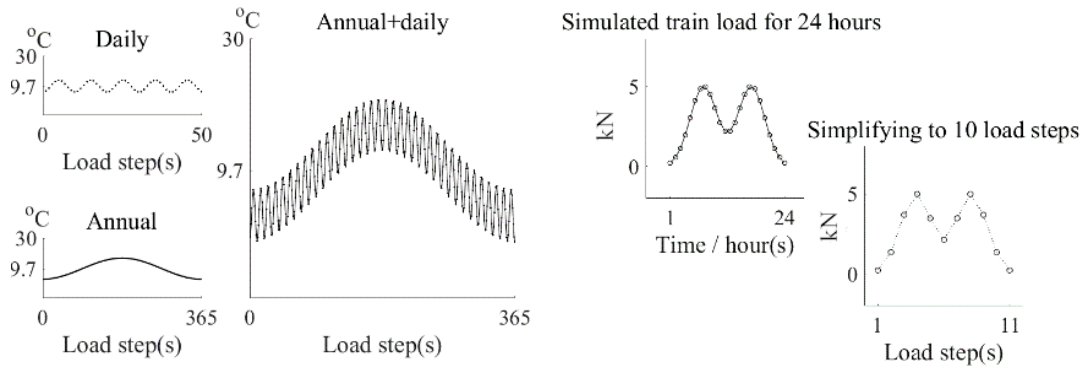

(a). Thermal loadings (b). Traffic loadings

Figure 4.2. Simulated loading conditions on FE model

4.1.2 Numerical evaluation of underdetermined methods

The organization of this sub-section is first given in Figure 4.3. It is apparent that the data investigation will be delivered from two parts: season temperature effect extraction and daily temperature effect extraction. For each temperature feature, seasonal or daily, both EPI (EMD+PCA+ICA) and EEPI (EEMD+PCA+ICA) are evaluated and compared.

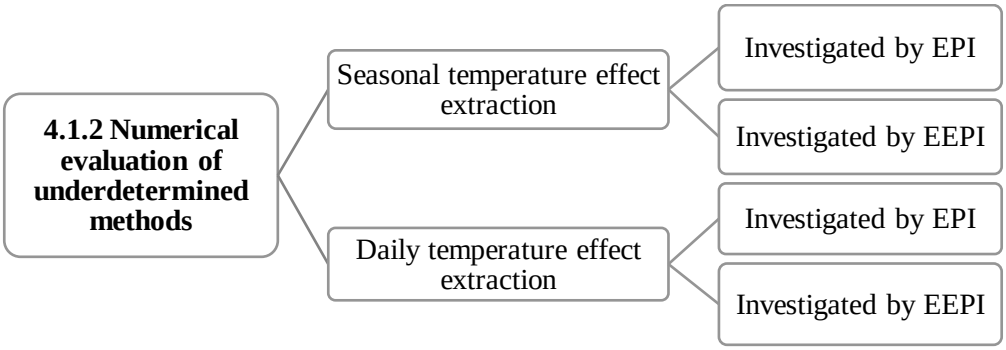

Figure 4.3. Organization of Section 4.1.2

The bridge is fixed in all directions at supporting ends A, B, C and D, seeing Figure 4.4. Four monitored chords are registered as SG1, SG2, SG3, and SG4, whose strain

measurements are of interests. The target of the proposed feature extraction method is to extract the temperature-induced strain from the mixed structural response. The mixed structural response in this case study means the strain measurements collected from the bridge under temperature and traffic loading conditions, as shown in Figure 4.5.

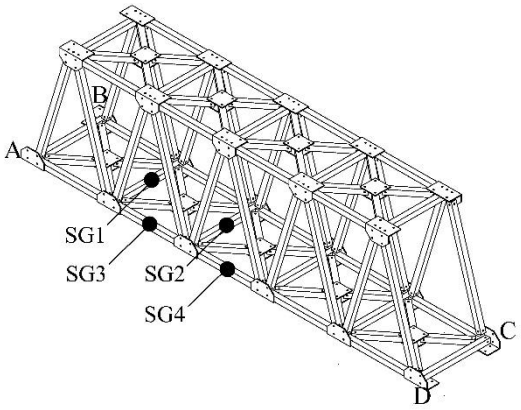

Figure 4.4. Sensor positions overview for underdetermined method evaluation

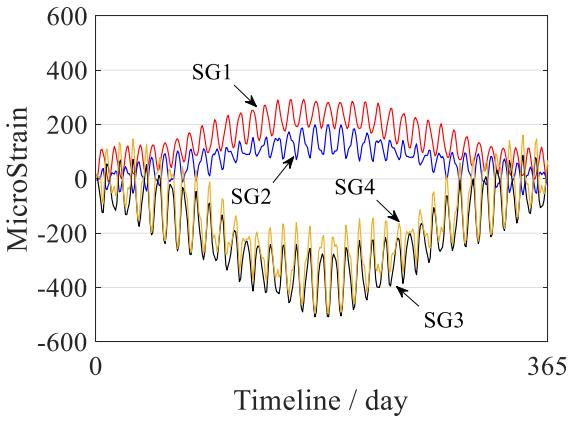

Figure 4.5. Strain measurements under temperature and traffic loadings conditions

4.1.2.1 Seasonal thermal feature extraction

This section will give an assessment and comparison between EPI and EEPI for extracting seasonal temperature-induced strain.

Data investigated by EPI

The separation results by applying EPI on the one-year monitoring data from SG1 are first given as the red line in Figure 4.7. The one-year data is last for 365 days as previously shown in Figure 4.5. The EPI extracted strain is compared with the pure

seasonal strain, represented as the blue dash line in Figure 4.7. The pure seasonal strain, or reference seasonal strain, is the structural response only affected by seasonal temperature variations. It is apparent from Figure 4.6 that the extracted seasonal thermal response does not match with the pure strain. The correlation between EPI extracted strain and reference strain is assessed by correlation coefficient value (*CC*) and relative root mean square error (*RRMSE*). The higher *CC* value and the lower *RRMSE* means the better separation performance. The correlation coefficient values between them is only 0.59, and relative root mean square error is over 81%, which can reflect that one-year data is not enough to extract seasonal thermal effects.

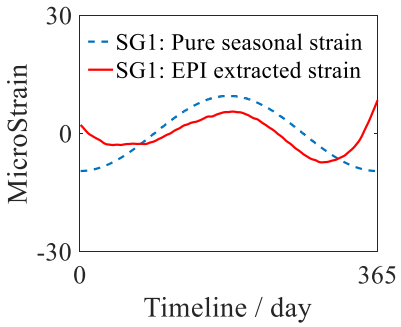

Figure 4.6. Seasonal thermal-strain separated by EPI on one-year data from SG1

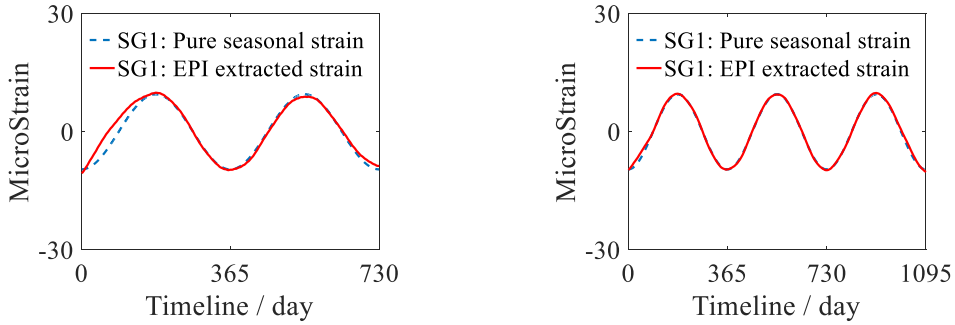

(a). two-year measurements (b). three-year measurements

Figure 4.7. Seasonal thermal-strain separated by EPI on two-year and three-year data from SG1.

Considering that the seasonal pattern of temperature variations can only become visible when the time duration is over two years or even longer, then two-year (730-day duration) and three-year (1095-day duration) mixed structural measurements are analysed by EPI. The time-history comparisons of SG1 between estimated seasonal strain and the pure seasonal temperature-induced strain are given in Figure 4.7. Obviously, the higher relation and better separation can be observed. For the two-year

data separation, as shown in Figure 4.7(a), the *CC* value is increased to 0.98 and *RRMSE* is decreased to 20%. Moreover, EPI performs even better on the three-year data, given in Figure 4.7(b), since the *CC* value increases to 1.00 and *RRMSE* is only 6%.

Same separation process by applying EPI are also conducted on SG2, SG3, and SG4 on one-year, two years and three years monitoring data. The separation results are given in Figure 4.8 for SG2, Figure 4.9 for SG3, and Figure 4.10 for SG4. From part (a) of Figure 4.8, Figure 4.9, and Figure 4.10, it is apparent that the extracted seasonal thermal response does not match with the pure strain for all other three strain measurements when the target data is only one year. But an evident improvement can be observed from part (b) of those figures when the data increases to two-year long. If enlarging the sample size to three years, seeing part (c) of those figures, a visible amendment for SG2 can be observed.

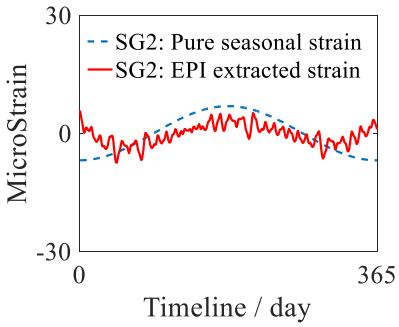

(a). one-year measurements

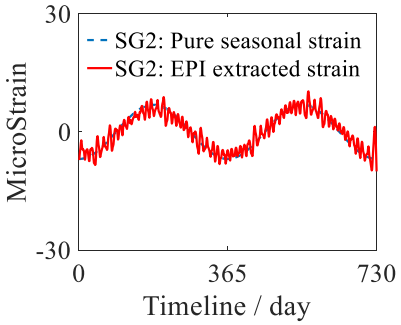

(b). two-year measurements

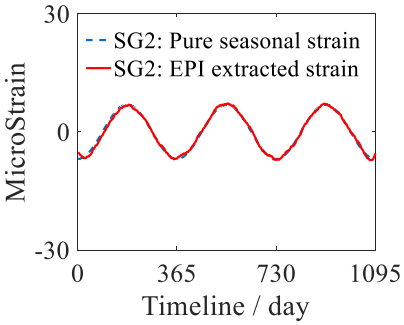

(c). three-year measurements

Figure 4.8. Seasonal thermal-strain separated by EPI on data from SG2

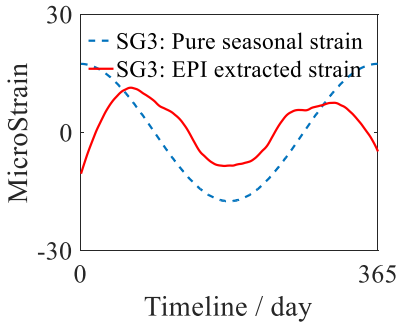

(a). one-year measurements

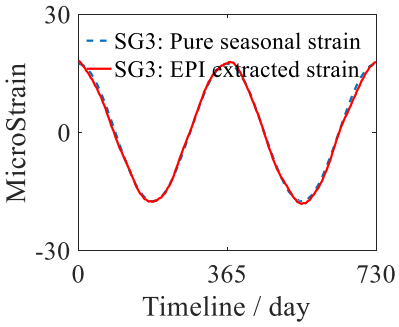

(b). two-year measurements

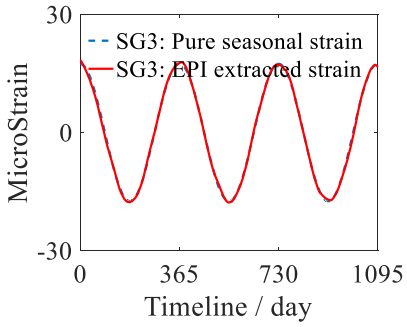

(c). three-year measurements

Figure 4.9. Seasonal thermal-strain separated by EPI on data from SG3.

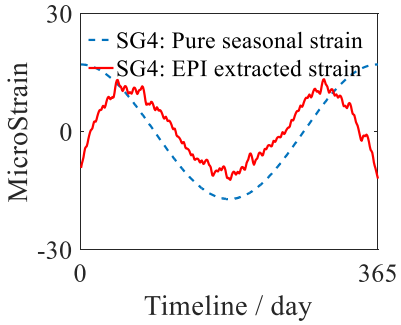

(a). one-year measurements

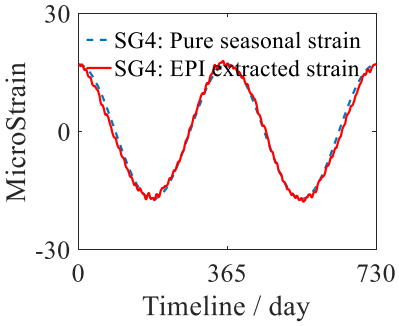

(b). two-year measurements

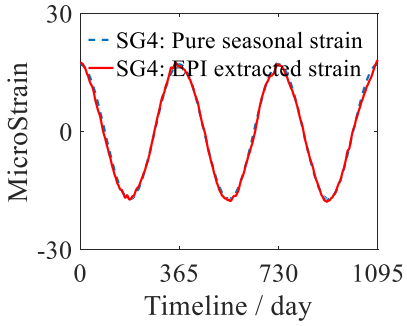

(c). three-year measurements

Figure 4.10. Seasonal thermal-strain separated by EPI on data from SG4.

The performance of EPI for SG2, 3, and 4 are also assessed by correlation coefficient values and relative root mean square errors between EPI extracted strain (i.e. the red line) and the reference seasonal strain (i.e. the blue dash line) showing in following figures. The *CC* values for SG2 are 0.54, 0.94, and 1.00 for one-year, two-year and three-year cases, while the *RRMSE* are 85%, 35%, and 8% respectively. The similar tendency can also be observed from SG3 and SG4, whose evaluation values are summarized in Table 4.2. In order to have a visible comparison, the bar figures based on the data from Table 4.2 is also given in Figure 4.11.

Table 4.2. Summary of seasonal thermal strain extraction by EPI

	Correlation coefficient				**RRMSE**			
	SG1	SG2	SG3	SG4	SG1	SG2	SG3	SG4
One-year data	0.59	0.54	0.55	0.63	81%	85%	85%	78%
Two-year data	0.98	0.94	1.00	1.00	20%	35%	5%	9%
Three-year data	1.00	1.00	1.00	1.00	6%	8%	3%	6%

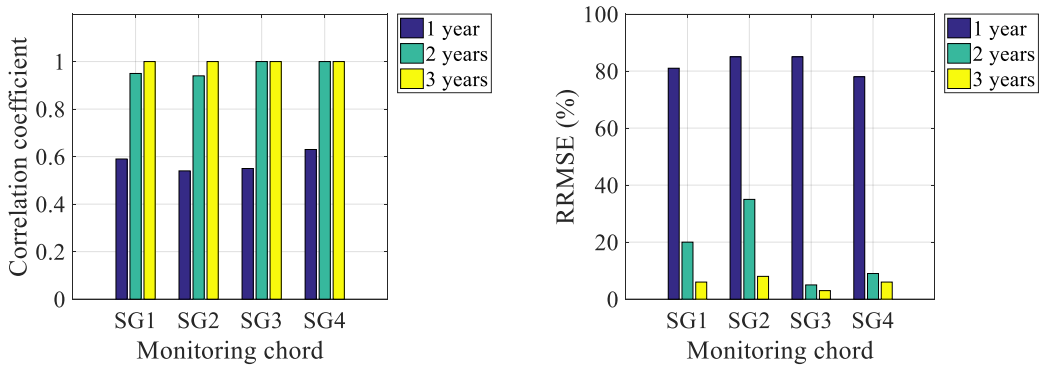

(a). Correlation coefficient (b). Relative root mean square error

Figure 4.11. Summary of seasonal thermal strain extraction by EPI

The examination results have demonstrated that the EPI's extracting capacity is related to the target signal's length. The separating results are not satisfactory with one-year data, as the '365' bar shown in Figure 4.11. The correlations are all below 0.63, as 0.59, 0.54, 0.55 and 0.63 for SG1-4 respectively, while the relative root mean square errors are quite high, around 80%. However, the separation results have a significant improvement when applying EPI on two-year strain measurements. In addition, the extracting results will be slightly enhanced when the cycles are enlarged from two years to three years. The correlation values are all reaching up to 1.00 for all

the monitored beams and the relative root mean square error decreases to 3%. The other advantage is the computational cost does not have any change while changing the size of the target signal. Therefore, EPI is qualified enough for separating seasonal temperature response from at least two years of measurements.

Data investigated by EEPI

When applying EEPI, the ensemble empirical mode decomposition (EEMD) is selected to decompose target single-channel signal. Two parameters, *NSR* (noise-signal ratio) and *N* (the number of trails) have a significant influence on the final separation results. Therefore, a series of *NSR* and *N* combinations are selected for their impact research. Considering the previous results, EPI is trustworthy and efficient enough when the target sources are over two-year duration, so EEPI will not be recommended for these cases, because of the higher computational cost when compared with EPI. Only one-year mixed strain is utilized for performing EEPI to extract seasonal temperature-induced strain, since EPI fails in this case.

The extracting results that are obtained by using various *NSR* and *N* values in EEMD have been compared with ideal temperature-induced structural strain for all sensors. The assessment is based on the correlation coefficient values (*CC*) between the EEPI separated strain and the reference seasonal temperature-induced strain. The assessment about *NSR* and *N* are delivered in Figure 4.12 and Figure 4.13 respectively. From Figure 4.12, it is apparent that *NSR* has an obvious effect on the performance of EEPI, while from Figure 4.13, the impact of *N* is less significant.

Among all the evaluation results, the best combination of *NSR*=1.1 and *N*=850 can be selected to optimized separation performance. Figure 4.14 shows the comparison between estimated strain, separated by EEPI, and ideal strain, induced by applying annual temperature load only. The seasonal thermal strain is not recovered very well. The correlation coefficient values are 0.85, 0.85, 0.86 and 0.84, while *RRMSE* are 56%, 57%, 54% and 58% for SG1-4 respectively, which is not high enough but much better than EPI's performance on one-year monitoring data. As aforementioned, EPI is efficient enough to extract seasonal temperature effects when the measurements are recorded over two years. Therefore, EEPI can be treated as an alternative method when the measurement sources are limited.

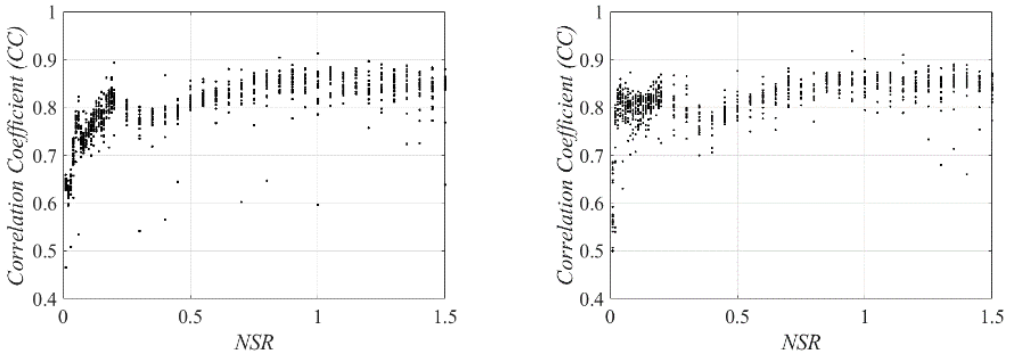

(a). SG1 (b). SG2

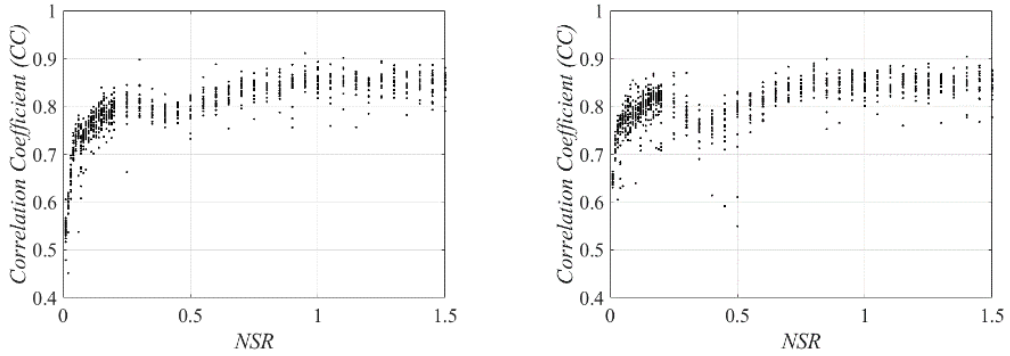

(c). SG3 (d). SG4

Figure 4.12. Effect of *NSR* for extracting seasonal thermal-strain by EEPI

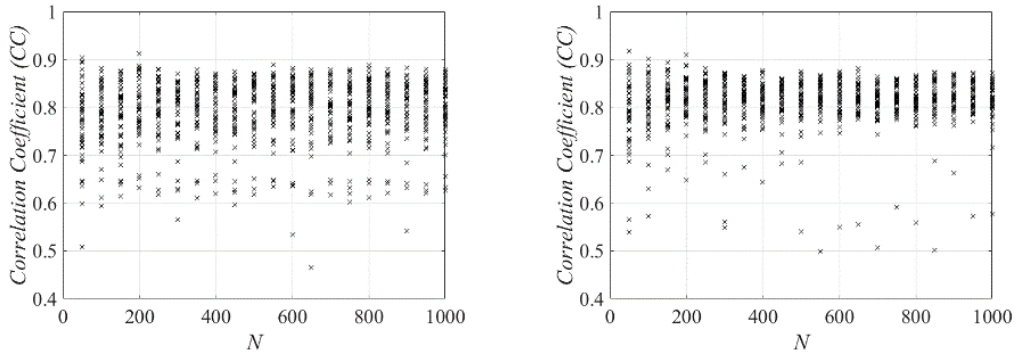

(a). SG1 (b). SG2

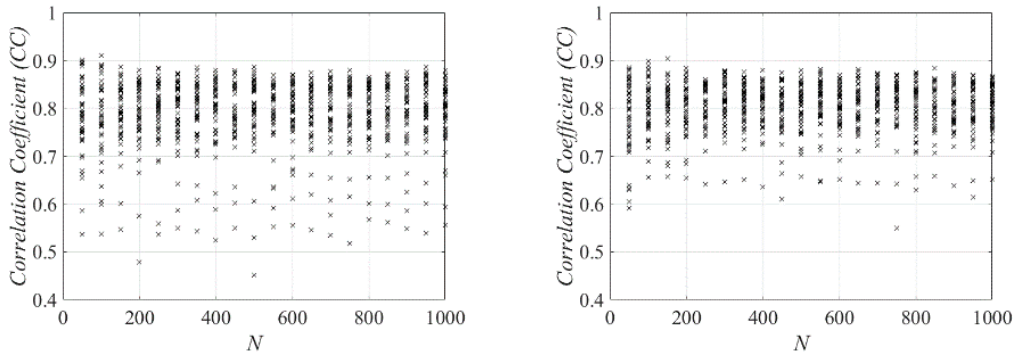

(c). SG3 (d). SG4

Figure 4.13. Effect of *N* for extracting seasonal thermal-strain by EEPI

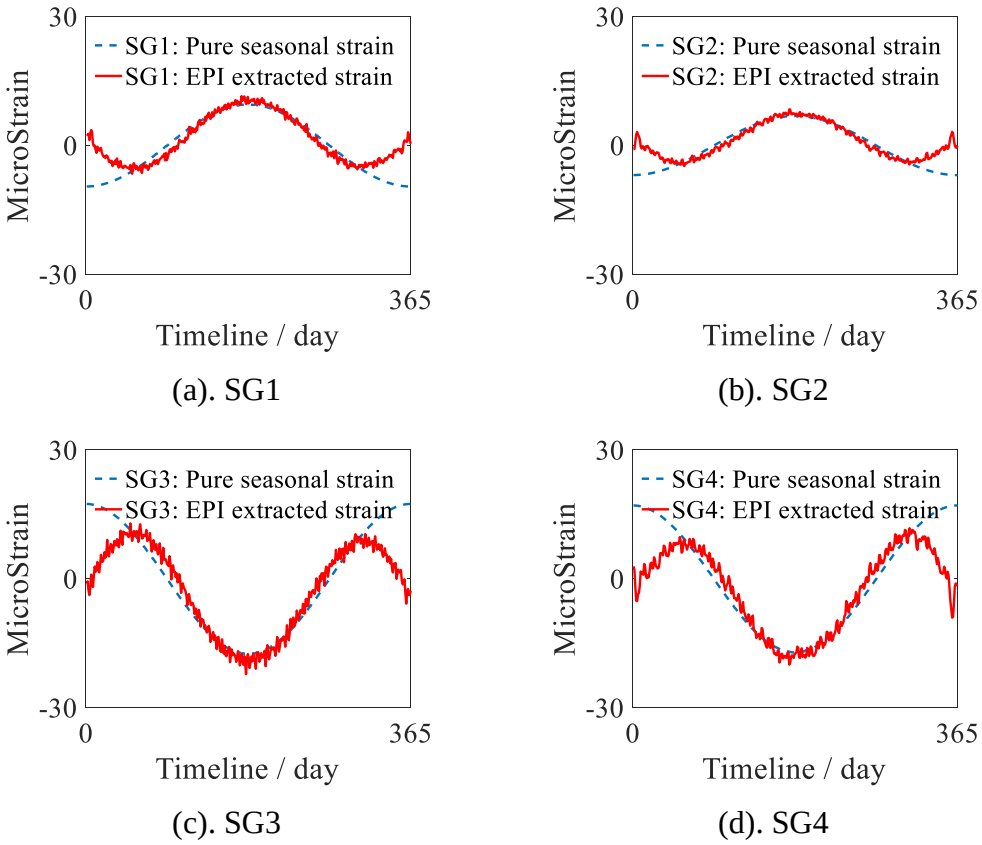

Figure 4.14.Seasonal thermal-strain separated by EEPI on data from SG1-4 (*NSR=1.1, N=850)*

4.1.2.2 Daily thermal feature extraction

For extracting the daily thermal features in this subsection, the performance EPI and EEPI is investigated respectively.

Data investigated by EPI

In the previous Section 4.1.2.1 for thermal feature extraction, the performance of EPI is heavily related with the data size. The rule is that the measurement duration should be no less than the longest variation period. Therefore, only one-year data should be adequate for daily case, since 36 daily cycles are simulated within one year. The effort to investigate the data length is also conducted and can approve this predication. As can been seen from Figure 4.15, the influence of data length is ignorable, since the correlation coefficient (*CC*) values and root mean square errors (*RRMSE*) are stable no matter the data length. For example, the *CC* values for SG1 and SG3 are at the same level. The visible influence due to data duration change can

only be observed in SG4, i.e. the *CC* value decreases from 0.81 to 0.61, while the value of *RRMSE* increases from 59% to 78%. This approves that the longer monitoring data does not have a positive effect on the daily feature separation. Instead, one-year data is enough to provide relatively better separation results for daily thermal feature extraction. Therefore, only one-year data is utilized for the following EPI and EEPI evaluations.

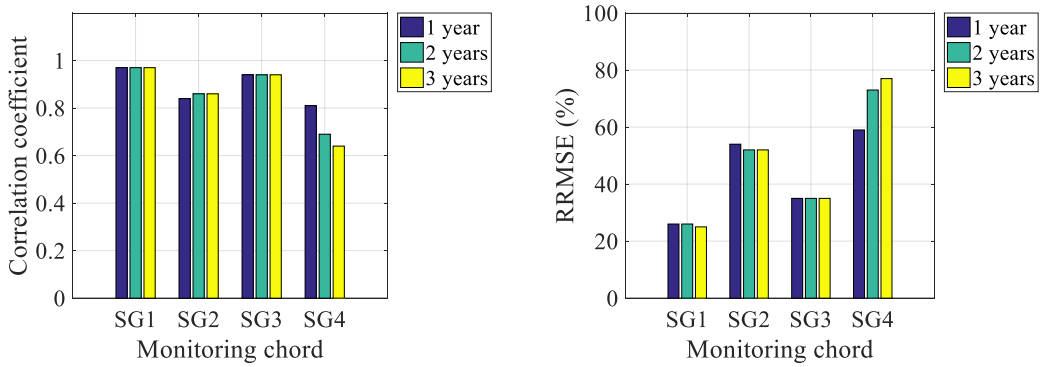

(a). Correlation coefficient (b). Relative root mean square error

Figure 4.15. Evaluation of EPI for DAILY thermal strain extraction

Figure 4.16(a) gives the EPI extracted signals from the data of SG1 in the time domain. The separated strain is compared with the pure daily strain, or reference daily strain, which is collected from SG1 when the bridge is only affected by the daily temperature loadings. To have a clear view of the separated results, Figure 4.16(b) then shows the relation between the separated results with temperature variations. The *CC* value between EPI estimated strain and the reference daily temperature-induced strain is 0.97, while *RRMSE* is only 26%.

EPI is also applied on SG2, SG3, and SG4 for daily feature extraction and the results are presented in Figure 4.17 for SG2, Figure 4.18 for SG3, Figure 4.19 for SG4 respectively. The *CC* and *RRMSE* values to assess the performance of EPI are subsequently summarized in Table 4.3. According to Table 4.3, the daily temperature-induced strains estimated from SG1 and SG3 are high related with the reference strains, since the correlation coefficient values are 0.97 and 0.94 for SG1 and SG3, and the relative low *RRMSE* values can be obtained, i.e. 26% and 35%. However, the results for SG2 and SG4 are not satisfied. The *CC* are between 0.81 and 0.84, and *RRMSE* are quite high, as 54% for SG2 and 59% for SG4.

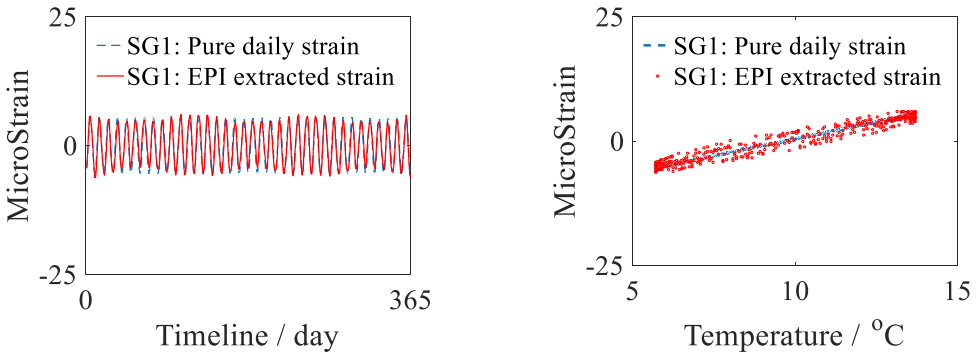

(a). strain in time domain (b). strain with temperature

Figure 4.16. Daily thermal-strain separated by EPI on data from SG1

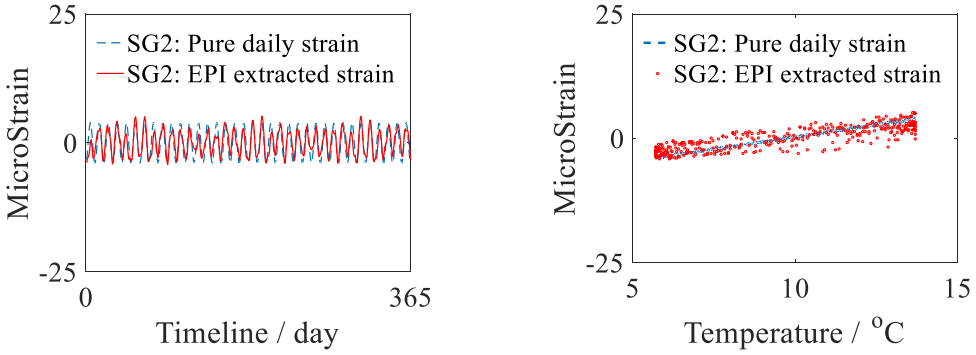

(a). strain in time domain (b). strain with temperature

Figure 4.17. Daily thermal-strain separated by EPI on data from SG2

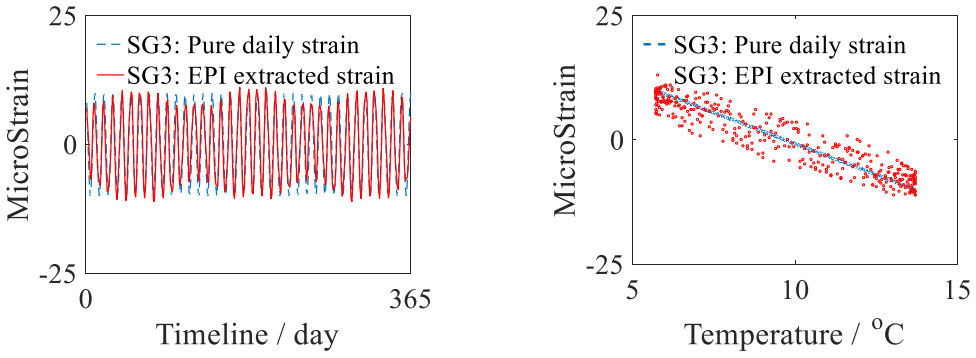

(a). strain in time domain (b). strain with temperature

Figure 4.18. Daily thermal-strain separated by EPI on data from SG3

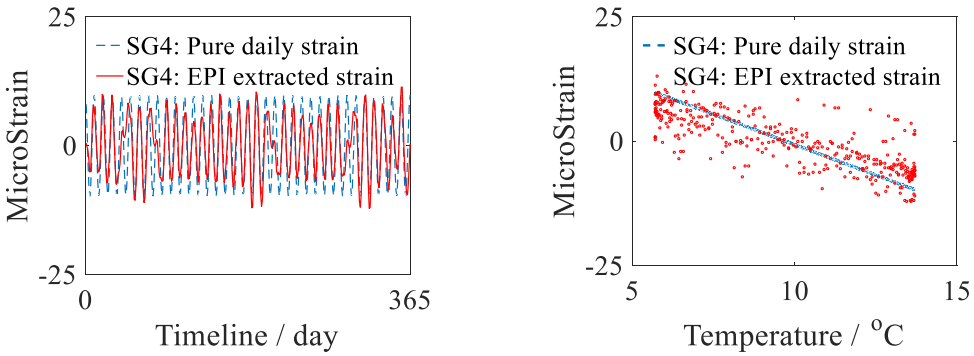

(a). strain in time domain (b). strain with temperature

Figure 4.19. Daily thermal-strain separated by EPI on data from SG4

Table 4.3. Evaluation of daily thermal-strain extraction by EPI

Method	**EPI for daily feature separation**			
Strain Gauge No.	**SG1**	**SG2**	**SG3**	**SG4**
Correlation coefficient	0.97	0.84	0.94	0.81
Relative Root Mean Square Error	26%	54%	35%	59%

Data investigated by EEPI

For evaluating the performance of EEPI deal with daily thermal issues, the research of how *NSR* (noise-signal ratio) and *N* (the number of trails) affect the final blind separation results will be given first. Similar as the previous part of seasonal strain recovery, Figure 4.20 and Figure 4.21 give an overview of the relationship among *NSR*, *N*, and separating results.

Referring to Figure 4.20, *NSR* has an obvious effect on the performance of EEPI, while *N* has a slight influence on the final separating results, seeing to Figure 4.21. When *NSR* is around 0.2, the blind separation results are reaching the peak value and stable for all monitored beams. The correlation coefficient results are generally around 0.80. And the recommended combination of *NSR*=0.11 and *N*=400.

Figure 4.22 then shows the extraction results in the time domain and their comparison with ideal strain, while Figure 4.23 shows the relation between temperature and temperature-induced strain.

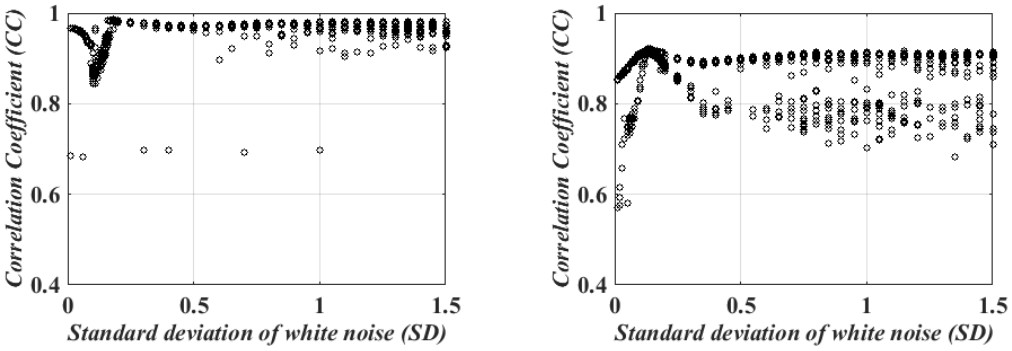

(a) SG1 (b) SG2

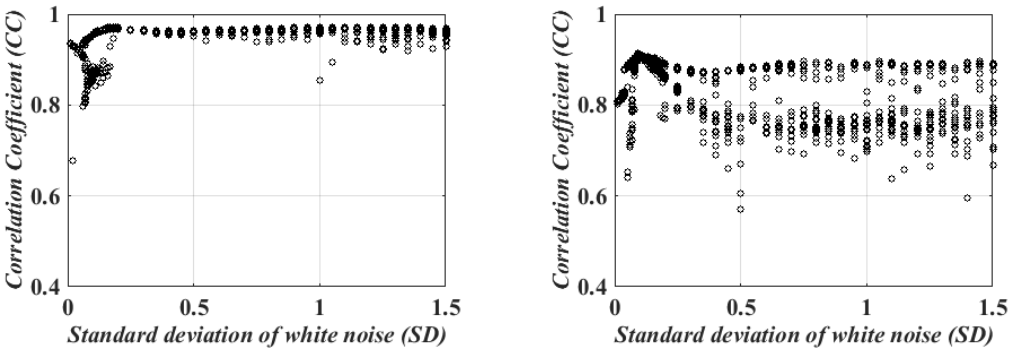

(c) SG3 (d) SG4

Figure 4.20 Effect of *NSR* for extracting daily thermal-strain by EEPI.

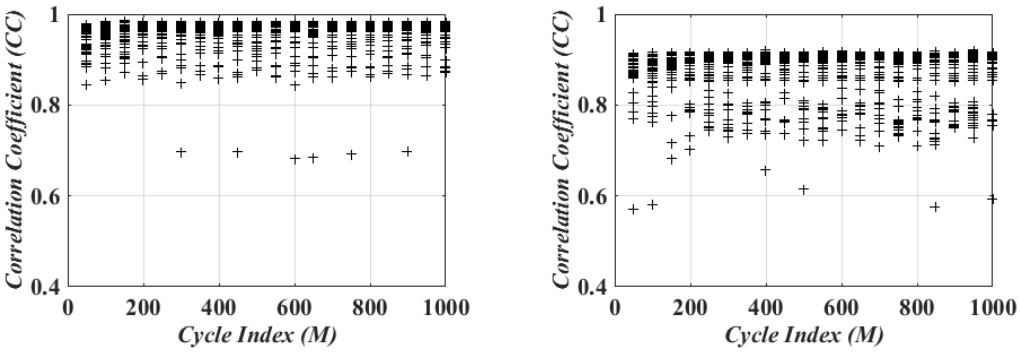

(a) SG1 (b) SG2

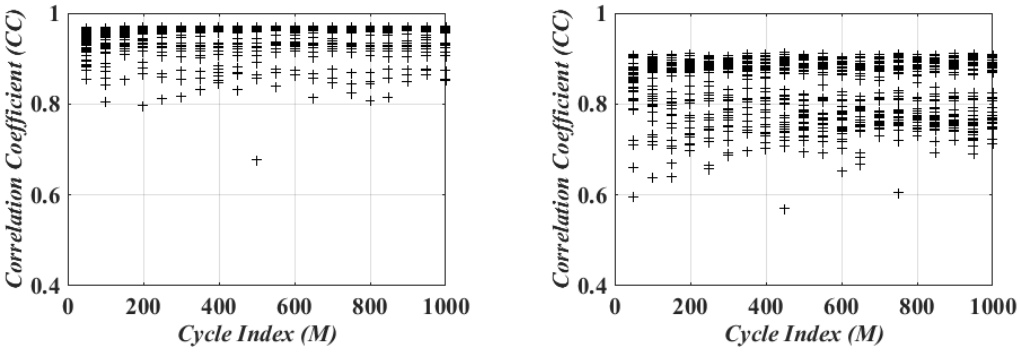

(c) SG3 (d) SG4

Figure 4.21. Effect of *NSR* for extracting daily thermal-strain by EEPI.

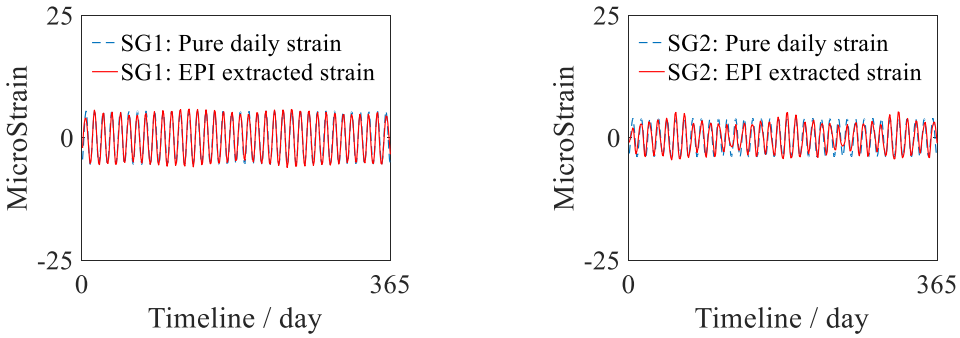

(a). SG1

(b). SG2

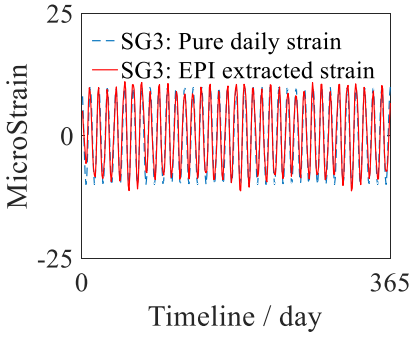

(c). SG3

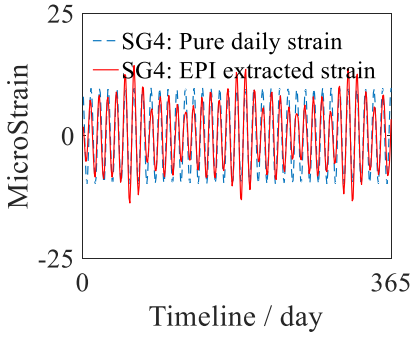

(d). SG4

Figure 4.22. Daily thermal-strain separated by EEPI: I

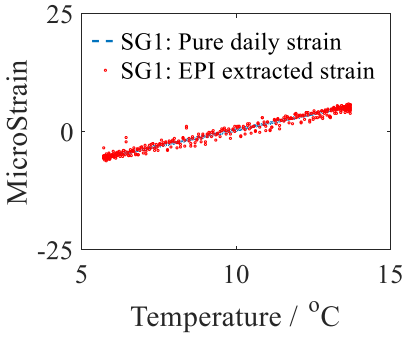

(a). SG1

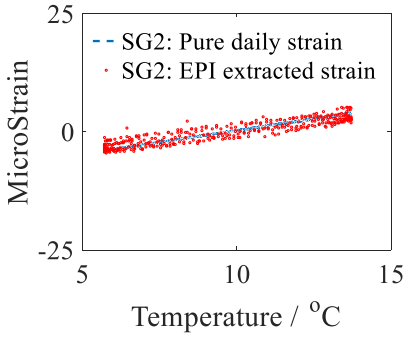

(b). SG2

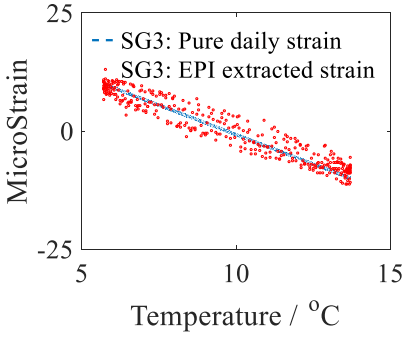

(c). SG3

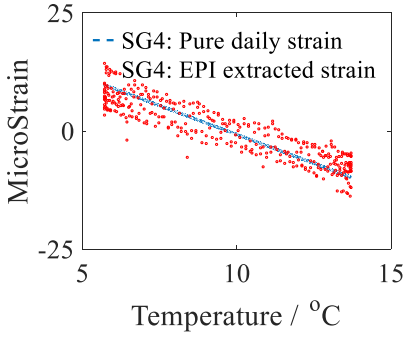

(d). SG4

Figure 4.23. Daily thermal-strain separated by EEPI: II

The assessment values, *CC* and *RRMSE*, are then listed in Table 4.4. As can be seen from Table 4.4, the correlation coefficient values for all sensors are over 0.91, and the *RRMSE* values are also lower than EPI, as previously shown in Table 4.3.

Table 4.4. Evaluation of daily thermal-strain extraction by EEPI (*NSR=0.11, N=400*)

Method	**EEPI for daily feature separation**			
Strain Gauge No.	**SG1**	**SG2**	**SG3**	**SG4**
Correlation coefficient (*CC*)	0.98	0.91	0.96	0.91
Relative Root Mean Square Error (*RRMSE*)	18%	41%	28%	42%

4.1.2.3 Results summary for underdetermined methods

The underdetermined thermal feature extraction method, EPI and EEPI, are evaluated in this section on a numerical truss model built through ANSYS. The purpose of EPI and EEPI is to extract seasonal and daily thermal strain sequences.

For separating temperature features, both seasonal and daily variations, the following three aspects of proposed methods, EPI and EEPI, can be summarize, which are based on the previous discussion in section 4.1.2.1 and section 4.1.2.2.

- The performance of EPI to recover seasonal temperature-induced strain is highly related to the signal's duration of interest. EPI can recover seasonal thermal features at a compelling level, with 0.99 correlation and lower computational cost, only when the target signal is over two-year's length. But EPI fails to uncover seasonal features when the target strain is only one-year measurements, because the periodic feature of seasonal temperature variations is not visible in only one-year data, which can cause unsatisfactory separating results with lower correlation coefficient values and higher relative root mean square error.
- When the monitoring data is limited, EEPI performs better than EPI, since the correlation coefficient values can be increased from 0.54-0.63 to 0.84-0.85 and the relative root mean square error can be reduced from 78%-85% to 54%-58%. However, the EEPI is not recommended for the cases when monitoring data is over two years, because of the large computational cost of EEPI.

- For the daily thermal feature extraction investigated in Section 4.1.2.2, EEPI has an evident improvement and relative higher robustness for extracting daily thermal strain. The performance of EPI shows 0.81-0.97 correlation value, while EEPI increases them to 0.91-0.96. Regarding the relative root mean square error, EEPI not only decreases EPI's result value (35%-59%) to 28%-42%, but also narrows the range, which means EEPI is more robust than EPI.

4.1.3 Numerical evaluation of overdetermined methods

In this section, the overdetermined method for thermal feature extraction is evaluated on the numerical truss model. The finite element model has been previously described in Section 4.1.1. Six strain measurements are of interest, whose location and labels are displayed in Figure 4.24. The structure is in health condition, which means no damage scenarios are simulated on the truss model. The bridge is under temperature and traffic load variations.

The first procedure of overdetermined method is applying Principal Component Analysis (PCA) to identify the minimum components among all sensor records. Two principal components can be identified from the six mixtures. Hence, at least two sensor records are selected from all measurements for next procedure of blind separation.

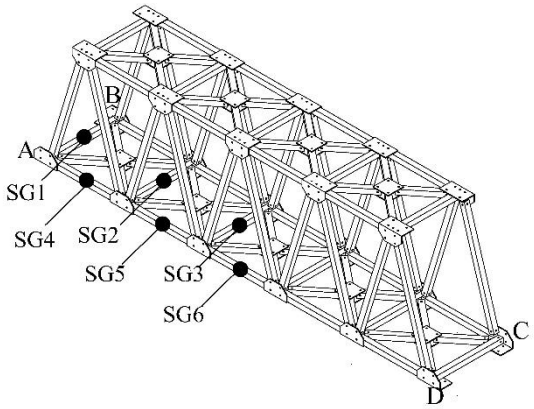

Figure 4.24. Sensor positions overview for overdetermined method evaluation

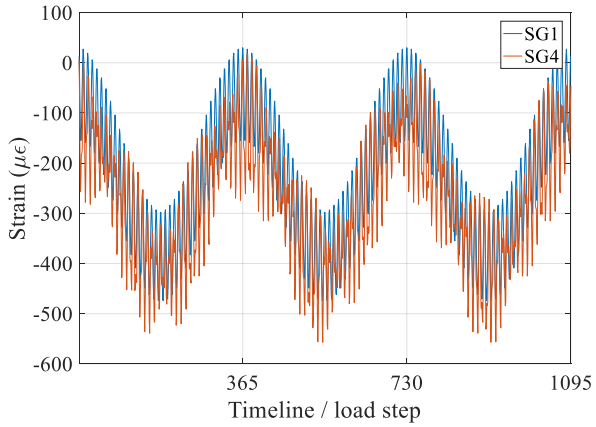

Figure 4.25. Strain measurements of SG1 and SG4 from the finite element model

The SG1 and SG4 are first selected as an example, whose time-history strain is displayed in Figure 4.25. The estimated outputs by applying independent component analysis (ICA) are given in the following Figure 4.26. As can be seen from Figure 4.26(a), the ICA can only separate the temperature-induced strain, but it cannot entirely distinguish the seasonal and daily features. The Figure 4.26(b) gives the separated traffic-induced strain variations. To assess the separating results, the independent components separated by ICA (Figure 4.26) are compared with the reference data. The reference data is the strain collected from the bridge when it is only in temperature or traffic loading condition. The zoom-in details can be found in Figure 4.27, with the corresponding correlation coefficient values (*CC*). It can be seen from Figure 4.27, the separated temperature-induced strain is highly related with the reference data, the same as the traffic-induced strain.

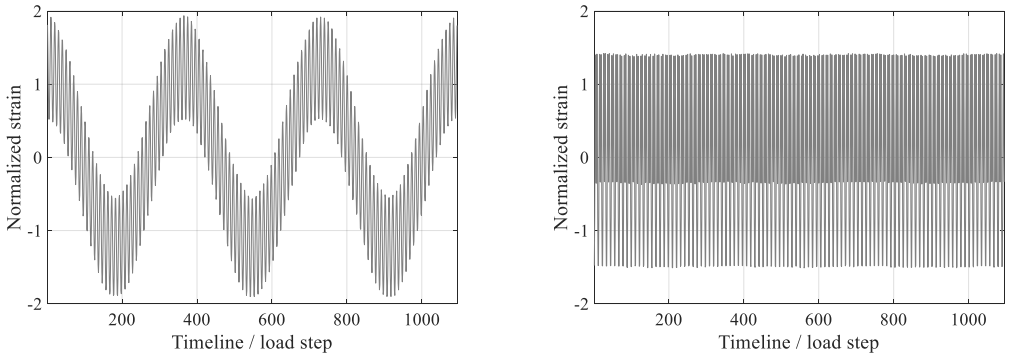

(a). Independent component 1 (b). Independent component 2

Figure 4.26. Separated components by employing overdetermined method

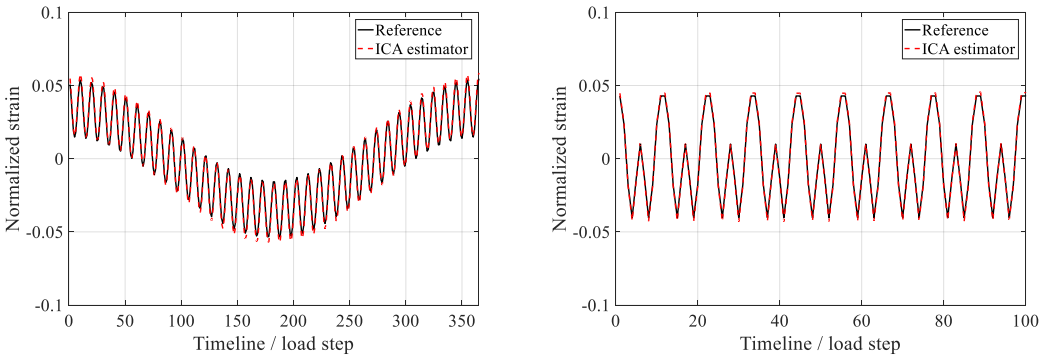

(a). Temperature-induced strain comparison, *CC*=1.00

(b). Traffic-induced strain comparison, *CC*=1.00

Figure 4.27. Comparison between reference data and ICA estimators (SG1 and SG4)

Various selections from six measurements have also been investigated. The same processes on SG1 and SG4 have been conducted on other sensor pairs, for example SG2 with SG5, SG3 with SG6, SG4 with SG5, SG5 with SG6, and SG6 with SG2. The separation performance is assessed by correlation coefficient value between separated strain and reference data. For example, Figure 4.28(a) gives the strain measurements recorded by sensor SG2 and SG5, while in part (b) and (c) of Figure 4.28, the ICA separated strains are compared with reference strains. Similarly, the measurements and ICA separation results from SG3 and SG6 are presented in Figure 4.29. Figure 4.30 is then showing the outcomes from SG4 and SG5, while Figure 4.31 and Figure 4.32 are the evaluation on SG5 with SG6 and SG6 with SG2.

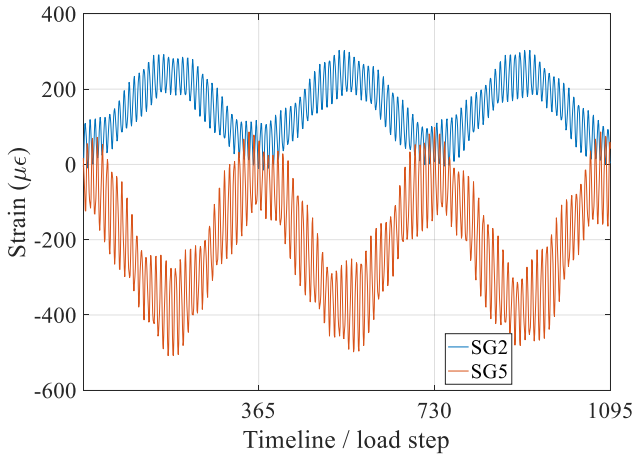

(a). Strain measurements from SG2 and SG5 under temperature and traffic loads

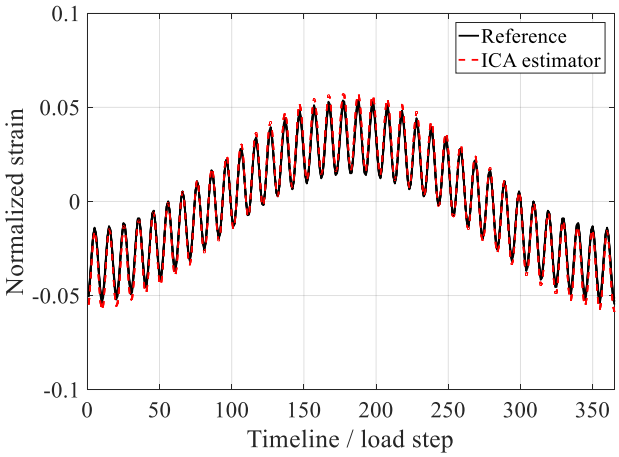

(b). Temperature induced strain comparison, *CC*=1.00

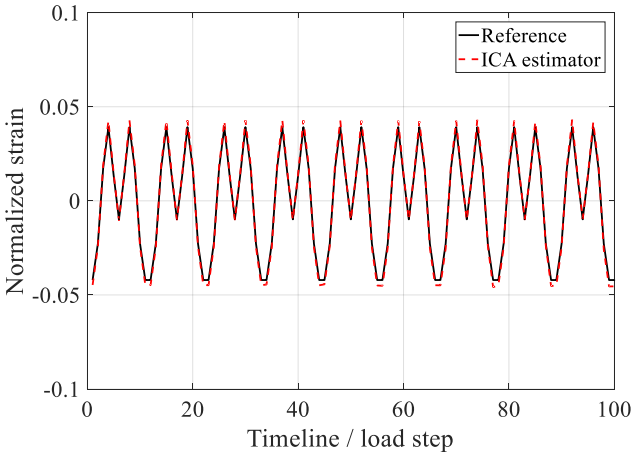

(c). Traffic induced strain comparison, *CC*=1.00

Figure 4.28. Application of overdetermined decomposition method on SG2 and SG5

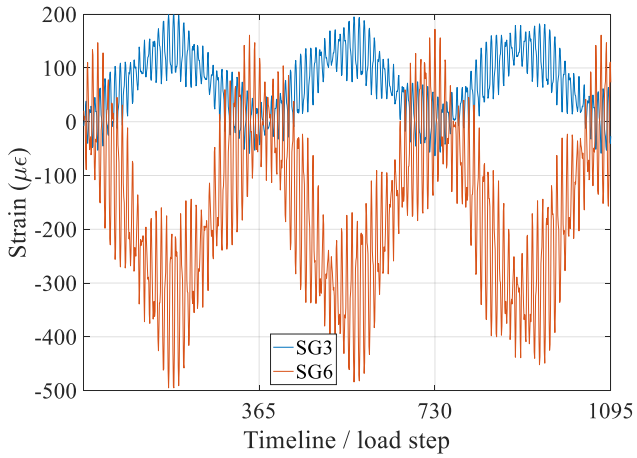

(a). Strain measurements from SG3 and SG6 under temperature and traffic loads

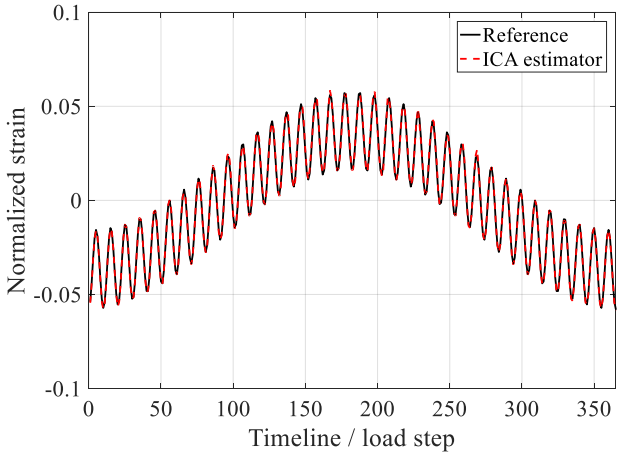

(b). Temperature induced strain comparison, *CC*=1.00

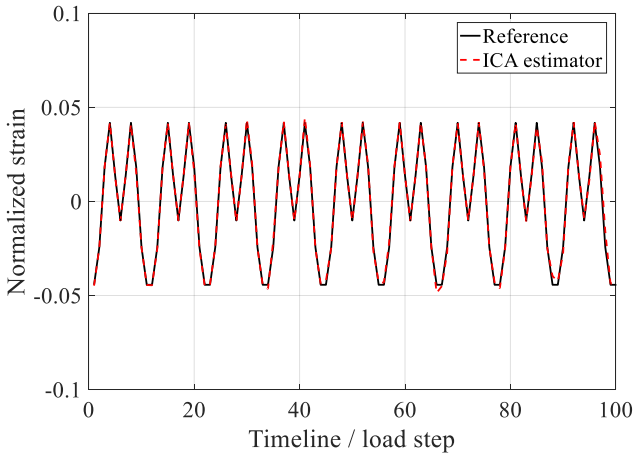

(c). Traffic induced strain comparison, *CC*=1.00

Figure 4.29. Application of overdetermined decomposition method on SG3 and SG6

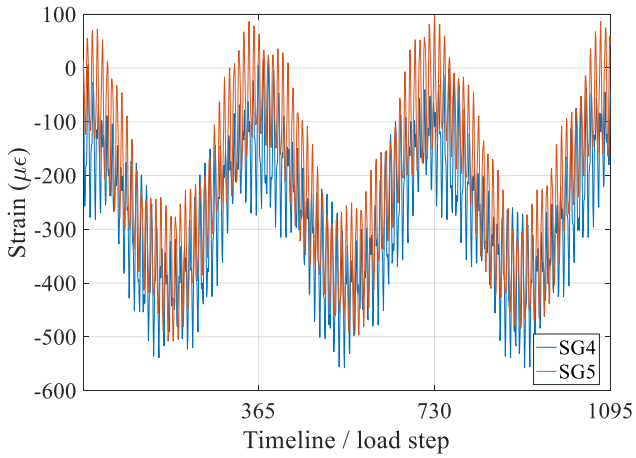

(a). Strain measurements from SG4 and SG5 under temperature and traffic loads

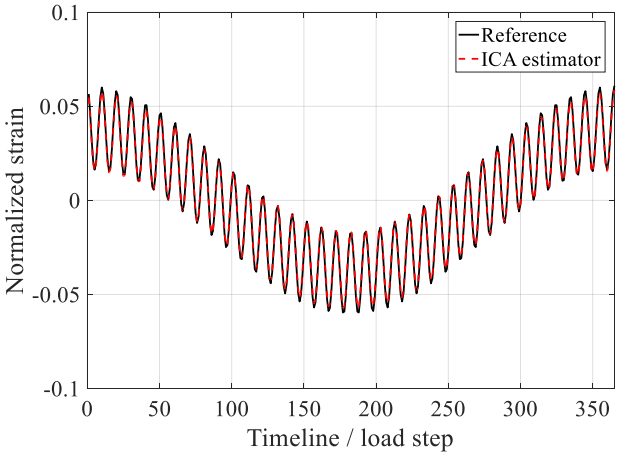

(b). Temperature-induced strain comparison, *CC*=1.00

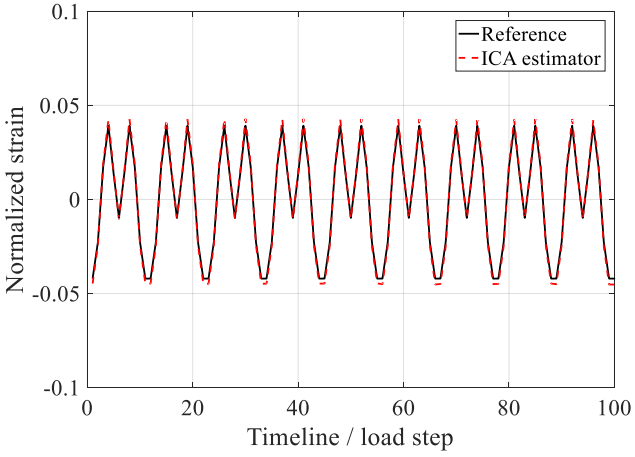

(c). Traffic-induced strain comparison, *CC*=1.00

Figure 4.30. Application of overdetermined decomposition method on SG4 and SG5

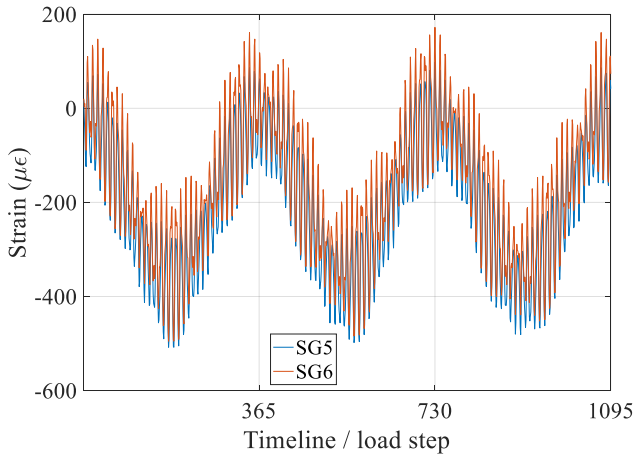

(a). Strain measurements from SG5 and SG6 under temperature and traffic loads

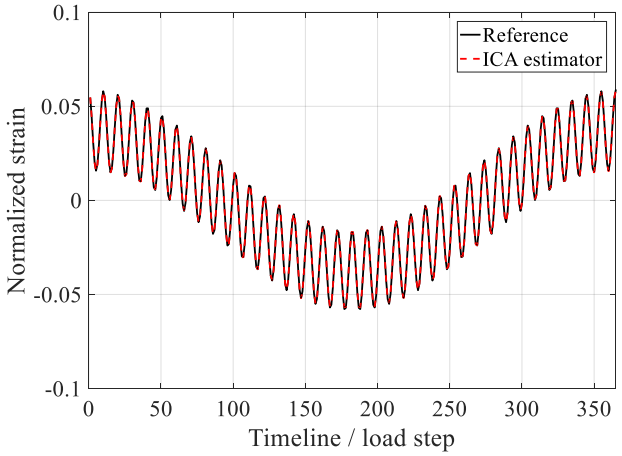

(b). Temperature induced strain comparison, *CC*=1.00

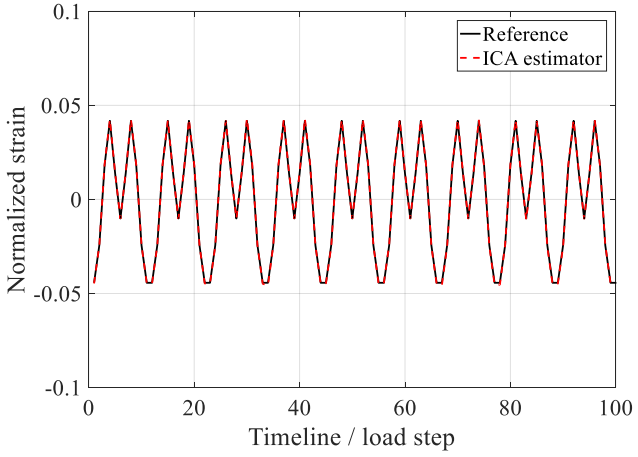

(c). Traffic induced strain comparison, *CC*=1.00

Figure 4.31. Application of overdetermined decomposition method on SG5 and SG6

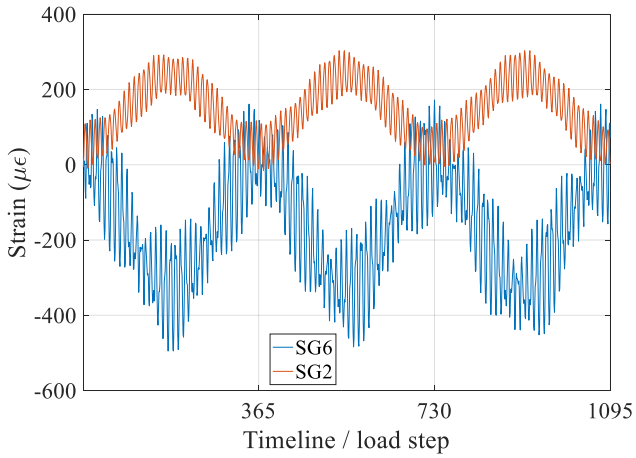

(a). Strain measurements from SG6 and SG2 under temperature and traffic loads

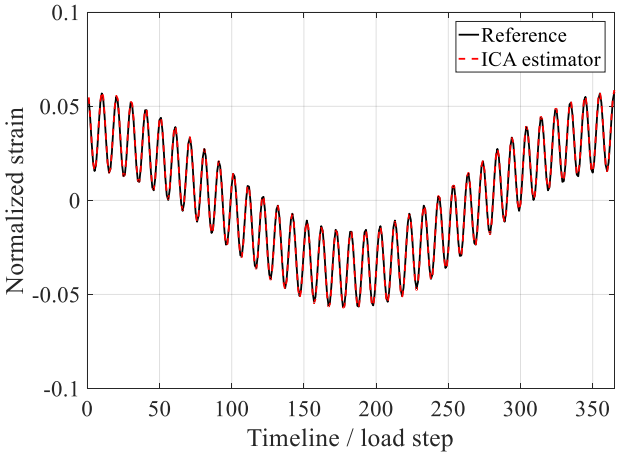

(b). Temperature induced strain comparison, *CC*=1.00

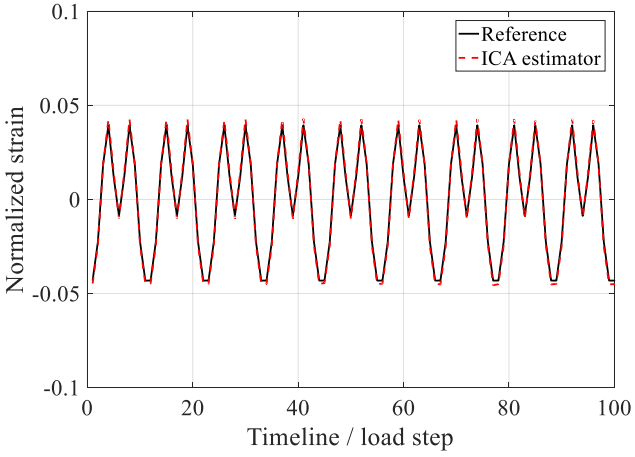

(c). Traffic induced strain comparison, *CC*=1.00

Figure 4.32. Application of overdetermined decomposition method on SG6 and SG2

To summarize the evaluation results and link with relative figures, the following Table 4.5 gives the overall information. As can be seen from Table 4.5 and relevant figures, the correlation coefficient values are all close to 1.00, which can demonstrate the separation ability of proposed overdetermined method to extract the thermal features.

However, one limitation of this overdetermined method is that the extracted features cannot exactly corresponding to one monitoring position. This is because the input data are consisted by over two channels, and there is only one separated thermal feature, which is hard to define the exact sensor location.

Table 4.5. Separation evaluation summary

Sensor pairs	**Temperature-induced strain**	**Traffic-induced strain**	**Relative figure**
SG1 & SG4	1.00	1.00	Figure 4.27
SG2 & SG5	1.00	1.00	Figure 4.28
SG3 & SG6	1.00	1.00	Figure 4.29
SG4 & SG5	1.00	1.00	Figure 4.30
SG5 & SG6	1.00	1.00	Figure 4.31
SG6 & SG2	1.00	1.00	Figure 4.32

4.1.4 Summary for the numerical case study

In this case study, the proposed thermal feature extraction methods, both underdetermined and overdetermined solutions, have been numerically evaluated.

Firstly, the underdetermined solutions, EPI and EEPI, are considered when sensors are limited in the sensor system. EPI and EEPI are proposed to interpret single-channel measurements directly and both seasonal and daily effects can be extracted from the mixed structural responses. As illustrated from the numerical case study, EPI performs robust enough to separate seasonal temperature effects, only if the monitoring data is over two years. In the meantime, the limitation for EPI is its vulnerable performance on one-year monitoring data. On the other hand, EEPI has shown to be a valuable tool to separate either daily and seasonal temperature variations from the mixed structural responses. The impact of two parameters, *Noise-Signal-Ratio (NSR)* and *number of*

trails (N), within EEPI has been evaluated. The recommendation for *Noise-Signal-Ratio* is 0.1-0.2 while for *number of trails* the author used 100 to 200.

Secondly, the overdetermined method includes pre-indication and blind separation, which is suitable for two or more channels measurements. PCA has been utilized for pre-indication to find the minimum input channels among all measurements for the subsequent blind separation procedure, running by Fast ICA. Six groups of data, selecting from all six sensors have been selected as the demonstrator. The separating results are stable and highly correlated with expected variations. Therefore, the proposed overdetermined method can be confirmed to separate the thermal features. But there has one limitation should be highlighted here. By using this overdetermined method, the extracted feature cannot be located precisely.

4.2 Experimental case study

In this section, the case study is conducted on an experimental truss bridge built for this Ph.D. work in the Structural Laboratory at the University of Warwick. This section is organized as follows: A brief introduction of the truss bridge is first given in Section 4.2.1; Section 4.2.2 is the case study on proposed underdetermined thermal feature extraction methods; Section 4.2.3 is investigating the performance of overdetermined method, followed by a summary, Section 4.2.4, to highlight the major findings of this case study.

4.2.1 Experiment introduction

The experimental truss bridge test was conducted in the Structural Laboratory in School of Engineering at the University of Warwick. The latest test area layout can be found in Figure 4.33.

There are four heating lamps on the top of this truss structure to provide the temperature loadings that applied on the bridge. The experimental test design is described in Appendix A in details, including the measurement system and heating system. This truss bridge is made by aluminium and includes three different length of chords with same cross-section dimension. The principal dimension and mechanical properties are given in Table 4.6. More detailed design information can be found in

Appendix B. The bridge is placed and supported by the Meccano and a steel bar at two ends, therefore, the bridge can be fixed, seeing Figure 4.34.

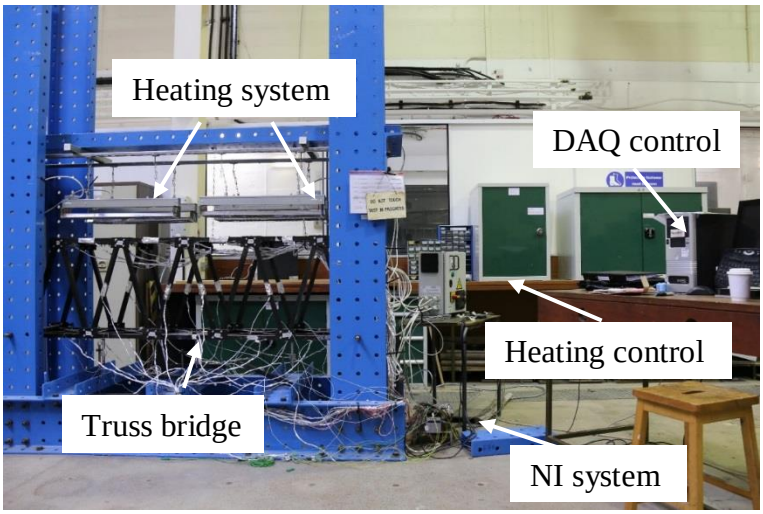

Figure 4.33. Truss bridge model in Structural Laboratory in University of Warwick

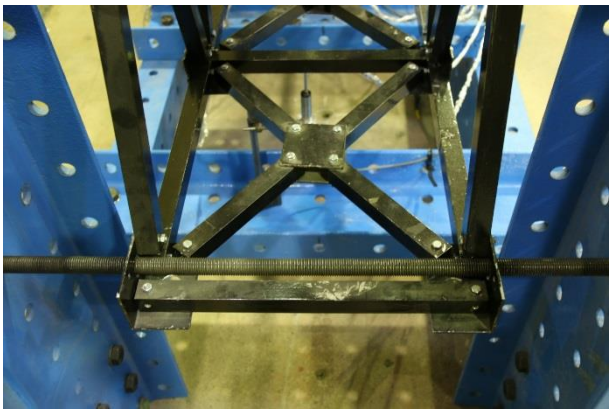

Figure 4.34. Boundary condition

Table 4.6. Key parameters of truss bridge

Bridge dimension / mm		**Bridge material properties**	
Short chord	203.47	Young's modulus	70 GPa
Medium chord	375.92	Density	$2.7g \cdot cm^{-3}$
Long chord	550.00	Poisson's ratio	0.35
Box section internal	18.90 × 18.90	Thermal expansion	23.1 $\mu m \cdot m^{-1} \cdot K^{-1}$
Box section external	25.40 × 25.40		

4.2.2 Experimental evaluation of underdetermined methods

This test was conducted in March 2017. Two types of loading conditions are considered, including temperature loadings and weights loadings. The loading positions can be found in Figure 4.35.

To evaluate the performance of EEPI and EPI methods for thermal feature separation, two groups of tests, reference test and hybrid test, are conducted on the healthy bridge. The definitions of reference and hybrid test are first given as follows:

- The reference test means only temperature load is applied on the bridge. The temperature variations are between 16 to 20 ℃. The linear relation between temperature and strain can be obtained, which is the basis rule to evaluate the performance of the proposed EEPI or EPI.
- The hybrid test means that the combined time-varying temperature and weight loadings are applied on the bridge. The temperature keeps fluctuating within 16-20 ℃. The 30 Kg weights are distributed into three loading positions, as shown in Figure 4.35.

From the reference test, the linear relation between strain and temperature can be obtained, therefore the correlation of estimated strain with relative temperature records is selected to assess the method's performance. In other words, the higher correlation coefficient with temperature variations, the better separated results.

The truss dimension and the monitoring system deployed can be found in Figure 4.36, which consists of four strain gauges, termed as SG-1 to SG-4, with three thermcouples notated as TH-A to TH-C. The SG1 is attached on the top surface of the longitudinal chord, while SG2 is attached on the bottom surface of the transversal chord. Both SG-3 and SG-4 are attached on the bottom surface of the target chords to avoid the direct radiation of heating lamps.

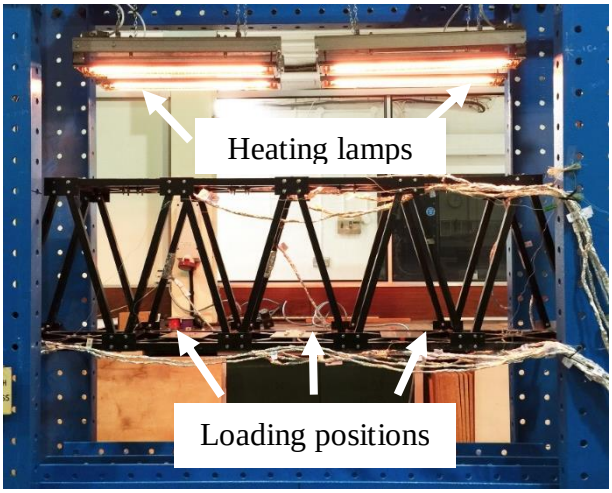

Figure 4.35. Loading positions overview

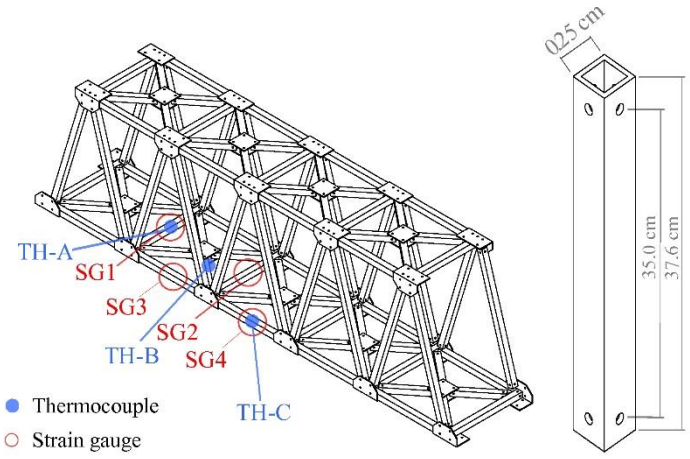

Figure 4.36. Sensor positions and the monitored chord dimension

Data investigated by EPI

The application of EPI is on above four monitoring chords individually, as shown in Figure 4.36. For each monitoring position, the separated independent components are first presented in time domain, followed by a figure to compare this 'EPI estimators' with the data from 'hybrid test' and 'reference test'. As mentioned previously, the higher correlated with temperature fluctuation, the better separation.

Taking the SG1 as the first example. The independent components separated by ICA are displayed in Figure 4.37. Their correlation coefficient value with temperature variations is also calculated and addressed in the sub-figures. The negative sign represents its negative relation with temperature, but the absolute value is of interest.

Therefore, the independent component 2 as shown in Figure 4.37(b) is higher related with temperature variations, which is then plotted in Figure 4.38 represented by the label of EPI estimated data.

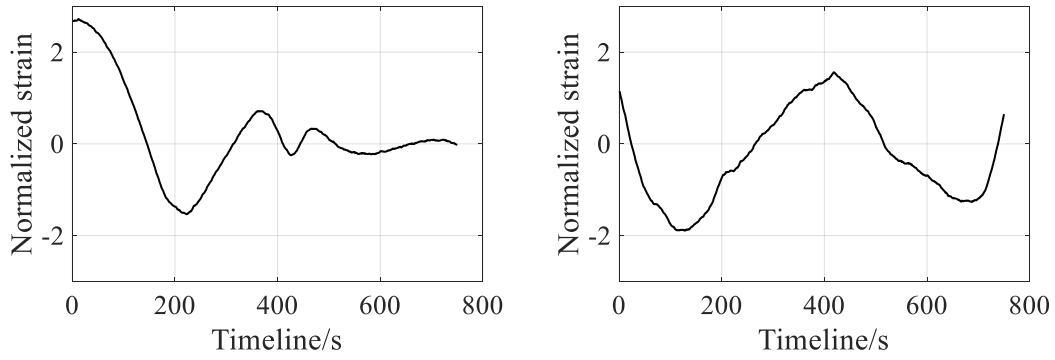

(a). Independent component 1 (*CC* = -0.60)

(b). Independent component 2 (*CC* = -0.65)

Figure 4.37. Independent components that separated from SG1

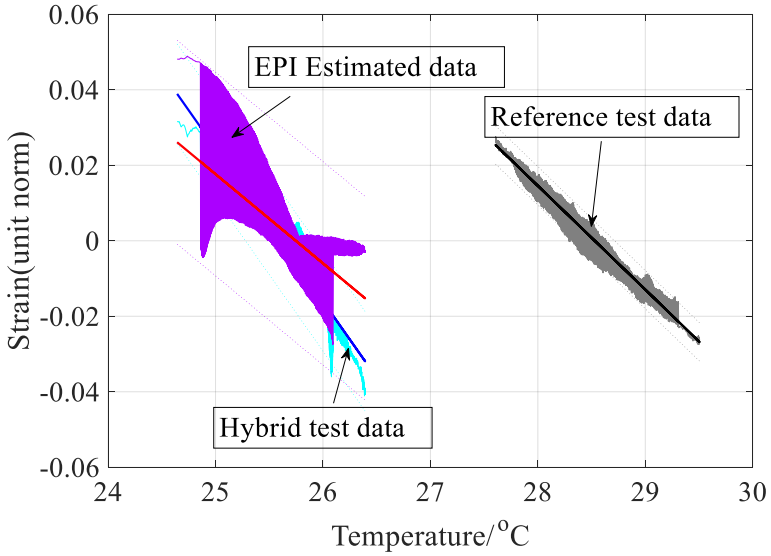

Figure 4.38. Evaluation of EPI-estimated data from SG1 (blue: *CC*=-0.95, purple: *CC*=-0.65, grey: *CC*=-0.99)

From Figure 4.38, the data from the hybrid test are all in blue area and the grey area represents the data from the reference test. It is obvious that the grey region is much narrower because only temperature loading is applied during the reference test. The correlation coefficient value is -0.99, which is higher related with temperature, because the reference data is from the test where only temperature load is applied on the bridge. The data from hybrid test is -0.95 correlated with temperature variations,

which is higher than the EPI estimated data. Hence, the separation of EPI on data from SG1 is not good enough.

The following two figures, Figure 4.39 and Figure 4.40, are given to present the test results from SG2. It can be seen from Figure 4.39 that the first independent component is higher related with temperature variations, since the *CC* value is 0.91. This is then compared with hybrid test data and reference data to assess the EPI separation performance. As can be seen from Figure 4.40, the EPI separated data is relatively high related with temperature records, but still not a big improvement when compare to the data from hybrid test.

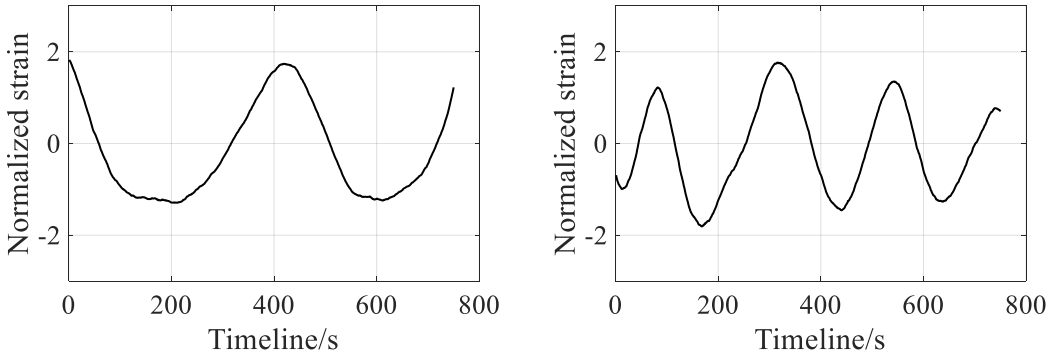

(a). Independent component 1 (*CC* = -0.91)

(b). Independent component 2 (*CC*= -0.10)

Figure 4.39. Independent components that separated by EPI from SG2

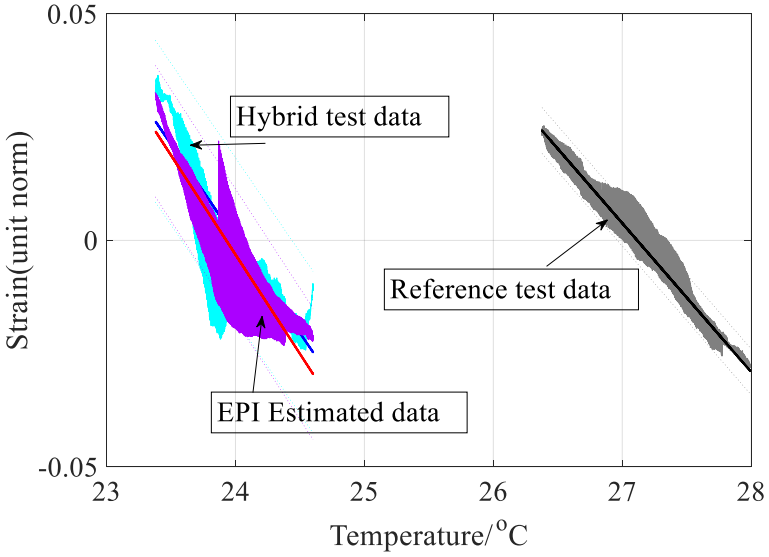

Figure 4.40. Evaluation of EPI-estimated data from SG2 (blue: *CC*=-0.95, purple: *CC*=-0.91, grey: *CC*=-0.99)

The application of EPI on SG3 and SG4 has also been conducted. The following Figure 4.41 and Figure 4.43 show the separated component by ICA, while Figure 4.42 and Figure 4.44 present the comparison results. According to the *CC* values, the separation results by EPI are all weak for SG3 and SG4, as the correlation coefficient values are just 0.32 and 0.28 respectively.

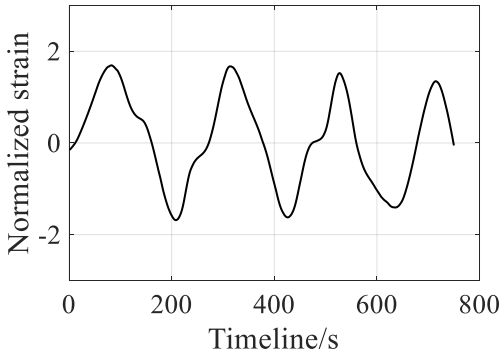

Figure 4.41. Independent component that separated by EPI from SG3 (*CC*=-0.32)

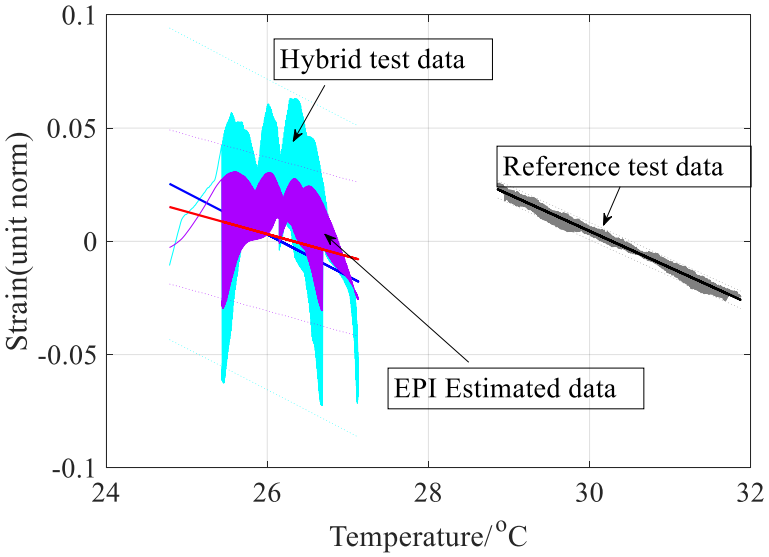

Figure 4.42. Evaluation of EPI-estimated data from SG3 (mix: *CC*=-0.95, estimated: *CC*=-0.32, reference: *CC*=-0.99)

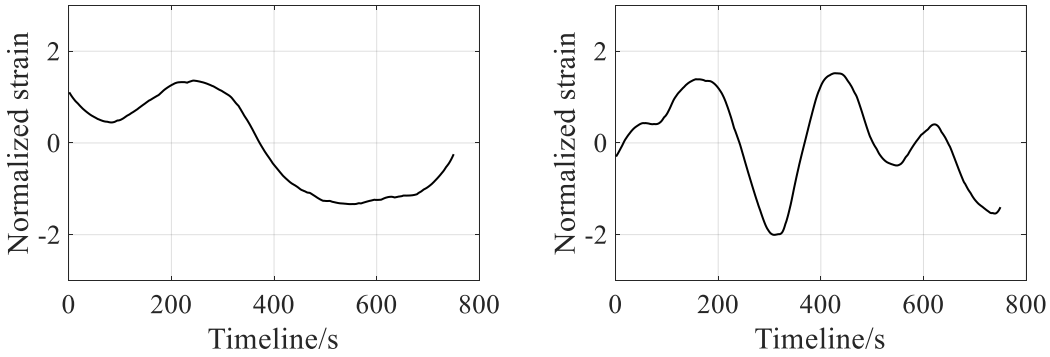

(a). Independent component 1 (*CC*=-0.28)

(b). ndependent component 2 (*CC*= -0.27)

Figure 4.43. Independent components that separated by EPI from SG4

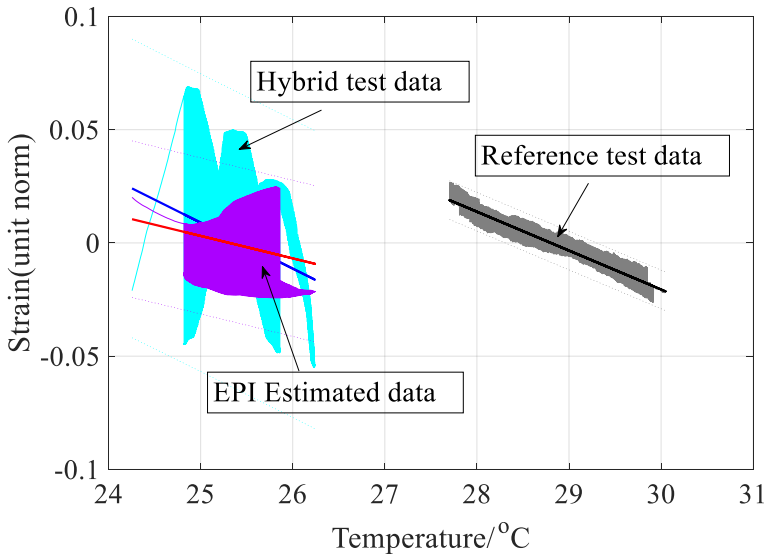

Figure 4.44. Evaluation of EPI-estimated data from SG4 (blue: *CC*=-0.95, purple: *CC*=-0.28, grey: *CC*=-0.99)

Data investigated by EEPI

The combination of *NSR* and *N* are examined, ranging from 0.01 to 0.5 every 0.01 for *NSR* and from 10 to 800 every 10-step for *N*. Therefore, 150-by-80 combinations of *NSR* and *N* have been investigated in this study. The time consumption is given in Figure 4.45. It is obvious the more number of trails the more time consumption. In Figure 4.45, there are two blocks, with which the time composition is higher than expected. This is because the different computers that are used for calculation. But in general, the time consumption is linear related with the number of trails, *N*. The Figure 4.46 gives the partial time consumption results operating by computer 1, where *NSR*

ranges from 0.01 to 0.5 and *N* ranges from 10 to 800. The major computational cost for various trails number, *N*, is also listed in Table 4.7 for reference. The recommend selection will be summarized at the end of this part.

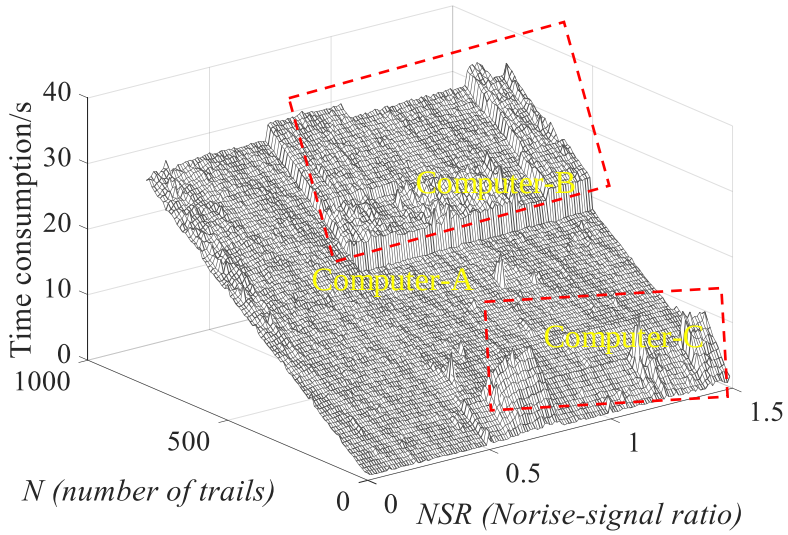

Figure 4.45. Time consumption of method EEPI with various *NRS* and *N* for SG1

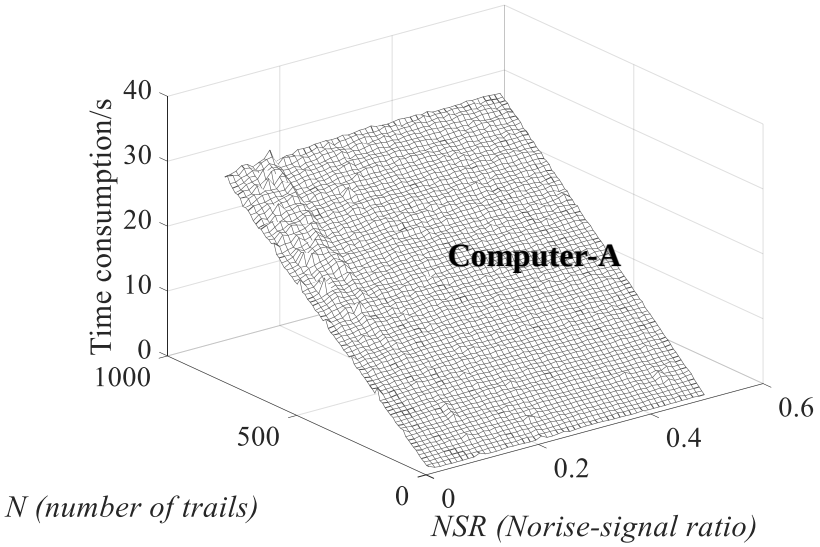

Figure 4.46. Time consumption of method EEPI with *NRS: 0.01~0.5* and *N: 10~800* on SG1 operating by Computer-A.

Table 4.7. The major time consumption list based on Computer-A

Number of trails N	100	200	300	400	500	600	700	800
Time consumption / s	4.1	8.1	12.1	16.1	20.1	24.1	28.2	32.2

The influence of *NSR* and *N* on the performance of EEPI is investigated respectively and are shown in Figure 4.47 and Figure 4.48 for SG1. The influence of *NSR* and *N* can be summarized as follows:

- The correlation coefficient represents the correlation between estimated strain, which is separated by EEPI, and temperature variation from THA. Therefore, the higher values of correlation coefficient, the better separation by EEPI.
- According to the average line, drawing as the blue line in Figure 4.47, the better and stable performance should occur when *NSR* between 0.03~0.1 and 0.4~0.5. The correlation coefficient is over 0.9, which means the separated strain are much correlated with temperature variations.
- When *NSR* is located in the area 0.03~0.1 is much more stable when compare with the range 0.4~0.5. This is because the standard deviation of previous range is narrower than the range 0.4~0.5. The upper red dash line that is shown in Figure 4.47 represents the average correlation coefficient among all attempts plus half relative standard deviation. The lower red dash line is the average value subtract half relative standard deviation. Hence the bandwidth of both red dash line represents the standard deviation. The bandwidth when NSR=0.03~0.1 is smaller than the bandwidth when NSR=0.4~0.5. This demonstrate the stability when *NSR* is smaller.
- Different from the *NSR*, the effect of the number of trails, *N*, is not visible, which also confirm the same conclusion in numerical case study. As showing in Figure 4.48, the average line is fluent, the same as the standard deviation, σ.

With the recommend values of *NSR* and *N*, the separating results are given in Figure 4.49. The estimated data with temperature relation is compared with reference data and hybrid data. The correlation coefficient, *CC*, values can be found in the figures too.

Following the same procedures to investigate the EEPI performance on SG2. The influence of *NSR* and *N* is first investigated and shown in Figure 4.50 and Figure 4.51.

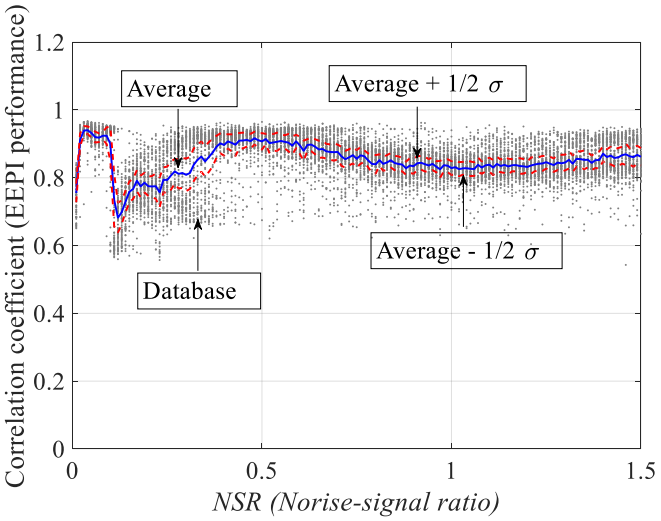

Figure 4.47. Influence of *NSR* on the performance of EEPI for SG1

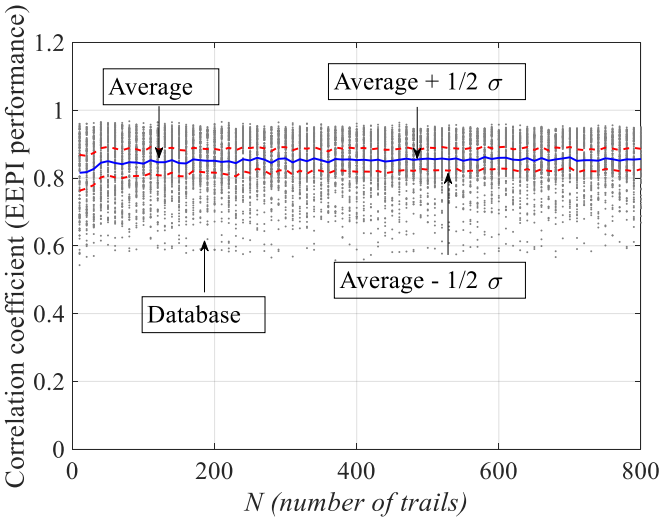

Figure 4.48. Influence of *N* on the performance of EEPI for SG1

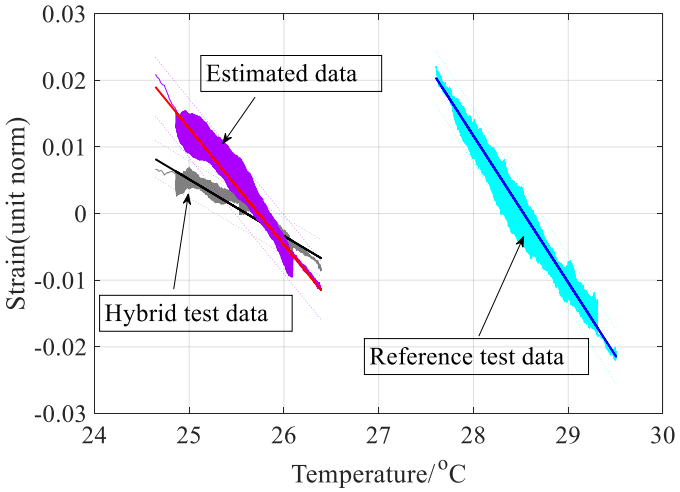

Figure 4.49. Evaluation of EEPI-estimated data from SG1 (grey: *CC*=-0.95, purple: *CC*=-0.97, blue: *CC*=-0.99): *NSR = 0.04*, *N=80*, time consumption: 3.09 seconds

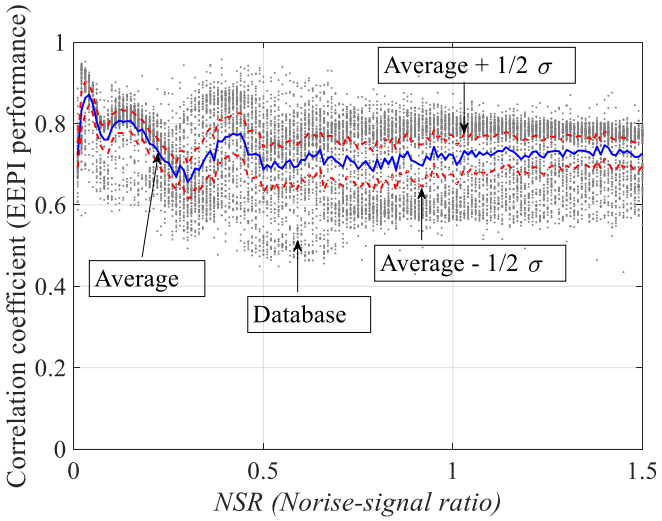

Figure 4.50. The influence of *NSR* on the performance of EEPI for SG2

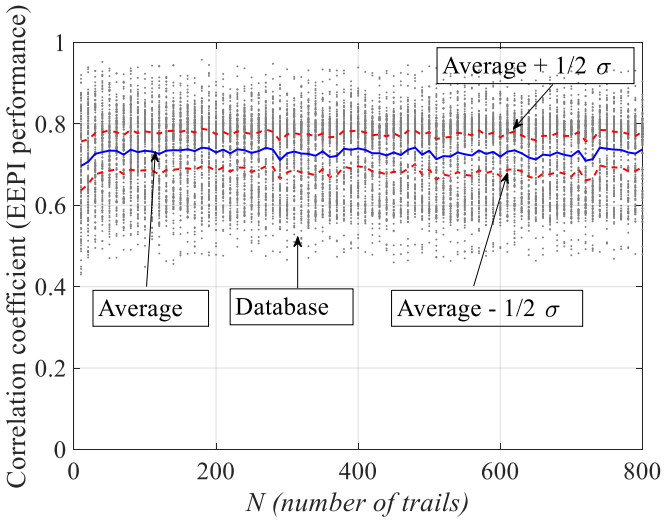

Figure 4.51. The influence of *N* on the performance of EEPI for SG2

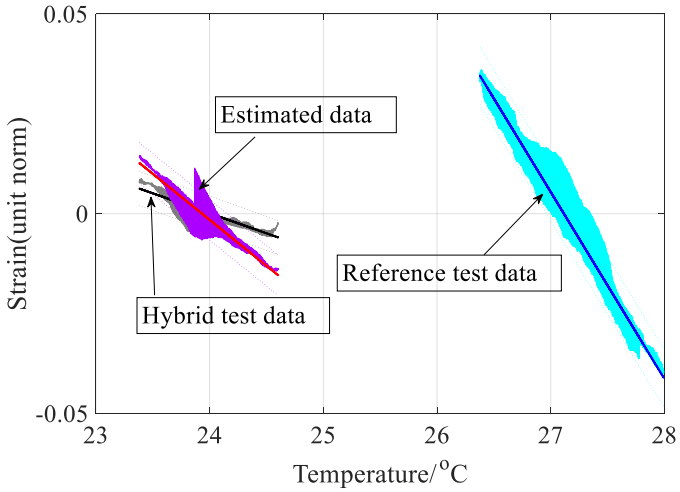

Figure 4.52. Evaluation of EEPI-estimated data from SG2 (grey: *CC*=-0.86, purple: *CC*=-0.96, blue: *CC*=-0.99): *NSR = 0.39, N=180,* time consumption: 7.29 seconds

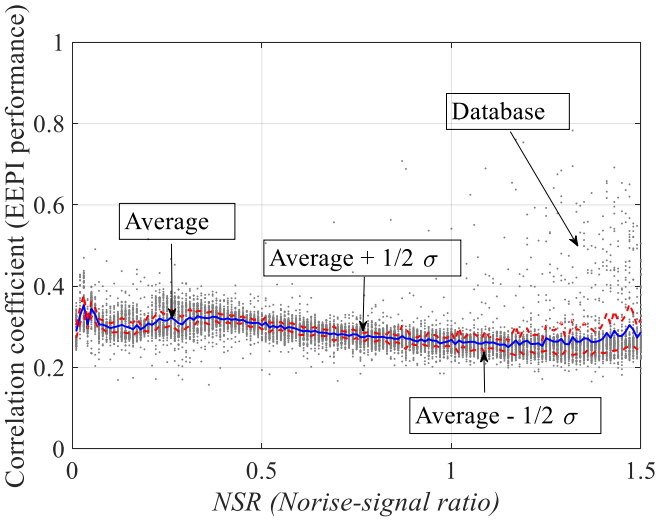

Figure 4.53. The influence of *NSR* on the performance of EEPI for SG3

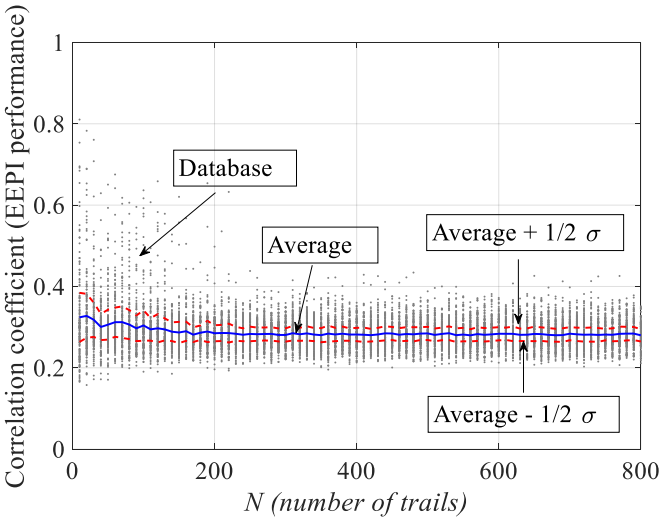

Figure 4.54. The influence of *N* on the performance of EEPI SG3

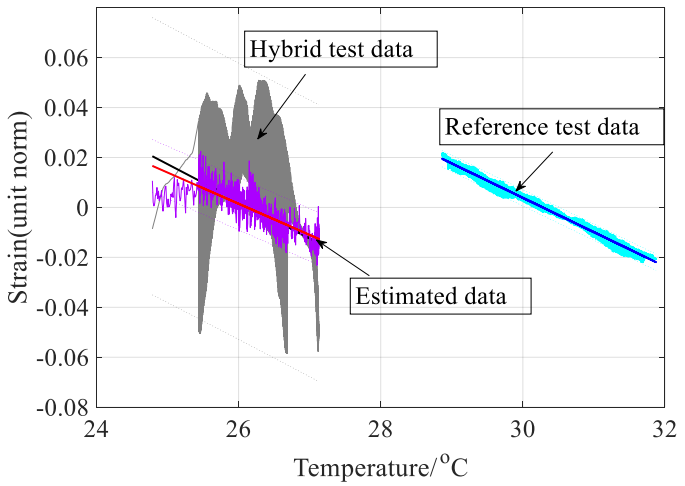

Figure 4.55. Evaluation of EEPI-estimated data from SG3 (grey: *CC*=-0.30, purple: *CC*=-0.81, blue: *CC*=-0.99): *NSR = 1.02, N=10,* time consumption: 0.72 seconds

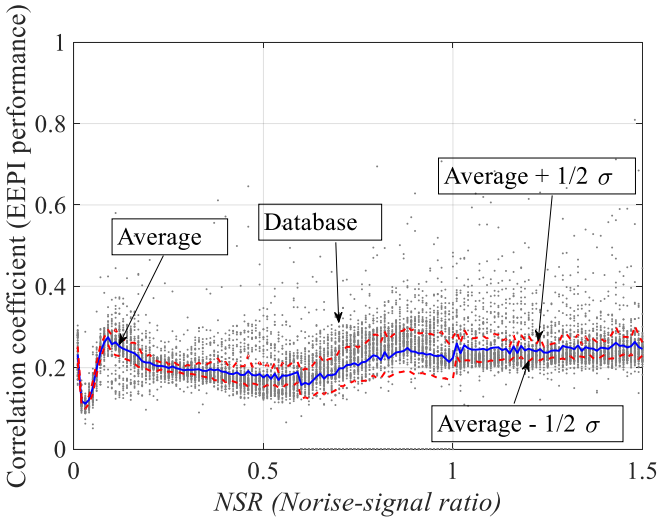

Figure 4.56. The influence of *NSR* on the performance of EEPI for SG4

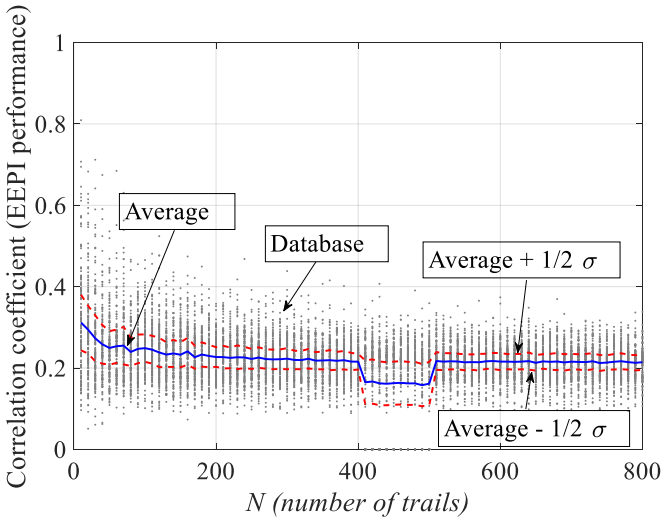

Figure 4.57. The influence of *N* on the performance of EEPI for SG4

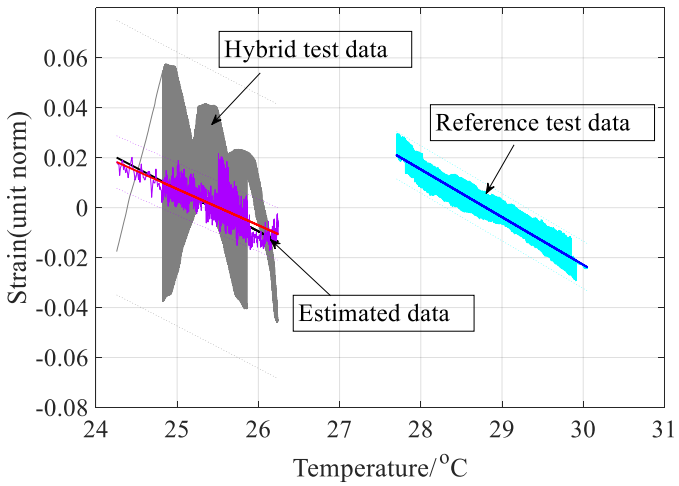

Figure 4.58. Evaluation of EEPI-estimated data from SG4 (grey: *CC*=-0.29, purple: *CC*=-0.81, blue: *CC*=-0.95): *NSR = 1.48, N=10,* time consumption: 0.89 seconds

The monitoring chords at position 3 and 4 are transversal direction, which are more sensitive with moving load. In another word, the temperature is not a major contribution in the measurements. But there are still some points can be summarized as follows.

- The influence of *NSR* can confirm the previous observation in longitudinal chords. The separating performance is relatively stable when *NSR* is located in 0.01 to 0.1. Because their standard deviations, σ, are relative narrow, which is shown as the bandwidth of two read dash lines in Figure 4.53.
- When the *NSR* is beyond 0.5, which means the added white noise is stronger, the performance in return is worse. As showing in Figure 4.53, the average line is going down and the standard deviation is bigger.
- The Figure 4.54 shows the influence of *N*. It is apparent the EEPI performance is more stable, i.e. stable average line and relative narrow standard deviation, when the number of trails, *N*, if over 200. But considering the time consumption due to the increase of *N*, the recommend value of *N* should be within 200 to 400.

The method EPI and EEPI have been investigated on four sensors records. The results are summarized into Table 4.8. Two findings can be obtained as follows:

- First of all, the higher correlation coefficient value, the better performance. Obviously, the performance of EEPI is better than EPI.
- The EEPI separated sources is more related with temperature variations when compared with data from hybrid test. For example, the hybrid test data is -0.95 correlated with temperature load, but the EEPI separated sources is increased to -0.97, which is closer to the reference value (-0.99).

Table 4.8. Summary of EPI and EEPI: correlation coefficient value with temperature variations

	Sensor SG1		**Sensor SG2**	
	EPI	EEPI	EPI	EEPI
Hybrid test data	-0.95	-0.95	-0.95	-0.86
Estimated data	**-0.65**	**-0.97**	**-0.91**	**-0.96**
Reference test data	-0.99	-0.99	-0.99	-0.99
Relative figure	Figure 4.38	Figure 4.40	Figure 4.42	Figure 4.44
	Sensor SG3		**Sensor SG3**	
	EPI	EEPI	EPI	EEPI
Hybrid test data	-0.95	-0.90	-0.95	-0.90
Estimated data	**-0.32**	**-0.81**	**-0.32**	**-0.81**
Reference test data	-0.99	-0.99	-0.99	-0.99
Relative figure	Figure 4.50	Figure 4.53	Figure 4.56	Figure 4.59

4.2.3 Experimental evaluation of overdetermined methods

This test was conducted during February 2018. Temperature load is still simulated by controlling the heating lamps, while the moving loading is applied on the bridge by using dumbbells and two leading wood tracks, seeing Figure 4.59. The sensor positions of interests in this case study is also given in Figure 4.60. For the detailed description of experimental systems, the reader can refer to Appendix A. For the dimension of this truss bridge, the reader can find design drawings in Appendix B.

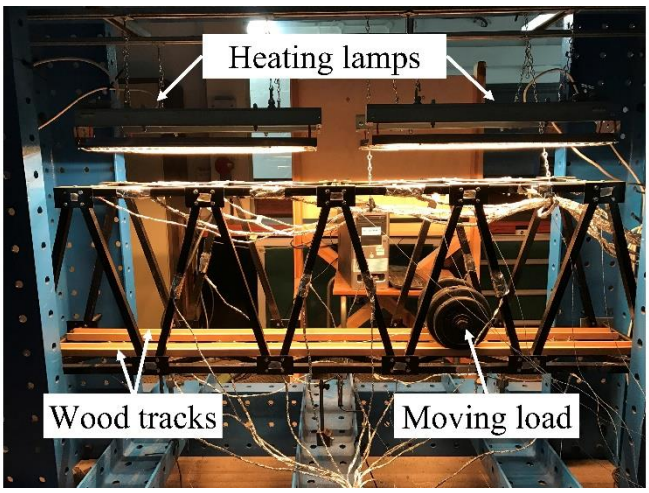

Figure 4.59. Bridge test overview with loading conditions

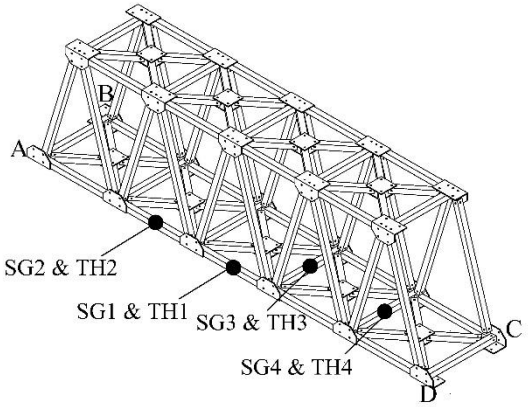

Figure 4.60. Sensor positions overview for Section 4.2.3 (SG: strain gauges; TH: thermocouples)

The tests are also classified into two types, reference test and hybrid test, considering the loading conditions. For the reference test, only temperature load is applied on the bridge, and the data collected is designed as reference data. For the hybrid test, the bridge is under temperature and moving loadings conditions, and the data collected from hybrid test is named as hybrid test data in following contents.

The measurements from hybrid tests are utilized to extract the temperature-induced structural responses by the proposed overdetermined methods. The reference data is then utilized to assess the estimated sources. The higher related with the reference data, the better separation performance.

As previously described in CHAPTER 3, the first step of proposed overdetermined method is pre-indication by applying principal component analysis (PCA). In this case, two principal components can be obtained after performing PCA on the target four sensor records, which means there have two contributors or load conditions that affect the final structural response. This can also be confirmed by the loading condition, since only temperature and traffic loads are applied on the bridge. However, there has no prior knowledge of the loading conditions in the real word structure, hence, the PCA can help to identify the principal loading conditions.

Based on the pre-indication results performed by PCA, the minimum number of inputs channels for the blind separation is two. Therefore, two sensor records, SG1 and SG2, are selected from the four strain gauges as a demonstration. The measurements from TH1 and TH2 are given in Figure 4.61(a), while the strain data

from the hybrid test is showing in Figure 4.61(b). Two cycles of temperature variations are recorded, during which four cycles of moving load variations are applied on the bridge. From Figure 4.61(b), the strain variations cause by moving load is not evident. In addition, the negative relation with the temperature can be observed, this is due to the strain gauges are attached underneath the chord to avoid the damage caused by wood tracks or unexpected interruption on the strain sensors.

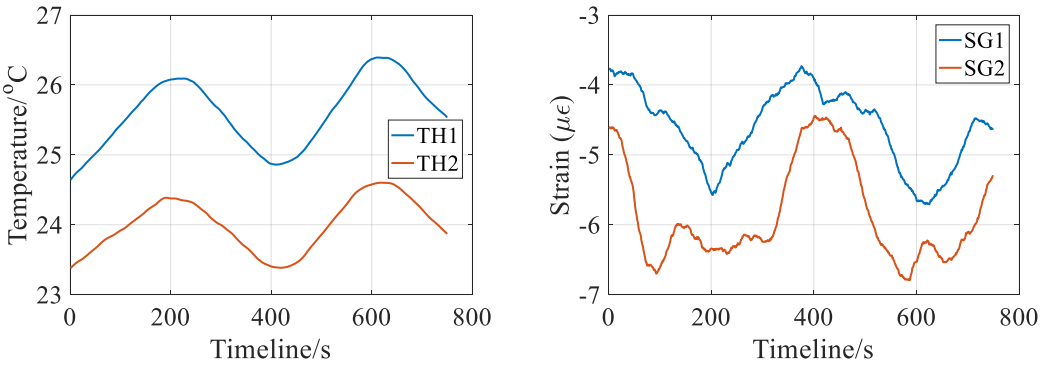

(a) thermocouple records (b) strain gauges records

Figure 4.61. Hybrid test data from SG1 and SG2

The second procedure of the overdetermined method is the blind separation, operated by Fast ICA, independent component analysis. Fast ICA is performed on the strain measurements collected from the hybrid test. The purpose of this step is to separate the temperature-induced variations and moving load induced variations. The separation results are given in Figure 4.62. It is obvious that Figure 4.62(a) is the thermal related strain, because the two cycles are visible, while Figure 4.62(b) represents the strain duo to moving load as four cycles are apparent.

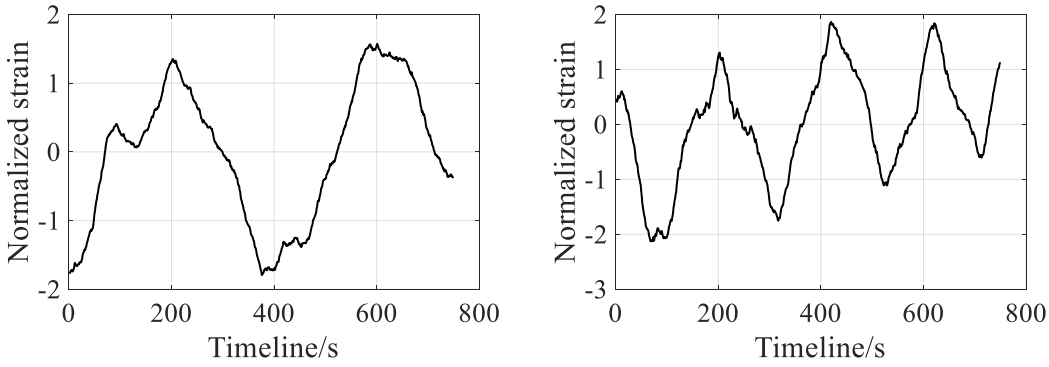

(a). Independent component 1 (b). Independent component 2

Figure 4.62. Independent components that separated by Fast ICA from SG1 and SG2

The following Figure 4.63, the temperature related strain separated by Fast ICA is plotted and all estimated data are normalized with the unit norm to compare with the reference data and Hybrid data.

As can be seen from Figure 4.63, the reference data is plotted into the grey area, and the black line is the linear fitting results based on all reference data. The hybrid test data, which means both temperature and traffic loads are applied on the bridge, is displayed in as the blue region. The estimated data by utilizing ICA is plotted as the purple. The correlation coefficient value (*CC*) with temperature records are also calculated and can be seen in the title of Figure 4.63. The absolute value of *CC* is of interest. The higher value of *CC*, the better separation results.

There is one thing must be emphasized again, the reference test and hybrid test cannot be conducted at the same time with the same temperature, hence the reader will find the temperature ranges for reference test and hybrid test are different. For example, in Figure 4.63, the temperature range for reference test is 26.3~28 ℃, but the hybrid test is conducted in different time, whose temperature range is 24.5~26.5 ℃.

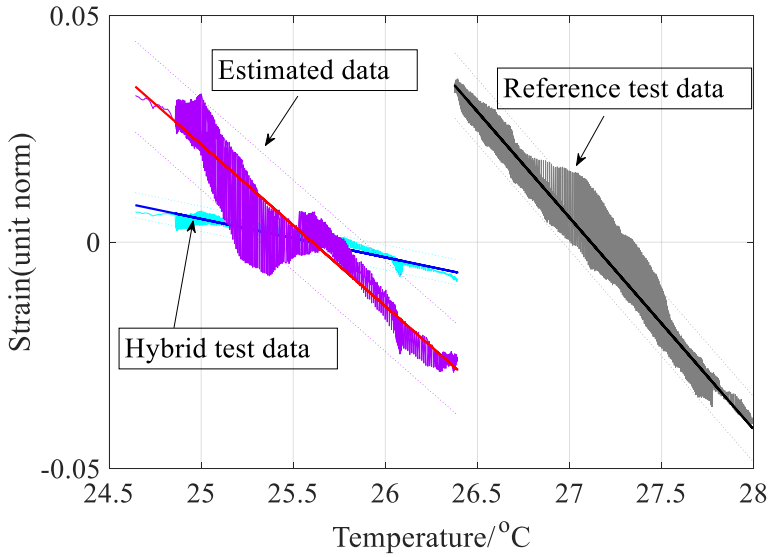

Figure 4.63. Evaluation of overdetermined method on data from SG1 and SG2 (blue: *CC*=-0.95, purple: *CC*=-0.96, grey: *CC*=-0.99)

From Figure 4.63, the estimated data is higher related with temperature variations, when compared with hybrid test data, since the correlation coefficient value is increased from 0.95 to 0.96. The gradients of linear fitting lines are also calculated.

For hybrid test and reference test, the gradient is -1.081 and -1.328 respectively. The gradient of the estimated is -1.307, which is close to reference data's gradient.

Similar as the sensor pairs SG1 and SG2, the other sensors are also investigated. The following Figure 4.64 gives the outcomes on SG2 with assistant sensor SG1, while Figure 4.65 and Figure 4.66 provides the separating results on SG3 and SG4 respectively. Among those figures, the separated independent components are presented in part (a) and (b), from which the temperature-related data is then plotted in part (c) to compare with the hybrid test data and the data from reference data. The correlation coefficient values are all calculated and will summarized in Table 4.9 for the discussion.

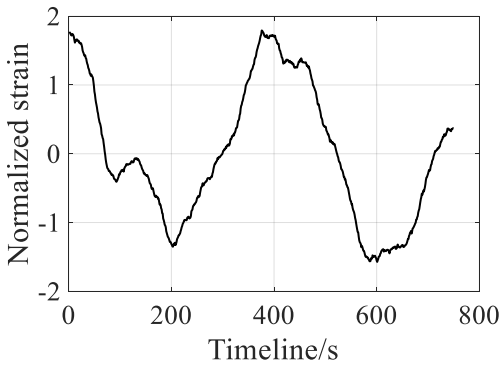

(a). Independent component 1

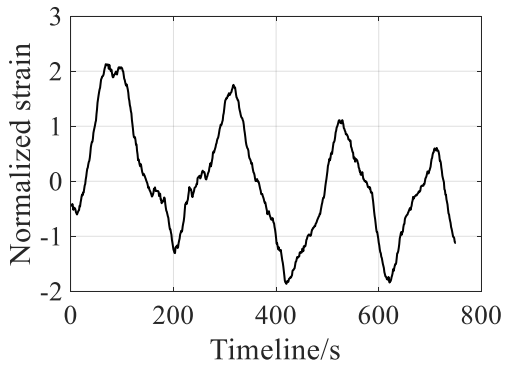

(b). Independent component 2

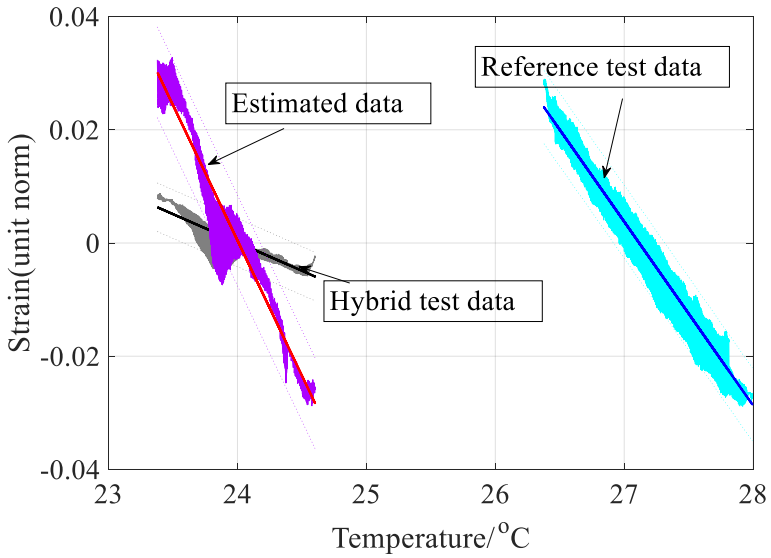

(c). Comparison with data from hybrid test and reference test

Figure 4.64. Evaluation of overdetermined method on data from SG2 and SG1 (blue: *CC*=-0.86, purple: *CC*=-0.97, grey: *CC*=-0.98)

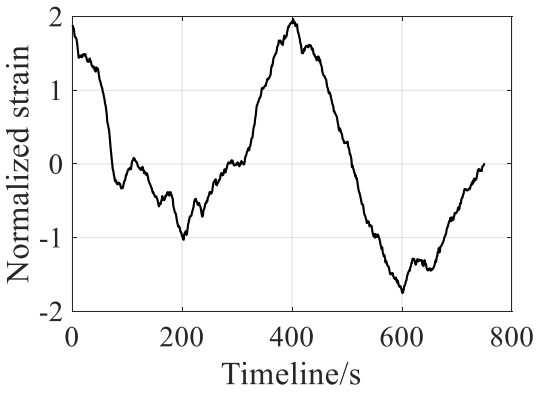

(a). Independent component 1

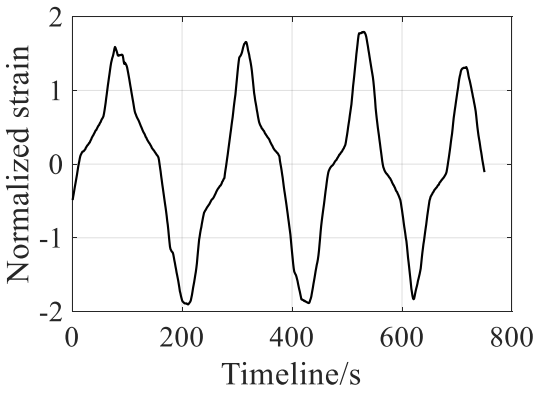

(b). Independent component 2

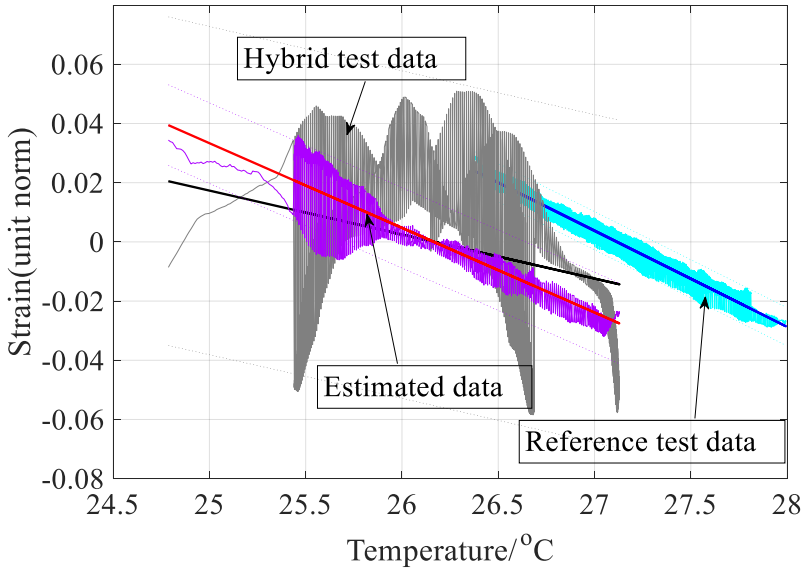

(c). Comparison with data from hybrid test and reference test

Figure 4.65. Evaluation of overdetermined method on data from SG3 and SG1 (blue: *CC*=-0.30, purple: *CC*=-0.93, grey: *CC*=-0.98)

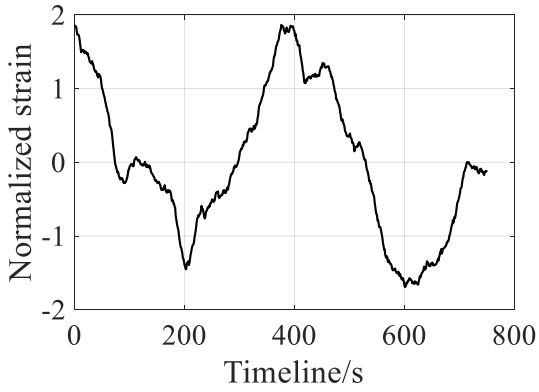

(a). Independent component 1

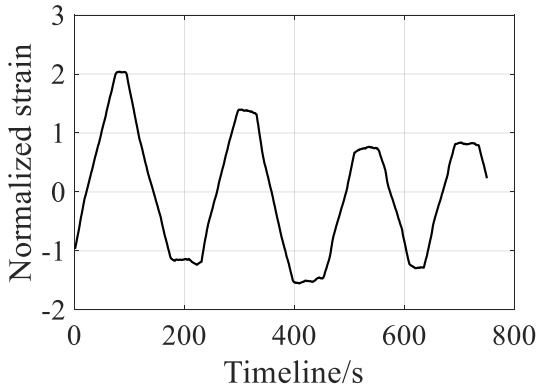

(b). Independent component 2

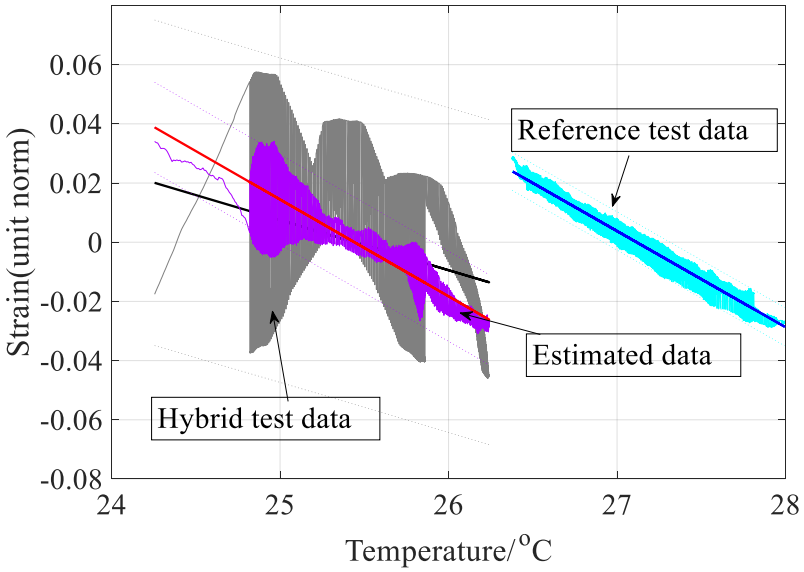

(c). Comparison with data from hybrid test and reference test

Figure 4.66. Evaluation of overdetermined method on data from SG4 and SG1 (blue: *CC*=-0.29, purple: *CC*=-0.91, grey: *CC*=-0.94)

Table 4.9. Summary of the correlation with temperature variations.

Sensor	Correlation coefficient with temperature variations			Relevant figure
	estimated data	hybrid test data	reference test data	
SG1	-0.9607	-0.9475	-0.9855	Figure 4.63
SG2	-0.9748	-0.8637	-0.9844	Figure 4.64
SG3	-0.9256	-0.2981	-0.9811	Figure 4.65
SG4	-0.9061	-0.2936	-0.9412	Figure 4.66

As can been seen from Table 4.9, the traffic loadings have an evident influence on SG3 and SG4 when comparing with other two sensor measurements. Because the correlation between hybrid test data and temperature variations are only 0.30 for SG3 and SG4, but over 0.86 for SG2 and 0.95 for SG1. The reason is because the chords of SG3 and SG4 are in transversal direction, while SG1 and SG2 are in longitudinal direction. The moving dumbbells will place the load directly on the transversal chords. Therefore, the linear correlation will be broken on SG3 and SG4.

From Table 4.9, the correlation between estimated strains with relative temperature variations are all above 0.90, which can demonstrate the performance of separation. Because the thermal strain with temperature variations are just between 0.9412 and 0.9855 even in the reference test with only temperature load. If comparing the correlation of estimated strain and hybrid test strain with temperature variations, it is obvious that the separated sources are more related with temperature, as the correlation values are all increased, especially for SG3 and SG4. The correlation coefficients of hybrid test data with temperature are only -0.2981 and -0.2936 for SG3 and SG4 respectively, but over 0.86 at SG1 and SG2. This can confirm the previous observation and conclusion that the moving load has a more significant influence on transversal chords, i.e. on SG3 and SG4, when comparing to longitudinal direction.

4.2.4 Summary for experimental case study

The laboratory case study for thermal feature extraction methods has been fully described above. Several points can be summarized and highlighted here.

- The proposed underdetermined method, EPI and EEPI, are two powerful tools to separate thermal features from single-channel strain measurements. And in laboratory case, EEPI performs better than EPI, and the recommend values for *NSR* is 0.1 – 0.2 and *N* is between 100 to 200.
- The proposed overdetermined method, PCA + Fast ICA, shows a stable capability to extract temperature related responses.

4.3 Concluding remarks

This chapter set out to evaluate the proposed thermal feature extraction methods. The first case study is a numerical truss model and the second one is the laboratory truss test. Both underdetermined and overdetermined methods have been examined by numerical truss model built by ANSYS and the experimental truss model built in Structural Laboratory at the University of Warwick.

In general, the EPI and EEPI, proposed for the underdetermined cases, have been applied on the single-channel measurements directly and the seasonal temperature-induced variations can be separated from the daily effects, while it is impossible in the overdetermined cases by applying PCA with Fast ICA.

As illustrated from the numerical case study, the performance of EPI is related to the length of monitoring data. Or in other word, the EPI outperforms than EEPI when the monitoring data is over two years, since the periodic features of seasonal temperature variations can be revealed in this situation. On the contrary, the EEPI outperforms than EPI when the data is less than two-year long.

Overall, EEPI has shown to be a valuable tool to separate either daily and seasonal temperature variations from the mixed structural responses. The impact of two parameters, *Noise-Signal-Ratio (NSR)* and *number of trails (N)*, within EEPI has also been evaluated and the recommended values have also been suggested.

Regarding the overdetermined method includes pre-indication and blind separation, which is suitable for two or more channels measurements. PCA has been utilized for pre-indication to find the minimum input channels among all measurements for the subsequent blind separation procedure, running by Fast ICA. The separating results are stable and highly correlated with expected variations. Therefore, the proposed

overdetermined method can be confirmed to separate the thermal features. But there has one limitation should be highlighted here. By using this overdetermined method, the extracted feature cannot be located precisely.

The numerical and experimental case studies also demonstrate that EPI and EEPI can extract the seasonal and daily thermal variations from the hybrid test data. This hybrid test data means the structural responses under various loading conditions, for example, the temperature and traffic loading conditions in this case study. But PCA + Fast ICA cannot distinguish the seasonal and daily variations respectively. This method was, however, forward to extract thermal features from other effects. The author recommends EEPI method when the available number of sensors is limited, for example, less than three. For best reliability and numerical accuracy for the extracted thermal response, the author will prefer to recommend PCA + Fast ICA.

In addition, the underdetermined decomposition approaches, EPI and EEPI, are proposed for the extreme condition, i.e. only one channel data is available. This situation is possible but not a common situation in the real world. Therefore, only overdetermined decomposition methods, i.e. PCA + Fast ICA, will be employed in the following CHAPTER 5 and 6 for the purpose of thermal feature extraction.

CHAPTER 5 ANOMALOUS BEHAVIOURS DETECTION: METHODOLOGY

From the foundation of previous two chapters, the temperature-driven anomaly detection method is proposed. This chapter reviewed the methodologies for anomaly detection that can be enhanced by combining thermal feature extraction method. The brief idea is first presented in Figure 5.1. In anomaly detection, four methods are investigated, Moving Principal Component Analysis (MPCA), Robust Regress Analysis (RRA), One-class Support Vector Machine (OCSVM) and Artificial Neural Network (ANN). Hence, the proposed temperature-driven anomaly detection methods can be designated as Td-MPCA, Td-RRA, Td-OCSVM and Td-ANN.

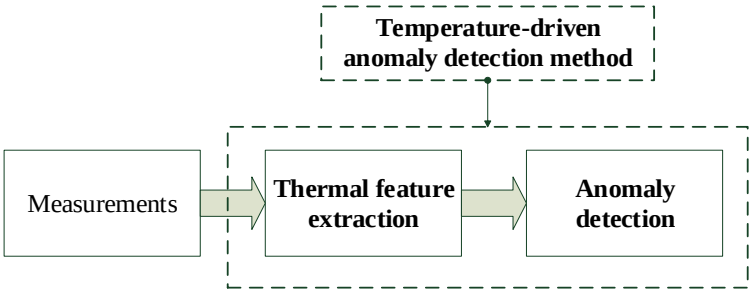

Figure 5.1. Brief idea of temperature-driven anomaly detection method

5.1 Temperature driven MPCA (Td-MPCA)

This section is mainly focusing on the theoretical background of involved methodology for anomaly detection, Moving Principal Component Analysis (MPCA).

The methodologies for thermal feature extraction, i.e. Principal Component Analysis (PCA) and Independent Component Analysis (ICA), have been introduced in CHAPTER 3. To clearly state the theoretical background of temperature-driven MPCA, which is termed as Td-MPCA, the bold capital letter is representing relative matrix, i.e. **X**. The notation of vector is small bold letter, i.e. **x**.

Since the decomposed covariance matrix, i.e. eigenvectors and its corresponding variances, are sensitive to anomalous behaviours (Hubert *et al.*, 2005), the eigenvector has potential to be a damage indicator for anomaly detection. However, the unsatisfactory performance of classic PCA is pointed as follows (Lanata *et al.*, 2007; Posenato *et al.*, 2008). The computation cost is increased when the observations number increases. Another issue is an evident delay in the time domain. Therefore, an improved statistical method, named as moving principal component analysis, is proposed (Lanata & Posenato, 2007; Lanata *et al.*, 2007; Posenato *et al.*, 2008). The difference between MPCA and PCA is that MPCA calculates covariance matrix within a pre-selected window size instead of the whole-time series, as shown in Figure 5.2. The box with dash line is the first active window of MPCA, where the variables inside are utilized for PCA interpretation, i.e. step 1 to 3 in Figure 3.5 in CHAPTER 3. The first eigenvector with maximum eigenvalue from this active window is saved as the eigenvector of this period at this step, i.e. t_1, which is the starting time of this active window. By this analogy, for the other active window, whose starting time is t_i, the first principal component of the data within that active window will be saved as the eigenvector at time t_i.

$$s(t) = \begin{bmatrix} s_1(t_1) & \cdots & s_{senN}(t_1) \\ s_2(t_2) & \cdots & s_{senN}(t_2) \\ \vdots & \ddots & \vdots \\ s_1(t_{Time}) & \cdots & S_{senN}(t_{Time}) \end{bmatrix}$$

Figure 5.2. Schematic graph of moving window of MPCA

According to Posenato *et al.* (Posenato *et al.*, 2008), the window size should be a multiple of the periodic variability. Therefore, a two-year window is selected to avoid temperature cycles' effect on threshold estimation. Furthermore, Laory *et al.* (2011) limited the window size to the same length of the longest periodic variability, i.e. a one-year window is enough for the consideration of seasonal thermal variability.

Therefore, in this study, a 365-day window is utilized for truss bridge case study and 48 hours for Ricciolo viaduct case study, as the target data duration is 730 days for truss bridge case and one month for Ricciolo viaduct case respectively.

Since the inconsequent behaviour due to structural damage will be reflected in the mean values of target data, as well as its covariance matrix and relative eigenvector-eigenvalue, the anomaly detection is catching those abnormal changes in eigenvectors from each time step. Therefore, a reference state is required to define the thresholds. In this study, the threshold is defined as three-times of standard deviation off the reference period, designated as $\pm 3\sigma$, instead of the $\pm 6\sigma$ in previous study (Laory *et al.*, 2011). The detailed reference period for each case studies will be stated in next section.

Based on previous two chapters, the proposed Td-MPCA method is operating MPCA on extracted thermal response. The flowchart in Figure 5.3 gives a visualized procedure, whose details can be found as follows.

Basically, Td-MPCA can be divided into three parts: pre-indication, blind separation and anomaly detection. The principal component analysis, also known as PCA, is first applied on all target strain measurements, e.g. *m* channels signals, to find the number of intrinsic components, notated as *n*. The number *n* represents the minimum input channels for ICA separation. Hence, *n*- channel measurements will be selected from all target signals, as a result, C_m^n various collections in total. The ICA is then operated on these various combinations individually. For each collection, the thermal-related strain is selected from ICA-estimators according to its correlation with an available temperature records, i.e. ambient temperature or closed position temperature. The one which is highest correlated with temperature fluctuation is saved as thermal-related strain for next step. Finally, the MPCA will be applied on previous saved thermal-related strain for anomaly detection. In addition, the MPCA is also performed on all target strain in case study, seeing flowchart in Figure 5.3. The results will be compared with the performance of Td-MPCA, and the improvement will be summarized in next chapter.

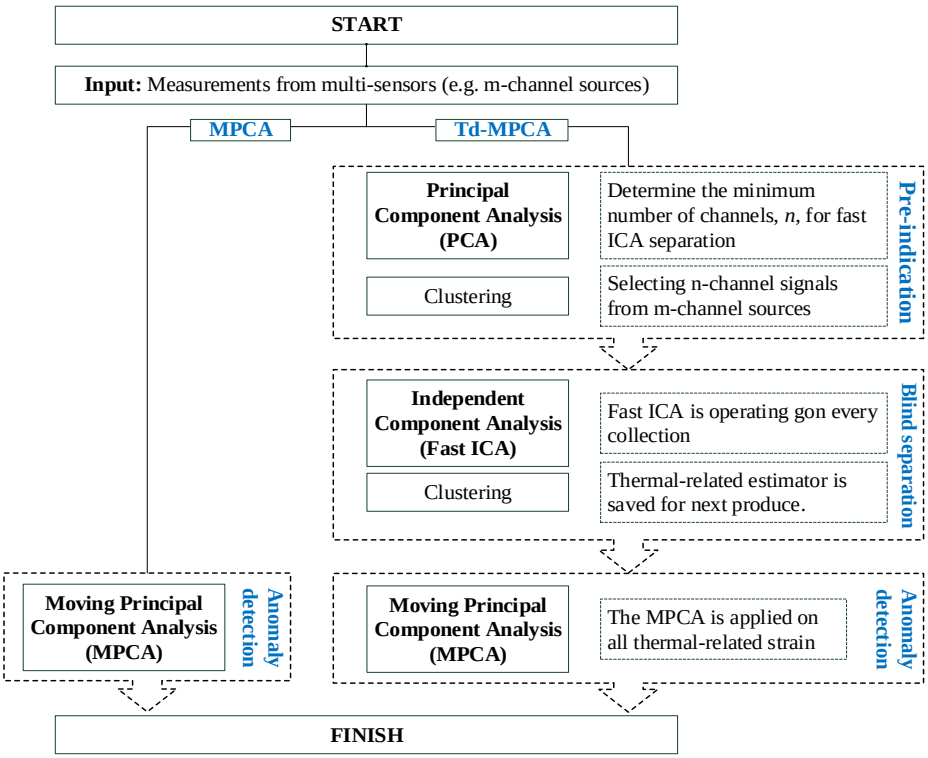

Figure 5.3. Flowchart of MPCA and proposed Td-MPCA anomaly detection method

5.2 Temperature driven RRA (Td-RRA)

The first step of RRA is the definition of correlated sensors. In following case studies, the correlation coefficient threshold, cc_t, is given first and depends on the sensor location. The correlation coefficient between any two sensors, i.e. s_i, s_j, are then calculated, designated as cc_{ij}. All the available pair can be clustered into two groups according to the relation between cc_{ij} and cc_t. The pairs whose $cc_{ij} \geq cc_t$ are saved and will be used to obtain the robust regression line of s_i and s_j. For example, $s_j^* = as_i + b$. The s_j^* is the estimated value of s_j, which is calculated according to its linear relation with s_i. a and b are the relative coefficients, which are predicated using iteratively reweighted least squares. After that, the difference between expected s_j^* and real s_j can be obtained according to the standard deviation, designated as follows. The threshold bounds of reference normal period is defined to be $2\sigma_{ij}$.

$$\sigma_{ij} = \sqrt{E\left[\left(s_j^* - s_j\right)^2\right]}$$

Eq. 5-1

In addition, a certain period, t_{out}, is also defined to avoid the false alarm. Because in the practical phase, the s_j^* and their difference $|s_j^* - s_j|$ are computed timely. The anomaly alarm will be given if the difference $|s_j^* - s_j|$ from current time, t, to a certain period, $t + t_{out}$, are exceeding the threshold continuously. The strategy of Td-RRA is given in Figure 5.4.

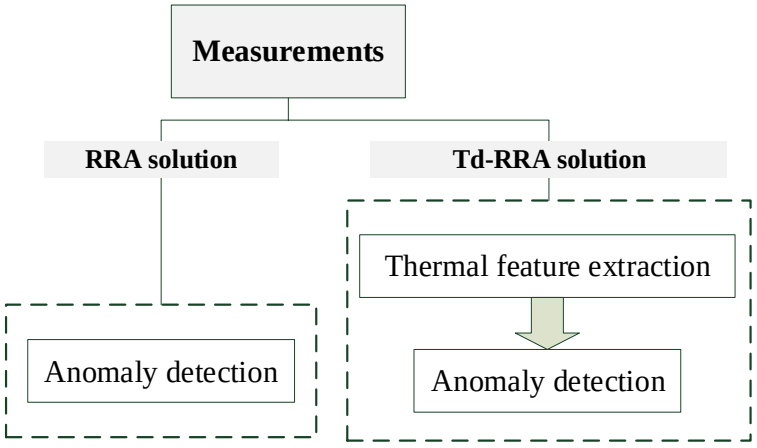

Figure 5.4. Strategy of Td-RRA

5.3 Temperature driven OCSVM (Td-OCSVM)

This approach requires fixing a priori the percentage of positive data allowed to fall outside the description of the 'normal' class. This makes the one-class SVM more tolerant to outliers in the 'normal' training data. However, setting this parameter strongly influences the performance of this approach (Manevitz *et al.*, 2001; Pimentel *et al.*, 2014). Pimentel *et al.* have reviewed various application of one-class SVM in different areas (Pimentel *et al.*, 2014).

A one-class SVM uses an implicit transformation function $\boldsymbol{\Phi}(\cdot)$ defined by the kernel to project the data into a higher dimensional space. The algorithm then learns the decision boundary (a hyperplane) that separates the majority of the data from the origin. Only a small fraction of data points is allowed to lie on the other side of the decision boundary. Those data points are considered as outliers. (Amer *et al.*, 2013)

The basic idea of SVM is to mapping the observations, e.g. $\boldsymbol{X}$, into another feature space, by using an specific and simple kernel (Schölkopf *et al.*, 2001; Vapnik, 2013). The feature space in SVM can be defined as the hyperplane, while in OCSVM, it is

termed as decision boundary. This hyperplane or decision boundary is corresponding to the following classification rule.

$$f(\boldsymbol{x}) = \boldsymbol{w^T} \cdot \boldsymbol{\Phi}(\boldsymbol{x}) - \rho$$

Where the $\boldsymbol{w}$ is the vector perpendicular to the decision boundary and ρ is the bias term. The following equation shows the decision function that one-class SVMs use in order to identify normal points. The function returns a positive value for normal points, negative otherwise:

$$F(\boldsymbol{x}) = sgn(f(x))$$

Where $sgn(\cdot)$ represents the sign of the number.

Among training data, those follow the classification rule with $f(\boldsymbol{x}) = 0$, will be defined as the support vectors. Since this is the application of OCSVM, all the data in train stage should obey $f(\boldsymbol{x}) > 0$. Subsequently, all the training data, $\boldsymbol{X}$, is assigned a label of 'normal'. Hence, the test data will be assigned as 'normal' if $f(\boldsymbol{x}) > 0$, in contrast, if $f(\boldsymbol{x}) < 0$, a corresponding 'abnormal' label will be labelled on that data.

The kernels, or also known as kernel functions, is the way how project the observations into a feature space, or in another word, the mapping solution. There are four typical kernels that have been discussed and applied (Heller *et al.*, 2003)

- Linera kernel: $K(\boldsymbol{x}, \boldsymbol{y}) = \boldsymbol{x}^T \boldsymbol{y}$
- Polynomial kernel: $K(\boldsymbol{x}, \boldsymbol{y}) = (\gamma \boldsymbol{x^T} \cdot \boldsymbol{y} + 1)^d$, where d represents the degree of the polynomial and γ is the constants.
- Gaussian kernel or Radial Basis Function kernel: $K(x, y) = e^{-\|x-y\|^2/(2\sigma^2)}$, where the σ^2 is the variance or width.
- Sigmoidal kernel: $K(\boldsymbol{x}, \boldsymbol{y}) = tanh(k\boldsymbol{x^T} \cdot \boldsymbol{y} - c)$, where k and c are constants.

The Gaussian kernel in particular guarantees the existence of such a decision boundary (Schölkopf *et al.*, 2001). By observing that all the kernel entries are non-negative, it can be concluded that all the data in their kernel space lies in the same quadrant. This makes the Gaussian kernel well suited to deal with any arbitrary dataset (Amer *et al.*, 2013)

The optimization strategy of OCSVM is separating the data from the origin with maximum margin by projecting them into a feature space according to the kernel function. To do that, the following quadratic program is addressed.

$$\min_{w,\xi,\rho} \frac{1}{2}\|w\|^2 + \frac{1}{\nu n}\sum_i \xi_i - \rho$$

Subject to the constraints

$$\boldsymbol{w^T} \cdot \boldsymbol{\Phi}(\boldsymbol{x_i}) \geq \rho - \xi_i, \xi_i \geq 0$$

Where n is the number of observations. $\nu \in (0,1]$ is a regularization parameter, which is controlling the trade-off between maximizing the distance of the hyperplane from the origin and the number of data points contained by the hyperplane. $\xi_i, \in R^n, i = 1, \dots, n$ is a nonzero slack variable for point i that allows it to lie on the other side of the decision boundary. $\boldsymbol{w}$ and ρ are corresponding to the decision boundary. $\boldsymbol{\Phi}$ is a kind of mapping function.

The deduction from the theoretical to the mathematical objective can be stated by the distance to the decision boundary. The decision boundary is then defined as

$$f(\boldsymbol{x}) = 0$$

In this context, the distance of any arbitrary data point to the decision boundary can be computed as:

$$d(\boldsymbol{x}) = \frac{|f(\boldsymbol{x})|}{\|\boldsymbol{w}\|}$$

Thus, the distance that the algorithm attempts to maximize can be obtained by plugging the origin into the equation yielding $\frac{\rho}{\|w\|}$. This can also be stated as the minimization of $\frac{1}{2}\|w\|^2 - \rho$.

The second part of the primary objective is the minimization of the slack variables ξ_i for all points. ν is the regularization parameter and it represents an upper bound on the fraction of outliers and a lower bound on the number of support vectors. Varying ν controls the trade-off between ξ and ρ.

To this end, the primary objective is transformed into a dual objective, shown in last equation. The transformation allows SVMs to utilize the kernel trick as well as to reduce the number of variables to one vector. It basically yields a Quadratic Programming (QP) optimization objective.

The Gaussian kernel is selected and considered further. To solve the optimization problem, the Lagrange multipliers $\alpha_i, \beta_i \geq 0, i = 1, \ldots, n$, are used to formulate the Lagrange equation as follow.

$$L(\boldsymbol{w}, \xi, \alpha, \beta) = \frac{1}{2}\|\boldsymbol{w}\|^2 + \frac{1}{\nu n}\sum_i \xi_i - \rho - \sum_i \alpha_i(\boldsymbol{w^T} \cdot \boldsymbol{\Phi}(\boldsymbol{x_i}) - \rho + \xi_i) - \sum_i \beta_i \xi_i$$

And the derivatives of the respective variables, $\boldsymbol{w}, \xi \; and \; \rho$, the following formulations can be obtained.

$$\frac{\partial L}{\partial \boldsymbol{w}} = 0 \Longrightarrow \boldsymbol{w} = \sum_i \alpha_i \boldsymbol{\Phi}(\boldsymbol{x_i})$$

$$\frac{\partial L}{\partial \xi_i} = 0 \Longrightarrow \alpha_i + \beta_i = \frac{1}{\nu n}$$

$$\frac{\partial L}{\partial \rho} = 0 \Longrightarrow \sum_i \alpha_i = 1$$

Then substituting those three derivative equations into Lagrange equation.

$$\max_{\alpha} \tfrac{1}{2}\textstyle\sum_{i,j} \alpha_i \alpha_j k(\boldsymbol{x_i}, \boldsymbol{x_j}), \text{ subject to } 0 \leq \alpha_i \leq \tfrac{1}{\nu n}, \textstyle\sum_i \alpha_i = 1$$

Where $k(\boldsymbol{x_i}, \boldsymbol{x_j})$ is a kernel function. According to above optimization process, the maximum α could be obtained first, followed by the constant $\rho = \sum_j \alpha_j k(x_j, x_i)$. With the two constants α and ρ, the design boundary could be obtained $f(\boldsymbol{x}) = \sum_i^n \alpha_i k(\boldsymbol{x_i}, \boldsymbol{x}) - \rho = 0$.

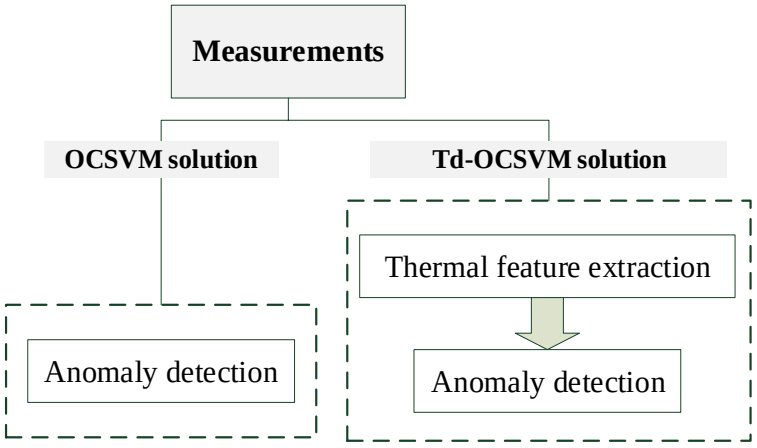

Figure 5.5. Strategy of Td-OCSVM

5.4 Temperature driven ANN (Td-ANN)

The learning process consists of minimizing the computed error value between the target and the network outputs obtained for successive iterations. Testing is carried out based on the data that the network has never seen before. The ability to produce such a prediction for the training set is called network generalization.

The feed-forward back-propagation (BP) network will be introduced in this section, whose structure can be found in Figure 5.6. At least three layers are constructing a BP network, which are an input layer, the hidden layers (at least one), and an output layer. The network is a feed-forward construction, as the input units fully connected to the neurons in the first hidden layer and forward to the following hidden layers, and the neurons of the last hidden layers are fully connected with the output units (Saduf, 2013). The input is propagated through the network until they reach the output unit by modifying the weight matrix that involved in the transferring process.

The process of BP learning algorithm are as follows.

1) Select the initial value of the weight & bias;

2) Calculate a ‘weighted sum’ of the inputs with initial settled weight coefficient and bias

3) Transfer to hidden layers.

4) The outputs from hidden layers are weighted with another weight and bias to get the network outputs.

5) Compute the difference between the network output and expected output for each neuron. The difference is the error.

6) The signal error can be obtained according to above error and the derivative of the transfer function.

7) The weights and bias between hidden layer and the network output layer is first modified and adjusted based on the delta rule, by means of learning rate, momentum term and other elements that pre-settled for the model (Chiba *et al.*, 2018).

8) Then the weights and bias between the input layer and hidden layer are secondly adjusted based on the error and delta rule.

9) An epoch is finished at this stage.

10) Repeat the process 2) – 9) until the error is within a prescribed tolerance.

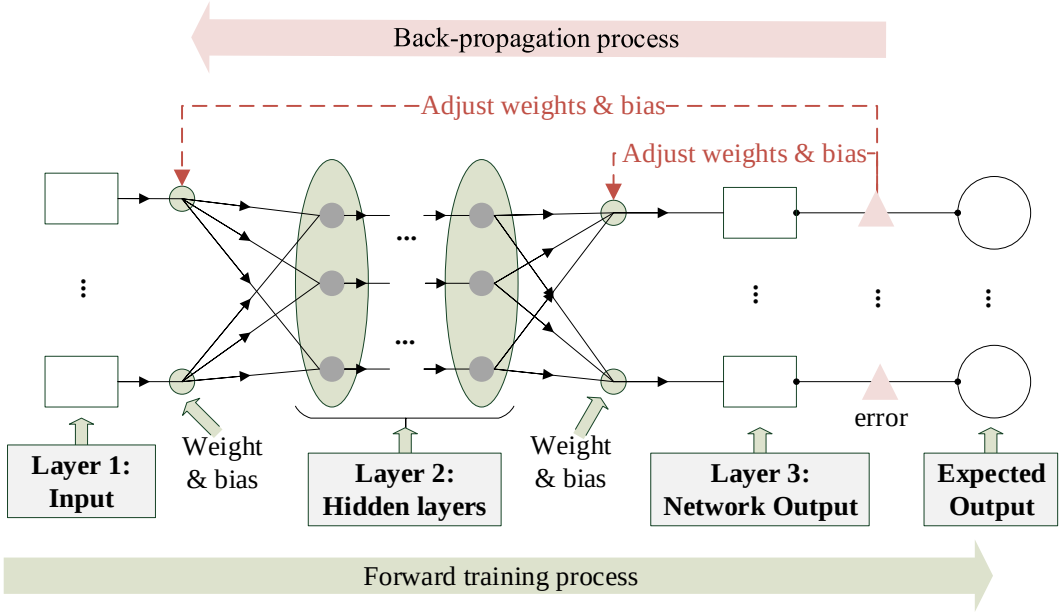

Figure 5.6. Structure of BP network

The following example is using the gradient of the empirical risk function.

Let us consider a training set $\boldsymbol{x} = \{x_1, \dots x_q\}$ with $\boldsymbol{y} = \{y_1, \dots, y_q\}$ or $\{(x_1, y_1), \dots (x_q, y_q)\}$, where $\boldsymbol{x} \in R, \boldsymbol{y} \in R$ and a neural network with m layers (with n_k neurons in the k-th layer, $k = 1, \dots, m$). The strategy can be found in Figure 5.7.

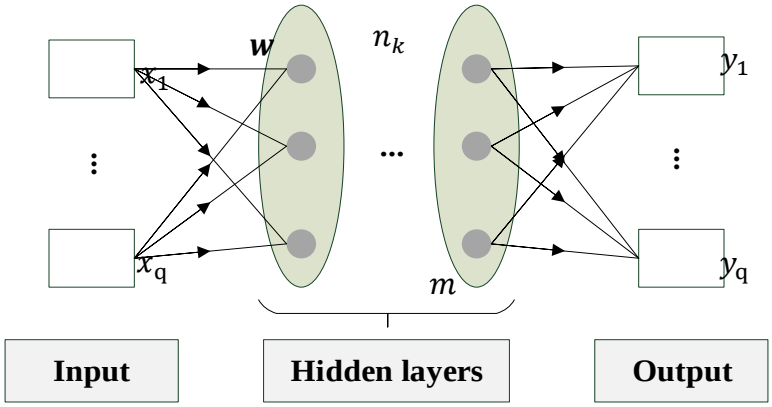

Figure 5.7. Demonstrator of back propagation network

The l-dimensional input vector at the k-th layer, where contains n_k neurons, can be expressed as $x_i(0) = [x_i^1(0), \dots, x_i^l(0)]$ where $i = 1, \dots, q$; and the image $x_i(k) = [x_i^1(k), \dots, x_i^{l_k}(k)]$ can be computed by a forward pass as in Eq. 5-2.

$$x_i(k) = \boldsymbol{S}_i\{(w(k)x_i(k-1))\}$$

Eq. 5-2

The $\boldsymbol{S}_i$ represents the neuron transfer function or activation function for i-th data of input, $\boldsymbol{x}$, and the $w(k)$ means the weighting matrix that connects the layer $k-1$ to k. Hence, the error propagated back, $b_k(k)$, from the output nodes to neurons in the k-th hidden layer can be computed by Eq. 5-3.

$$b_i(k) = \boldsymbol{w}^T(k+1)\nabla\boldsymbol{S}_i\{\boldsymbol{w}(k+1)x_i(k)\}b_i(k+1)$$

Eq. 5-3

The weight matrix can be updated as follows in Eq. 5-4.

$$\boldsymbol{w}(k) = \boldsymbol{w}(k) - \xi\sum_{i=1}^{q} b_i(k)\nabla\boldsymbol{S}_i\{\boldsymbol{w}(k)x_i(k-1)\}\boldsymbol{w}(k)x_i^T(k-1)$$

Eq. 5-4

After iteratively modifying them, the final weighting matrix should within a pre-defined confidence interval.

The crucial issue in anomaly detection by using ANN based methods is the proper choice of features that could reflect anomalies inside the structure. Nazarko and Ziemianski mentioned three potential aspects that could help improving the accuracy

of neural networks, which are tuning the architecture, pre-processing the data and utilizing another training algorithm.

In this study, the back propagation (BP) network is selected, with one hidden layer and the Levenberg-Marquardt train algorithm is employed according to previous efforts in (Tan *et al.*, 2017).

5.5 Concluding Remarks

This chapter has described the four temperature-driven anomaly detection methods, including their development background and theoretical information.

The first approach is Td-MPCA, which is applying Moving Principal Component Analysis (MPCA) on the extracted thermal features. The MPCA was developed based on Principal Component Analysis (PCA). The MPCA, as an anomaly detection method, has already been evaluated by Posenato *et al.* (2010) and Laory *et al.* (Laory, 2013). In this thesis, the performance of MCPA and Td-MPCA are all evaluated and compared in next chapter.

The second approach is Td-RRA, where Robust Regression Analysis (RRA) method is investigated. The detectability of RRA again was previously assessed by Laory (2011). The purpose in this thesis is to compare the performance of Td-RRA and RRA only.

The third approach is Td-OCSVM, along with OCSVM. The One-Class Support Vector Machine (OCSVM) is a typical machine learning method, within which only normal data is used to train the model. The next chapter will present the performance and evaluation of OCSVM and Td-OCSVM.

The fourth approach is Td-ANN. A brief introduction of Artificial Neural Network (ANN) has been explored in section 5.4. The widely explored back-propagation network has been employed in this study. The ANN and Td-ANN are occupied to both classify various damage conditions and detect anomalous behaviours in following chapter.

CHAPTER 6 ANOMALOUS BEHAVIOURS DETECTION: CASE STUDY

Three case studies are demonstrated in this chapter to appraise the ability of the four proposed temperature-driven anomaly detection methods, which are temperature-driven moving principal component analysis (Td-MPCA), temperature-driven robust regression analysis (Td-RRA), temperature-driven one-class support vector machine (Td-OCSVM), and temperature-driven artificial neural network (Td-ANN). The first case study in Section 6.1 is the numerical truss model built in ANSYS, including four subsections of each temperature-driven method respectively. Section 6.2 describes the laboratory test on a truss bridge built in the Structural Laboratory at the University of Warwick. This section also consists of four independent subsections to assess the different temperature-driven methods. Section 0 is based on the monitoring data from Ricciolo curved viaduct in Switzerland. The viaduct has been monitored since its construction period, all four methods are performed on this bridge and the evaluations are conducted. At the end of this chapter, a comprehensive summary with essential findings is presented.

6.1 Case study 1: Numerical truss bridge

This case study is based on a truss bridge and built in ANSYS. The finite element model is first introduced in Section 6.1.2, followed by the other four sections, 6.1.2 to 6.1.5, to investigate the proposed temperature-driven methods respectively. A summary will also be listed at the end of this section in 6.1.6.

6.1.1 Introduction

This case study is on a numerical truss bridge built through ANSYS, which is only affected by temperature and traffic loads. Figure 6.1 gives the bridge geometry and sensor placement information. The bridge is fixed at the four ends, 1 to 4, as shown in Figure 6.1. The sensors are placed in chords 71, 73, 75, 80, 81, and 82, which will be abbreviated as C71, C73, C75, C80, C81 and C82 individually. The length of floor chords, i.e. C71, 73 and 75, is 382 mm and the length of bottom chord C74, 80, 81 and 82 is 406 mm. The bridge is made by aluminium, whose Young's modulus is $70GPa$, density is $2.7g/cm^3$, Poisson's ration is 0.35, and the thermal expansion coefficient is $23.1\mu m \cdot m^{-1}K^{-1}$. For detailed geometry information of the bridge, the reader can refer to Appendix B. Comparing to the numerical model in CHAPTER 4, this model is simulated by using beam element, instead of link model, but the material properties and geometry dimension are the same.

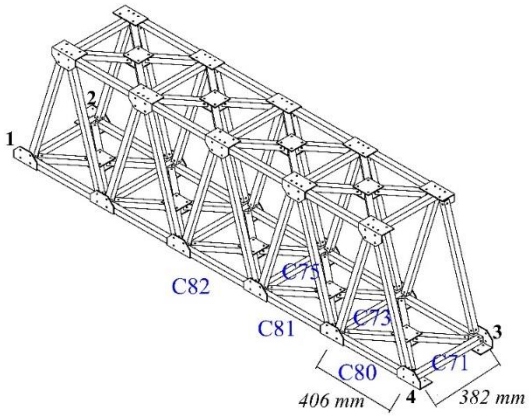

Figure 6.1. Case study 1: truss bridge model information

This simulation on this aluminium truss model is only affected by temperature and traffic loads. The temperature loading is simulated as 9.7 ℃ average value with maximum 4℃ daily variations and maximum 7℃ seasonal fluctuations. The simulated duration is 2 years, while the sampling ratio is approximately 2.4 hours per day, but only 3-day variations are simulated for each month. Hence, the 730-day measurements only contain 72 daily cycles. The traffic load is simulated with double peaks within 24 hours and applied on all bottom nodes of the bridge model. The daily traffic load is varying from 0 KN to 5 KN and decreasing to approximately 2.5 KN at noon before

increasing back to the second peak value. After that, the recession period leads the value to 0 KN again to complete the daily variation.

The damage is introduced as the stiffness reduction on target chords, which will be fully explained in the following subsections for various temperature-driven methods, i.e. Td-MPCA, Td-RRA, Td-OCSVM, and Td-ANN.

6.1.2 Numerical evaluation of the Td-MPCA method

In this section, the performance of Td-MPCA for anomaly detection is evaluated and compared with employing MPCA directly without the temperature-driven process. Figure 6.2 shows the damage position first. The damage is simulated on the bottom chord C74, which is away from the sensors. The Young's modulus of chord C74 is reduced 5%, from 70 GPa to 66.5 GPa, from the 500th day to the end of the simulation.

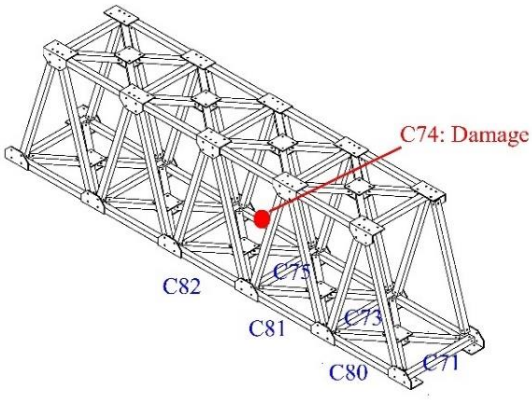

Figure 6.2. Damage and sensor position for the evaluation of Td-MPCA method

As mentioned, the truss bridge is only affected by temperature and traffic loadings. Figure 6.3 then presents the strain measurements under temperature and traffic variations, which is designed as the overall strain. To have a clear vision of all measurements, six sensors records are displayed in part (a) and (b) of Figure 6.3. In addition, Figure 6.4 also gives the detailed measurements from six sensors under various loading conditions, including the temperature-induced strain (i.e. black dash line), the traffic-induced strain (i.e. grey solid line), and the overall strain (i.e. black solid line). As can be obtained from Figure 6.4, the overall strain is a linear combination of the strains under traffic and temperature loadings. More specifically, the overall strain is following the tendency of thermal strain. The strain variations

caused by temperature changes can be partially neutralized by traffic impacts. The traffic variations have some slighter effects on transversal floor beams, i.e. C71, C73 and C75, than the longitudinal chords, and i.e. C80, C81 and C82. The impact due to 5% stiffness reduction in chord No.74 is not visible in the overall strain of C71, C73, C80, and C81, but slightly more visible in C75 and C82. The probable reason is that C75 and C82 are close to the damaged chord than other sensors.

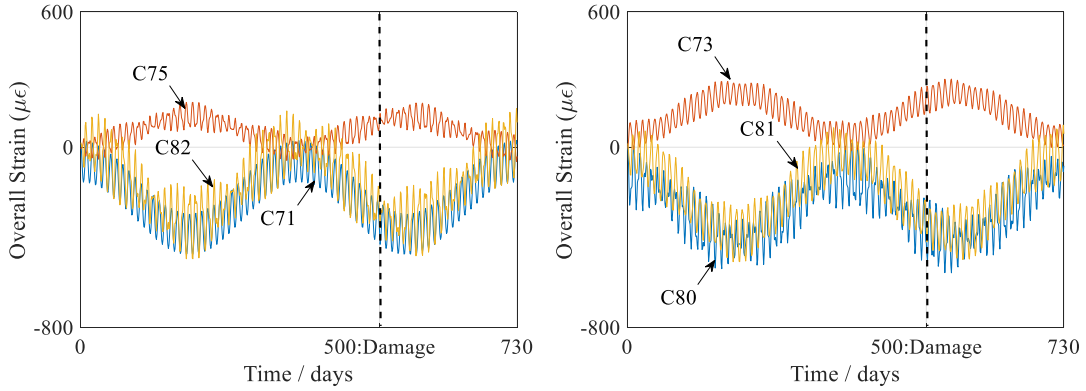

(a). C71, C75, and C82 (b). C73, C80, and C81

Figure 6.3. Overall strain measurements from six sensors

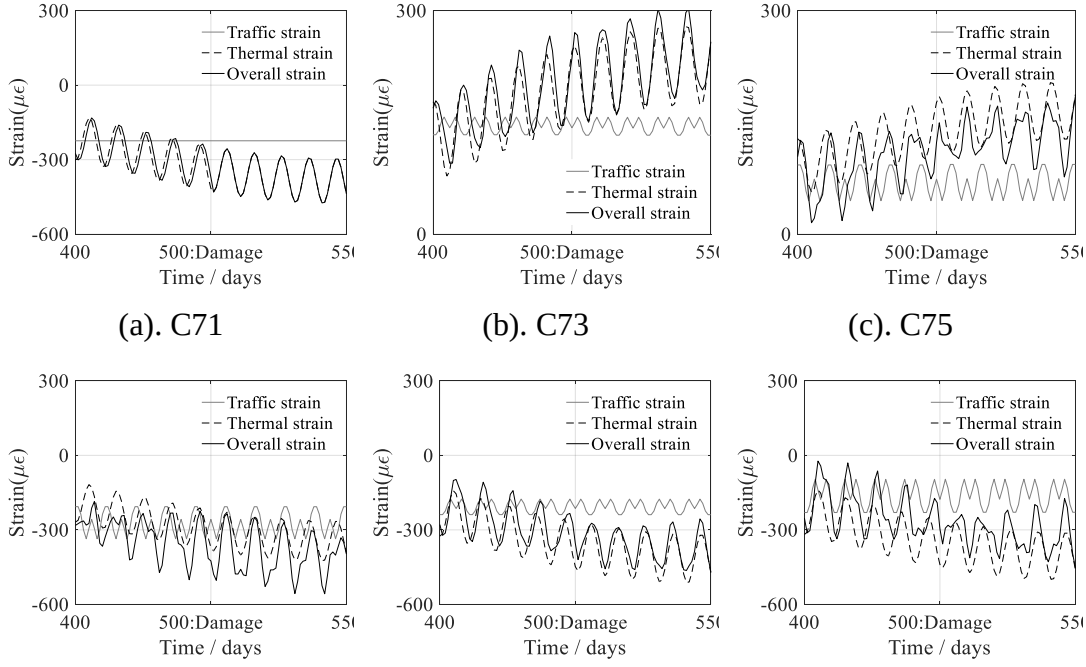

(a). C71 (b). C73 (c). C75

(d). C80 (e). C81 (f). C82

Figure 6.4. Detailed measurements from six sensors under various loading conditions

Based on the overall strain, Td-MPCA is applied and evaluated. As previously described in Figure 5.3 in CHAPTER 5, the first step in implementing Td-MPCA is pre-indication, where the principal component analysis (PCA) is first utilized to estimate the minimum components among all sensor records.

As can be seen from Table 6.1, the first two components are satisfactory, because the cumulative variance of the select principal components should be over 95% of the total variation and they contribute almost 99.9% variance. This minimum number indicates that the recommended input sources for second procedure, blind separation, is over two but less than the total number of sensors. Hence the option can be three, four or five. Taking three as the first example. The clustering process within pre-indication is selecting 3-channel sources from 6-channel measurements. Hence, $C_6^3 = 20$ collections are obtained.

Table 6.1. Pre-indication of Td-MPCA by PCA

		1st principal component	**2nd principal component**
Coefficients of each sensor measurements with principal component	C71	0.464	0.117
	C73	-0.271	-0.189
	C75	-0.202	0.193
	C80	0.403	0.758
	C81	0.506	-0.189
	C82	0.502	-0.550
Eigenvalue/ variance		80475.179	4683.102
Cumulative percentage of total variation		94.5%	99.9%

In the second step of Td-MPCA, which is blind separation, the 20 collections are investigated, among which the collection includes C71, C73, and C75 is selected as a demonstration in this section. The overall strains of C71, C73, and C75 are previously presented in Figure 6.3. The ICA-estimated strain components are given in Figure 6.5, with zero mean and unit norm. It is apparent that the expected temperature-related strain (Figure 6.5(a)) and traffic-correlated strain (Figure 6.5(b)) are separated by fast ICA from the overall strain of C71, C73, and C75. Comparing Figure 6.5 (a-b) with

Figure 6.3, the abnormal shift on the 500th day is much more visible after ICA separation. This is because the 5% reduction of stiffness is a negligible-level damage. Hence, it is hard to be reflected in any single-channel overall measurements, for example, C71, C73 or C75, as shown in Figure 6.3. However, the aggregation of three sensors can enlarge and deepen the impact of stiffness loss during ICA estimation process to uncover that.

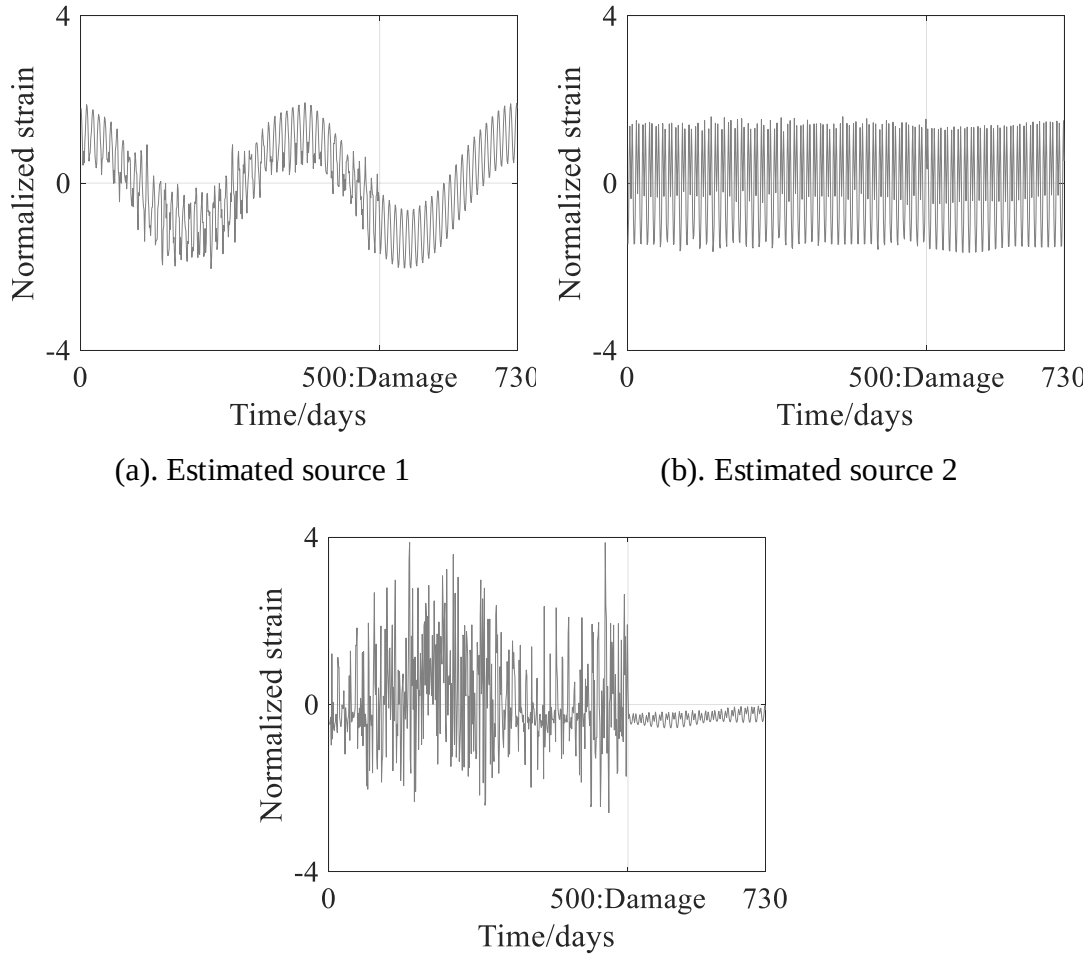

(a). Estimated source 1

(b). Estimated source 2

(c). Estimated source 3: residual source

Figure 6.5. Blind separated results by ICA from C71, C73, and C75

The Figure 6.5(c) shows the third estimated source, designed as a residual source. The apparent shift at the expected 500th day in residual sources can demonstrate that the temperature-induced strain is possible to cover real damage-induced variation in measurements. However, the potential ability and utilization of this residual source for anomaly detection should be a future research topic, since the physical meaning of this residual source cannot be answered by the author at this stage.

The other combinations of three strain records have also been examined, among which all temperature-related strain, similar to Figure 6.5(a), is of interest and saved for the final step of Td-MPCA. The final process is anomaly detection, where MPCA is employed and applied on ICA-separated results. The detection results of Td-MPCA are displayed in Figure 6.6(a). The window size of 365 days and the reference period of 135 days are considered to establish the threshold. In this study, the threshold is defined and narrowed as two times of standard deviation of the reference period, designated as $\pm 2\sigma$, instead of the $\pm 3\sigma$ in previous studies (Laory *et al.*, 2011, 2013). The non-negligible shift at the 500th day is obvious.

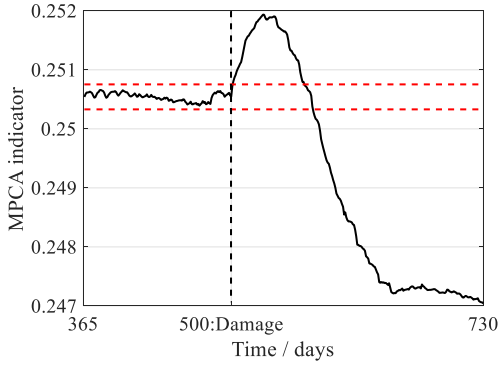

(a). Td-MPCA: three inputs for fast ICA

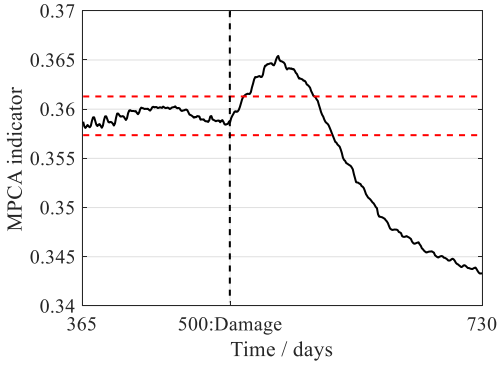

(b). Td-MPCA: four inputs for fast ICA

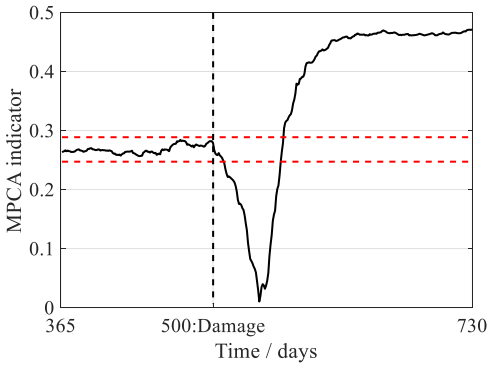

(c). Td-MPCA: five inputs for fast ICA

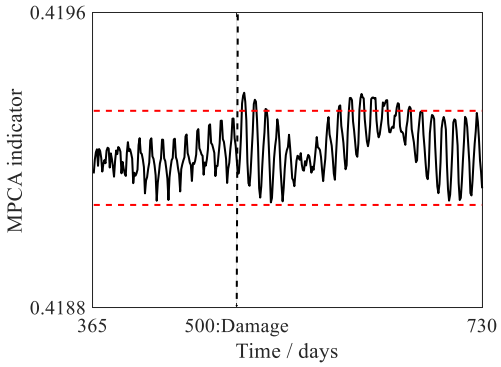

(d). MPCA only

Figure 6.6. Anomaly detection by Td-MPCA (with various inputs for ICA) and MPCA only (threshold: $\pm 2\sigma$ over 135 days reference period)

As mentioned previously, the recommended number of inputs is over two. Hence, the ICA estimation process on four and five should also be able to reveal the concealed temperature-related and traffic-induced strain. This prediction can be verified in Figure 6.6(b) and (c). The six inputs for ICA estimation will not be considered within

Td-MPCA, because, the assumption of MPCA is that the input sources must be correlated, at least not independent. However, the ICA estimators from six sensors are independent with each other, therefore, it will be meaningless. As shown in Figure 6.6(b) and (c), the evident shift at the 500^{th} day could be clearly observed.

To have a visible comparison of Td-MPCA and MCPA, the MPCA is also applied to six overall strain measurements. The detection results are shown in Figure 6.6(d). The failure of detection is apparent due to the damage level is quite negligible, only 5% stiffness reduction.

Overall, three findings from the first case study for Td-MPCA evaluation can be summarized as follows:

- Firstly, the thermal effects can cover the damage-induced variations in observed signals (Figure 6.3), however, the ICA separation process can separate these mixed components and damage is much more apparent in the ICA-estimated components (Figure 6.5).
- Secondly, the fast ICA is able to separate thermal-related strain from the influence of traffic loading conditions.
- Thirdly, the proposed Td-MPCA is more sensitive than the application of MPCA only. This is because, the simulated 5% stiffness loss cannot be detected directly by MPCA, as shown in Figure 6.6(d). In contrary, the performance of Td-MPCA has been approved without this limitation. Figure 6.6(a-c) demonstrate that the punctual anomaly alarm can be obtained by employing Td-MPCA.

6.1.3 Numerical evaluation of the TD-RRA method

In this section, the properties of method Td-RRA are investigated on the numerical truss model and compared with the performance of RRA without temperature driven process. According to the existing researches by Posenato *et al.* (2010) and Laory *et al.* (2011), the performance of RRA is slightly fallible than MPCA. To compare with Td-MPCA, the damage conditions concerned for Td-RRA have two levels as follows:

- Damage level 1: The Young's modulus of chord No.74 is reduced 5% from 70 GPa to 66.5 GPa from day 900 to the end of the simulation. This damage level is the same as previous damage condition in Section 6.1.2.

- Damage level 2: The Young's modulus of chord No.74 is reduced 10% from 70 GPa to 63 GPa from day 900 to the end of the simulation.

The following Figure 6.7 shows the damage position and two strain measurements of interest, C75 and C82. The measurements from the closest chords, C75 and C82, are delineated in Figure 6.8. The anomalous behaviours induced by either 5% stiffness loss or 10% stiffness loss apparently are not evident from the time-history measurements.

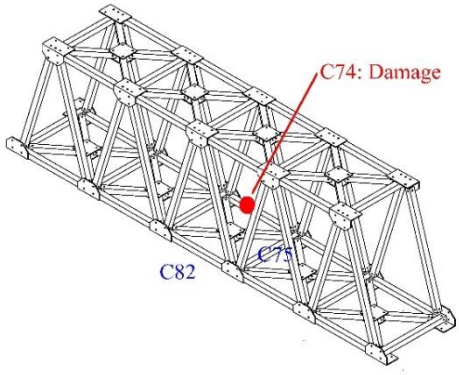

Figure 6.7. Damage and sensor position for the evaluation of Td-RRA method

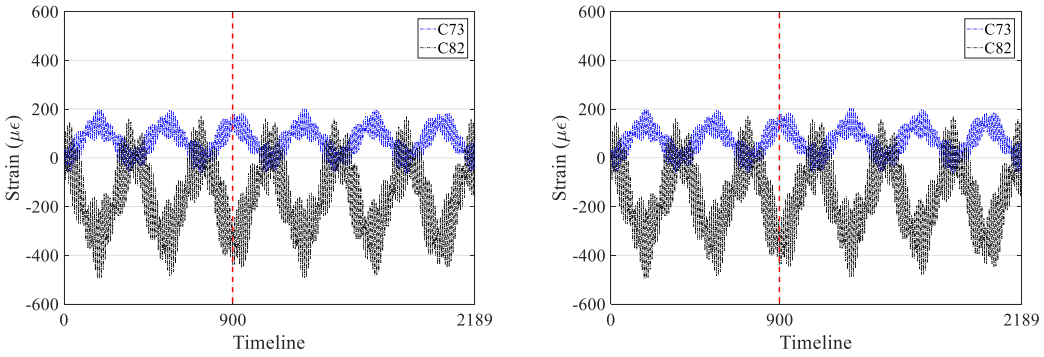

(a). Damage level 1 (b). Damage level 2

Figure 6.8. Strain measurements from C73 and C82 with various damage levels

The anomaly detection process is then performed by Td-RRA and RRA. For the first damage level, as shown in Figure 6.9(b), the damage cannot be exposed by RRA directly. But, the Td-RRA is capable to detect this slight damage, as displayed in Figure 6.9(a). When the damage level increases to 10%, both RRA and Td-RRA could be able to detect the novelty from 900 load steps as expected, as demonstrated in Figure 6.10. But a much more distinct variation can be disclosed through Td-RRA

practice. To quantify this distinct variation, a simple deviation, Δ, is utilized here, seeing Eq. 6-1. The higher Δ, the better performance of the detection method.

$$\Delta = \frac{\max\limits_{t \geq 900} |S_{real}(t) - S_{est}(t)|}{\max\limits_{t < 900} |S_{real}(t) - S_{est}(t)|}$$

Eq. 6-1

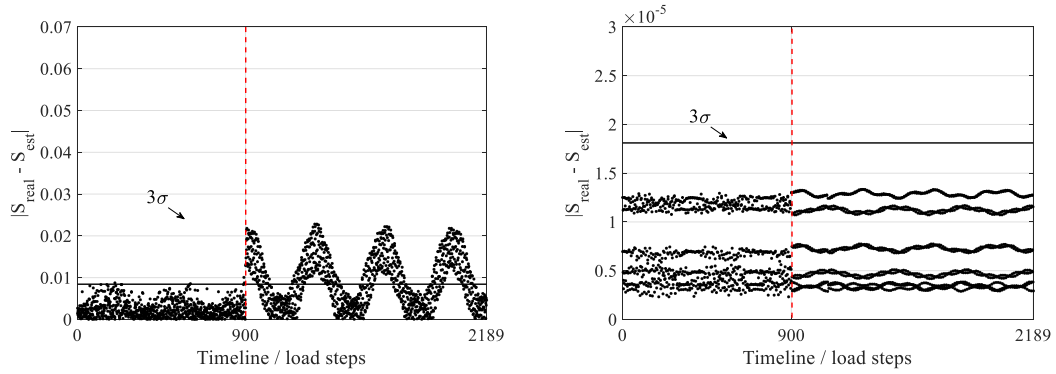

(a). Td-RRA detection results (b). RRA directly detection results

Figure 6.9. Anomaly detection by Td-RRA and RRA (damage level 1: 5% stiffness loss)

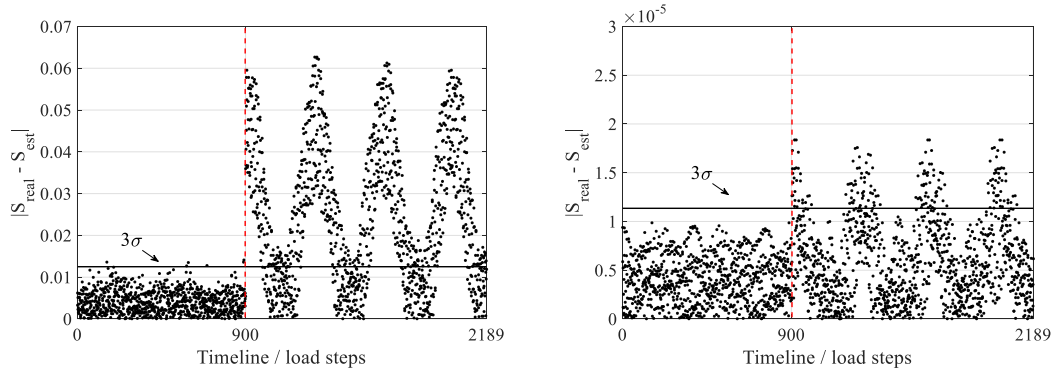

(a). Td-RRA detection results, Δ≈ 0.9 (b). RRA directly detection results, Δ≈ 0.6

Figure 6.10. Anomaly detection by Td-RRA and RRA (damage level 2: 10% stiffness loss)

The numerical case study carried out above for Td-RRA evaluation can demonstrate the following highlights.

- The RRA is still failed to uncover the anomaly when stiffness loss is only 5% on C74 (seeing Figure 6.9(b)), the same as MPCA performance in Figure 6.6(d). In contrast, the Td-RRA is confirmed as an enhanced abnormality detection method

because the aberrant responses can be delineated by Td-RRA, as shown in Figure 6.9(a).

- When the damage aggravates to 10% stiffness loss on C74, both RRA and Td-RRA could reveal deviant data points after the anticipated time. But the variations of Td-RRA is more evident than RRA outcomes, seeing Figure 6.10.

6.1.4 Numerical evaluation of the Td-OCSVM method

The third temperature-driven method investigated here is related to One-class Support Vector Machine (OCSVM). Four damage conditions are considered in this section. Figure 6.11 shows their position with sensors of interests. The damage levels are described as follows:

- Damage condition 1: 50% stiffness loss on C82
- Damage condition 2: 25% stiffness loss on C82
- Damage condition 3: 10% stiffness loss on C82
- Damage condition 4: 5% stiffness loss on C74

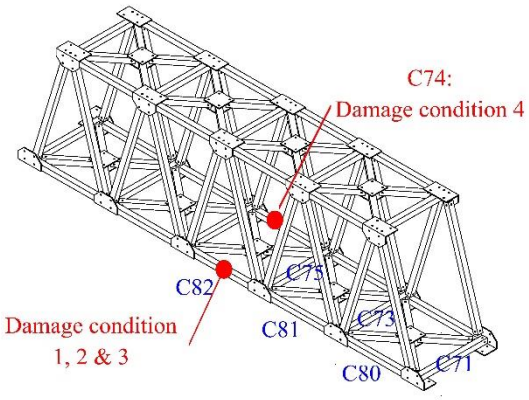

Figure 6.11. Damage and sensor position for the evaluation of Td-OCSVM method

The Gaussian kernel is employed for all application of one-class SVM. The outlier fraction is set to zero because the training data is prior known without any anomaly inside the truss. Training the data from relative strain gauges, i.e. C71, C73, C75, C80, C81 and C82, with its corresponding temperature variations.

Taking C82 as the first example. The OCSVM is applied on C82 records with its relative temperature variations directly under four various damage levels. The data without damage is used for training the OCSVM model and the data with damage is

used for testing the model. The evaluation is judged from two categories, the chance of false alarm before the damage was introduced and the ability or sensitivity to detect anomalies. The formal is termed as 'false alarm' in the following content and the detection ability is marked as 'detected' or 'detected anomaly' in the following figures or text.

The Figure 6.12(a) shows the detecting outcomes in the time domain, the normal records are marked as black dots and it is obvious that no false alarm was given before 900 seconds. After that, the blue dots represent the anomalous measurements and the detected points are hence marked out in red square. The percentage of detection is 30% by OCSVM to uncover the first damage condition on C82. The Figure 6.12(b) gives another view of the training model and detection results. The normal data are still marked as black dots and represents the data to build the OCSVM model. The support vectors are also circled corresponding to the decision boundary, which obey $f(x) = 0$. The contour lines stand for the classification rules. The data with $f(x) < 0$ is assigned as 'detected', as showing in Figure 6.12(b). However, there is some data could not be detected even they are belonging to the 'anomaly' group, marked as blue '+' in Figure 6.12(b). This is because they fall inside the design boundary, or $f(x) \geq 0$. Hence, they are not detected.

For another two minor damage conditions on C82, the detection results by OCSVM without the temperature-driven process are displayed in Table 6.2. The evident weaken detectability can be observed if compared with the first damage condition. Because the detectability is only 6% and 1% for the second and third damage levels respectively. Another minor damage condition, 5% stiffness loss on C74, which is opposite to C82, is also investigated by using OCSVM, seeing Table 6.2. The attempt of OCSVM on C82 measurements is failed, which is predictable since it even cannot disclose the 10% stiffness loss on C82 itself.

Table 6.2. Summary of Td-OCSVM and OCSVM on SG82 under various damage conditions

Damage levels	***Detectability by OCSVM***	**Detectability by Td-OCSVM**
50% stiffness loss on C82	*30%*	100%

25% stiffness loss on C82	*6%*	97%
10% stiffness loss on C82	*1%*	58%
5% stiffness loss on C74	*1%*	44%

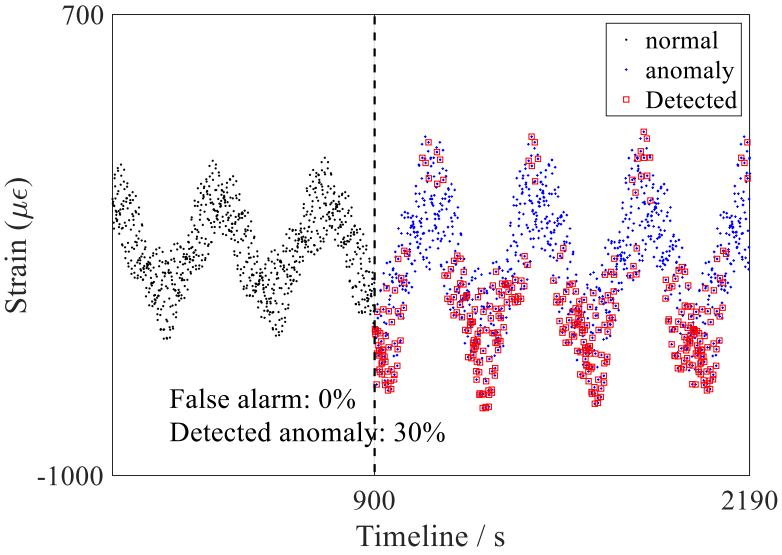

(a). Detection results showing in time domain

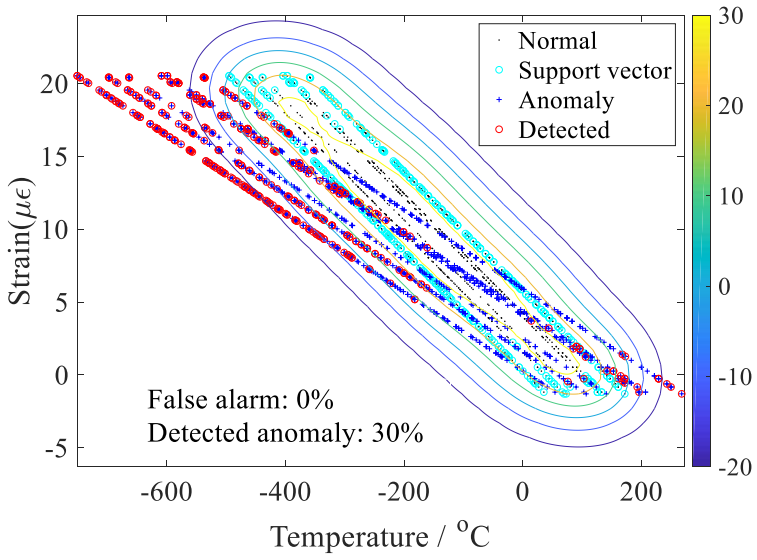

(b). Detection results showing in strain-temperature relation view

Figure 6.12. Anomaly detection by OCSVM directly on C82 under damage level 1

The application of Td-OCSVM is conducted on C82 and results are also summarized in Table 6.2. Apparently, the detectability by using Td-OCSVM are 100% and 97% for the first two damage conditions on C82. For the last two minor damage

conditions, the Td-OCSVM can improve the detection ability to 58% and 44% respectively. Figure 6.13 shows the comparison between Td-OCSVM and OCSVM on SG82 under damage level 4. In general, a great improvement can be observed by Td-OCSVM if compared with the OCSVM's performance.

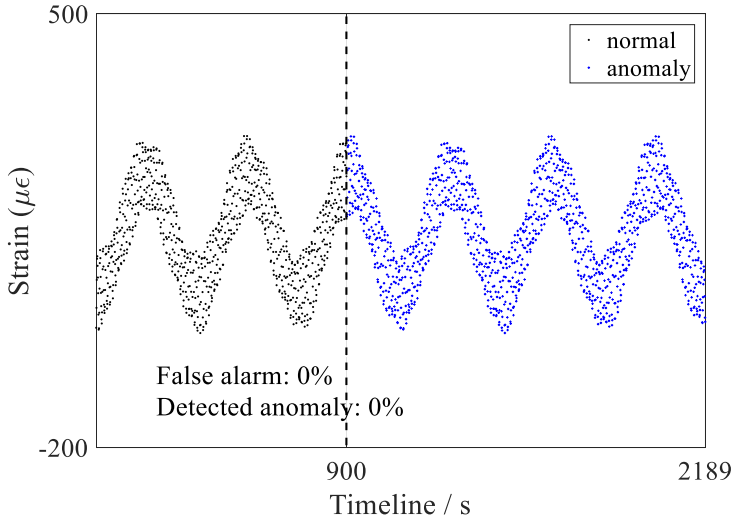

(a). OCSVM on C82

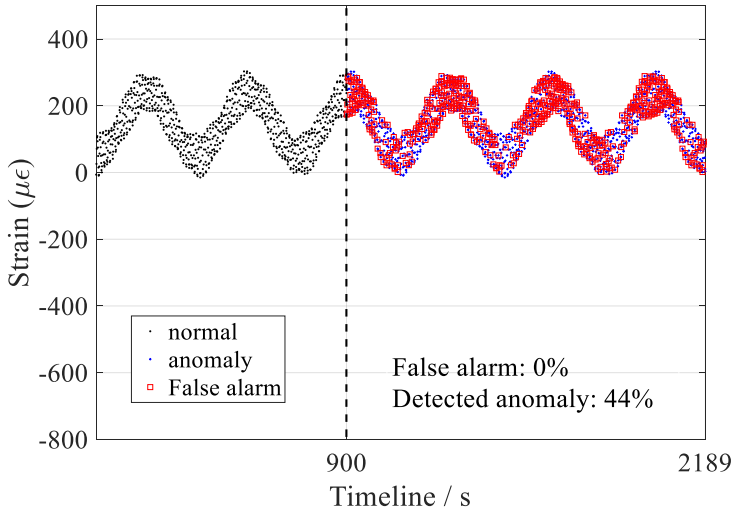

(b). Td-OCSVM on C82

Figure 6.13. Anomaly detection by Td-OCSVM and OCSVM on C82 under damage level 4

All the other detecting results by OCSVM and Td-OCSVM are summarized in Table 6.3 and Table 6.4 respectively, including six sensors of C71, 73, 75, 80, 81, and 82 under four damage conditions.

For damage condition 1, which is the heaviest stiffness loss in this case study, the detectability for C82 increases from 30% to 100%, while for C73, it was increased from 84% to 98%. The attempts of OCSVM on C71, C75, C80 and C81 under damage condition 1 are all failed, as shown in Table 6.3 and have been marked in red. However, the Td-OCSVM increases them to 94%, 98%, 92% and 94% respectively.

For damage condition 2, which is slightly lighter than damage condition 1. As can be seen from Table 6.3, the OCSVM without temperature-driven process can detect 45% and 6% anomalies from C73 and C82 measurements but failed for other sensors records. But, from Table 6.4, the improvement by Td-OCSVM is obvious that over 68% anomalies can be detected.

For damage condition 3, OCSVM only detected 1% anomalies from C82 but nothing from other sensors, seeing Table 6.3. Because this damage is still on C82, hence, sensor C82 is more sensitive to the damage. The results obtained from Table 6.4 proves the outperformance of Td-OCSVM again. For example, over 54% anomalies can be identified from C73, C75, C80, C81, and C82. The improvement on C71 is not evident due to the long distance between damage location and C71.

For damage condition 4, 5% loss on C74, which is the minimal stiffness condition, the OCSVM are all failed according to Table 6.3. This is foreseeable if considering the OCSVM performance to uncover the third damage condition. However, the Td-OCSVM still can detect 72% anomalies from C75 and C82, 65% anomalies from C81, and 45% anomalies from C73. The relative lower detectability, 18%, can be obtained from both C71 and C80, because of the long distance between damage position and C71 or C80.

To have a visible comparison between Td-OCSVM and OCSVM without temperature-driven process, a Figure 6.14 is followed. According to Table 6.3 and Table 6.4, the false alarms for both methods are all 0%, which is due to the training data are all health data without any uncertainty. Hence, only the detectability of OCSVM and Td-OCSVM under four damage conditions are summarized in Figure 6.14. For the special condition of 0% detectability, a value of 0.1% will be drawn in the figure for convenience.

Table 6.3. Summary of OCSVM on various sensors directly

	Damage level 1 50% stiffness loss on C82		**Damage level 2** 25% stiffness loss on C82		**Damage level 3** 10% stiffness loss on C82		**Damage level 4** 5% stiffness loss on C74	
	False alarm	Detected	False alarm	Detected	False alarm	Detected	False alarm	Detected
C71	0%	0%	0%	0%	0%	0%	0%	0%
C73	0%	**84%**	0%	**45%**	0%	0%	0%	0%
C75	0%	0%	0%	0%	0%	0%	0%	0%
C80	0%	0%	0%	0%	0%	0%	0%	0%
C81	0%	0%	0%	0%	0%	0%	0%	0%
C82	0%	**30%**	0%	**6%**	0%	**1%**	0%	0%

Table 6.4. Summary of Td-OCSVM on various sensors

	Damage level 1 50% stiffness loss on C82		**Damage level 2** 25% stiffness loss on C82		**Damage level 3** 10% stiffness loss on C82		**Damage level 4** 5% stiffness loss on C74	
	False alarm	Detected	False alarm	Detected	False alarm	Detected	False alarm	Detected
C71	0%	94%	0%	91%	0%	**17%**	0%	**18%**
C73	0%	**98%**	0%	**97%**	0%	82%	0%	45%
C75	0%	98%	0%	97%	0%	63%	0%	72%
C80	0%	92%	0%	84%	0%	84%	0%	**18%**
C81	0%	94%	0%	68%	0%	54%	0%	65%
C82	0%	**100%**	0%	**97%**	0%	**58%**	0%	72%

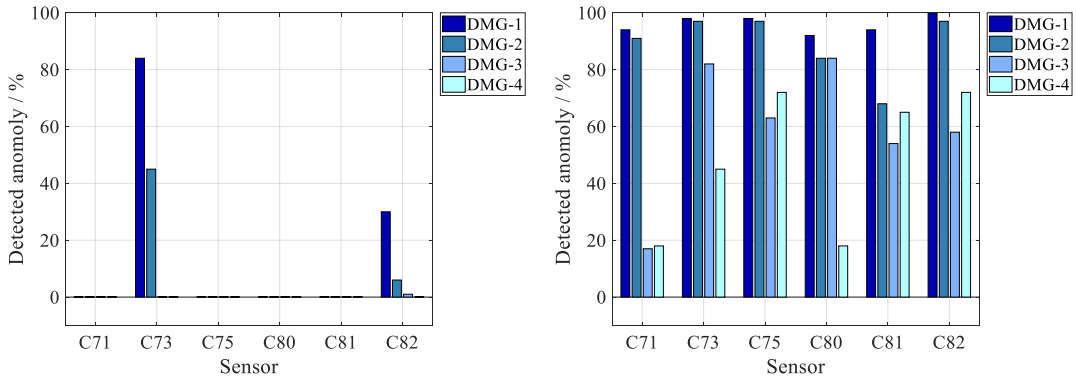

(a). OCSVM (b). Td-OCSVM

Figure 6.14. Detection results summary (DMG: damage condition)

According to Figure 6.14 and above discussions, several points can be summarized and highlighted here.

- The ability of either Td-OCSVM or OCSVM without temperature driven process depends on the location of sensors, the closer to the damage, the more possibility to detect the damage.
- The OCSVM is only successful when the damage is at a serious level, i.e. the 50% stiffness loss on C82. The OCSVM cannot find out the anomalous for the other damage conditions.
- The Td-OCSVM has a dramatical improvement when comparing with OCSVM.

6.1.5 Numerical evaluation of the Td-ANN method

This section is to assess the last temperature-driven method, which implements the artificial neural network. The capability of Td-ANN and ANN without the temperature driven process are evaluated in this section after the introduction of neural network setting.

A traditional three-layer back propagation network is employed here based on MATLAB 2018a, seeing Figure 6.15 which is the diagram of MATLAB train tool user interface. The detailed introduction of this neural network can refer to CHAPTER 5. The input is the sensor measurements under four various damage conditions, termed as Dmg. The damage conditions with their logical numbers are listed in Table 6.5.

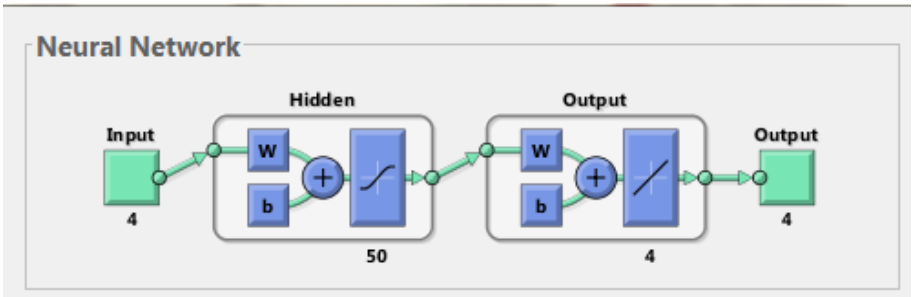

Figure 6.15. A three-layer neural network diagram

The logical numbers are the outputs of this neural network model to identify different damage level. For example, ‘0’ represents the reference condition without damage, while ‘5, 6, 7, 8’ are utilized to distinguish four damage levels. The logical numbers are not exclusive and can be others.

Table 6.5. Bridge condition with relative logical numbers

Bridge condition	Description	Logical numbers
Reference condition	Without damage	'0'
Damage condition 1 (Dmg-1)	5% stiffness loss in C74	'5'
Damage condition 2 (Dmg-2)	10% stiffness loss in C82	'6'
Damage condition 3 (Dmg-3)	25% stiffness loss in C82	'7'
Damage condition 4 (Dmg-4)	50% stiffness loss in C82	'8'

The number of maximum iterations is set to 1000. The evaluation process is determined by the ability of identifiability of both damage and damage level.

Another essential parameter is the number of neurons in the hidden layer, which is first investigated. Up to 50 neuromas are considered, the identifiability for C71 is shown in Figure 6.16 as an example, while others are listed in Table 6.6. Apparently, the identifiability for each sensor of four damage conditions are roughly similar and stable, i.e. 19~22% for C71, 95~96% for C73, 90~94% for C75, 84~85% for C80, 70~74% for C81, and 87%~88% for C82. Therefore, the influence of neurons number is slight, which is due to the linear correlation between the temperature variations and temperature-induced strain. Hence, increasing the number of neuromas may only result in the high computational cost and over-training results. Since there is no significant improvement can be observed when increasing the number of neuromas with ANN, the default number in MATLAB will be selected. Hence, the identifiability of ANN with 10 neurons will be adopted for the following parts.

Table 6.6. Evaluation results of various neuromas

Sensor	Neuromas	Average identifiability			
		Dmg-1	Dmg-2	Dmg-3	Dmg-4
C71	1~50	20%	20%	21%	23%
C73	1~50	91%	91%	91%	92%
C75	1~50	87%	88%	89%	90%
C80	1~50	76%	77%	78%	79%
C81	1~50	74%	75%	75%	76%
C82	1~50	84%	84%	85%	85%

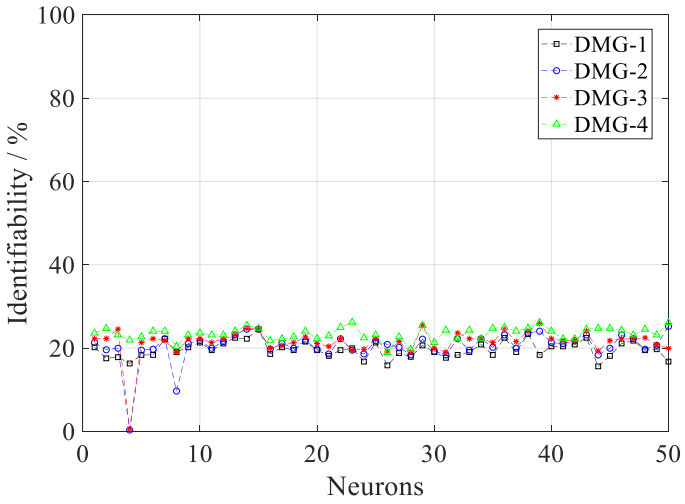

Figure 6.16. Investigation of neuromas on C71

Within the neural network training, the data is automatically and randomly divided into three datasets to train a model, e.g. train, validation and test, hence the model will be slightly variable even with all the same parameters inside the model. To avoid the side effect, the training process is running ten times and the one with the best performance (smallest mean square error) will be selected as the final model before going through the evaluation procedure.

The following Table 6.7 and Table 6.8 present the detection results of Td-ANN and ANN respectively. To have a visible comparison between Td-ANN and ANN directly without the temperature driven process, the Figure 6.17 is followed.

Table 6.7. Identifiability by using ANN directly

Sensor	**Neuromas**	**MSE**	**Iterations**	**Identifiability**			
				Dmg-1	**Dmg-2**	**Dmg-3**	**Dmg-4**
C71	10	3.528363	8	0%	0%	0%	0%
C73	10	1.52E-10	1000	92%	91%	91%	90%
C75	10	0.002982	201	75%	71%	70%	66%
C80	10	0.003503	103	61%	58%	56%	54%
C81	10	1.22E-09	1000	68%	67%	67%	66%
C82	10	2.93E-12	1000	79%	78%	78%	77%

Table 6.8. Identifiability by using Td-ANN

Sensor	Neuromas	MSE	Iterations	Identifiability			
				Dmg-1	Dmg-2	Dmg-3	Dmg-4
C71	10	0.118399	106	51%	47%	46%	42%
C73	10	2.84E-08	1000	84%	83%	82%	81%
C75	10	1.54E-13	84	91%	90%	90%	90%
C80	10	6.66E-08	294	75%	75%	73%	73%
C81	10	5.96E-12	260	84%	84%	84%	84%
C82	10	6.04E-11	909	78%	77%	77%	77%

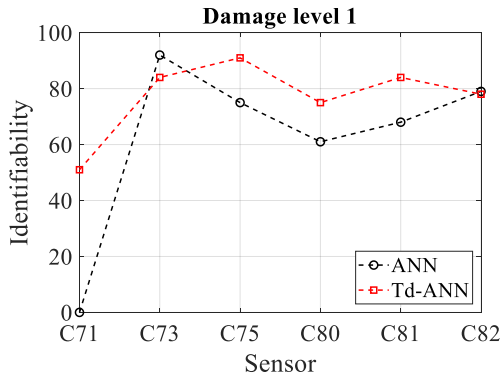

(a). 5% stiffness loss on C74

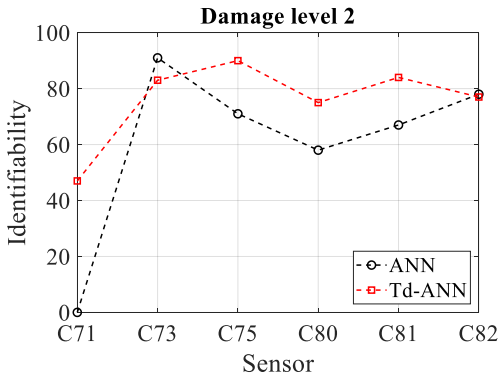

(b). 10% stiffness loss on C82

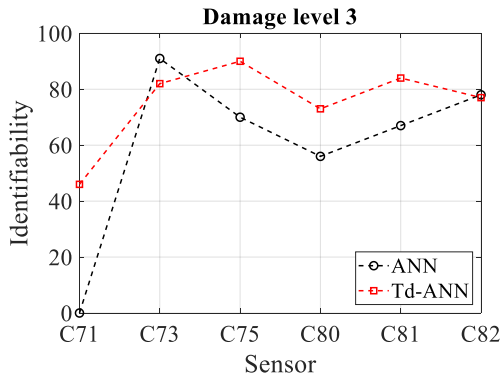

(c). 25% stiffness loss on C82

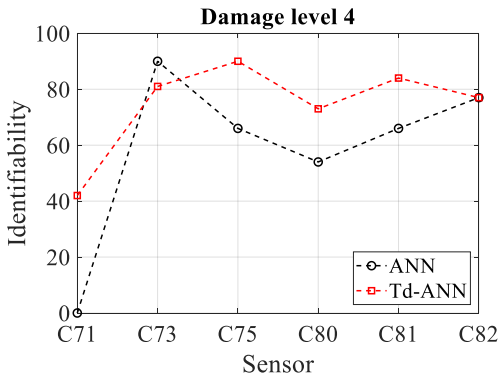

(d). 50% stiffness loss on C82

Figure 6.17. Identifiability comparison between Td-ANN and ANN

According to Figure 6.17, the distinct improvement of Td-ANN, compared with ANN, can be observed in C71, C75, C80, and C81. For example, the ANN is failed to detect any anomalies from C71 measurements, while Td-ANN can disclose around 42~51% anomalies from C71. For detections results from C75 measurements, the identifiability is increased from 66~75% by ANN directly to 90~91% by Td-ANN.

Moreover, the Td-ANN also identifies 73~75% anomalies from C80 and 84% from C81, while ANN's detectability is 54~61% from C80 and 66~68% from C81. However, non-improvement has been observed from the C73 and C82.

In general, the Td-ANN can increase the anomaly detectability by 20%.

6.1.6 Summary for numerical case study

From the above numerical case study conducted for evaluating the performance of Td-MPCA, Td-RRA, Td-OCSVM, and Td-ANN, several findings can be summarized and highlighted as follows.

- The thermal effects can cover the damage-induced variations in the observed signals, and anomalies behaviours can be observed after interpreted by Independent Component Analysis (ICA).
- In this case study, the detection performance of proposed temperature-driven methods all depends on the sensor locations for investigation, the closer to the damage, the more possibility to detect the damage.
- According to the investigation conducted in Section 6.1.2, the proposed Td-MPCA is more sensitive than the application of MPCA directly without the temperature-driven process, since the simulated 5% stiffness loss in can be detected by Td-MPCA but cannot be detected by MPCA.
- In Section 6.1.3, the RRA is also failed to detect the 5% stiffness loss. In contrast, the Td-RRA is confirmed as an enhanced abnormality detection method because the aberrant responses can be delineated by Td-RRA.
- Regarding to the evaluation results obtained in Section 6.1.4, the OCSVM is only successful when the damage is at a serious level, i.e. the 50% stiffness loss. But the Td-OCSVM has a dramatical improvement for all the damage levels considered in this case study.
- An improvement of Td-ANN can be observed in Section 6.1.5, as the Td-ANN can increase the anomaly detectability by 20%.

6.2 Case study 2: Laboratory truss bridge

The second case study for evaluation of temperature-driven methods is on a purposed constructed truss bridge in the Structure Laboratory at the University of the Warwick. In this section, the brief introduction of this experiment is first given, including the test design, sensor placement, and damage scenarios. After that, the proposed temperature-driven methods, Td-MPCA, Td-RRA, Td-OCSVM, and Td-ANN, are investigated and the detection results are presented, followed by a summary of major findings from this laboratory case study.

6.2.1 Introduction

The experimental truss bridge set up is shown in Figure 6.18. The aluminium truss bridge is the same dimension and material as the first numerical case study in Section 6.1. For detailed geometry information of the bridge, the reader can refer to Appendix B. As illustrated in Figure 6.18, temperature load is simulated by controlling the heating lamps, while the moving load is applied on the bridge by using dumbbells and two leading wood tracks. For the detailed description of experimental systems, the reader can refer to Appendix A.

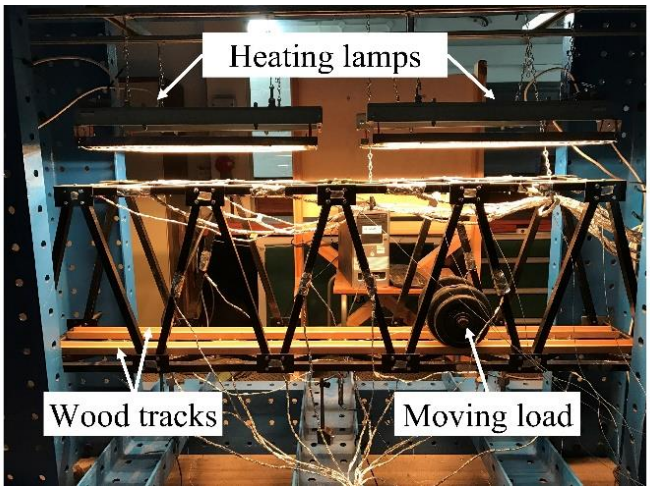

Figure 6.18. Case study 2: laboratory truss bridge test system

The sensors, including strain gauges, thermocouples and displacement transducers, are classified into six groups as shown in Figure 6.19 as follows:

- Group 1 includes the bottom longitudinal sensors of SG2, 4, 6, 8, and 10, with three thermocouples adjacent to SG6, 8, and 10, seeing Figure 6.19(a);

- Group 2 includes the bottom transversal sensors of SG11, 12, 13, and 14, with three thermocouples close to SG11, 13, and 14, seeing Figure 6.19(b);
- Group 3 contains the top longitudinal sensors of SG16, 18, 20, and 22, with two thermocouples next to SG20 and 22, seeing Figure 6.19(c);
- Group 4 has the top transversal sensors of SG23, 24, 25, and 26, with three thermocouples near SG23, 24, and 25, seeing Figure 6.19(d);
- Group 5 is the side sensors of SG28, 29, 30, and 31, seeing Figure 6.19(e);
- Group 6 is the displacement transducers of DT1, 2, and 3, seeing Figure 6.19(f).

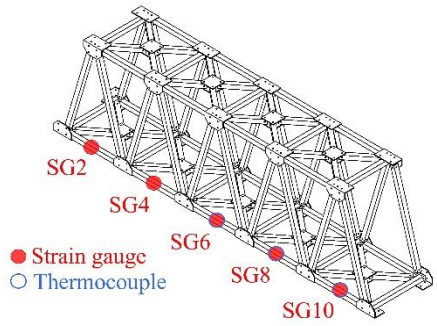

(a). Group 1: bottom longitudinal sensors

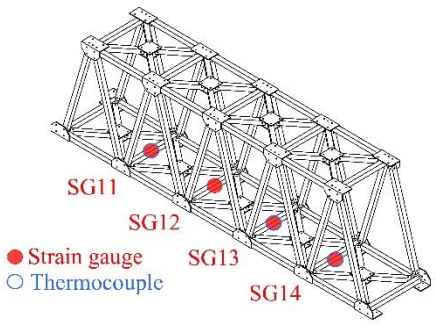

(b). Group 2: bottom transversal sensors

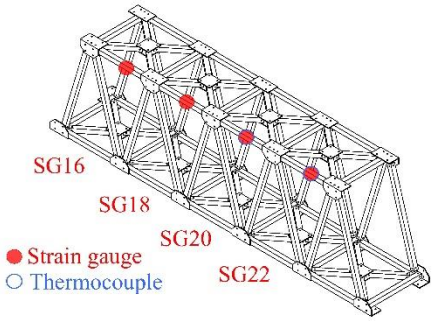

(c). Group 3: top longitudinal sensors

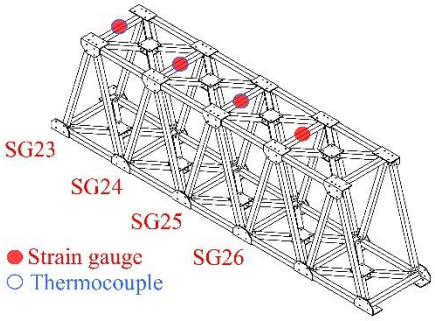

(d). Group 4: top transversal sensors

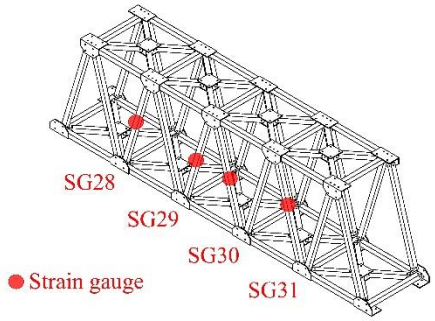

(e). Group 5: side sensors

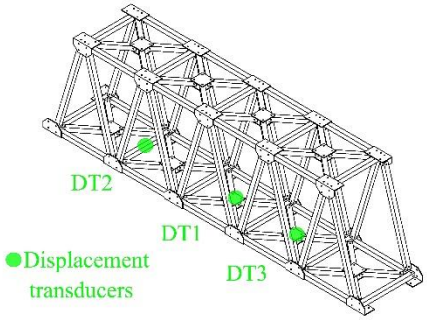

(f). Group 6: displacement transducers

Figure 6.19. Case study 2: sensor placement and classification

Four damage scenarios, named as DS-1 to DS-4, are simulated on the experimental bridge for anomaly detection as follows:

- DS-1: one side chord, close to SG28 and 29, is disconnected, seeing Figure 6.20 (a);
- DS-2: another side chord, opposite to the DS-1 position, is disconnected, seeing Figure 6.20 (b);
- DS-3: the bottom chord opposite to SG6 is disconnected, seeing Figure 6.20 (c).
- DS-4: removing the connectors of target chord, which is opposite to SG20, seeing Figure 6.20 (d).

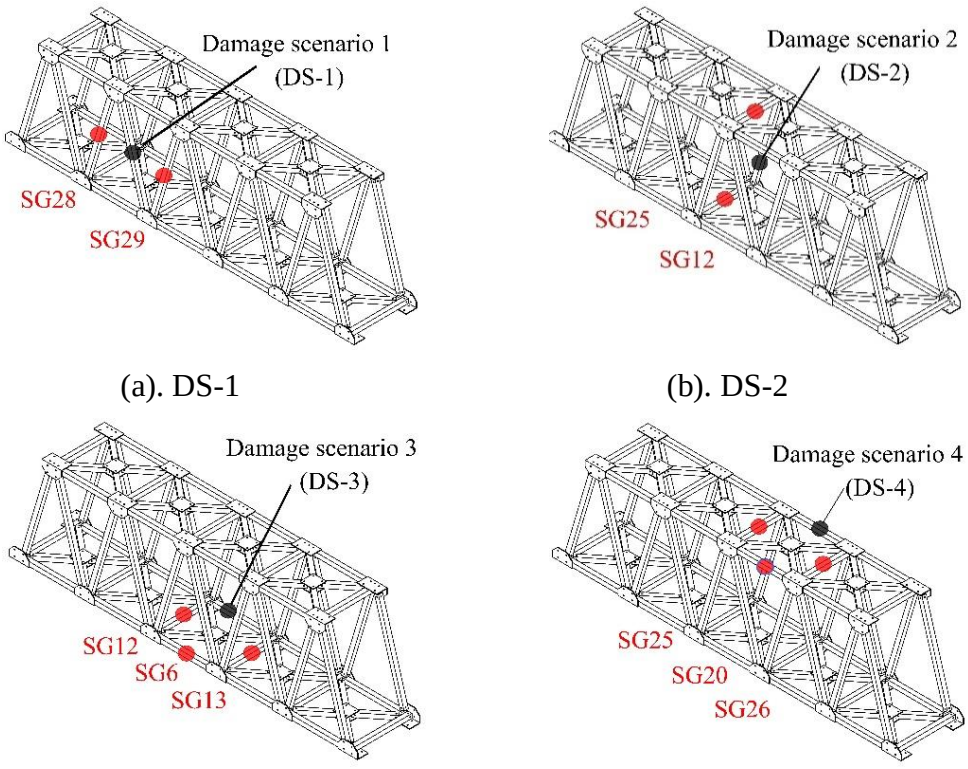

(a). DS-1 (b). DS-2

(c). DS-3 (d). DS-4

Figure 6.20. Case study 2: location of damage scenario 1-4 (DS1, 2, 3, and 4)

6.2.2 Laboratory evaluation of the Td-MPCA method

In this subsection, the temperature-driven MPCA is evaluated on the laboratory truss bridge for anomaly detection. Figure 6.21 shows the sensor group and damage scenarios of interests. Two damage conditions, DS-1 and DS-2, on side beams are considered, as previously shown in Figure 6.20 (a, b). The DS-1 is introduced on the

side beam between SG28 and SG29, while the DS- 2 is opposite and away from sensors of interest. The sensors of interests are group 1 of SG2, SG4, SG6, SG8, and SG10. The classification of sensor groups can be found in previous Figure 6.19.

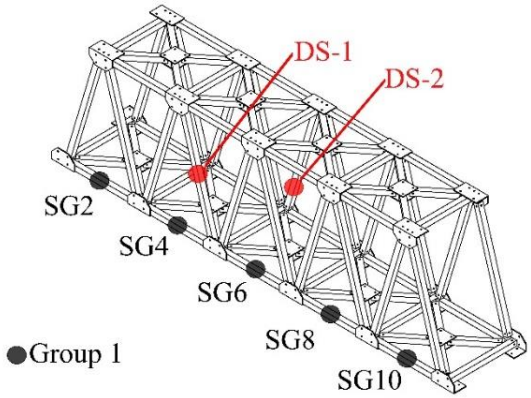

Figure 6.21. Sensor position and damage conditions for Td-MPCA evaluation

The bridge is under temperature and traffic loading conditions in the laboratory environment. Figure 6.22 is then showing measurements with zero mean value collected from strain gauges of group 1.

Figure 6.22 (a) presents the strain measurements under DS-1 effect. The experimental test duration is 1586 seconds and DS-1 is introduced from 1128 seconds. The distinct vibration at expected damage introduced time is observed in SG2 and SG4, due to their nearest location to the damage. To challenge the proposed Td-MPCA method, the detection excludes the SG2 and SG4 measurements.

In part (b) of Figure 6.22, the test duration under DS-2 is 2250 seconds, while damage is introduced from 902 seconds.

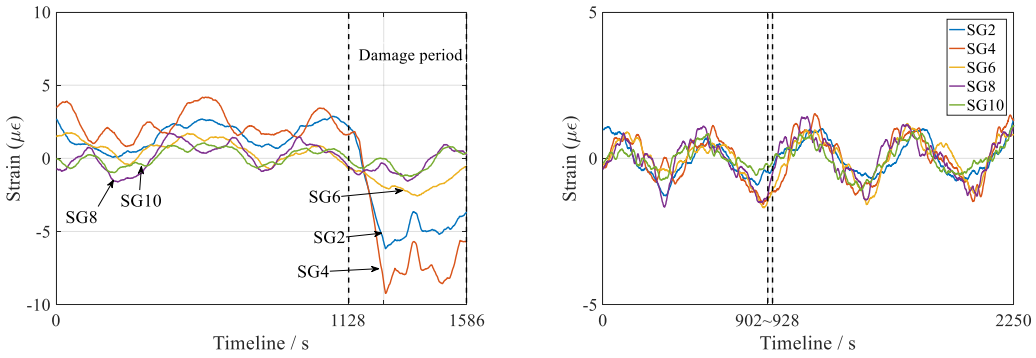

(a). Group 1 measurements under DS-1 (b). Group 1 measurements under DS-2

Figure 6.22. Measurements (group 1) with damage scenarios (DS-1 and DS-2)

The window size for Td-MPCA equals to 1~1.5 times of an entire temperature cycle. The exact window size for various tests are slightly adjusted because the temperature cycle duration is not constant. The heating system is controlled by LabVIEW program automatically according to the control thermocouple attached on the bridge. Hence, the heating and cooling time cannot be the same.

The following Figure 6.23 shows the detection results of Td-MPCA and MPCA directly to uncover the first damage condition, DS-1. The operation to introduce damage is starting from time 1128s and finishing at 1265s, hence the successful detection is between 1128s and 1265s. As shown in Figure 6.23(a), a distinct swerve is observed by applying Td-MPCA, however, none anomaly can be noticed in Figure 6.23(b) by MPCA. Hence, the MCPA is failed, while Td-MPCA is successful.

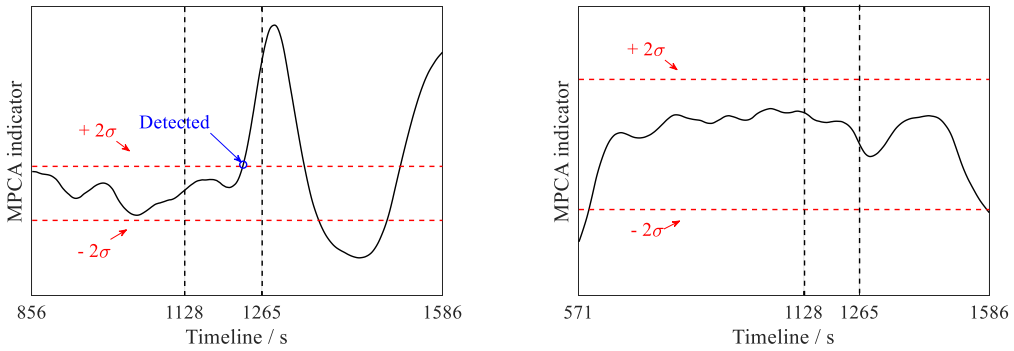

(a). Td-MPCA on group 1 sensors (b). MPCA directly on group 1 sensors

Figure 6.23. Td-MPCA and MPCA detection results under DS-1

The attempt of Td-MPCA and MPCA to detect DS-2 is presented in Figure 6.24. The detection is not as precise as previous damage condition, due to DS-2 is far away from group 1 sensors. But the Td-MPCA could detect the exceeding status timelier than MPCA. As can be seen from Figure 6.24(a), the Td-MPCA could give a 59 seconds early alarm while the MPCA detect the anomaly 362 seconds after expected time.

Due to the page limitation, only group 1 sensors are presented above to assess the performance of Td-MPCA and compare with the performance of MPCA without temperature-driven process. The other detection results are summarized in Table 6.9 for DS-1 and Table 6.10 for DS-2.

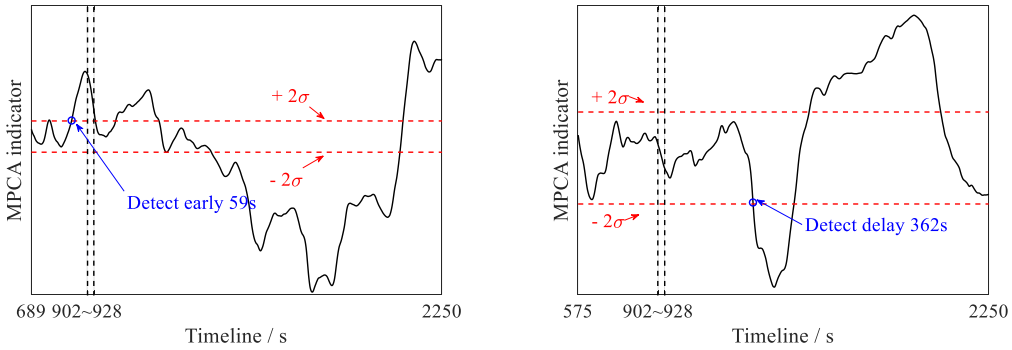

(a). Td-MPCA on group 1 sensors (b). MPCA directly on group 1 sensors

Figure 6.24. Td-MPCA and MPCA detection results under DS-2

Table 6.9. Summary for Td-MPCA under damage condition 1 (DS-1)

Sensor group no.	Sensor no.	MPCA detection	Td-MPCA detection	Relevant figure
1	SG6, 8, 10	Fail	Success	Figure 6.23
2	SG11, 13, 14	59s early	36s early	Appendix C
3	SG16, 18, 20, 22	Fail	Success	Appendix C
4	SG23-26	Success	Success	Appendix C
5	SG23-26, 30, 31	Fail	Success	Appendix C

Table 6.10. Summary for Td-MPCA under damage condition 2 (DS-2)

Sensor group no.	Sensor no.	MPCA detection	Td-MPCA detection	Relevant figure
1	SG6, 8, 10	362s delay	59s early	Figure 6.24
2	SG11, 12, 13, 14	false alarm	Success	Appendix C
3	SG16, 18, 20, 22	60s early	Success	Appendix C
4	SG23-26	82s early	Success	Appendix C
5	SG23-26, 30, 31	false alarm	97s early	Appendix C

From Table 6.9 and Table 6.10, it is obvious that Td-MPCA outperforms than MPCA only. For example, Table 6.9 illustrates that the Td-MPCA can successfully detect damage, DS-1, from sensor groups 1, 3, and 5, where MPCA failed to uncover. The outperformance of Td-MPCA compared to MPCA can also be observed from the

group 2 case, where MPCA gave a 59s early warning, while Td-MPCA improved to 36s early alarm. In addition, both Td-MPCA and MPCA are successfully detect anomalies from the sensor group no.4. From the results obtained from Table 6.10, the Td-MPCA still performs better than MPCA to uncover DS-2. For example, the successful detection can be observed from groups 2, 3, and 4, while the MPCA fails to detect. The results from the other two groups of 1 and 5 can demonstrate the enhancement of Td-MPCA.

6.2.3 Laboratory evaluation of the Td-RRA method

The damage conditions that considered in this case study are DS-1 and DS-2, as shown in Figure 6.25 or previously described in Figure 6.20 (a) and (b) respectively.

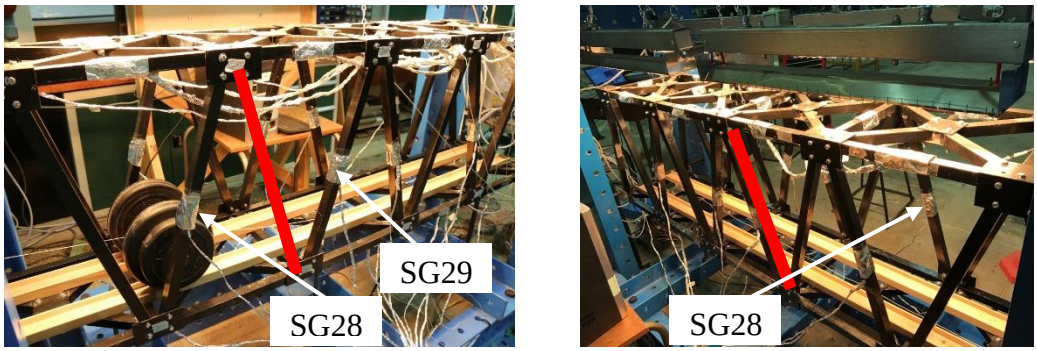

(a). Damage condition 1 (DS-1) (b). Damage condition 2 (DS-2)

Figure 6.25. Damage position for Td-RRA evaluation

The bridge is under temperature and traffic loading conditions in the laboratory environment. Figure 6.22. The detection processes of Td-RRA and RRA are presented in Figure 6.26 for DS-1 and Figure 6.27 for DS-2. The correlation coefficient threshold for the sensor selection, cc_t, is 0.8. The threshold bound of the reference period is 2σ. The certain period defined to avoid the false alarm here, $t_{out} = 371s$, is a half period of temperature variations. The detailed explanation of the above parameters, the reader can refer to Section 5.2.

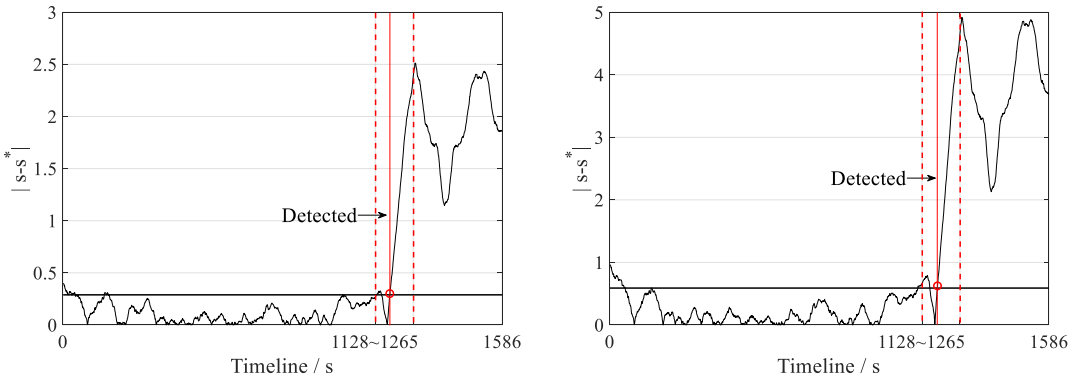

(a). Td-RRA detection results (b). RRA directly detection results

Figure 6.26. Td-RRA and RRA detection results on group 1 sensors under DS-1

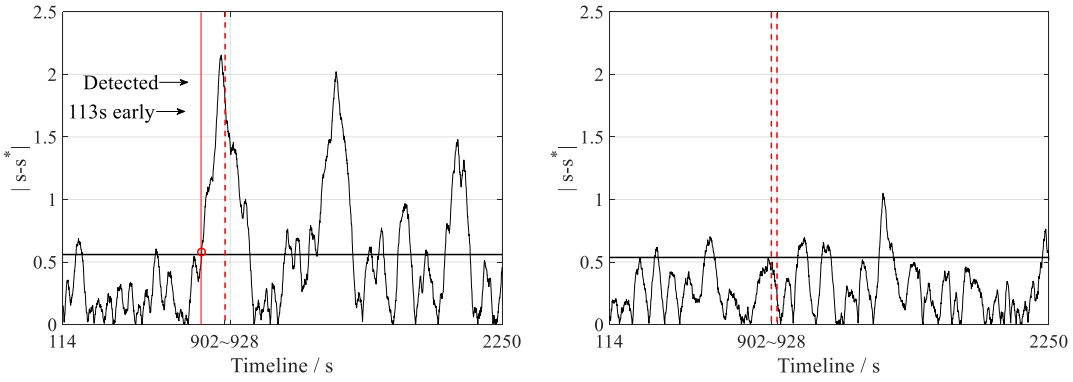

(a). Td-RRA detection results (b). RRA directly detection results

Figure 6.27. Td-RRA and RRA detection results on group 1 sensors under DS-2

As shown in Figure 6.26, the successful detection can be observed by applying both Td-RRA and RRA with damage condition DS-1. However, for the lighter damage condition, DS-2, the RRA is failed to observe any abnormal signal, while Td-RRA gives a 113s early alarm, as shown in Figure 6.27.

Due to the page limitation, only group 1 sensors are presented above to assess the performance of Td-RRA and compare with the performance of RRA without temperature-driven process. The other detection results are summarized in Table 6.11 for DS-1 and Table 6.12 for DS-2.

From Table 6.11, it is obvious that Td-RRA outperforms than RRA for detecting the first damage scenario. For example, the Td-RRA can successfully detect damage, DS-1, from sensor groups 2, 3, and 4 when the damage was introduced into the testing system, where RRA gives an early alarm. Moreover, the group 5 sensors are less

sensitive to damage, where RRA is failed to find abnormal information but Td-RRA can give an alarm with 48s early.

From the results obtained in Table 6.12, the Td-RRA still performs better than RRA to uncover DS-2, since the RRA failed on most groups. The performance of Td-RRA on group 1,3, and 5 is not as satisfied as the previous results given in Table 6.11, because DS-2 is away from sensors of group 1, 3, and 5, when compared with the position of DS-1.

Table 6.11. Summary for Td-RRA under damage condition 1 (DS-1)

Sensor group no.	Sensor no.	Td-RRA results	RRA results	Relevant figure
1	SG6, 8, 10	Success	Success	Figure 6.26
2	SG11, 13, 14	Success	60s early	Appendix
3	SG16, 18, 20, 22	Success	142s early	Appendix
4	SG23-26	Success	87s early	Appendix
5	SG23-26, 30, 31	48s delay	Fail	Appendix

Table 6.12. Summary for Td-RRA under damage condition 2 (DS-2)

Sensor group no.	Sensor no.	RRA results	Td-RRA results	Relevant figure
1	SG2, 4, 6, 8, 10	Fail	113s early	Figure 6.27
2	SG11, 12, 13, 14	Fail	57s early	Appendix
3	SG16, 18, 22	Fail	Fail	Appendix
4	SG23-25	382s early	284s early	Appendix
5	SG23-26, 30, 31	Fail	750s delay	Appendix

6.2.4 Laboratory evaluation of the Td-OCSVM method

In this section, the Td-OCSVM is examined. Four damage conditions, i.e. DS-1, 2, 3, and 4, are considered, which are presented previously in Figure 6.20. The following Figure 6.28 briefly shows the damage locations. All six groups of sensors, including

strain gauges and displacements, are considered in this section. For the detailed classification of sensor groups, the reader can refer to Figure 6.19 in Section 6.2.1.

Taking the SG2 from group 1 and SG14 from group 2, with damage scenario 3, as an example. The Figure 6.29 shows the relative strain measurements. The damage is introduced from 1220 seconds and remained until 1980 seconds. The period from 1220s to 1302s represents the time when introducing damage manually.

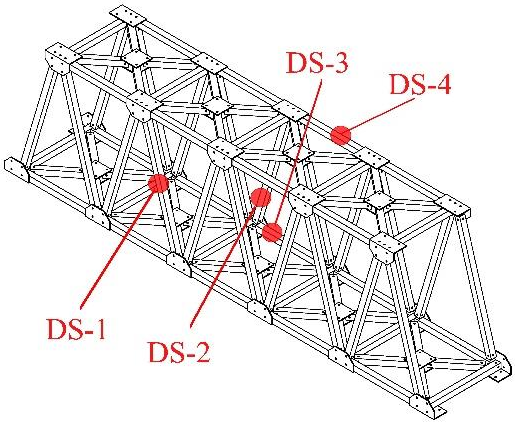

Figure 6.28. Damage position for Td-OCSVM evaluation

The application of Td-OCSVM is to identify the abnormal data within the time domain. For example, the data points collected after 1220 seconds are all abnormal since the damage has been introduced into the bridge system, therefore, they should be detected by Td-OCSVM. The performance of Td-OCSVM is accessed by the percentage of detectable data points. Figure 6.30 then shows the detection results of Td-OCSVM on SG2 and SG14. The detectability of Td-OCSVM on SG2 is 100%, while on SG14 is 83%.

The performance of Td-OCSVM on SG2 and SG14 has also been investigated with another three damage scenarios and compared with the application of OCSVM directly without the temperature-driven process. Table 6.13 summarized the detectability of Td-OCSVM and OCSVM for SG2 and SG14. The improvement of Td-OCSVM can be observed for all damage scenarios since the detectability is higher than OCSVM.

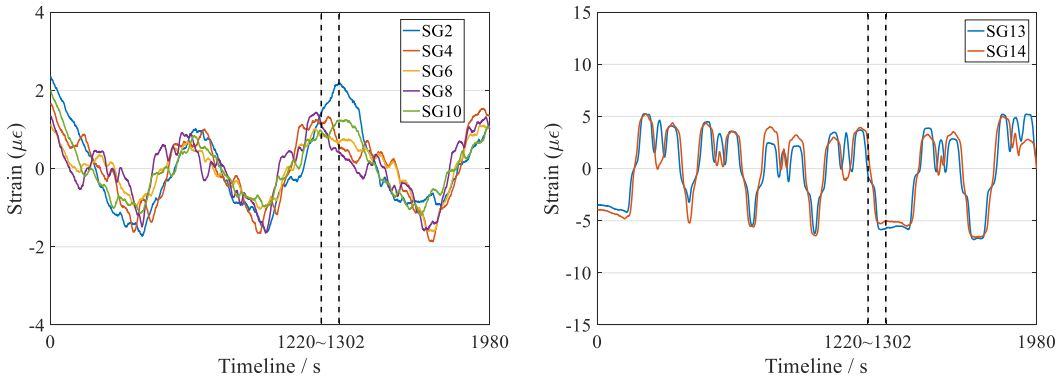

(a). Group 1 sensors measurements (b). Group 2 sensors measurements

Figure 6.29. Measurements of group 1 and 2 sensors with damage scenario 3

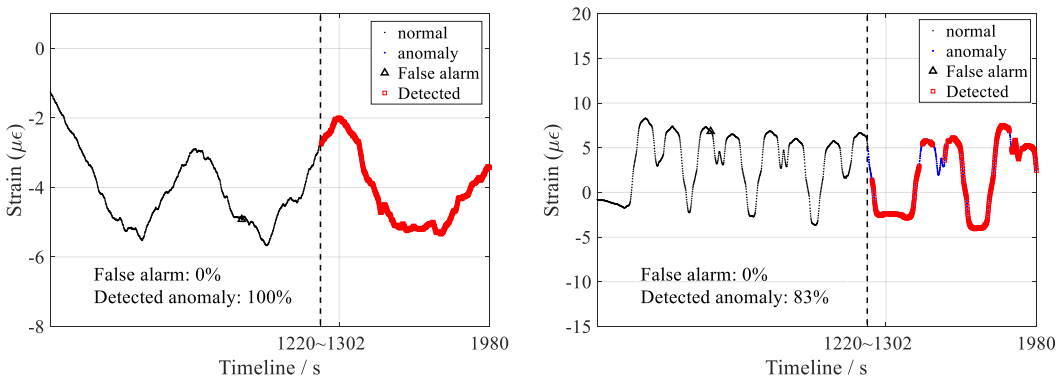

(a). SG2, detectability is 100% (b). SG14, detectability is 83%

Figure 6.30. Td-OCSVM on SG2 and SG14 with damage scenario 3

Table 6.13. Anomaly detectability of Td-OCSVM and OCSVM on SG2 and SG14.

	Damage scenario-1		**Damage scenario-2**	
	Td-OCSVM	*OCSVM*	Td-OCSVM	*OCSVM*
SG2	100	*89*	100	*76*
SG14	100	*68*	87	*52*
	Damage scenario-3		**Damage scenario-4**	
	Td-OCSVM	*OCSVM*	Td-OCSVM	*OCSVM*
SG2	**100**	*31*	100	*54*
SG14	**83**	*29*	91	*59*

The following four figures show the detectability between Td-OCSVM and OCSVM without temperature-driven process. Figure 6.31 presents the percentage of detected anomaly with damage scenario 1, while Figure 6.32, Figure 6.33, and Figure 6.34 give the comparison results of damage scenario 2, 3, and 4 respectively.

Apparently, all black dot date points are higher than the pink triangle data points in Figure 6.31 to Figure 6.34. This represents that Td-OCSVM outperforms than OCSVM without the temperature-driven process because their percentage values of the detected anomaly are all higher than OCSVM. For the exact values of each data points showing in Figure 6.31 to Figure 6.34, the reader can refer to Appendix C.3.

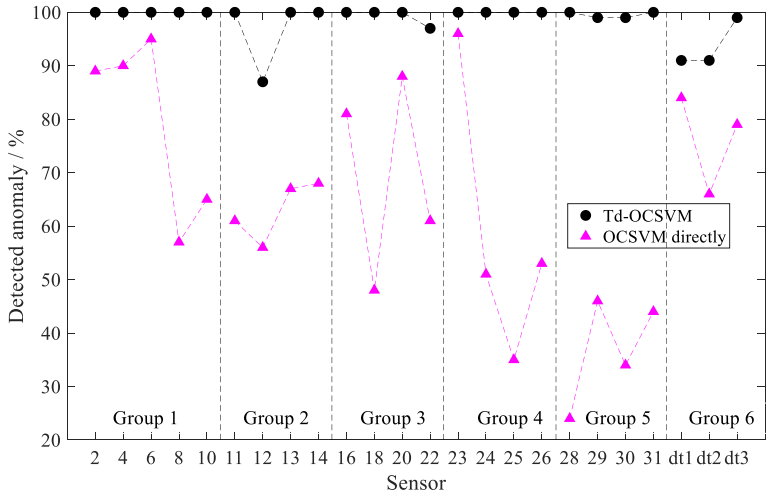

Figure 6.31. Detectability of Td-OCSVM and OCSVM under damage condition 1

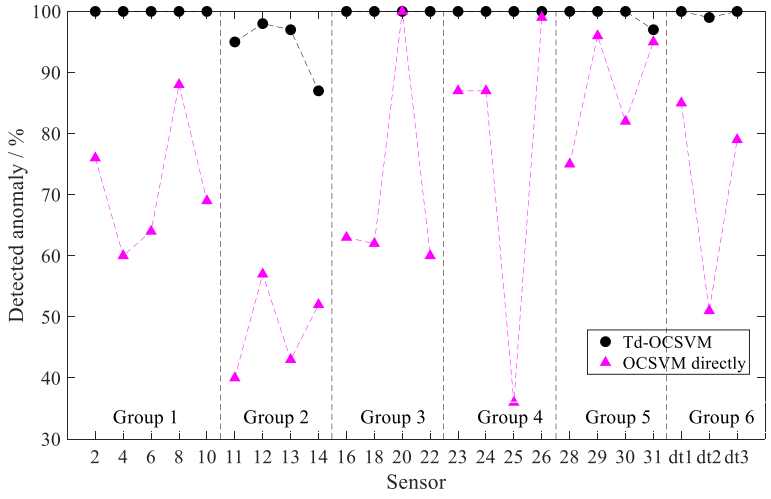

Figure 6.32. Detectability of Td-OCSVM and OCSVM under damage condition 2

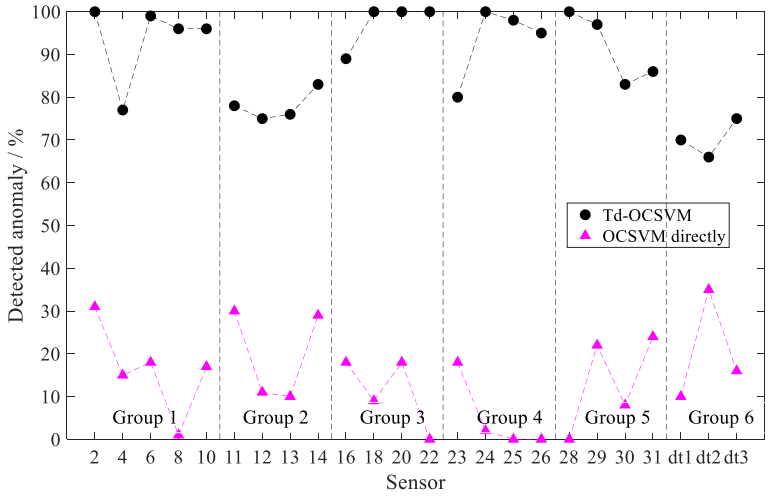

Figure 6.33. Detectability of Td-OCSVM and OCSVM under damage condition 3

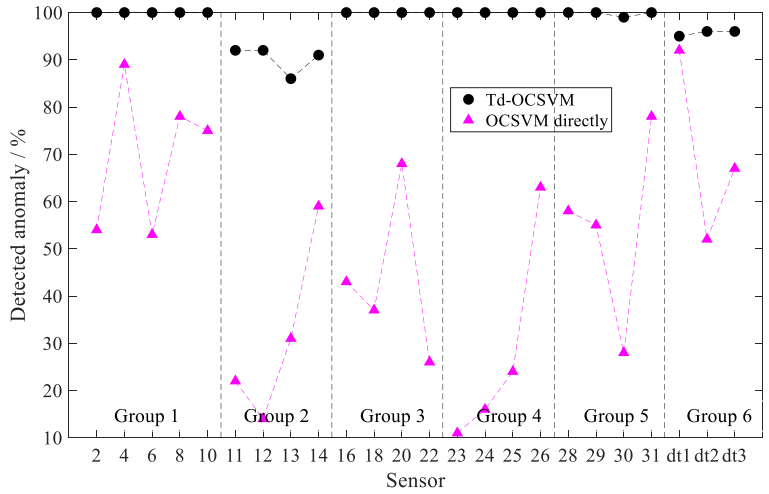

Figure 6.34. Detectability of Td-OCSVM and OCSVM under damage condition 4

6.2.5 Laboratory evaluation of the Td-ANN method

The neural network-based method is employed here to identify the potential various damage levels. The damage conditions considered here contain DS1-4, which are presented previously in Figure 6.20. The performance of Td-ANN and ANN directly are presented in Table 6.14 and Table 6.15 and compared in Figure 6.35 to Figure 6.38.

Regarding to the damage condition 1 (DS-1) as given in Figure 6.35, both Td-ANN and ANN could detect anomalies in group 1, 3, 4 with high accuracy. The Td-ANN

performs better than ANN in Group 5 and 6, with 10% improvement. But the Td-ANN is failed in Group 2 when compared with ANN.

In terms of damage condition 2 (DS-2) as shown in Figure 6.36, the improvement by Td-ANN can be observed from group 2 sensors application, but no major improvement can be observed from the other groups 1,3,4,5 and 6.

Regarding to the damage condition 3 (DS-3) as shown in Figure 6.37, the Td-ANN only enhanced the detection performance in Group 1 and 3.

Regarding to the damage condition 4 (DS-4) as shown in Figure 6.38, the detected ability for all sensor groups are below 35%, an improvement of Td-ANN can be observed in Group 3.

Table 6.14. Anomaly detection by Td-ANN on all measurements

	Correct alarm				**False alarm**			
	DS-1	**DS-2**	**DS-3**	**DS-4**	**DS-1**	**DS-2**	**DS-3**	**DS-4**
Group 1	100%	98%	37%	24%	0.0%	0.0%	0.0%	0.2%
Group 2	31%	63%	32%	12%	1.7%	0.1%	0.1%	0.3%
Group 3	100%	100%	24%	13%	0.0%	0.1%	0.1%	0.2%
Group 4	94%	100%	16%	33%	0.1%	0.0%	0.1%	0.0%
Group 5	37%	72%	19%	16%	0.7%	0.0%	0.2%	0.0%
Group 6	100%	25%	28%	12%	0.1%	0.7%	0.2%	0.5%

Table 6.15. ANN on measurements from temperature and traffic load test

	Correct alarm				**False alarm**			
	DS-1	**DS-2**	**DS-3**	**DS-4**	**DS-1**	**DS-2**	**DS-3**	**DS-4**
Group 1	100%	98%	28%	24%	0%	0%	0%	0%
Group 2	54%	36%	32%	20%	1%	0%	0%	0%
Group 3	100%	100%	16%	13%	0%	0%	0%	0%
Group 4	95%	100%	17%	13%	0%	0%	0%	0%
Group 5	25%	70%	25%	16%	0%	0%	0%	0%
Group 6	92%	31%	34%	16%	0%	0%	0%	0%

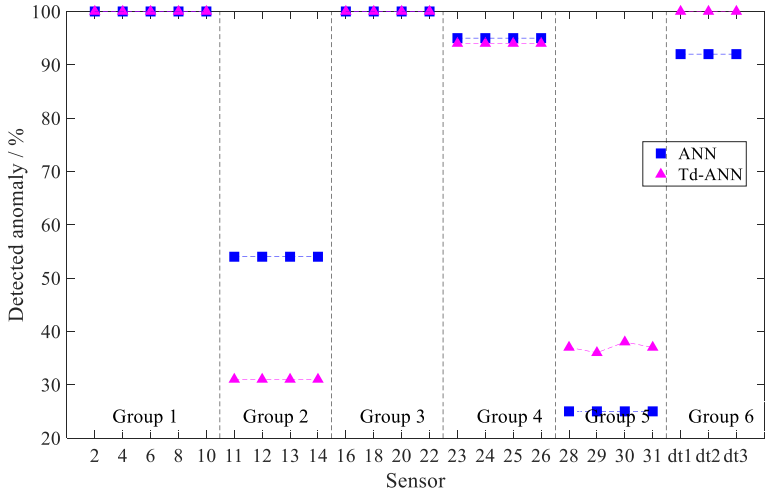

Figure 6.35. Anomaly detection comparison by Td-ANN and ANN for DS-1

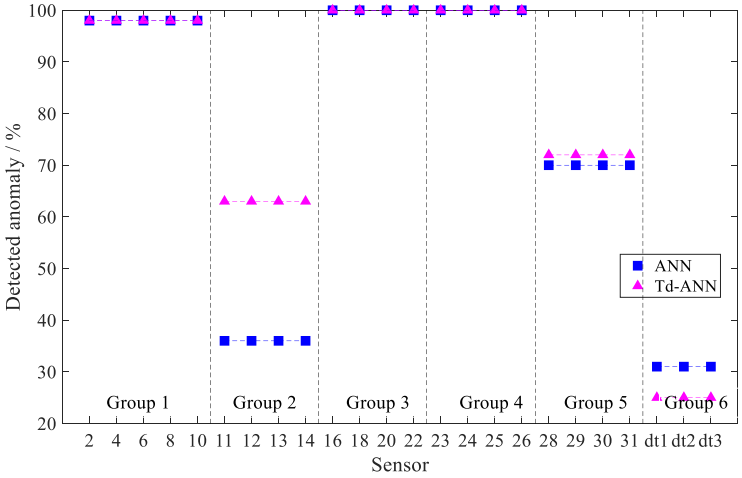

Figure 6.36. Anomaly detection comparison by Td-ANN and ANN for DS-2

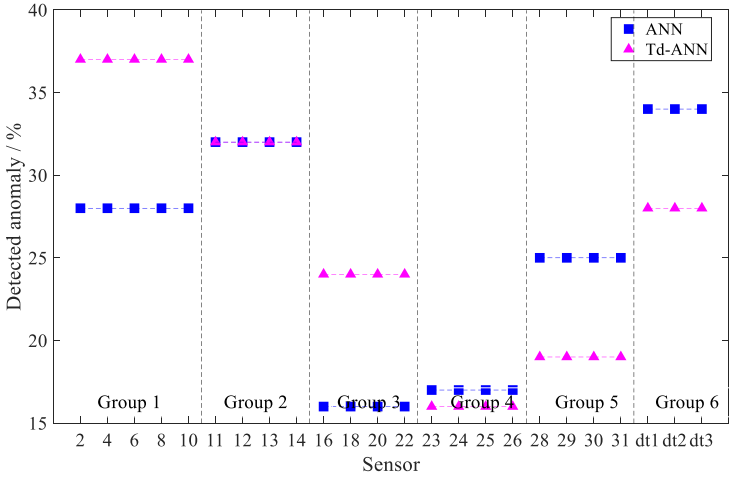

Figure 6.37. Anomaly detection comparison by Td-ANN and ANN for DS-3

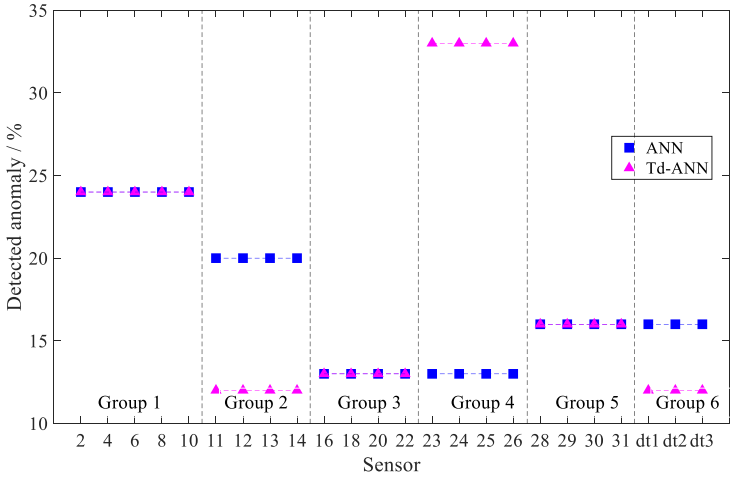

Figure 6.38. Anomaly detection comparison by Td-ANN and ANN for DS-4

6.2.6 Summary for laboratory case study

This present case study was designed to investigate the promoted temperature-driven methods in the laboratory environment. This case study has firstly described the laboratory test system, including the sensor placement and damage scenarios in Section 6.2.1.

From the Section 6.2.2 conducted for the evaluation of Td-MPCA, the outperformance of Td-MPCA to identify the damage condition DS-1 and DS-2 can be demonstrated when compared with MPCA without temperature-driven process.

The similar conclusions can be drawn for Td-RRA in Section 6.2.3 when compared with RRA directly without the temperature-driven process. As demonstrated, the Td-RRA can successfully detect anomalies from several sensor groups, while from which the RRA gives early alarms or fail to uncover any anomalies. In the examination of damage scenario 2, DS-2, which is far away from most sensors, the Td-RRA can uncover anomalies but with evident uncertainties.

Conducted in Section 6.2.4, the detection ability of Td-OCSVM has been evaluated with four damage conditions, DS-1 to DS-4. The outcomes have approved the improvement and outperformance of Td-OCSVM when compared with OCSVM directly.

The fourth evaluation is conducted for accessing Td-ANN, where DS-1, 2, 3, and 4 damage conditions are investigated. Based on the results obtained from Section 6.2.5, the improvement of Td-ANN is not very significant. For most conditions, the detectability of Td-ANN is similar as ANN directly on the target signals without the temperature-driven process.

6.3 Case study 3: Ricciolo curved viaduct

The third case study undertaken to evaluate the proposed temperature-driven anomaly detection methods is on the monitoring data collected from Ricciolo curved viaduct in Switzerland. The brief introduction of Ricciolo curved viaduct is first presented in Section 6.3.1. After that, the proposed temperature-driven methods are investigated and discussed separately in Section 6.3.2 for Td-MPCA, in Section 6.3.3 for Td-RRA, in Section 6.3.4 for Td-OCSVM, and in Section 6.3.5 for Td-ANN.

6.3.1 Introduction

The Ricciolo curved viaduct is part of Swiss motorway A2 and has been monitored since construction from 2005. The monitoring system has been installed at the longest span (35m long). The measurement system layout can be found in Figure 6.39, while the cross-section view with information of sensor placement can refer to Figure 6.40.

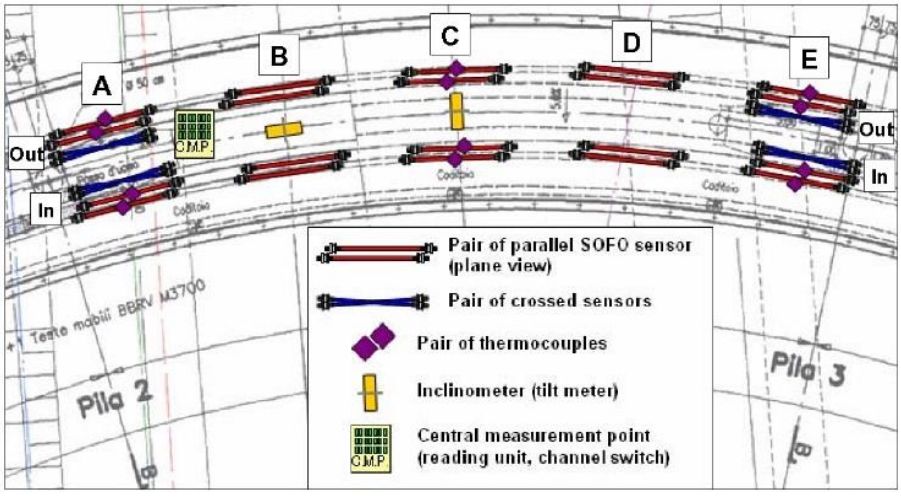

Figure 6.39. Case study 3: sensor placement overview of Ricciolo curved viaduct, reprinted from (Glišić *et al.*, 2008)

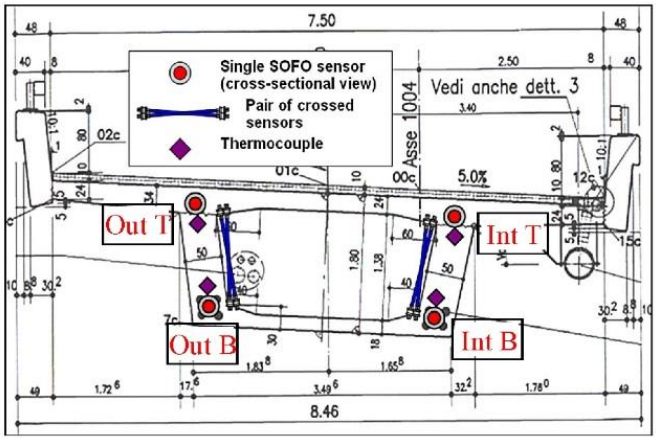

Figure 6.40. Case study 3: sensor placement at cross-section A and E of Ricciolo curved viaduct, reprinted from (Glišić et al., 2008)

The measurement system started monitoring from 11/01/2005 to 23/02/2006. The following Table 6.16 summarizes the information regarding to the monitoring data and construction actions. The detailed construction information can be found in (Glišić *et al.*, 2008; Posenato *et al.*, 2008)

Table 6.16. Data acquisition system details and viaduct condition summary

Start Time	End Time	Frequency	Duration	Condition
11/01/2005 19:07	12/01/2005 03:07	Every 1 h	1 day	Clear*
12/01/2005 15:33		Single record	<1 day	Construction
12/01/2005 15:45		Single record	<1 day	Construction
12/01/2005 15:56	12/01/2005 22:26	Every 0.5 h	<1 day	Construction
13/01/2005 14:39	14/01/2005 04:39	Every 1 h	<1 day	Construction
14/01/2005 10:35	18/01/2005 13:35	Every 1 h	3 days	Construction
18/01/2005 17:03	31/01/2005 11:03	Every 1 h	14 days	Construction
31/01/2005 14:51	01/02/2005 10:51	Every 1 h	<1 day	Construction
01/02/2005 11:26		One record	<1 day	Construction
01/02/2005 11:36	02/02/2005 09:36	Every 2 h	<1 day	Construction
02/02/2005 15:33	01/03/2005 09:33	Every 2 h	27 days	Construction
01/03/2005 11:03	01/04/2005 07:03	Every 2 h	31 days	Construction
01/04/2005 12:03		One record	<1 day	Construction

Start Time	End Time	Frequency	Duration	Condition
02/04/2005 00:03	02/05/2005 12:03	Every 4 h	31 days	Construction / Clear
02/05/2005 16:20	01/06/2005 16:20	Every 6 h	31 days	Clear
01/06/2005 18:03	11/01/2006 12:03	Every 6 h	7 m 10 d	Clear
12/01/2006 04:03	23/02/2006 04:03	Every 12 h	43 days	Clear

** Clear means no construction work is recorded*

6.3.2 Ricciolo viaduct evaluation of the Td-MPCA method

In this study, two months data from 00:03 in 02/04/2005 to 16:20 in 01/06/2005 are selected for anomaly detection, as listed in Table 6.17. The construction events that happened during this period are described as follows: (a) Construction of lateral protection walls from 02/04/2005 to 22/04/2005; (b) Post-tensioning, cast of left side wing and removal of external formworks from 25/04/2005 to 26/04/2005. The bridge is assumed working properly after 27/04/2005, because of no construction work since then.

To detect the anomalous behaviour, the time scale will be inverted from 01/06/2005 to 02/04/2005, since MPCA requires a training period as the reference state of the bridge. Therefore, the reference period, i.e. healthy condition, ranges from 01/06/2005 to 28/04/2005. The abnormal changes should be detected at 27/04/2005. This time reversal procedure utilized construction as a damage scenario when looking backwards in time.

Table 6.17. Monitoring period for Td-MPCA evaluation

Start Time	End Time	Frequency	Duration	Condition
02/04/2005 00:03	02/05/2005 12:03	Every 4 hours	31 days	Construction + Clear
02/05/2005 16:20	01/06/2005 16:20	Every 6 hours	31 days	Clear

** Clear means no construction work is recorded*

The measurements from the cross-section A is interpreted in this case study. The axial strain and corresponding temperature measurements from the extremities of the span are displayed in Figure 6.41, where the maximal negative vertical bending occurs. The detection results by applying Td-MPCA are subsequently shown in Figure 6.42 (a). The detection is successful without any delay. The performance of MPCA on all four sensors records directly is given in Figure 6.42 (b). However, the delay of detection is obvious.

Overall, from the comparison between Figure 6.42 (a) and (b), the delay anomaly alarm by applying MPCA directly can be solved properly. It corroborates that the proposed temperature-driven anomaly detection method is a more efficient anomaly detection method.

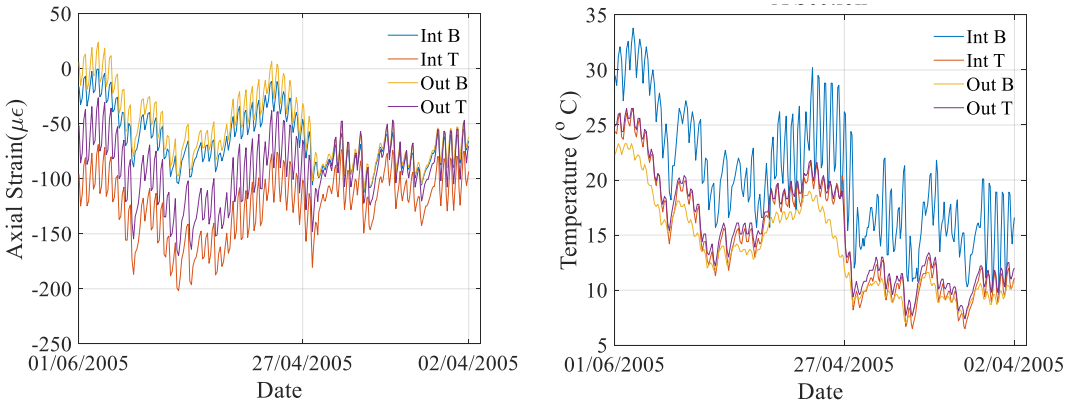

(a). Strain measuremetns (b). Temperature measurements

Figure 6.41. Axial strain and temperature measurements from cross-section A

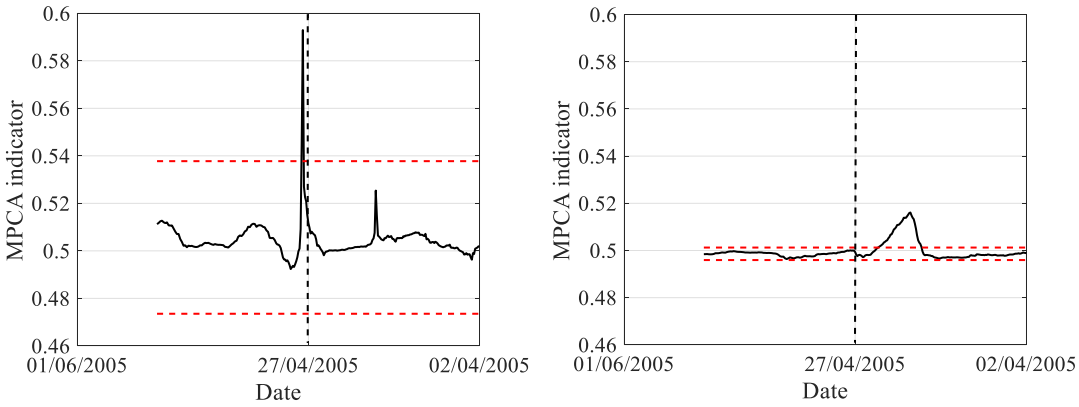

(a). Td-MPCA detection (b). MPCA detection

Figure 6.42. Anomaly detection results by Td-MPCA and MPCA. (window size: 48 hours, and threshold: $\pm 2\sigma$ over 120 hours reference period).

6.3.3 Ricciolo viaduct evaluation of the Td-RRA method

In this study, the target monitoring period is the same as in the Section 6.3.2, which is two months data from 02/04/2005 to 01/06/2005, as listed in Table 6.17. As previously described, the timeline is inverted. The abnormal changes should be detected at 27/04/2005, after which the construction work was conducted. The cross-section A and E are considered to examine the Td-RRA, whose strain measurements are given in Figure 6.43. The data missing condition can also be observed in Figure 6.43(b), which is an extra abnormal condition should be detected. The detection results by applying Td-RRA on cross-section A and E are subsequently shown in Figure 6.44 and Figure 6.45 respectively.

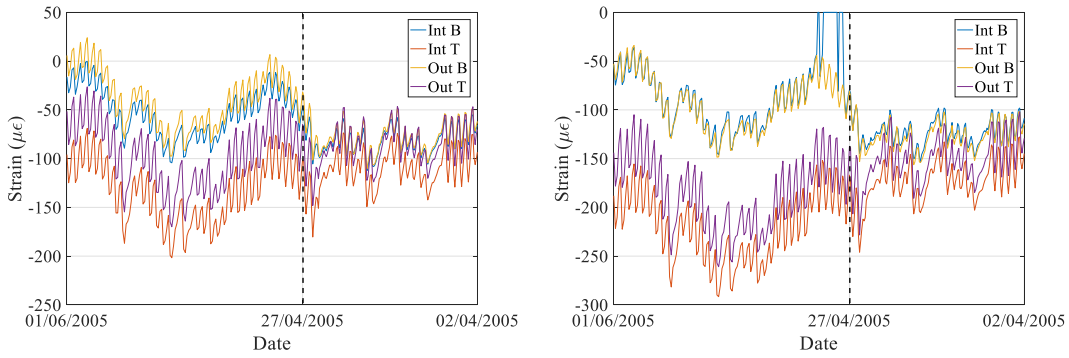

(a). Axial strain from cross-section A (b). Axial strain from cross-section E

Figure 6.43. Axial strain measurements from cross-section A and E

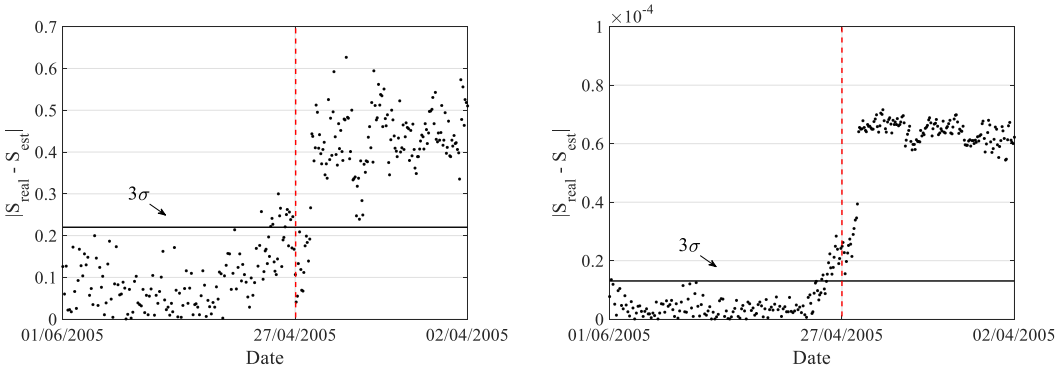

(a). Td-RRA detection (b). RRA directly detection

Figure 6.44. Anomaly detection results by Td-RRA and RRA on data from cross-section A

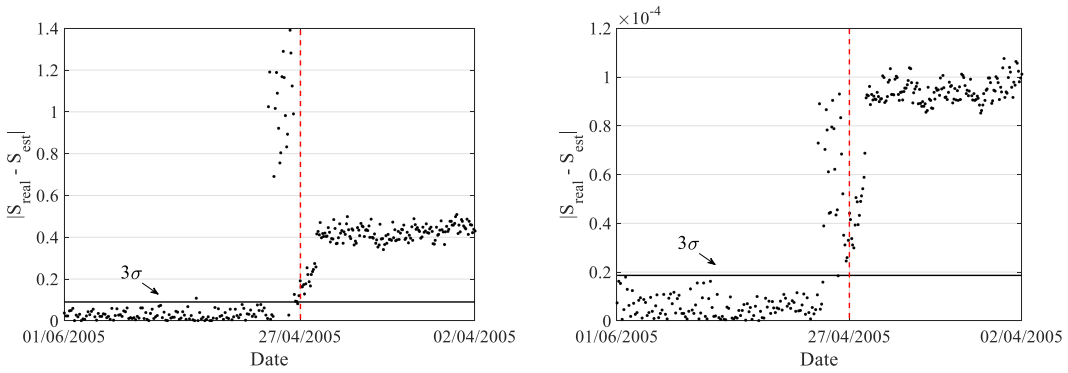

(a). Td-RRA detection (b). RRA directly detection

Figure 6.45. Anomaly detection results by Td-RRA and RRA on data from cross-section E

In general, both Td-RRA and RRA can find out the abnormal changes at the expected date. The data missing condition at cross-section E can also be addressed by applying Td-RRA and RRA. Therefore, the results presented above can confirm that the Td-RRA does not have a significant improvement when compared with RRA without temperature-driven process.

6.3.4 Ricciolo viaduct evaluation of the Td-OCSVM Method

The monitoring period considered in this part is from 18/01/2005 to 23/02/2006. The important construction events are given as follows, followed by the Figure 6.46 to show a timeline with the date of interests.

- Event 1 (18/01/2005 – 22/04/2005): Construction of lateral protection walls
- Event 2 (25/04/2005 – 26/04/2005): Post-tensioning from 70% to 100%
- Event 3 (25/04/2005 – 27/04/2005): Cast of left side wing

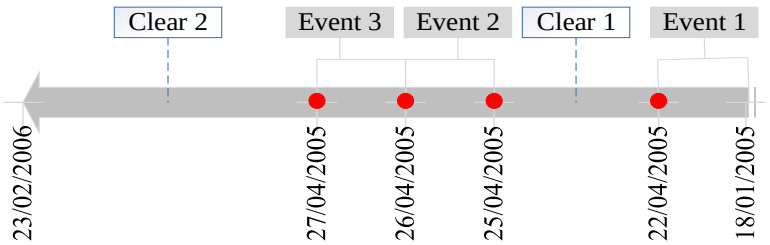

Figure 6.46. Timeline of interests

Taking the sensor ‘A_Int_B’ in the cross-section A as an example, the Figure 6.47(a) shows the strain measurements in the time domain, the red dash line is the time

when all construction works are finished in 27/04/2005, which is the end of event 3. The Figure 6.47(b) gives the correlation between temperature and strain, from which, the clear 1 and 2 are corresponding to the time without construction work, seeing Figure 6.46. It is apparent that the measurements from 22/04/2005 to 25/04/2005 are still offline since there still has more work need to be done after 22/04/2005. Hence the date of interest should be the 27/04/2005, when the abnormal behaviour should be uncovered since then.

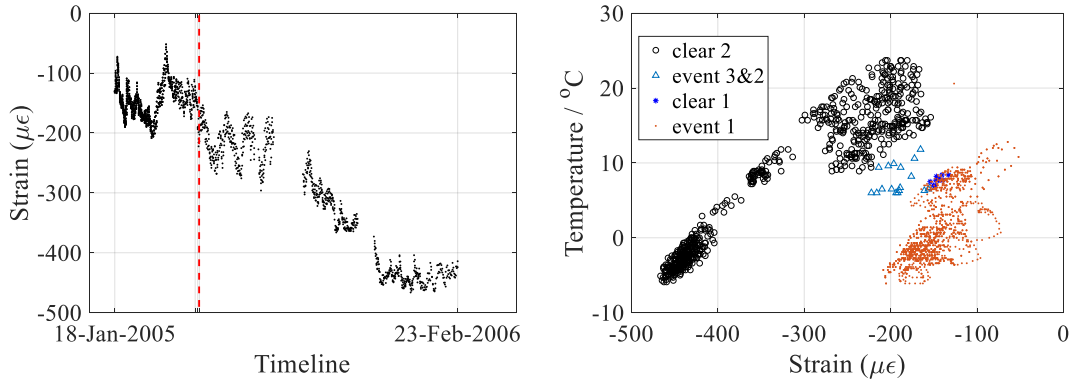

(a). Strain measurements in time domain

(b). Strain vs. temperature

Figure 6.47. Measurements of sensor 'A_Int_B' at the cross-section A

The Figure 6.48(a) below shows the correlation of strain measurements and temperature from sensor 'A_Int_B' in cross-section A. The black data points represent the data in clear stage, which means there is no construction event was recorded. The blue dots show the data under construction events, which should be discovered by Td-OCSVM.

The OCSVM without the temperature-driven process is applied to find the measurements that under the construction events. The detection results are showing in Figure 6.48(b). As can be seen, only 53% blue data points can be identified. Moreover, the missing data could be detected from the normal dataset, representing as zero strain with pink false alarm markers in Figure 6.48(b). However, the false alarm is still low and roughly 0%.

The attempt of Td-OCSVM is shown in Figure 6.48(c). Approximately 100% of anomalous behaviours could be identified by Td-OCSVM with roughly 0% false alarm.

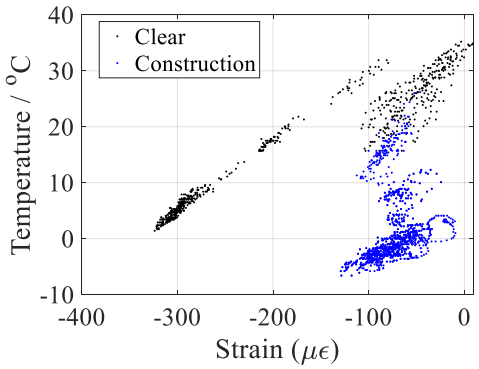

(a). Measurements form sensor A_Int_B (blue dots should be detected)

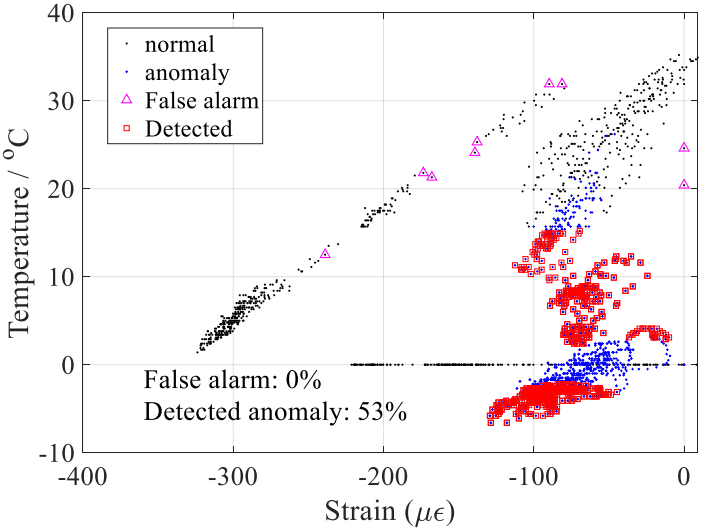

(b). Detection results by OCSVM directly

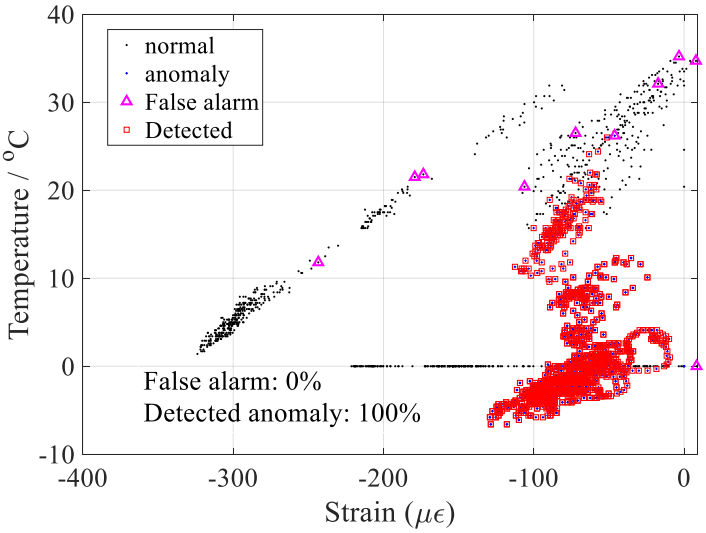

(c). Detection results by Td-OCSVM

Figure 6.48. Anomaly detection by Td-OCSVM and OCSVM.

The applications of Td-OCSVM on other sensors have also been conducted, the results are listed in Table 6.18 for the OCSVM application and in Table 6.19 for the Td-OCSVM application. To have a visible comparison, Figure 6.49 is presented, from which the improvement of Td-OCSVM is obviously for all sensors.

Table 6.18. Summary of detectability by applying OCSVM

Sensor location	Detected anomaly	Sensor location	Detected anomaly	Sensor location	Detected anomaly
A_Int_B	53%	C_Int_B	60%	E_Int_B	59%
A_Int_T	41%	C_Int_T	77%	E_Int_T	63%
A_Ont_B	36%	C_Ont_B	97%	E_Ont_B	72%
A_Ont_T	38%	C_Ont_T	32%	E_Ont_T	44%

Table 6.19. Summary of detectability by applying Td-OCSVM

Sensor location	Detected anomaly	Sensor location	Detected anomaly	Sensor location	Detected anomaly
A_Int_B	100%	C_Int_B	100%	E_Int_B	100%
A_Int_T	96%	C_Int_T	100%	E_Int_T	100%
A_Ont_B	100%	C_Ont_B	100%	E_Ont_B	100%
A_Ont_T	100%	C_Ont_T	100%	E_Ont_T	99%

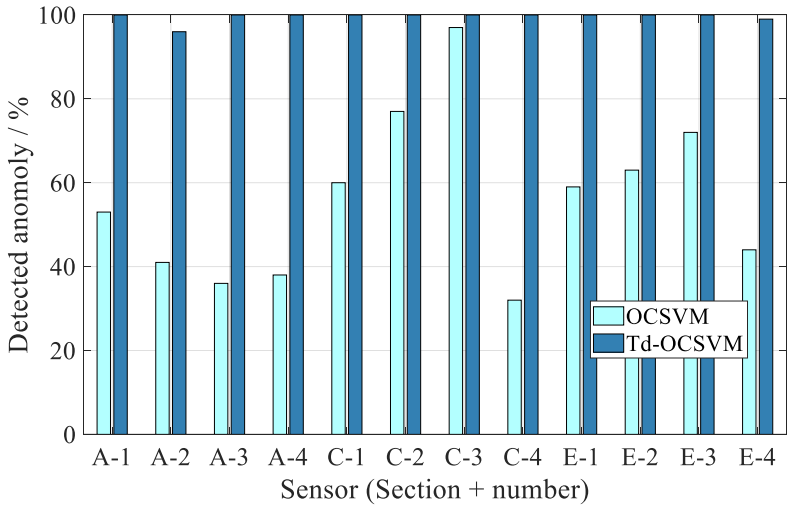

Figure 6.49. Comparison of Td-OCSVM and OCSVM

6.3.5 Ricciolo viaduct evaluation of the Td-ANN Method

In this study, two months data from 02/04/2005 to 01/06/2005 are selected for anomaly detection, as previously listed in Table 6.17. The bridge is under construction work from 02/04/2005 to 27/04/2005 and is assumed working in healthy state from 27/04/2005 to 01/06/2005.

To detect the anomalous behaviour, the time scale will be inverted from 01/06/2005 to 02/04/2005, since the neural network requires a reference period for network training. The abnormal changes should be detected from 27/04/2005 to 02/04/2005.

As previous described, there are four strain measurement from each cross-section, as shown in Figure 6.40. The four strain measurements are utilized to train one neural network first. The anomaly detection results by Td-ANN and ANN are presented subsequently in Table 6.20, while Figure 6.50 presents the cross-section A and C anomaly identification in the time domain.

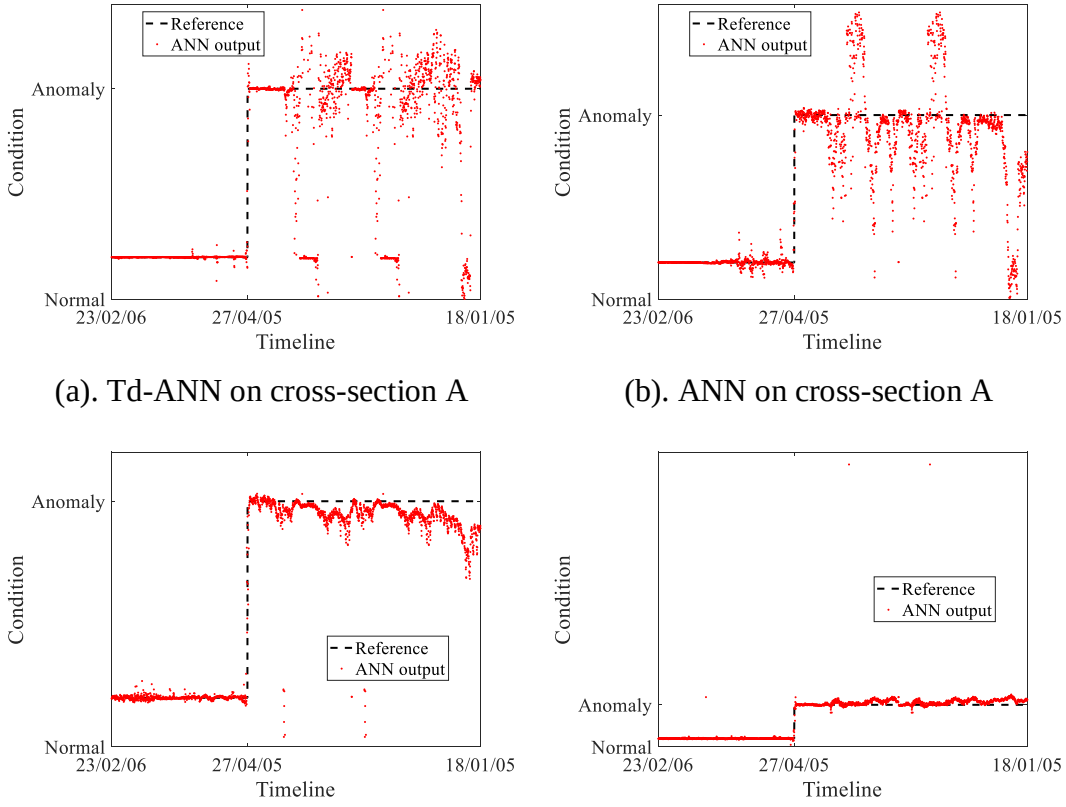

(a). Td-ANN on cross-section A

(b). ANN on cross-section A

(c). Td-ANN on cross-section C

(d). ANN on cross-section C

Figure 6.50. Anomaly identification of Td-ANN and ANN on cross-section A and C

From Figure 6.50 and Table 6.20, a slight improvement by using Td-ANN can be observed in cross-section A. For other four cross-sections, the performance of Td-ANN is close to ANN without improvement.

Table 6.20. Comparison of Td-ANN and ANN

Cross-section	Correct alarm		False alarm	
	ANN	**Td-ANN**	***ANN***	**Td-ANN**
A	*58%*	62%	*0%*	0%
B	*30%*	23%	*2%*	2%
C	*76%*	71%	*1%*	1%
D	*40%*	31%	*1%*	1%
E	*50%*	41%	*0%*	1%

6.3.6 Summary for Ricciolo curved viaduct case study

From the above Ricciolo curved viaduct case study, the ability of Td-MPCA, Td-RRA, Td-OCSVM, and Td-ANN to discover abnormal changes before and after construction period has been conducted and assessed. Several findings can be summarized and highlighted as follows.

In general, all temperature-driven methods can notice the abnormal changes before and after construction. The delay anomaly alarm by applying MPCA directly can be solved properly by using Td-MPCA in Section 6.3.2.

In Section 6.3.3, both Td-RRA and RRA can find out the abnormal changes at the expected date. The data missing condition at cross-section E can also be addressed by applying Td-RRA and RRA. But the improvement of Td-RRA has not been observed from this case study.

For the third temperature-driven method, Td-OCSVM, the significant improvement for OCSVM has been obtained from Section 6.3.4. Its detectability is close to 100%, increasing around 60% when compared with OCSVM.

The last evaluation is on Td-ANN, both Td-ANN and ANN can address the anomalies when the bridge in under construction events. A slight improvement for ANN is recorded but there is no significant benefit by using Td-ANN instead of ANN.

6.4 Concluding remarks

In this chapter, the temperature driven anomaly detection methods have been examined by three case studies, including the numerical truss model in Section 6.1, laboratory test in Section 6.2, and the Ricciolo curved viaduct in Section 0. The methods are designed to detect abnormal behaviours according to the separated thermal-related responses, which have been examined in previous CHAPTER 4. The outcomes from those three case studies are summarized as follows.

From Section 6.1, a numerical truss bridge was first investigated. The damage conditions were simulated by reducing the stiffness on target chords. The findings obtained from this case study can be summarized as follows.

(a) In this case study, the detection performance of proposed temperature-driven methods all depends on the sensor locations for investigation, the closer to the damage, the more possibility to detect the damage.
(b) The proposed Td-MPCA is more sensitive than the application of MPCA directly without the temperature-driven process, since the simulated 5% stiffness loss in can be detected by Td-MPCA but cannot be detected by MPCA.
(c) The proposed Td-RRA has also been confirmed as an enhanced abnormality detection method, since RRA is failed to detect the 5% stiffness loss. But the aberrant responses can be delineated by Td-RRA.
(d) The OCSVM is only successful when the damage is at a serious level, i.e. the 50% stiffness loss. But the Td-OCSVM has a dramatical improvement for all the damage levels considered in this case study.
(e) An improvement of Td-ANN can be demonstrated, as the Td-ANN can increase the anomaly detectability by 20%.

From Section 6.2, the second case study has conducted on a laboratory truss bridge with four damage conditions. The research findings of four temperature-driven methods can be summarized as follows.

(a) Outperformance of Td-MPCA, compared with MPCA, and outperformance of Td-RRA, compared with RRA, have been examined and identified for uncovering two introduced damage scenarios (DS-1 and DS-2).

(b) The results obtained from the evaluation on Td-OCSVM has confirmed the positive impact of temperature-driven to OCSVM, since the improvement can be observed in all four simulated damage conditions (DS-1, 2, 3, and 4).

(c) However, the improvement of Td-ANN compared with ANN is not very significant. For most damage conditions (DS-1, 2, 3, and 4), the detectability of Td-ANN is as same as ANN directly on the target signals without the temperature-driven process.

The third attempt, presented in Section 6.3.5, is on the monitoring data from Ricciolo viaduct in Switzerland. According to the outcomes, all temperature-driven methods can notice the abnormal changes before and after construction. The following facts can be summarized.

(a) The delay anomaly alarm by applying MPCA directly can be solved properly by using Td-MPCA.

(b) Both Td-RRA and RRA can find out the abnormal changes at the expected date. The data missing condition at cross-section E can also be addressed by applying Td-RRA and RRA. But the improvement of Td-RRA has not been observed from this case study.

(c) Td-OCSVM has shown the satisfactory detection ability when compared with OCSVM.

(d) Both Td-ANN and ANN can identify the anomalies due to construction actions. However, the improvement for ANN by applying temperature-driven process has not been observed in this case study.

In general, those three case studies have confirmed that apparent anomalous changes can be observed after ICA separation. This can demonstrate that thermal effects could cover the damage-induced variations in the observed signals, and anomalies behaviours could be observed after interpreted by Independent Component Analysis (ICA). The enhancement of temperature-driven to MPCA, RRA, OCSVM, and ANN can also be demonstrated through three case studies. In particular, Td-MPCA performs more sensitive to slight damage condition and more reliable than MCPA in above three case studies. The detection ability of RRA is slightly weaker than MPCA under the same damage conditions. But improvement of Td-RRA is clear when compare to the

application of RRA only. Td-OCSVM performs reliable and sensitive than OCSVM too. Finally, Td-ANN has also confirmed a slightly improvement.

CHAPTER 7 CONCLUSIONS

7.1 Research and contribution summary

Civil infrastructures are exposed to the complex surroundings, the thermal loadings due to temperature variations can alter the structural characteristics resulting in the challenge for detecting structural anomalies.

The author's PhD work is mainly contributed to the research on temperature effects in Structural Health Monitoring area. The major contribution of author's work is to propose the temperature-driven anomaly detection methods. Based on the literature review works conducted in CHAPTER 2, the temperature effects have been reviewed and previous solutions proposed by other researches have been classified into elimination of temperature effect and utilization of temperature effect. The author's work contributes to the second solution. But different from previous efforts, the thermal features of interests are directly and blindly separated from the collected structural responses, without any prior knowledge of structural physical model or loading conditions.

The proposed temperature-driven anomaly detection method consists two major procedures, the thermal feature extraction and the anomaly detection. This thesis first introduced the thermal feature extraction methods with regards of mathematic background and case studies in CHAPTER 3 and CHAPTER 4 respectively. In present research, the author has proposed the thermal feature extractions for both underdetermined cases, i.e. single-channel data is available as the input signal, and overdetermined cases, i.e. multi-channel data is available as the input sources. In CHAPTER 3, the adopted methodologies for thermal feature separation, including Empirical Mode Decomposition (EMD), Ensemble Empirical Mode Decomposition

(EEMD), Principal Component Analysis (PCA), and Independent Component Analysis (ICA), for thermal feature extraction have been introduced. The author has designated the underdetermined solutions as EPI and EEPI, which stand for the combination of EMD, PCA with ICA and EEMD, PCA with ICA respectively. While deal with overdetermined conditions, the PCA and ICA are proposed to interpret measurements of interest. The novelty of aforementioned solution to separate the thermal features is employing Blind Source Separation (BSS) method into author's research. By employing the EPI or EEPI on the single-channel sources, both seasonal and daily temperature effects can be identified, however the overdetermined solution, PCA + Fast ICA, could only separate the entire temperature features from other loading conditions' effects, instead of distinguishing seasonal features from and daily variations. Therefore, the author recommends EEPI method when the available number of sensors is limited, for example, less than three. For best reliability and numerical accuracy for the extracted thermal response, the author will prefer to recommend PCA + Fast ICA.

After extracted the temperature-induced responses from sensor measurements, the following procedure is the anomaly detection by applying Moving Principal Component Analysis (MPCA), Robust Regression Analysis (RRA), One-Class Support Vector Machine (OCSVM), and Artificial Neural Network (ANN). The temperature-driven anomaly detection methods are then designated as Td-MPCA, Td-RRA, Td-OCSVM, and Td-ANN, whose mathematical background has been introduced in CHAPTER 5. The evaluation and assessment of temperature-drivne methods have then undertaken in CHAPTER 6 through numerical truss model, experimental truss bridge and an extra case study on Ricciolo curved viaduct.

The MPCA and RRA have already evaluated in previous published work for the purpose of damage detection. The author's contribution is improving the performance of MPCA and RRA by introducing the process of temperature-driven. The Td-MPCA and Td-RRA are more sensitive to uncover the slight damage while MPCA and RRA cannot identify the abnormal changes or have an evident delay before giving the correct alarms.

Regarding the other two methods, Td-OCSVM and Td-ANN, the numerical, experimental and in-situ case studies have demonstrated that Td-OCSVM could

identify all simulated damage conditions while OCSVM is not sensitive to damage conditions. In particular, the detection performance of Td-ANN and ANN are at the same level. Therefore, the Td-ANN does not show a significant improvement for ANN from author's case studies.

7.2 Future work recommendations

The author's current researches have approved that temperature features can be used to improve the performance of anomaly detection methods. However, there are still some uncertainties remain and some future works are recommended as follows.

There have some empirical-dependent parameters existing in proposed temperature driven method. For example, the assignment of threshold parameters in the application of outlier detection usually according to experience. There is not a general rule or recommendation in different case studies.

The underdetermined method, EPI and EEPI, are not fully explored in anomaly detection part since the purpose of this research is to detect damage. But the potential ability of EPI and EEPI to locate the damage can be further studied.

Appendix A. Experimental Test System Description

A.1. Measurement system

The sensor involved into this test includes displacement, strain gauges, thermocouple and heating lamps. The quantity and model information are listed in Table A.7.1, while the following sections will describe more details of sensor set up in this test.

Table A.7.1. Measurement system list

Sensor type	Quantity	Model	Brand	Relative control module
Displacement	3	HS50	Micro Measurements	NI 9237, NI 9949
Strain gauges	Up to 32	FLAB-6-23	TML	NI9235
Thermocouple	12	No. 621-2170	RS	NI9219
Heating lamp	4	-	-	USB-6001

A.1.1 Displacement

The displacement sensor used in this test is HS50 linear displacement sensors from Micro Measurements (Vishay Precision Group, 2014). The datasheet is available online. Several key specifications are given in Table A.7.2. And the displacement setup is presented in Figure A.1.

NI 9237 from National Instrument (National Instruments, 2015) is implemented to collect data from HS50, which has 4 – RJ-50 inputs. Connection between displacement sensors (HS50) and NI 9237 is presented in Figure A.2,which shows that RJ-50 cable and NI 9949 (National Instruments, 2009) are required to connect the HS50 with NI9237. The connection between HS50 and NI9949 is also displayed in Table A.7.3.

Table A.7.2. HS50 linear displacement sensor specifications

Parameters	**Description**
Displacement range	2 in (51.5mm)
Weight	0.44 lb (200g)
Excitation	2 to 10 V, AC or DC
Frequency response	5-mm displacement: 100 Hz; 100-mm displacement: 10Hz
Temperature range	+15 to 140 °F (-10 to +60 °C)

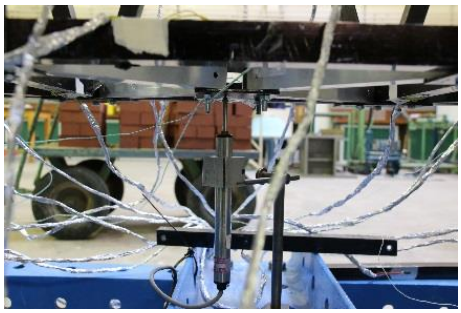

(a). DT1 (middle span)

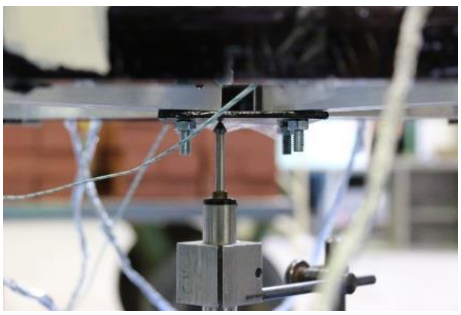

(b). DT2

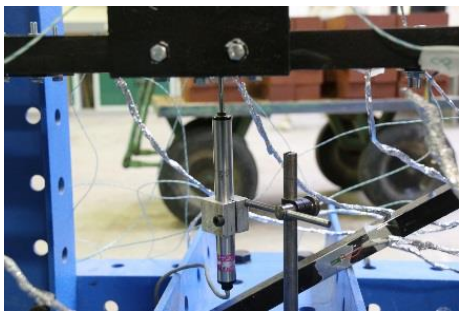

(c). DT3

Figure A.1. Photo of displacement setup

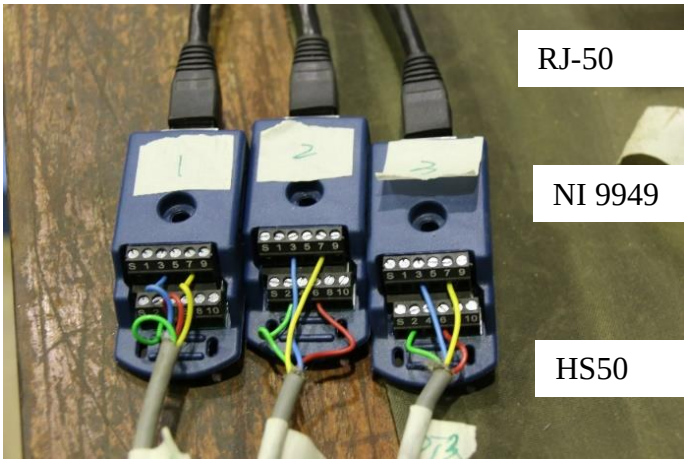

Figure A.2. Displacement sensor connection

Table A.7.3. Connection between NI 9949 and HS50

HS50 (4-RJ-50 inputs)	**NI 9949**	
	Number	**Port**
Red	6	EX+
Blue	3	AI-
Green	2	AI+
Yellow	7	EX-

After setup the connection, all displacement sensors should be calibrated before collecting data. The progress of displacement calibration are as follows.

- Data collected by using gauges blocks, ranging from 3mm to 30 mm for 3 times, seeing Figure A.3. The deformation towards the floor is assumed as negative, hence the measurements of displacements are all negative.
- Allow data collection for 10 seconds for each gauge condition.
- Calculating the average values for each gauge of each displacement.
- Using MATLAB to do curve fitting to find the linear relation between strain and displacement. As shown in Figure A.4, X-axis is the measuring strain data, while Y-axis represents displacement. Therefore, the displacement value can then be obtained by transferring strain measurement into displacement according to their linear relation. The parameters of this linear relation can be found in Table A.7.4.

(a). DG2 with 3 mm gauge block (b). DT1 with 30 mm gauge block

Figure A.3. Schematic diagram of displacement calibration

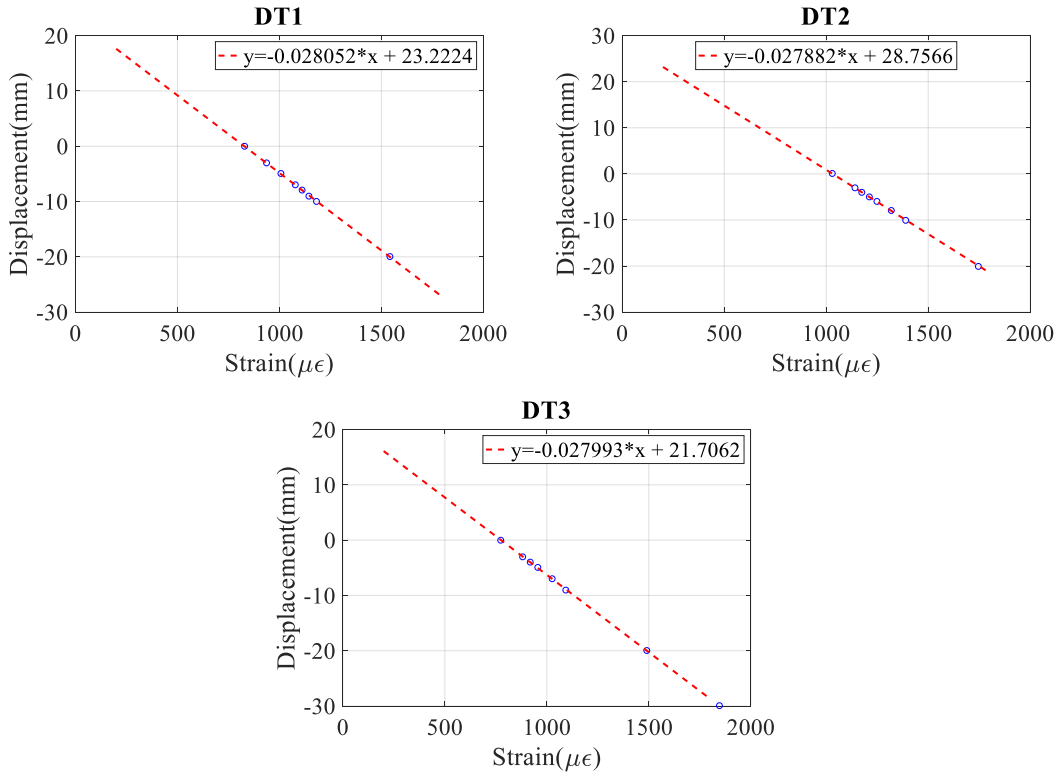

Figure A.4. Displacement calibration results

Table A.7.4. Calibration results

	Slope: a		Offset: b
	$\mu\epsilon\ vs.mm$	$\epsilon\ vs.mm$	$\mu\epsilon\ vs.mm$ / $\epsilon\ vs.mm$
DT1	-0.028052	-28052.10298	23.222439
DT2	-0.027882	-27882.07695	28.756631
DT3	-0.027993	-27993.04718	21.706211

A.1.2 Strain gauges

The strain gauges used here is TML FLAB-6-23 (Tokyo Sokki Kenkyujo, n.d.), which is purchased from Techni Measure. The strain gauges installation process placement can be summarized as follows.

- Burnish the surface by using sand paper P120 first, and finish with P400 with water, seeing Figure A.5(a).
- Clean the surface by using Acetone. Careful with plastic items.
- Glue the strain gauges and terminals on the target position.
- Soldering the wires with strain gauges through the terminals, seeing Figure A.5(b).
- Check and test. The lead wire should not be attached on the surface of the chord. The resistance between two terminals should be 120 Omh. Using NI MAX software to check the stability of strain gauges again before installing on the bridge, seeing Figure A.5 (c), (d).

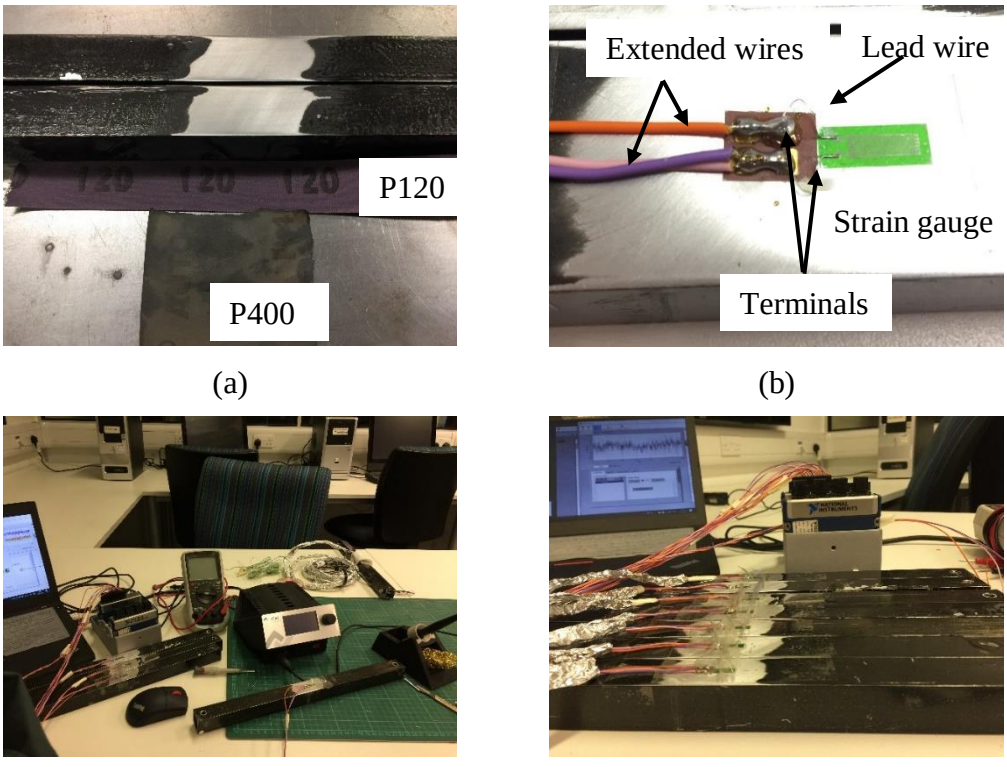

(a) (b)

(c) (d)

Figure A.5. Strain gauges installation

A.1.3 Thermocouple

The thermocouple is from RS Components (RS Components, n.d.), which is easily attached on the surface of element, seeing Figure A.6.

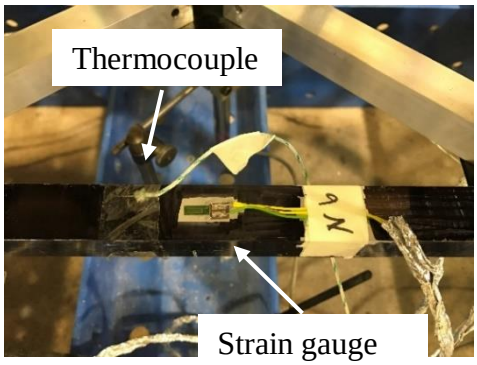

Figure A.6. Overview of thermocouple

A.2. Heating system

The heating system is described in Figure A.7.

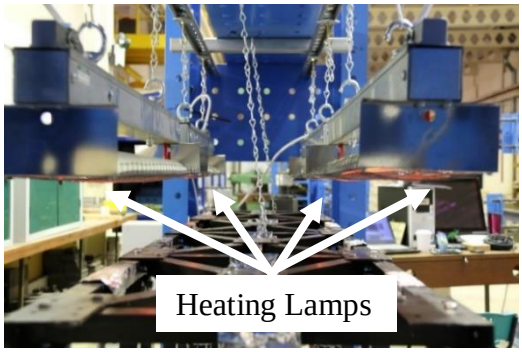

(a). Heating lamps

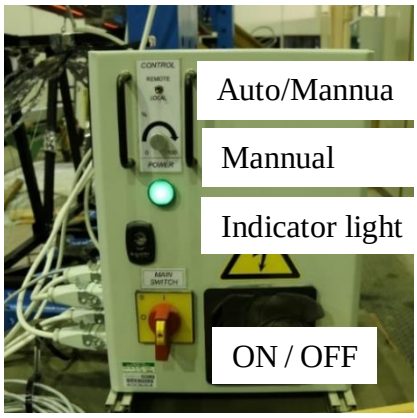

(b). Power supply control 1

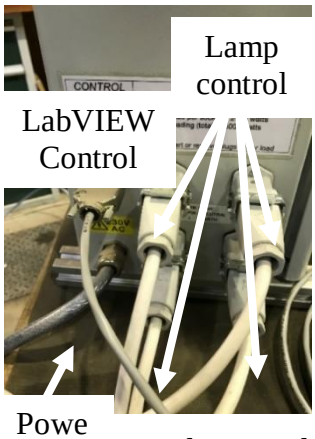

(c). Power supply control 2

Figure A.7. Heating system description

Appendix B. Truss bridge design drawings

ITEM NO.	PART NAME	DESCRIPTION	QTY.
1	Box Section Beam LONG	sheet 7 of 8	20
2	Bracket	sheet 4 of 8	18
3	Box Section Beam SHORT	sheet 3 of 8	36
4	Gusset Plate	sheet 5 of 8	22
5	Box Section Beam MEDIUM	sheet 6 of 8	29
6	Bolt	6mm diameter bolt	240
7	Gusset Plate for Pin Supports	Similar to item no. 3 but with additional 20mm diameter hole sheet 8 of 8	4

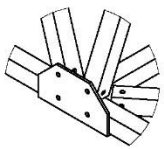

DETAIL V
SCALE 1 : 5

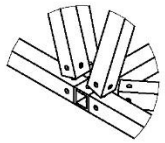

DETAIL W
SCALE 1 : 5

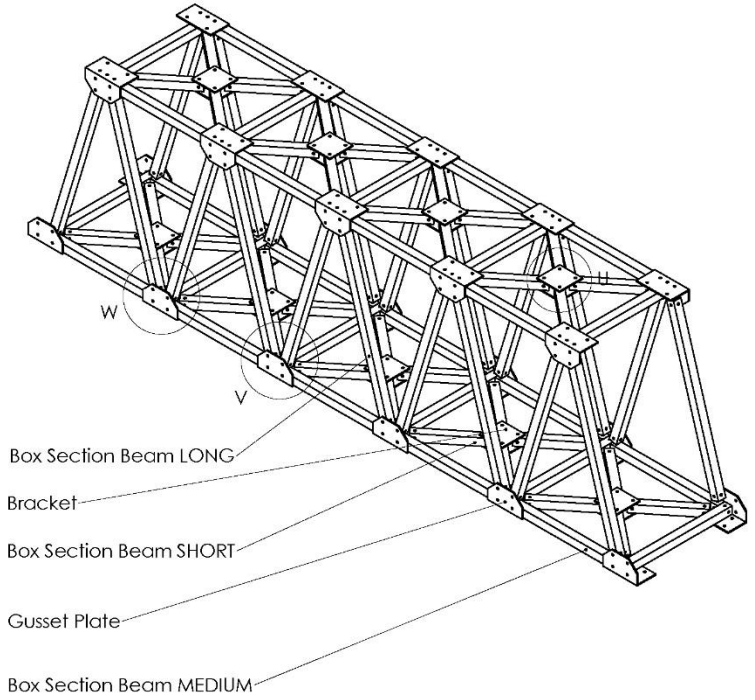

4 Box Section Beams (SHORT) bolted to 2 bracket lying parallel to each other

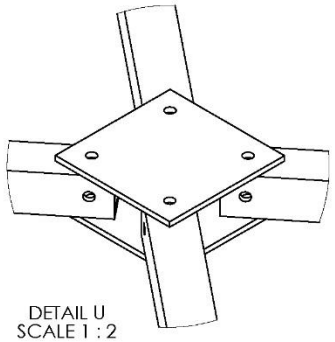

DETAIL U
SCALE 1 : 2

UNLESS OTHERWISE SPECIFIED: DIMENSIONS ARE IN MILLIMETERS SURFACE FINISH: TOLERANCES: LINEAR: ANGULAR:			FINISH:			DEBUR AND BREAK SHARP EDGES	DO NOT SCALE DRAWING	REVISION
	NAME	SIGNATURE	DATE					
DRAWN	H. Abdulkarim		25/11/14				TITLE: DETAILS & BILL OF MATERIALS	
CHK'D								
APP'VD								
MFG								
Q.A				MATERIAL:			DWG NO. ES327	A3
				WEIGHT:			SCALE:1:1	SHEET 1 OF 8

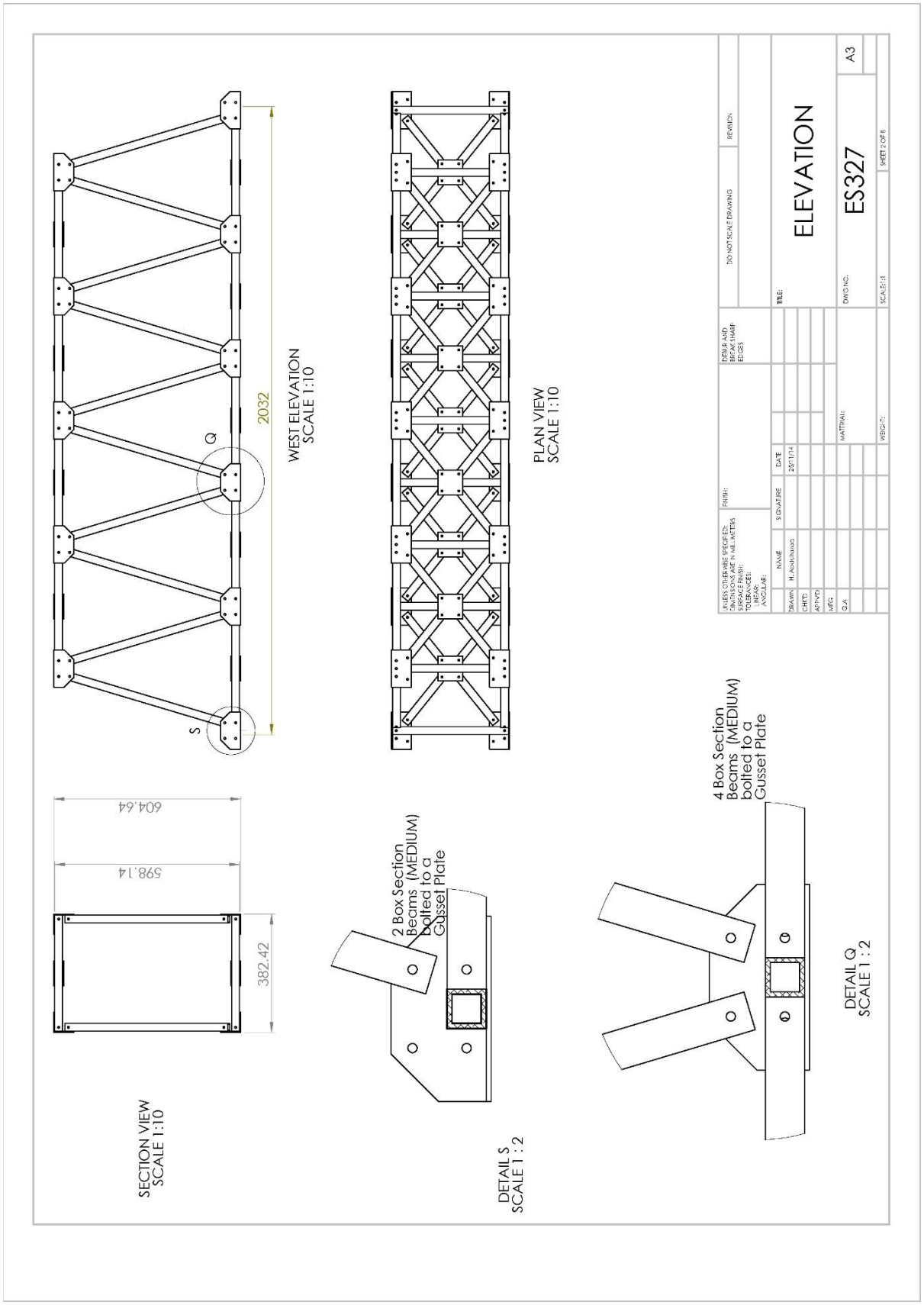
WEST ELEVATION
SCALE 1:10
2032
Q
S
PLAN VIEW
SCALE 1:10
SECTION VIEW
SCALE 1:10
604.64
598.14
382.42
DETAIL S
SCALE 1 : 2
2 Box Section
Beams (MEDIUM)
bolted to a
Gusset Plate
DETAIL Q
SCALE 1 : 2
4 Box Section
Beams (MEDIUM)
bolted to a
Gusset Plate
ELEVATION
ES327
A3

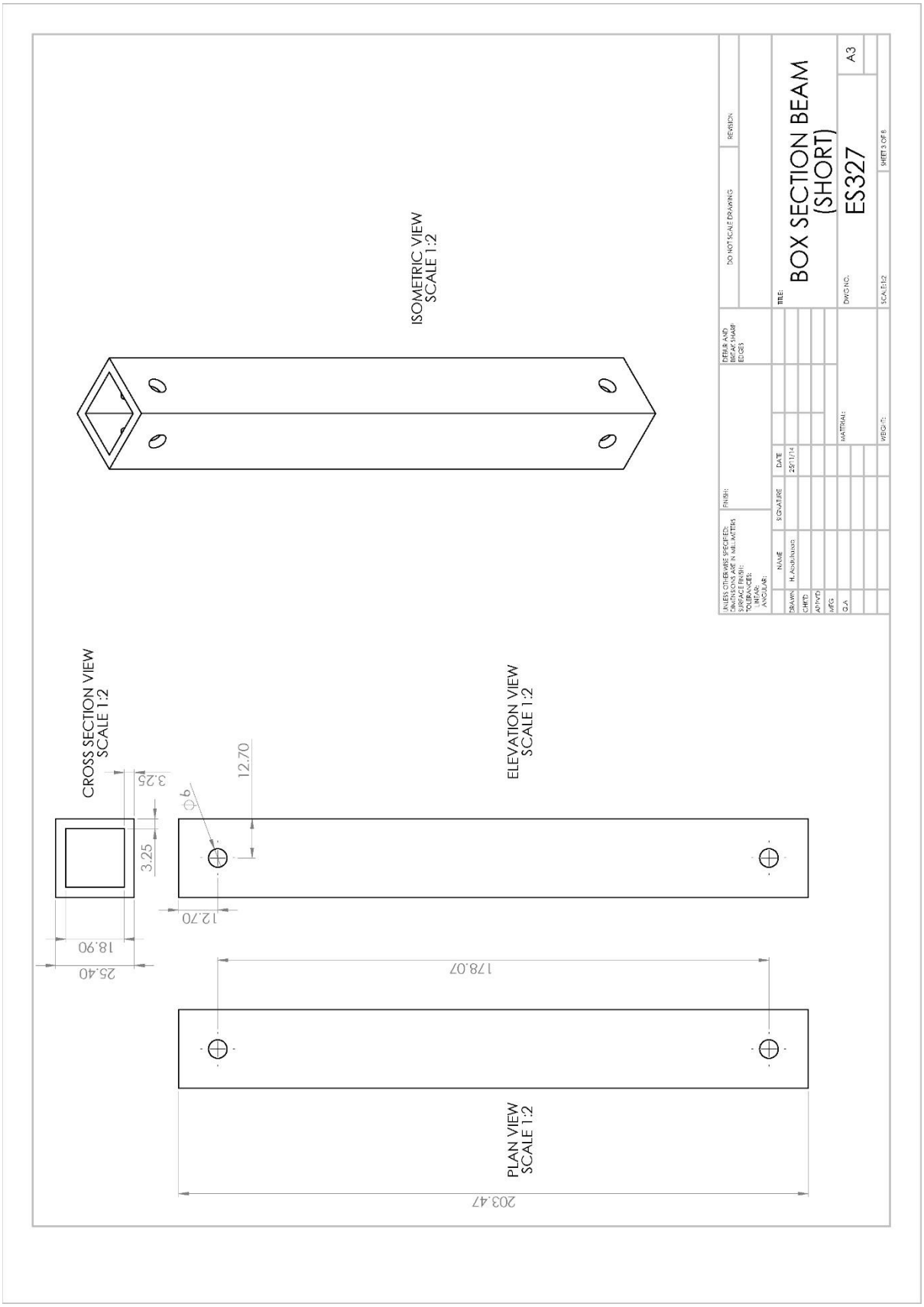
ISOMETRIC VIEW
SCALE 1:2
CROSS SECTION VIEW
SCALE 1:2
ELEVATION VIEW
SCALE 1:2
PLAN VIEW
SCALE 1:2
3.25
3.25
Φ6
12.70
12.70
18.90
25.40
178.07
203.47
BOX SECTION BEAM
(SHORT)
ES327
A3
DO NOT SCALE DRAWING
REVISION
UNLESS OTHERWISE SPECIFIED:
DIMENSIONS ARE IN MILLIMETERS
SURFACE FINISH:
TOLERANCES:
LINEAR:
ANGULAR:
FINISH:
DEBUR AND
BREAK SHARP
EDGES
NAME
SIGNATURE
DATE
DRAWN
H. Abdulkarim
29/7/14
CHK'D
APP'D
MFG
Q.A
MATERIAL:
WEIGHT:
SCALE:1:2
SHEET 3 OF 8

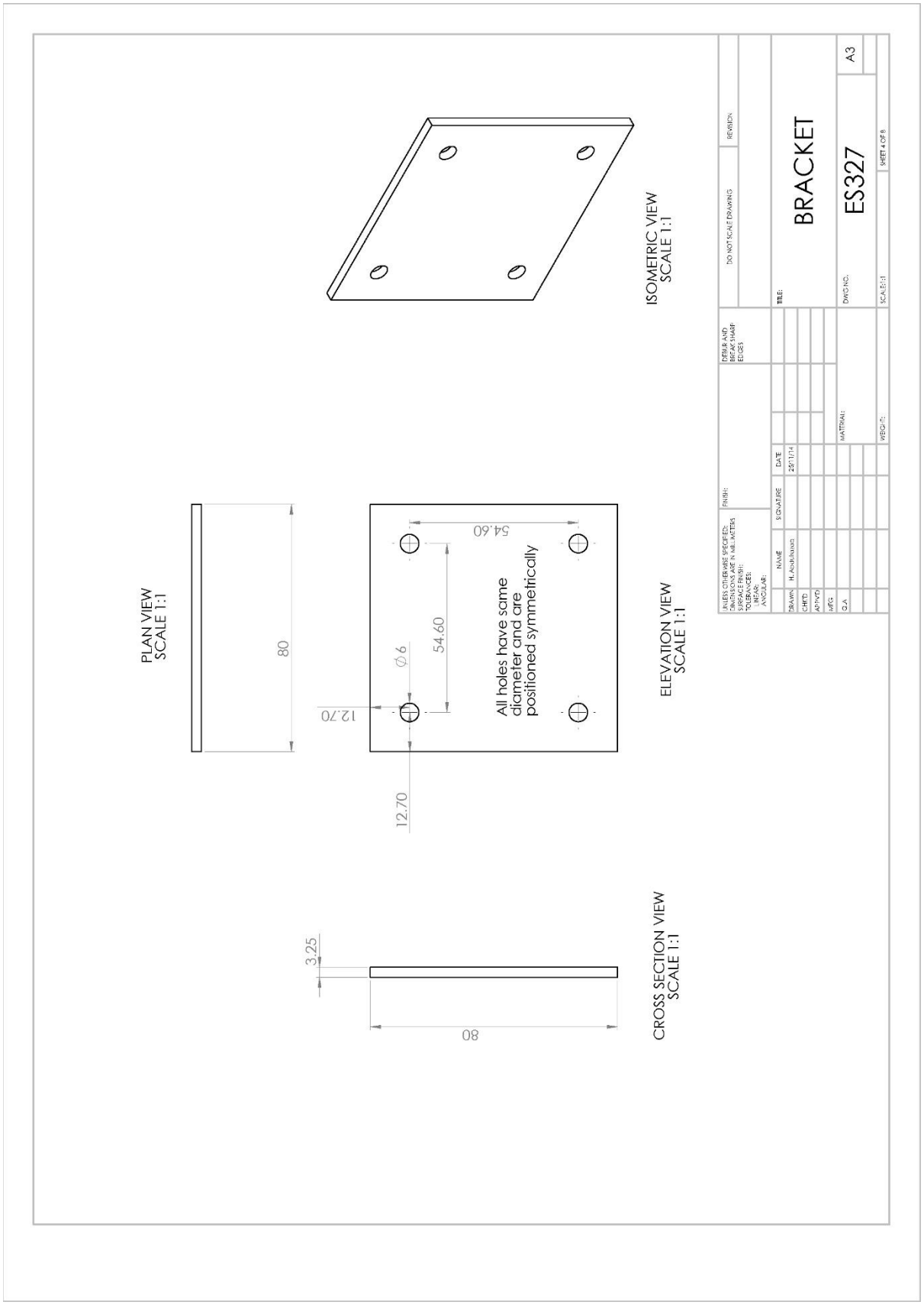
ISOMETRIC VIEW
SCALE 1:1
PLAN VIEW
SCALE 1:1
80
ELEVATION VIEW
SCALE 1:1
54.60
Ø6
54.60
12.70
12.70
All holes have same diameter and are positioned symmetrically
CROSS SECTION VIEW
SCALE 1:1
3.25
80
UNLESS OTHERWISE SPECIFIED:
DIMENSIONS ARE IN MILLIMETERS
SURFACE FINISH:
TOLERANCES:
LINEAR
ANGULAR
FINISH:
NAME
SIGNATURE
DATE
DRAWN
H. Abdulkarim
29/7/14
CHK'D
APP'D
MFG
Q.A
MATERIAL:
WEIGHT:
REMOVE ALL BURR AND BREAK ALL SHARP EDGES
DO NOT SCALE DRAWING
REVISION
TITLE:
BRACKET
DWG NO.
ES327
A3
SCALE:1:1
SHEET 4 OF 8

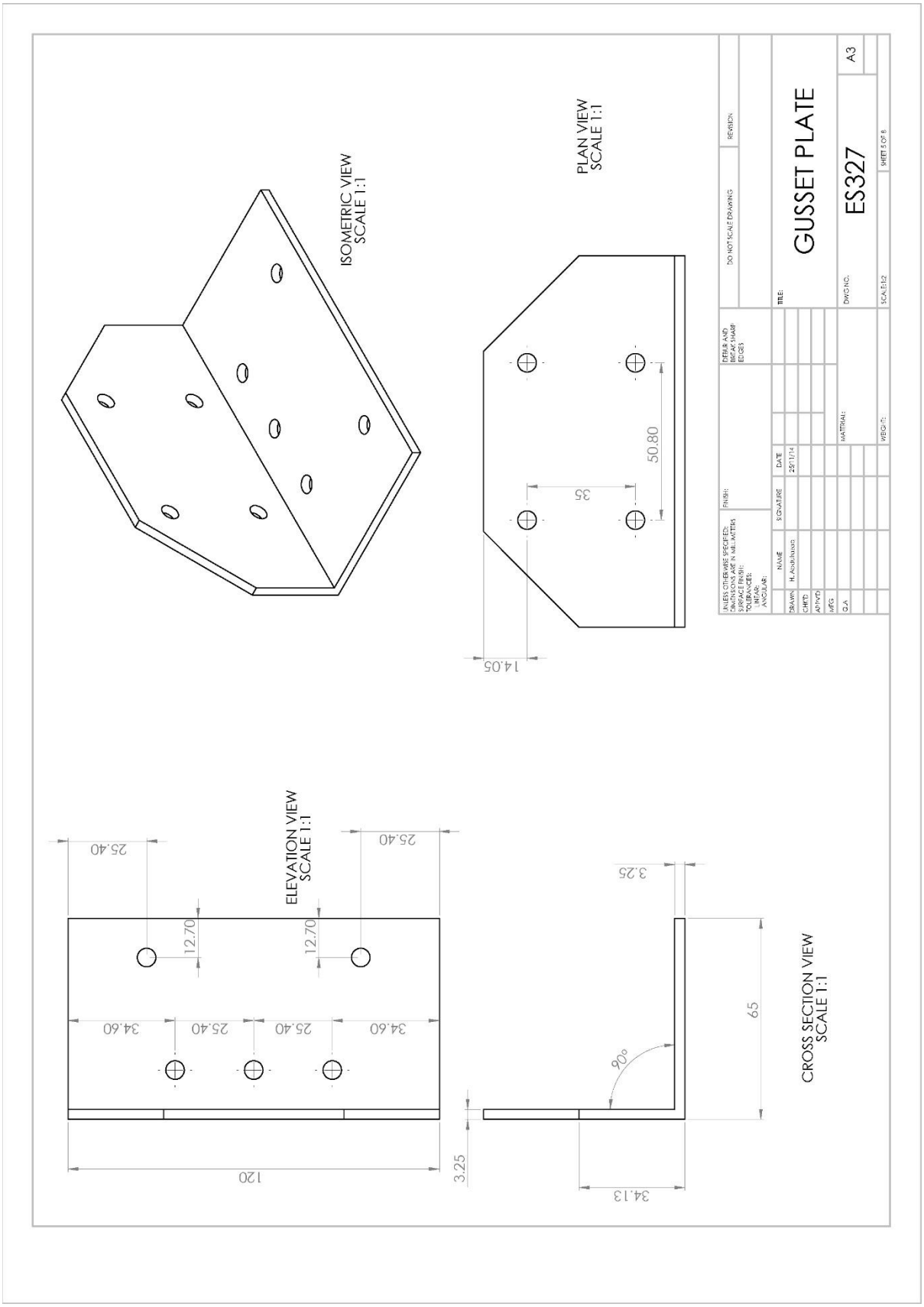
ISOMETRIC VIEW
SCALE 1:1
PLAN VIEW
SCALE 1:1
ELEVATION VIEW
SCALE 1:1
CROSS SECTION VIEW
SCALE 1:1
GUSSET PLATE
ES327
A3
DO NOT SCALE DRAWING
REVISION
TITLE:
DWG NO.
MATERIAL
WEIGHT:
SCALE:1:2
SHEET 5 OF 8
DRAWN
H. Abdulkarim
CHK'D
APP'D
MFG
Q.A
NAME
SIGNATURE
DATE
29/7/14
FINISH:
DEBUR AND BREAK SHARP EDGES
UNLESS OTHERWISE SPECIFIED:
DIMENSIONS ARE IN MILLIMETERS
SURFACE FINISH:
TOLERANCES:
LINEAR:
ANGULAR:
50.80
35
14.05
25.40
25.40
12.70
12.70
34.60
25.40
25.40
34.60
120
3.25
3.25
65
90°
34.13

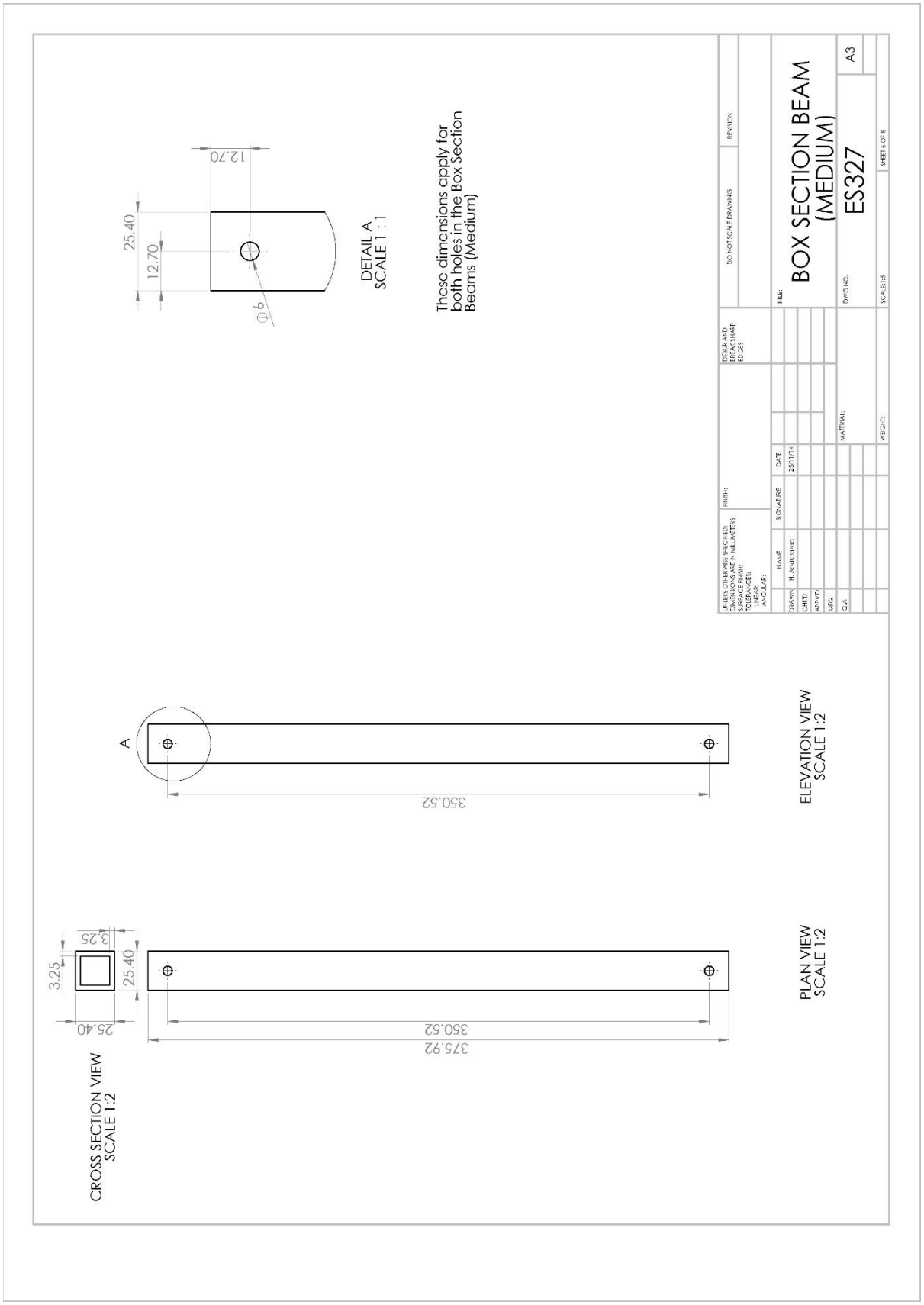
12.70
25.40
12.70
Φ6
DETAIL A
SCALE 1 : 1
These dimensions apply for both holes in the Box Section Beams (Medium)
A
350.52
ELEVATION VIEW
SCALE 1:2
3.25
3.25
25.40
25.40
375.92
350.52
CROSS SECTION VIEW
SCALE 1:2
PLAN VIEW
SCALE 1:2
UNLESS OTHERWISE SPECIFIED:
DIMENSIONS ARE IN MILLIMETERS
SURFACE FINISH:
TOLERANCES:
LINEAR
ANGULAR
FINISH:
DEBUR AND BREAK SHARP EDGES
NAME
SIGNATURE
DATE
DRAWN
H. Abdulkarim
29/7/14
CHK'D
APP'D
MFG
Q.A
MATERIAL:
WEIGHT:
DO NOT SCALE DRAWING
REVISION
TITLE:
BOX SECTION BEAM (MEDIUM)
DWG NO.
ES327
A3
SCALE:1:5
SHEET 1 OF 8

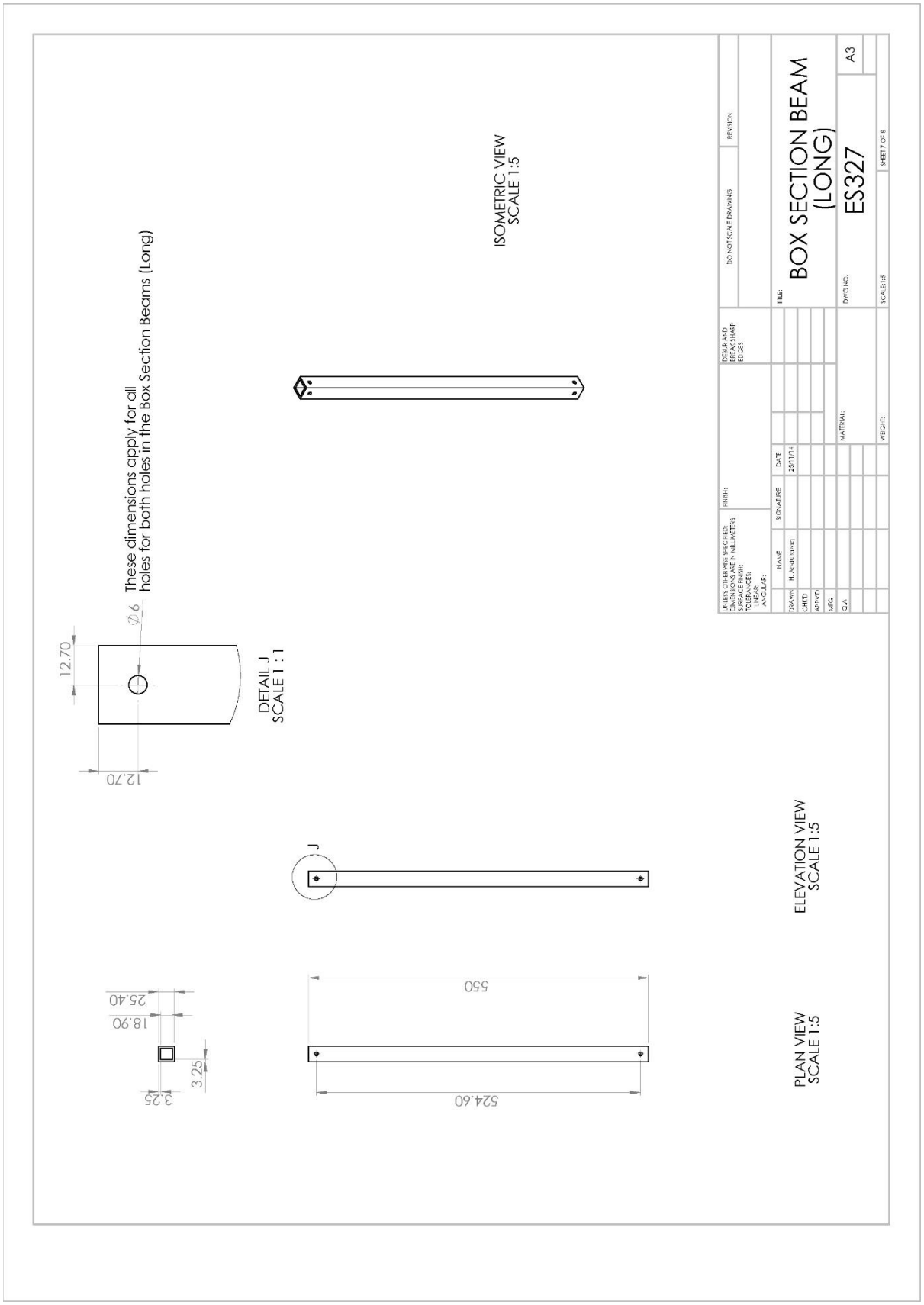
These dimensions apply for all holes for both holes in the Box Section Beams (Long)
ISOMETRIC VIEW SCALE 1:5
DETAIL J SCALE 1 : 1
ELEVATION VIEW SCALE 1:5
PLAN VIEW SCALE 1:5
BOX SECTION BEAM (LONG)
ES327
A3
DO NOT SCALE DRAWING
REVISION
UNLESS OTHERWISE SPECIFIED: DIMENSIONS ARE IN MILLIMETERS SURFACE FINISH: TOLERANCES: LINEAR: ANGULAR:
FINISH:
DEBUR AND BREAK SHARP EDGES
NAME
SIGNATURE
DATE
DRAWN H. Abdulkarim 29/11/14
CHK'D
APP'D
MFG
Q.A
MATERIAL:
WEIGHT:
SCALE:1:5
SHEET 7 OF 8
550
524.60
25.40
18.90
3.25
12.70
Ø6

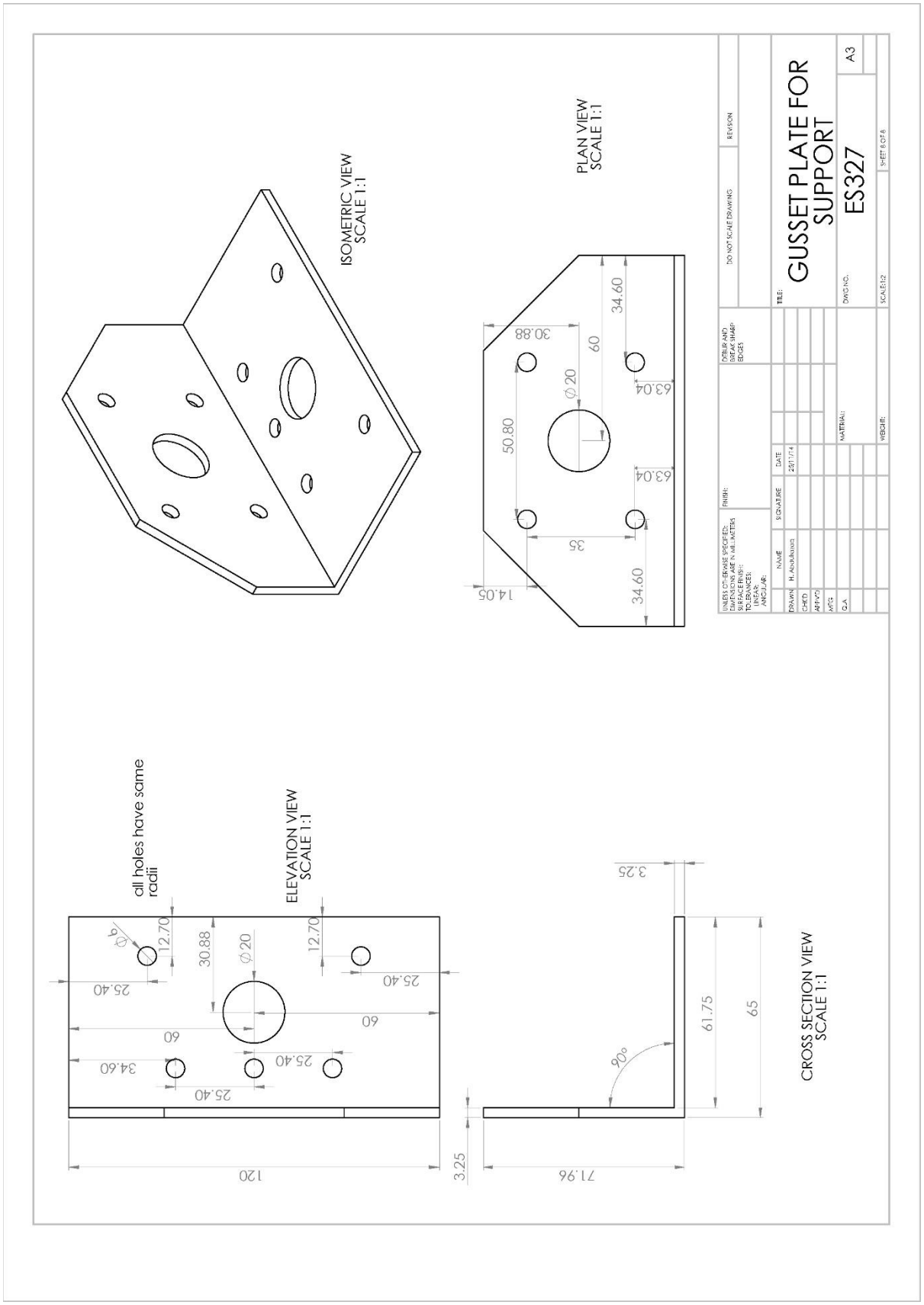
ISOMETRIC VIEW
SCALE 1:1
PLAN VIEW
SCALE 1:1
ELEVATION VIEW
SCALE 1:1
all holes have same radii
CROSS SECTION VIEW
SCALE 1:1
GUSSET PLATE FOR SUPPORT
ES327
A3
DO NOT SCALE DRAWING
REVISION
UNLESS OTHERWISE SPECIFIED:
DIMENSIONS ARE IN MILLIMETERS
SURFACE FINISH:
TOLERANCES:
LINEAR
ANGULAR
FINISH:
DEBURR AND BREAK SHARP EDGES
NAME
SIGNATURE
DATE
DRAWN
H. Abdulkarim
2/01/14
CHK'D
APP'D
MFG
Q.A
MATERIAL:
WEIGHT:
SCALE:1:2
SHEET 1 OF 1
DWG NO.
TITLE:

Appendix C. Laboratory case study for anomaly detection

This appendix presents the additional anomaly detection results of Td-MPCA, Td-RRA, in Section 6.2 of CHAPTER 6.

C.1. Td-MPCA detection results

The data interpretation on sensor group 2, 3, 4, and 5 are presented here to support the outcomes listed in Table 6.7 and Table 6.8. Two damage conditions, DS-1 and DS-2, are considered in this study.

C.1.1 Td-MPCA on group 2 sensors

The group 2 sensors are on bottom transversal chords including SG11, SG12, SG13 and SG14. The loading conditions consist by temperature variations and moving loadings. For the first damage condition, DS-1, the measurements with zero mean value are presented in Figure C.8, while Figure C.9 shows the measurements under the second damage condition, DS-2. Since the group 2 sensors are heavily affected by the moving loads, explanations are given based on the first damage condition, as follows:

- The frequency of moving load variations is controlled as two times of temperature variations. As displayed in Figure C.8 (a), three periodic temperature variations are conducted in this test. Thus, six periodic traffic-induced fluctuations can be observed in Figure C.8 (b, c).

- The positive tendency can be observed between SG13 and 14 measurements in Figure C.8 (b), while the negative trend between SG11 and 13 in Figure C.8 (c). Since the SG11 and12 are adjacent, the positive correlation should also be observed between SG11 and 12. However, Figure C.8 (d) shows that some unexpected negative trends are existed between SG11 and 12, which have been outlined. Those unexpected periods are due to the inevitable operations during the test, when the dumbbell cannot stay at the expected position before this was solved manually. This operation error was only happened when the dumbbell was passing SG11 and SG12.
- The damage induced variations are not visible in this group of sensors, which is because those transversal chords are very sensitive to moving loadings.

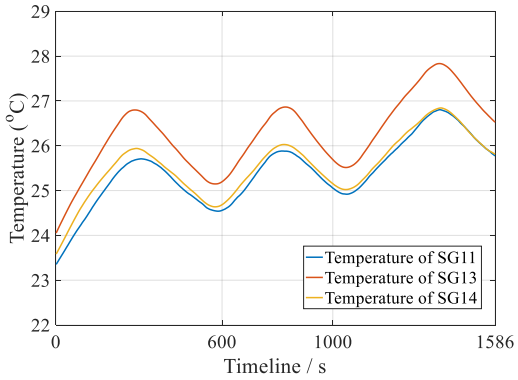

(a). Temperature records

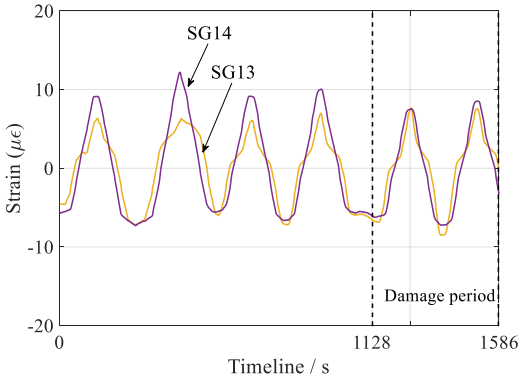

(b). SG13 and SG14

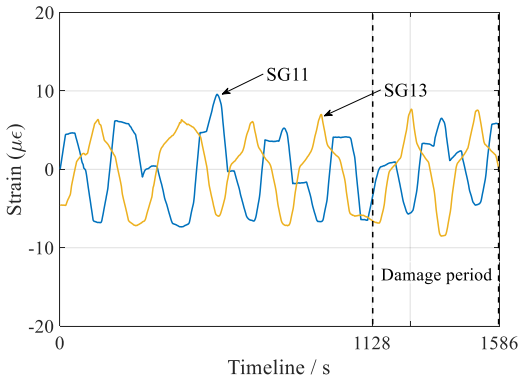

(c). SG11 and SG13

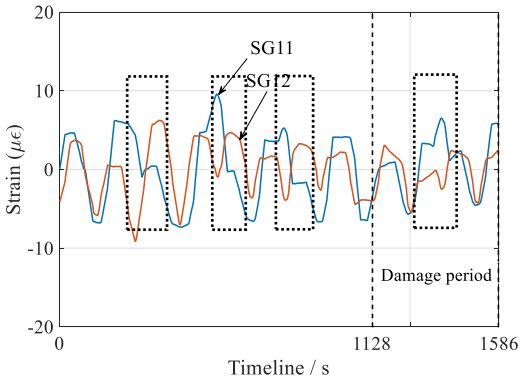

(d). SG11 and SG12

Figure C.8. Group 2: Measurements with damage scenario 1 (DS-1)

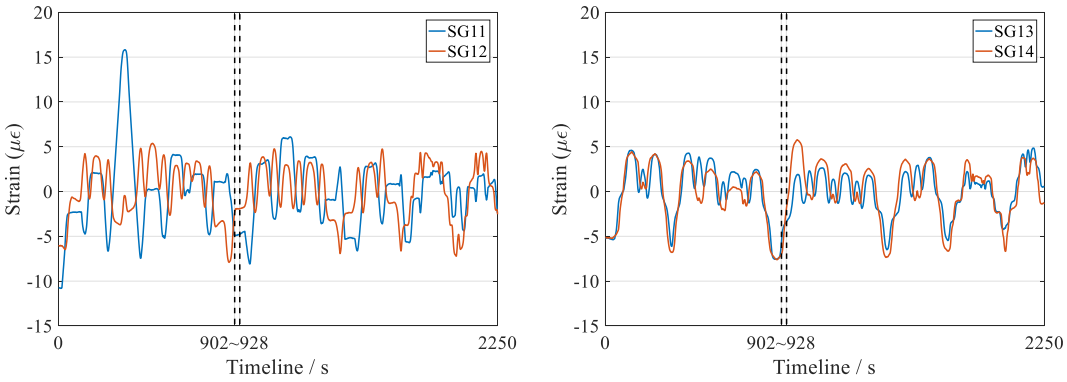

(a). SG11 and SG12 (b). SG13 and SG14

Figure C.9. Group 2: Measurements with damage scenario 1 (DS-2)

The detection results by Td-MPCA to uncover DS-1 are then given in Figure C.10(a). The window size is still 1~1.5 times of temperature variations (570s). The detection is start from 286 seconds to avoid the boundary effect due to ICA separation. The alarm is 36s early than expected time, however, a relative flat can be obvious during damage introduced period, if compared with reference period. Hence, the detection by Td-MPCA on transversal direction chords on the bottom is judged as success with 36s early.

The application of MPCA and Td-MPCA are both employed for detecting DS-2, as showing in Figure C.11. The improvement of Td-MPCA is conspicuous, as the MPCA could indicate the exceeding status but the uncertainty existed in the beginning shows the unstable performance of MPCA.

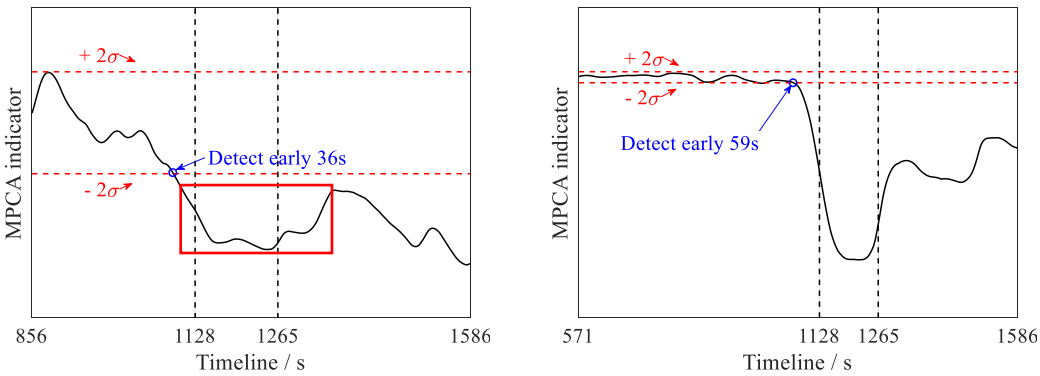

(a). Td-MPCA directly (b). MPCA directly

Figure C.10. Group 2: Td-MPCA and MPCA detection results under DS-1

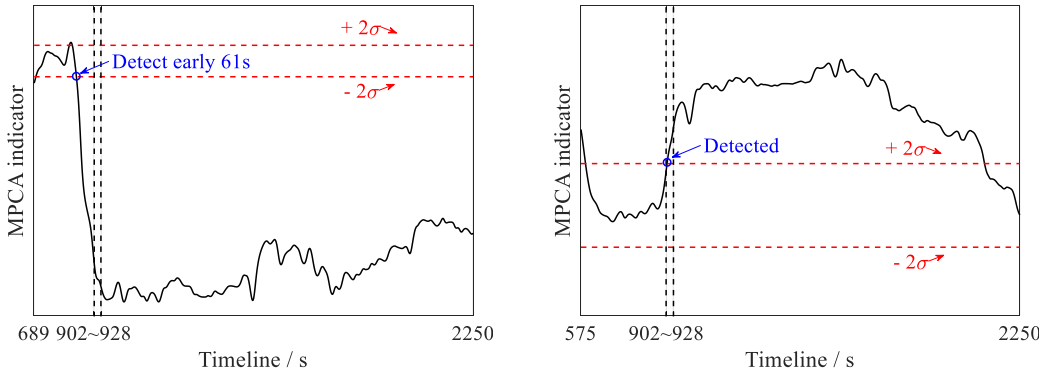

(a). Td-MPCA directly (b). MPCA directly

Figure C.11. Group 2: Td-MPCA and MPCA detection results under DS-2

C.1.2 Td-MPCA on group 3 sensors

The group 3 sensors are on the top longitudinal chords, including SG16, SG18, SG20 and SG22. The measurements with zero mean value are presented in Figure C.12 under temperature and traffic loadings conditions.

There has no sign of damage or moving dumbbell's effect because the top chords are more sensitive to the temperature variations, since the heating lamps are just at the top of the truss. The unstable condition of SG20 is evident in Figure C.12(b), hence the subsequent detection process will exclude it. The detection processes by employing Td-MPCA and MPCA are subsequently presented in Figure C.13 for DS-1 and Figure C.14 for DS-2.

For the case of DS-1, the successful detection is between 1128s and 1265s. It can be seen from Figure C.13(a) that the Td-MPCA can uncover the damage between 1128-1265 seconds. However, the MPCA cannot detect the damage if considering the evident variations at the beginning period, seeing Figure C.13(b). For the case of DS-2, the successful detection can be obtained by applying Td-MPCA during 902-928 seconds, seeing Figure C.14(a), while a 60s early alarm can be observed by MPCA in Figure C.14(b).

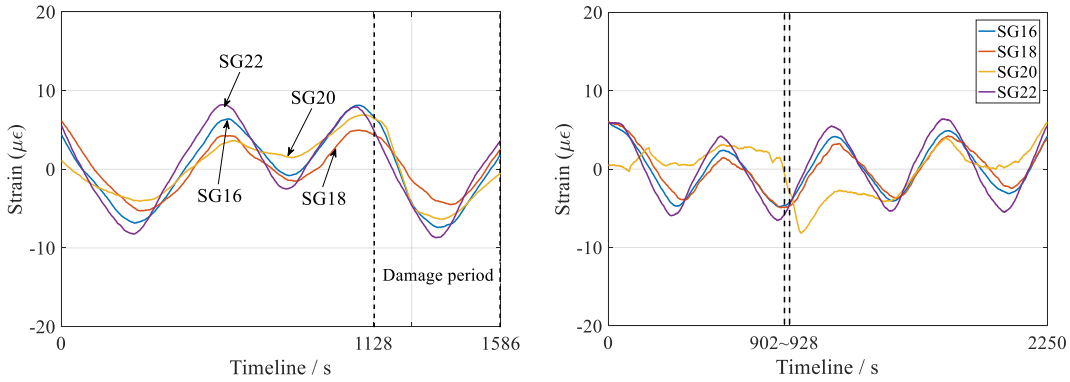

(a). Group 3 measurements under DS-1 (b). Group 3 measurements under DS-2

Figure C.12. Group 3: Measurements with damage scenarios (DS-1 and DS-2)

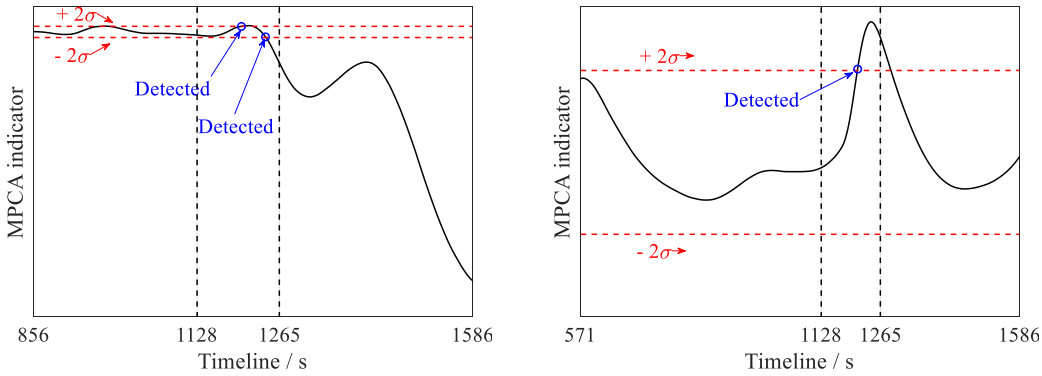

(a). Td-MPCA (b). MPCA directly

Figure C.13. Group 3: Td-MPCA and MPCA detection results under DS-1

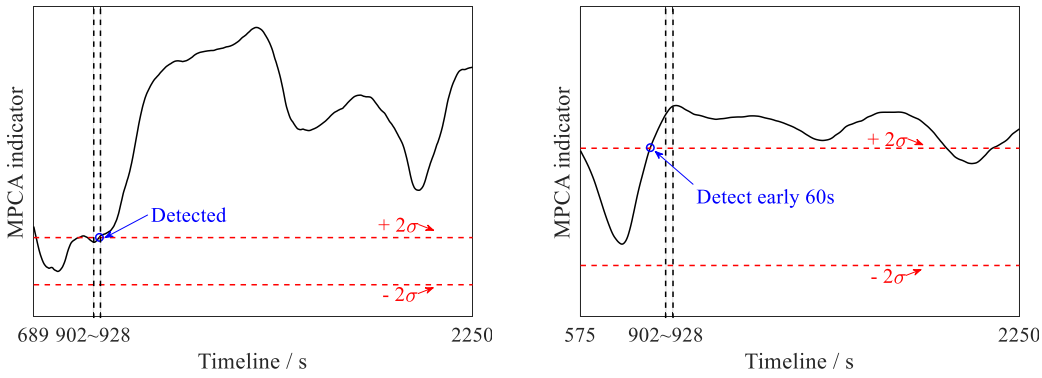

(a). Td-MPCA (b). MPCA directly

Figure C.14. Group 3: Td-MPCA and MPCA detection results under DS-2

C.1.3 Td-MPCA on group 4 sensors

The group 4 sensors are on the top transversal chords, including SG23, SG24, SG25, SG26 and SG27. The measurements with zero mean value are presented in Figure C.15 under temperature and traffic loadings conditions.

The damage is slightly obvious in the measurements of SG26, but the moving load variations cannot be observed in time-history records, since those sensors are close to heating lamps on the top.

The damage detections by applying MPCA and Td-MPCA, are presented in Figure C.16 for damage condition 1 (DS-1) and in Figure C.17 for damage condition 2 (DS-2).

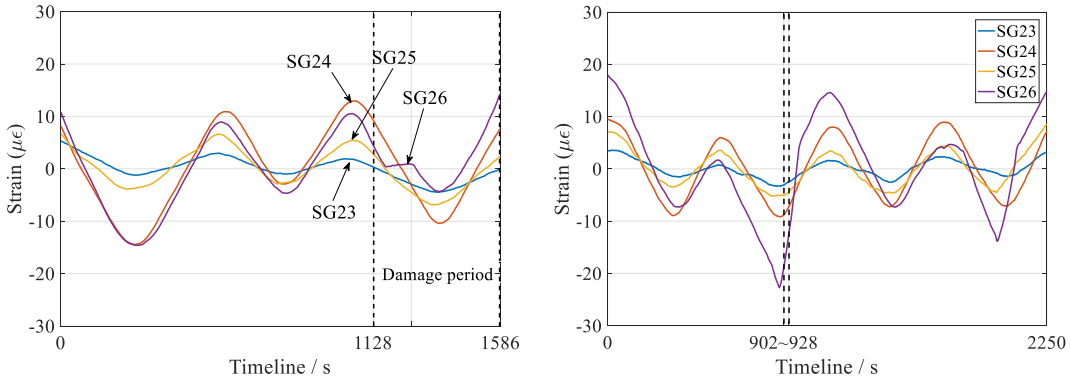

(a). Group 4 measurements under DS-1 (b). Group 4 measurements under DS-2

Figure C.15. Group 4: Measurements with damage scenarios (DS-1 and DS-2)

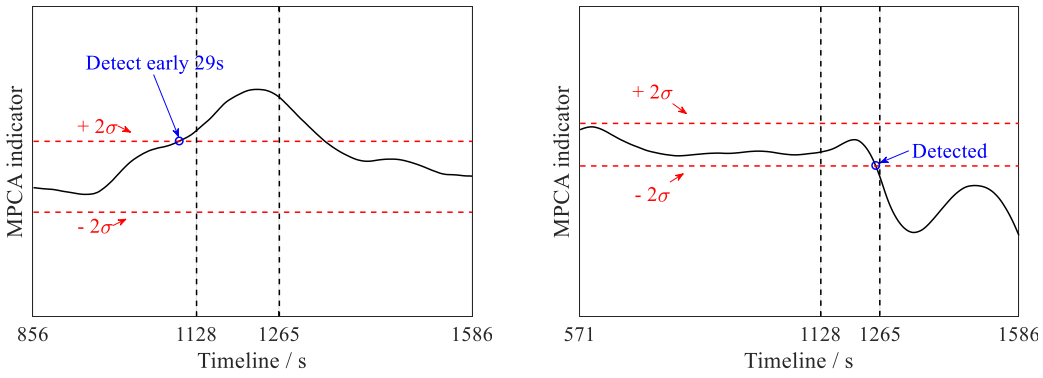

(a). Td-MPCA (b). MPCA directly

Figure C.16. Group 4: Td-MPCA and MPCA detection results under DS-1

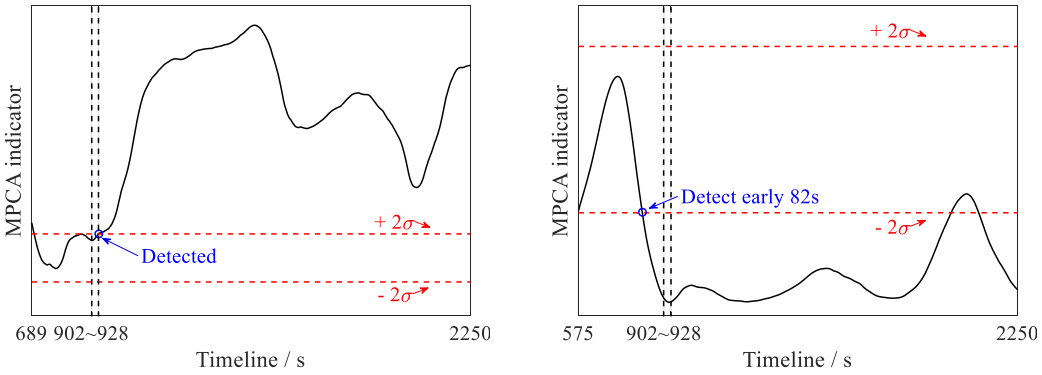

(a). Td-MPCA (b). MPCA directly

Figure C.17. Group 4: Td-MPCA and MPCA detection results under DS-2

Apparently, both attempts can disclose the anomalies, but with some uncertainties. In Figure C.16 for DS-1, the distinct swerve can be observed in MPCA application during 1128s and 1265s and the MPCA indicator is exceeding the threshold before 1265s, hence this detection is successful. However, the alarm given by Td-MPCA is early and the abnormal changes are not evident after DS-1 is introduced. Since the obvious swerve can be noticed during the damage introduced time (1128s-1265s). Therefore, both applications can be accepted as success detection for DS-1. For the other case of detecting DS-2, the outperformance of Td-MPCA is visible, since the MPCA gives an early warning.

C.1.4 Td-MPCA on group 5 sensors

The group 5 sensors are on side chords, including SG28, SG29, SG30 and SG31. The measurements with zero mean value are presented in Figure C.18 (under DS-1 effect) and in Figure C.19 (under DS-2 effect). The loading conditions include temperature and traffic loadings.

The damage detections by applying MPCA and Td-MPCA, are presented in Figure C.20 for damage condition 1 (DS-1). As shown in Figure C.20(b), the fake alarm is apparently which induce the failure detection of MPCA. However, the Td-MPCA could give a in time alarm, as showing in Figure C.20(a). To uncover the lighter damage condition, DS-2, the performance of Td-MPCA and MPCA are presented in Figure C.21(a) and (b) respectively. The detection results are not distinct enough with heavy uncertainties.

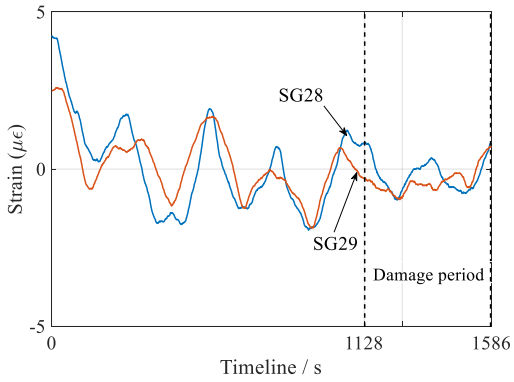

(a). SG28 and SG29 under DS-1

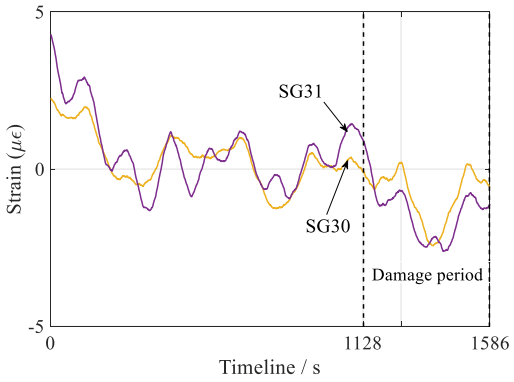

(b). SG30 and SG31 under DS-1

Figure C.18. Group 5: Measurements with damage scenario 1 (DS-1)

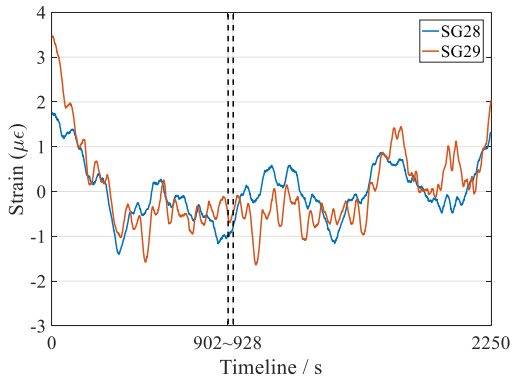

(a). SG28 and SG29 under DS-2

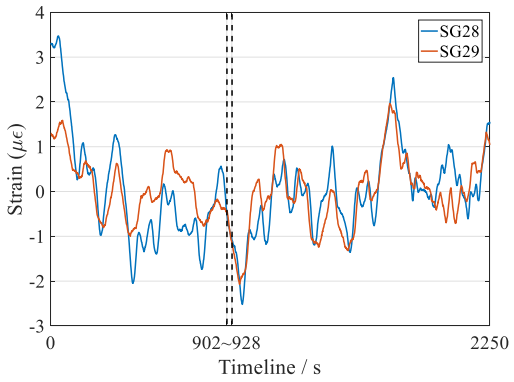

(b). SG30 and SG31 under DS-2

Figure C.19. Group 5: Measurements with damage scenario 2 (DS-2)

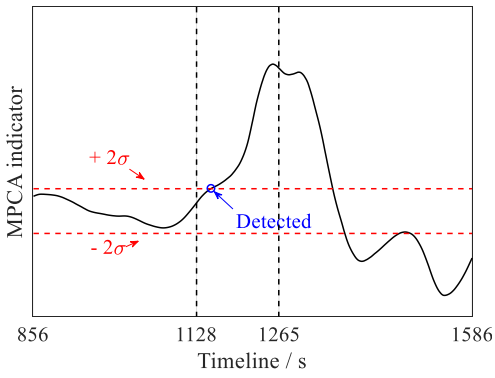

(a). Td-MPCA

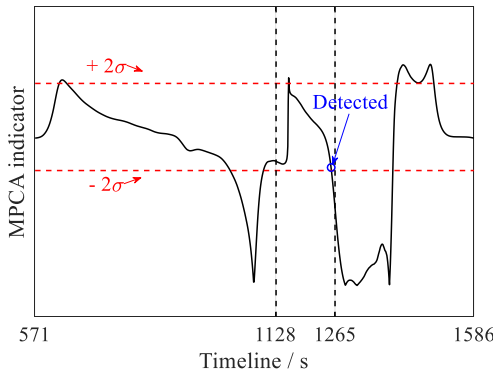

(b). MPCA directly

Figure C.20. Group 5: Td-MPCA and MPCA detection results under DS-1

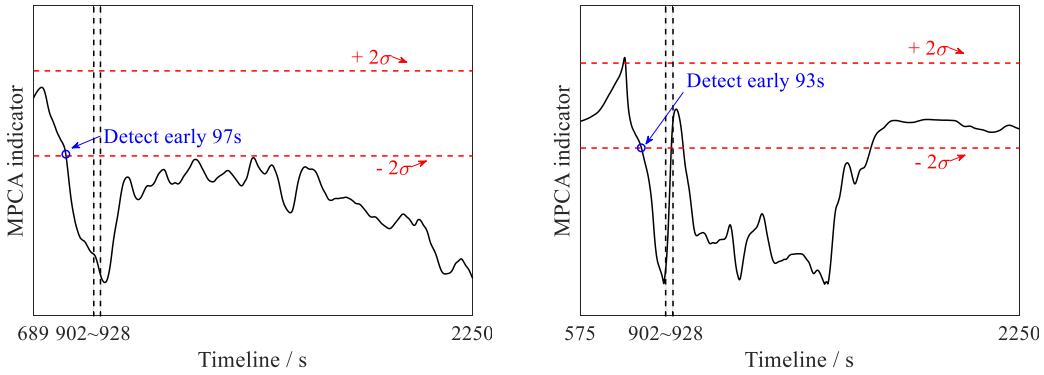

(a). Td-MPCA (b). MPCA directly

Figure C.21. Group 5: Td-MPCA and MPCA detection results under DS-2

C.2. Td-RRA detection results

In this section, the data interpretation on sensor group 2, 3, 4, and 5 are presented here to support the outcomes by Td-RRA that are listed in Table 6.11 and Table 6.12. Two damage conditions, DS-1 and DS-2, are considered in this study.

C.2.1 Td-RRA on group 2 sensors

The group 2 sensors include SG11, SG12, SG13, and SG14. The anomaly detections based on group 2 sensors are presented in following Figure C.22 and Figure C.23 for DS-1 and DS-2 respectively.

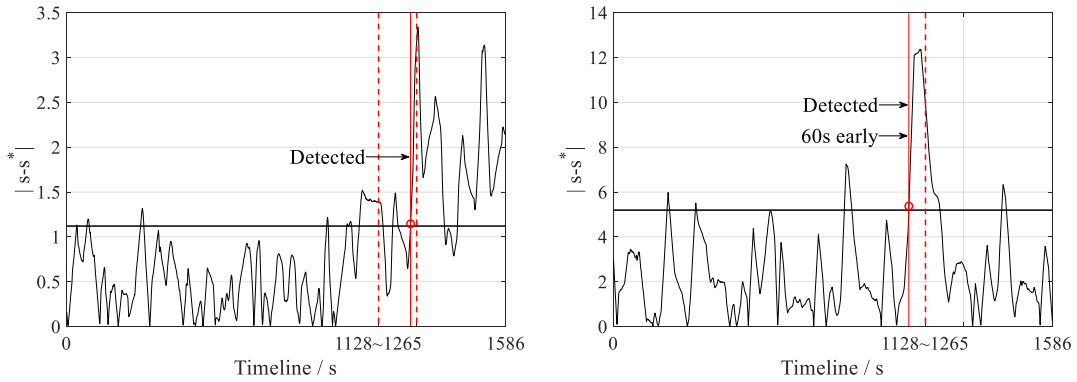

(a) Td-RRA detection results (b) RRA directly detection results

Figure C.22. Td-RRA and RRA detection results on group 2 sensors under DS-1

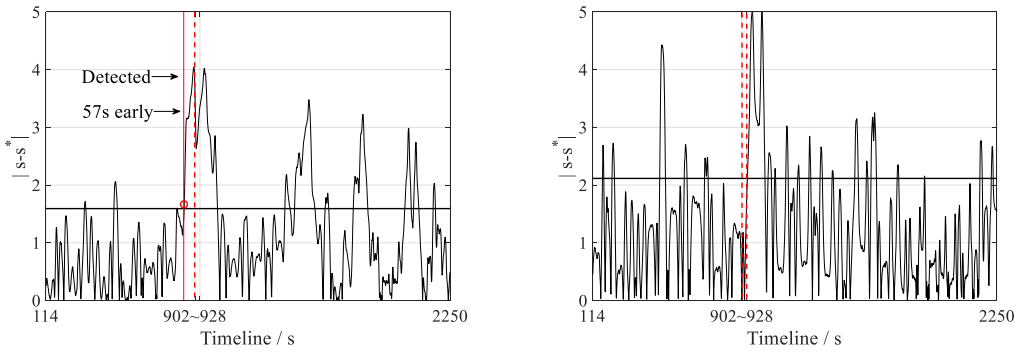

(a) Td-RRA detection results (b) RRA directly detection results

Figure C.23. Td-RRA and RRA detection results on group 2 sensors under DS-2

C.2.2 Td-RRA on group 3 sensors

The group 3 sensors include SG16, SG18, SG20, and SG22. The anomaly detections based on group 2 sensors are presented in following Figure C.24 and Figure C.25 for DS-1 and DS-2 respectively.

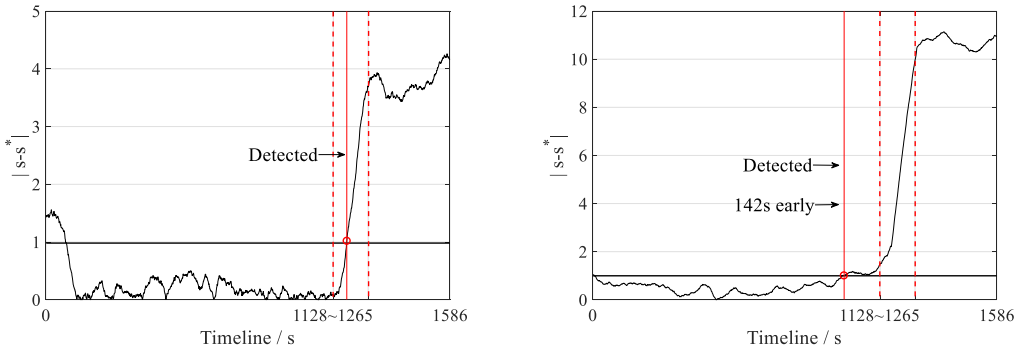

(a) Td-RRA detection results (b) RRA directly detection results

Figure C.24. Td-RRA and RRA detection results on group 3 sensors under DS-1

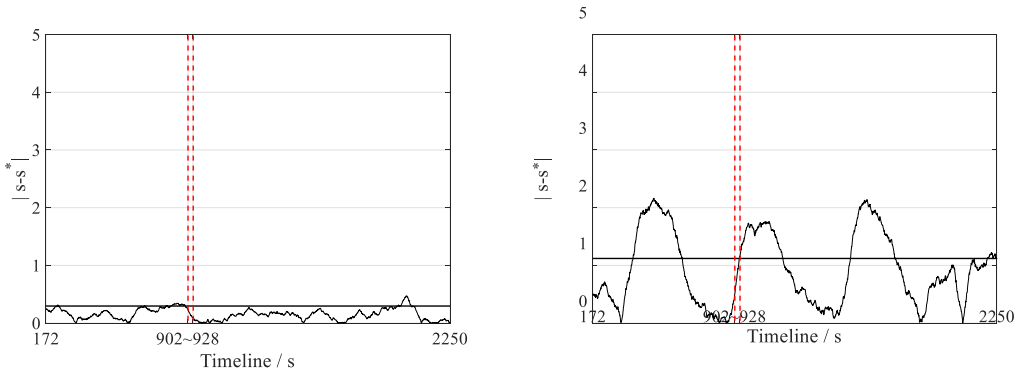

(a) Td-RRA detection results (b) RRA directly detection results

Figure C.25. Td-RRA and RRA detection results on group 3 sensors under DS-2

C.2.3 Td-RRA on group 4 sensors

The sensors in group 4 include SG23, SG24, SG25, and SG26. The anomaly detections based on group 2 sensors are presented in following Figure C.26 and Figure C.27 for DS-1 and DS-2 respectively.

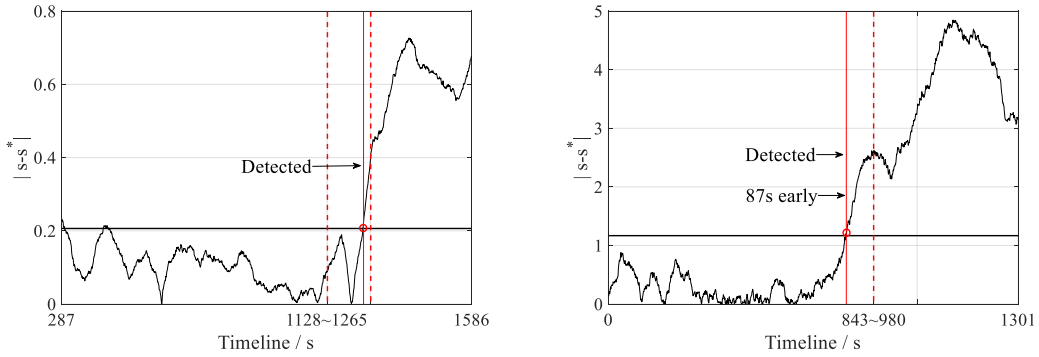

(a) Td-RRA detection results (b) RRA directly detection results

Figure C.26. Td-RRA and RRA detection results on group 4 sensors under DS-1

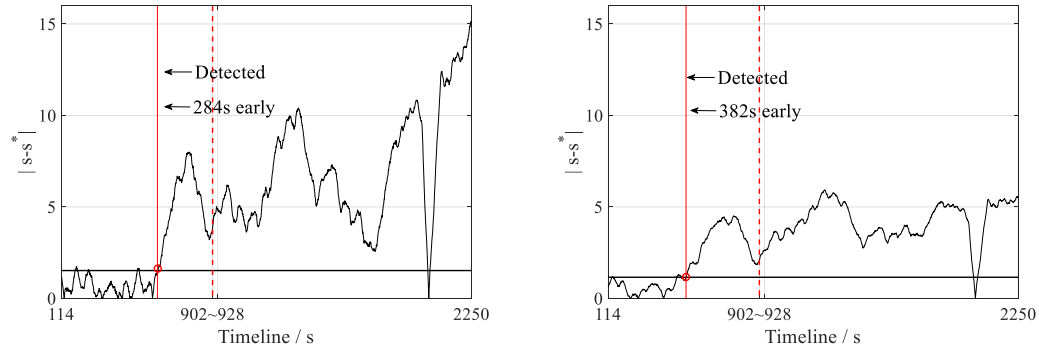

(a) Td-RRA detection results (b) RRA directly detection results

Figure C.27. Td-RRA and RRA detection results on group 4 sensors under DS-2

C.2.4 Td-RRA on group 5 sensors

The group 5 sensors include SG28, SG29, SG30, and SG31. The anomaly detections are presented in following Figure C.28 and Figure C.29 for DS-1 and DS-2 respectively.

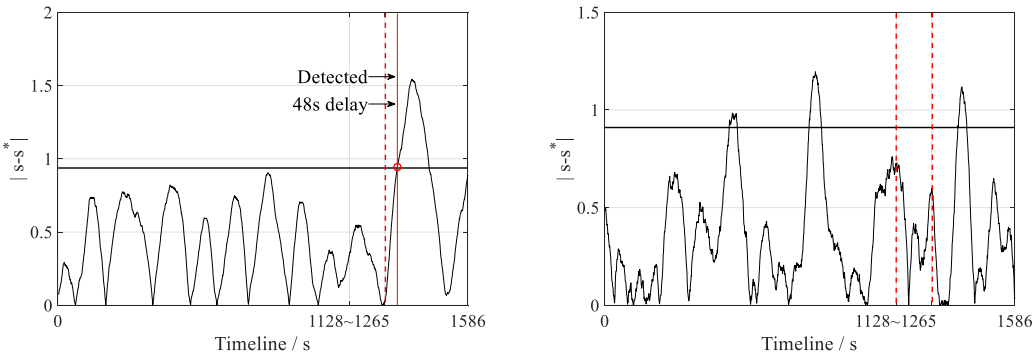

(a) Td-RRA detection results (b) RRA directly detection results

Figure C.28. Td-RRA and RRA detection results on group 5 sensors under DS-1

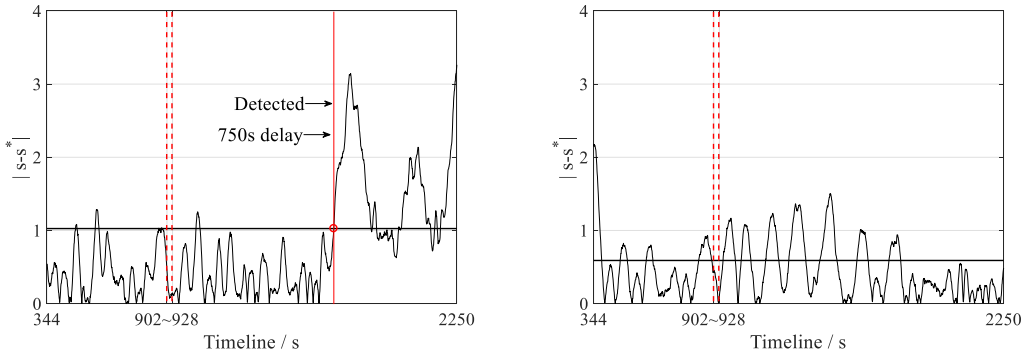

(a) Td-RRA detection results (b) RRA directly detection results

Figure C.29. Td-RRA and RRA detection results on group 5 sensors under DS-2

C.3. Td-OCSVM detection results

In this section, the anomaly detectability of Td-OCSVM and OCSVM are listed in tables as follows:

- Table C.7.5: group 1 sensors of SG2, 4, 6, 8, and 10 are investigated under four damage scenarios;
- Table C.7.6: group 2 sensors of SG11, 12, 13, and 14 are investigated under four damage scenarios;
- Table C.7.7: group 3 sensors of SG16, 18, 20, and 22 are investigated under four damage scenarios;
- Table C.7.8: group 4 sensors of SG23, 24, 25, and 26 are investigated under four damage scenarios;

- Table C.7.9: group 5 sensors of SG28, 29, 30, and 31 are investigated under four damage scenarios;
- Table C.7.10: group 6 sensors of DT1, 2, and 3 are investigated under four damage scenarios.

Table C.7.5. Anomaly detectability of Td-OCSVM and OCSVM on group 1 sensors

		Damage scenario-1		**Damage scenario-2**	
		Td-OCSVM	*OCSVM*	Td-OCSVM	*OCSVM*
Group 1	SG2	100%	*89%*	100%	*76%*
	SG4	100%	*90%*	100%	*60%*
	SG6	100%	*95%*	100%	*64%*
	SG8	100%	*57%*	100%	*88%*
	SG10	100%	*65%*	100%	*69%*
		Damage scenario-3		**Damage scenario-4**	
		Td-OCSVM	*OCSVM*	Td-OCSVM	*OCSVM*
Group 1	**SG2**	**100%**	*31%*	100%	*54%*
	SG4	100%	*15%*	100%	*89%*
	SG6	100%	*18%*	100%	*53%*
	SG8	100%	*1%*	100%	*78%*
	SG10	100%	*17%*	100%	*75%*

Table C.7.6. Anomaly detectability of Td-OCSVM and OCSVM on group 2 sensors

		Damage scenario-1		**Damage scenario-2**	
		Td-OCSVM	*OCSVM*	Td-OCSVM	*OCSVM*
Group 2	SG11	100%	*61%*	95%	*40%*
	SG12	87%	*56%*	98%	*57%*
	SG13	100%	*67%*	97%	*43%*
	SG14	100%	*68%*	87%	*52%*
		Damage scenario-3		**Damage scenario-4**	
		Td-OCSVM	*OCSVM*	Td-OCSVM	*OCSVM*
Group 2	SG11	78%	*30%*	92%	*22%*
	SG12	75%	*11%*	92%	*14%*
	SG13	76%	*10%*	86%	*31%*
	SG14	**83%**	*29%*	91%	*59%*

Table C.7.7. Anomaly detectability of Td-OCSVM and OCSVM on group 3 sensors

		Damage scenario-1		**Damage scenario-2**	
		Td-OCSVM	*OCSVM*	Td-OCSVM	*OCSVM*
Group 3	SG16	100%	*81%*	100%	*63%*
	SG18	100%	*48%*	100%	*62%*
	SG20	100%	*88%*	100%	*100%*
	SG22	97%	*61%*	100%	*60%*
		Damage scenario-3		**Damage scenario-4**	
		Td-OCSVM	*OCSVM*	Td-OCSVM	*OCSVM*
Group 3	SG16	89%	*18%*	100%	*43%*
	SG18	100%	*9%*	100%	*37%*
	SG20	100%	*18%*	100%	*68%*
	SG22	100%	*0%*	100%	*26%*

Table C.7.8. Anomaly detectability of Td-OCSVM and OCSVM on group 4 sensors

		Damage scenario-1		**Damage scenario-2**	
		Td-OCSVM	*OCSVM*	Td-OCSVM	*OCSVM*
Group 4	SG23	100%	*96%*	100%	*87%*
	SG24	100%	*51%*	100%	*87%*
	SG25	100%	*35%*	100%	*36%*
	SG26	100%	*53%*	100%	*99%*
		Damage scenario-3		**Damage scenario-4**	
		Td-OCSVM	*OCSVM*	Td-OCSVM	*OCSVM*
Group 4	SG23	80%	*18%*	100%	*11%*
	SG24	100%	*2%*	100%	*16%*
	SG25	98%	*0%*	100%	*24%*
	SG26	95%	*0%*	100%	*63%*

Table C.7.9. Anomaly detectability of Td-OCSVM and OCSVM on group 5 sensors

		Damage scenario-1		**Damage scenario-2**	
		Td-OCSVM	*OCSVM*	Td-OCSVM	*OCSVM*
Group 5	SG28	100%	*24%*	100%	*75%*
	SG29	99%	*46%*	100%	*96%*
	SG30	99%	*34%*	100%	*82%*
	SG31	100%	*44%*	97%	*95%*
		Damage scenario-3		**Damage scenario-4**	
		Td-OCSVM	*OCSVM*	Td-OCSVM	*OCSVM*
Group 5	SG28	100%	*0%*	100%	*58%*
	SG29	97%	*22%*	100%	*55%*
	SG30	83%	*8%*	99%	*28%*
	SG31	86%	*24%*	100%	*78%*

Table C.7.10. Anomaly detectability of Td-OCSVM and OCSVM on group 6 sensors

		Damage scenario-1		**Damage scenario-2**	
		Td-OCSVM	*OCSVM*	Td-OCSVM	*OCSVM*
Group 6	SG28	91%	*84%*	100%	*85%*
	SG29	91%	*66%*	99%	*51%*
	SG30	99%	*79%*	100%	*79%*
		Damage scenario-3		**Damage scenario-4**	
		Td-OCSVM	*OCSVM*	Td-OCSVM	*OCSVM*
Group 6	SG28	70%	*10%*	95%	*92%*
	SG29	66%	*35%*	96%	*52%*
	SG30	75%	*16%*	96%	*67%*

Bibliography

Abrard, F. & Deville, Y. 2005. A time–frequency blind signal separation method applicable to underdetermined mixtures of dependent sources. *Signal Processing*. **85** (7): 1389–1403. DOI: 10.1016/j.sigpro.2005.02.010.

Aissa-El-Bey, A., Linh-Trung, N., Abed-Meraim, K., Belouchrani, A. & Grenier, Y. 2007. Underdetermined Blind Separation of Nondisjoint Sources in the Time-Frequency Domain. *IEEE Transactions on Signal Processing*. **55** (3): 897–907. DOI: 10.1109/TSP.2006.888877.

Amer, M., Goldstein, M. & Abdennadher, S. 2013. Enhancing one-class support vector machines for unsupervised anomaly detection. In *Proceedings of the ACM SIGKDD Workshop on Outlier Detection and Description - ODD'13*. Chicago,USA. DOI: 10.1145/2500853.2500857.

American Society of Civil Engineers. 2013. *Structural Identification of Constructed Systems*. F.N. Çatbaş, T. Kijewski-Correa, & A.E. Aktan, Eds. Reston, VA: American Society of Civil Engineers. DOI: 10.1061/9780784411971.

American Society of Civil Engineers. 2017. *2017 Infrastructure report card*. Reston, VA.

Amezquita-Sanchez, J.P. & Adeli, H. 2016. Signal Processing Techniques for Vibration-Based Health Monitoring of Smart Structures. *Archives of Computational Methods in Engineering*. **23** (1): 1–15. DOI: 10.1007/s11831-014-9135-7.

Antoni, J. 2005. Blind separation of vibration components: Principles and demonstrations. *Mechanical Systems and Signal Processing*. **19** (6): 1166–1180. DOI: 10.1016/j.ymssp.2005.08.008.

Antoni, J., Garibaldi, L., Marchesiello, S. & Sidhamed, M. 2004. New Separation Techniques for Output-Only Modal Analysis. *Shock and Vibration*. **11** (3–4): 227–242. DOI: 10.1155/2004/560576.

Antoni, J., Castiglione, R. & Garibaldi, L. 2017. Interpretation and generalization of complexity pursuit for the blind separation of modal contributions. *Mechanical Systems and Signal Processing*. **85** (June 2016): 773–788. DOI: 10.1016/j.ymssp.2016.09.009.

Azzara, R.M., De Roeck, G., Girardi, M., Padovani, C., Pellegrini, D. & Reynders, E. 2018. The influence of environmental parameters on the dynamic behaviour of the San Frediano bell tower in Lucca. *Engineering Structures*. **156** (March 2017): 175–187. DOI: 10.1016/j.engstruct.2017.10.045.

Bell, A.J. & Sejnowski, T.J. 1995. An Information-Maximization Approach to Blind Separation and Blind Deconvolution. *Neural Computation*. **7** (6): 1129–1159. DOI: 10.1162/neco.1995.7.6.1129.

Bofill, P. & Zibulevsky, M. 2001. Underdetermined blind source separation using sparse representations. *Signal Processing*. **81** (11): 2353–2362. DOI: 10.1016/S0165-1684(01)00120-7.

Brownjohn, J.M.W. 2007. Structural health monitoring of civil infrastructure. *Philosophical Transactions of the Royal Society A: Mathematical, Physical and Engineering Sciences*. **365** (1851): 589–622. DOI: 10.1098/rsta.2006.1925.

Van Buren, K., Reilly, J., Neal, K., Edwards, H. & Hemez, F. 2017. Guaranteeing robustness of structural condition monitoring to environmental variability. *Journal of Sound and Vibration*. **386**: 134–148. DOI: 10.1016/j.jsv.2016.08.038.

Cardoso, J.-F. 1998. Blind signal separation: statistical principles. *Proceedings of the IEEE*. **86** (10): 2009–2025. DOI: 10.1109/5.720250.

Catbas, F.N., Susoy, M. & Frangopol, D.M. 2008. Structural health monitoring and reliability estimation: Long span truss bridge application with environmental monitoring data. *Engineering Structures*. **30** (9): 2347–2359. DOI: 10.1016/j.engstruct.2008.01.013.

Cavadas, F., Smith, I.F. & Figueiras, J. 2013. Damage Detection Using Data-Driven Methods Applied to Moving Load Responses. *Mechanical Systems and Signal Processing*. **39** (1): 409–425. DOI: 10.1016/j.ymssp.2013.02.019.

Chandola, V., Banerjee, A. & Kumar, V. 2009. Anomaly detection: a survey. *ACM Computing Surveys*. **41** (3): 1–58. DOI: 10.1145/1541880.1541882.

Chandra, P. & Singh, Y. 2004. An activation function adapting training algorithm for sigmoidal feedforward networks. *Neurocomputing*. **61** (1–4): 429–437. DOI: 10.1016/j.neucom.2004.04.001.

Chang, J., Liu, W., Hu, H. & Nagarajaiah, S. 2016. Improved independent component analysis based modal identification of higher damping structures. *Measurement*. **88**: 402–416. DOI: 10.1016/j.measurement.2016.03.021.

Chang, P.C., Flatau, A. & Liu, S.C. 2003. Review paper: Health monitoring of civil infrastructure. *Structural Health Monitoring*. **2** (3): 257–267. DOI: 10.1177/145792103036169.

Chaumette, E., Comon, P. & Muller, D. 1993. ICA-based technique for radiating sources estimation: application to airport surveillance. *IEE Proceedings F Radar and Signal Processing*. **140** (6): 395. DOI: 10.1049/ip-f-2.1993.0058.

Chen, G., Asce, M., Yang, X., Alkhrdaji, T., Wu, J. & Nanni, A. 1999. Condition Assessment of Concrete Structures By Dynamic Signature Tests. In *13th Engineering Mechanics Specialty Conference*.

Chen, L., Nagarajaiah, S. & Sun, L. 2015. Modal Identification of a Long-span Cable-stayed Bridge by Blind Source Separation. In *The 6th World Conference on Structural Control and Monitoring*. Barcelona, Spain. 2522–2531.

Chen, Y., Nyemba, S. & Malin, B. 2012. Detecting anomalous insiders in collaborative information systems. *IEEE Transactions on Dependable and Secure Computing*. **9** (3): 332–344. DOI: 10.1109/TDSC.2012.11.

Chiba, Z., Abghour, N., Moussaid, K., El Omri, A. & Rida, M. 2018. A novel architecture combined with optimal parameters for back propagation neural networks applied to anomaly network intrusion detection. *Computers and Security*. **75**: 36–58.

DOI: 10.1016/j.cose.2018.01.023.

Choi, S., Cichocki, A., Park, H. & Lee, S. 2005. Blind Source Separation and Independent Component Analysis: *A Review, Neural Information Processing -Letters and Reviews, Vol. 6, No.* **1** (1): 1–57.

Cichocki, A. 2002. *Adaptive Blind Signal and Image Processing: Learning Algorithms and Applications*.

Comisu, C.-C., Taranu, N., Boaca, G. & Scutaru, M.-C. 2017. Structural health monitoring system of bridges. *Procedia Engineering*. **199**: 2054–2059. DOI: 10.1016/j.proeng.2017.09.472.

Comon, P. 1994. Independent component analysis, A new concept? *Signal Processing*. **36** (3): 287–314. DOI: 10.1016/0165-1684(94)90029-9.

Comon, P., Jutten, C. & Herault, J. 1991. Blind separation of sources, part II: Problems statement. *Signal Processing*. **24** (1): 11–20. DOI: 10.1016/0165-1684(91)90080-3.

Cross, E.J., Manson, G., Worden, K. & Pierce, S.G. 2012. Features for damage detection with insensitivity to environmental and operational variations. *Proceedings of the Royal Society A: Mathematical, Physical and Engineering Sciences*. **468** (2148): 4098–4122. DOI: 10.1098/rspa.2012.0031.

Cross, E.J., Koo, K.Y., Brownjohn, J.M.W. & Worden, K. 2013. Long-term monitoring and data analysis of the Tamar Bridge. *Mechanical Systems and Signal Processing*. **35** (1–2): 16–34. DOI: 10.1016/j.ymssp.2012.08.026.

Dan, C.A., Kudela, P. & Ostachowicz, W. 2014. Compensation of Temperature Effects on Guided Wave Based Structural Health Monitoring Systems. *Proceedings of 7th European Workshop on Structural Health Monitoring*. 355–362.

Datteo, A., Lucà, F. & Busca, G. 2017. Statistical pattern recognition approach for long-time monitoring of the G.Meazza stadium by means of AR models and PCA. *Engineering Structures*. **153**: 317–333. DOI: 10.1016/j.engstruct.2017.10.022.

Deng, Y., Li, A., Liu, Y. & Chen, S. 2018. Investigation of temperature actions on flat steel box girders of long-span bridges with temperature monitoring data. *Advances*

in Structural Engineering. (April, 2): 1–15. DOI: 10.1177/1369433218766946.

Deraemaeker, A., Reynders, E., De Roeck, G. & Kullaa, J. 2008. Vibration-based structural health monitoring using output-only measurements under changing environment. *Mechanical Systems and Signal Processing*. **22** (1): 34–56. DOI: 10.1016/j.ymssp.2007.07.004.

Dervilis, N., Worden, K. & Cross, E.J. 2015. On robust regression analysis as a means of exploring environmental and operational conditions for SHM data. *Journal of Sound and Vibration*. **347**: 279–296. DOI: 10.1016/j.jsv.2015.02.039.

Diamanti, K. & Soutis, C. 2010. Structural health monitoring techniques for aircraft composite structures. *Progress in Aerospace Sciences*. **46** (8): 342–352. DOI: 10.1016/j.paerosci.2010.05.001.

Dilger, W.H., Ghali, A., Chan, M., Cheung, M.S. & Maes, M. a. 1983. Temperature Stresses in Composite Box Girder Bridges. *Journal of Structural Engineering*. **109** (6): 1460–1478. DOI: 10.1061/(ASCE)0733-9445(1983)109:6(1460).

Ding, Y. & Li, A. 2011. Temperature-induced variations of measured modal frequencies of steel box girder for a long-span suspension bridge. *International Journal of Steel Structures*. **11** (2): 145–155. DOI: 10.1007/s13296-011-2004-4.

Doebling, S.W.S., Farrar, C.R.C., Prime, M.B.M. & Shevitz, D.W.D. 1996. Damage identification and health monitoring of structural and mechanical systems from changes in their vibration characteristics: a literature review. *Los Alamos National Laboratory*. 133p. DOI: 10.2172/249299.

Dutta, H., Giannella, C., Borne, K. & Kargupta, H. 2007. Distributed top-k outlier detection from astronomy catalogs using the DEMAC system. *SIAM International Conference on Data Mining*. (May 2014): 473–478. DOI: 10.1137/1.9781611972771.47.

Dwivedi, S.K., Vishwakarma, M. & Soni, P.A. 2018. Advances and Researches on Non Destructive Testing: A Review. *Materials Today: Proceedings*. **5** (2): 3690–3698. DOI: 10.1016/j.matpr.2017.11.620.

Emanuel, J.H. & Hulsey, J.L. 1978. Temperature Distributions in Composite Bridges. *Journal of the Structural Division - ASCE*. **104** (1): 65–78. Available: https://www.scopus.com/inward/record.uri?eid=2-s2.0-0017922557&partnerID=40&md5=c940a56043bbe0370f4fdde119c579e0.

Farrar, C.R. & Worden, K. 2007. An introduction to structural health monitoring. *Philosophical Transactions of the Royal Society A: Mathematical, Physical and Engineering Sciences*. **365** (1851): 303–315. DOI: 10.1098/rsta.2006.1928.

Figueiredo, E., Park, G., Figueiras, J., Farrar, C. & Keith, W. 2009. Structural Health Monitoring Algorithm Comparisons Using Standard Data Sets. *Los Alamos National Laboratory*. Available: https://permalink.lanl.gov/object/tr?what=info:lanl-repo/lareport/LA-14393.

Gabriel, K.R. 1971. The biplot graphic display of matrices with application to principal component analysis. *Biometrika*. **58** (3): 453–467. DOI: 10.1093/biomet/58.3.453.

Glišić, B., Posenato, D., Inaudi, D. & Figini, A. 2008. Structural health monitoring method for curved concrete bridge box girders. In *Sensors and Smart Structures Technologies for Civil, Mechanical, and Aerospace Systems*. DOI: 10.1117/12.778643.

Guo, Y. & Kareem, A. 2016. System identification through nonstationary data using Time–Frequency Blind Source Separation. *Journal of Sound and Vibration*. **371**: 110–131. DOI: 10.1016/j.jsv.2016.02.011.

Guo, T., Liu, J., Zhang, Y. & Pan, S. 2015. Displacement Monitoring and Analysis of Expansion Joints of Long-Span Steel Bridges with Viscous Dampers. *Journal of Bridge Engineering*. **20** (9): 04014099. DOI: 10.1061/(ASCE)BE.1943-5592.0000701.

He, W.-Y. & Zhu, S. 2016. Moving load-induced response of damaged beam and its application in damage localization. *Journal of Vibration and Control*. **22** (16): 3601–3617. DOI: 10.1177/1077546314564587.

Heller, K., Svore, K., Keromytis, A.D. & Stolfo, S. 2003. One class support vector machines for detecting anomalous windows registry accesses. *Workshop on Data Mining for Computer Security (DMSEC), Melbourne, FL, November 19, 2003*. Available: http://sneakers.cs.columbia.edu/ids/publications/ocsvm.pdf.

Helmicki, A., Hunt, V., Shell, M., Lenett, M., Turer, A., Dalal, V. & Aktan, A. 1999. Multidimensional performance monitoring of a recently constructed steel-stringer bridge. In *2nd international workshop on structural health monitoring*. Stanford University, Palo Alto, CA. 408–416.

Herdovics, B. & Cegla, F. 2018. Compensation of phase response changes in ultrasonic transducers caused by temperature variations. *Structural Health Monitoring*. 1–16. DOI: 10.1177/1475921718759272.

Hernandez-Garcia, M.R. & Sanchez-Silva, M. 2007. Learning machines for structural damage detection. In *Intelligent Computational Paradigms in Earthquake Engineering*. 158–187. DOI: 10.4018/978-1-59904-099-8.ch008.

Hotelling, H. 1933. Analysis of a complex of statistical variables into principal components. *Journal of Educational Psychology*. **24** (6): 417–441. DOI: 10.1037/h0071325.

Hu, W.-H., Said, S., Rohrmann, R.G., Cunha, Á. & Teng, J. 2017. Continuous dynamic monitoring of a prestressed concrete bridge based on strain, inclination and crack measurements over a 14-year span. *Structural Health Monitoring*. 1–22. DOI: 10.1177/1475921717735505.

Huang, J.C. 2010. Remote health monitoring adoption model based on artificial neural networks. *Expert Systems with Applications*. **37** (1): 307–314. DOI: 10.1016/j.eswa.2009.05.063.

Huang, N.E., Shen, Z., Long, S.R., Wu, M.C., Shih, H.H., Zheng, Q., Yen, N.-C., Tung, C.C., et al. 1998. The empirical mode decomposition and the Hilbert spectrum for nonlinear and non-stationary time series analysis. *Proceedings of the Royal Society A: Mathematical, Physical and Engineering Sciences*. **454** (1971): 903–995. DOI: 10.1098/rspa.1998.0193.

Huang, Q., Crosetto, M., Monserrat, O. & Crippa, B. 2017. Displacement monitoring and modelling of a high-speed railway bridge using C-band Sentinel-1 data. *ISPRS Journal of Photogrammetry and Remote Sensing*. **128**: 204–211. DOI: 10.1016/j.isprsjprs.2017.03.016.

Hubert, M., Rousseeuw, P.J. & Vanden Branden, K. 2005. ROBPCA: A New

Approach to Robust Principal Component Analysis. *Technometrics*. **47** (1): 64–79. DOI: 10.1198/004017004000000563.

Hyvärinen, A. 2001. Complexity pursuit: separating interesting components from time series. *Neural computation*. **13** (4): 883–98. DOI: 10.1162/089976601300014394.

Hyvärinen, A. & Oja, E. 2000. Independent component analysis: Algorithms and applications. *Neural Networks*. **13** (4–5): 411–430. DOI: 10.1016/S0893-6080(00)00026-5.

Hyvärinen, A., Karhunen, J. & Oja, E. 2004. *Independent component analysis*. John Wiley & Sons.

Inaudi, D. 2010. Long-term static Structural Health Monitoring. 566–577. DOI: 10.1061/41130(369)52.

Ivorra, S. & Pallarés, F.J. 2006. Dynamic investigations on a masonry bell tower. *Engineering Structures*. **28** (5): 660–667. DOI: 10.1016/j.engstruct.2005.09.019.

Jin, C., Li, J., Jang, S., Sun, X. & Christenson, R. 2015. Structural damage detection for in-service highway bridge under operational and environmental variability. J.P. Lynch, Ed. 94353A. DOI: 10.1117/12.2084384.

Jin, S.-S., Cho, S. & Jung, H.-J. 2015. Adaptive reference updating for vibration-based structural health monitoring under varying environmental conditions. *Computers & Structures*. **158**: 211–224. DOI: 10.1016/j.compstruc.2015.06.001.

Jolliffe, I. 2011. Principal Component Analysis. In *International Encyclopedia of Statistical Science*. Berlin, Heidelberg: Springer Berlin Heidelberg. 1094–1096. DOI: 10.1007/978-3-642-04898-2_455.

Jutten, C. & Herault, J. 1991. Blind separation of sources, part I: An adaptive algorithm based on neuromimetic architecture. *Signal Processing*. **24** (1): 1–10. DOI: 10.1016/0165-1684(91)90079-X.

Kennedy, J.B. & Soliman, M.H. 1987. Temperature Distribution in Composite Bridges. *Journal of Structural Engineering*. **113** (3): 475–482. DOI: 10.1061/(ASCE)0733-9445(1987)113:3(475).

Kisilev, P., Zibulevsky, M. & Zeevi, Y.Y. 2004. A Multiscale Framework For

Blind Separation of Linearly Mixed Signals Pavel. *The Journal of Machine Learning Research*. **4** (7–8): 1339–1364. Available: http://www.crossref.org/deleted_DOI.html.

Ko, J.M. & Ni, Y.Q. 2005. Technology developments in structural health monitoring of large-scale bridges. *Engineering Structures*. **27** (12): 1715–1725. DOI: 10.1016/j.engstruct.2005.02.021.

Kohonen, T. 1998. The self-organizing map. *Neurocomputing*. **21** (1–3): 1–6. DOI: 10.1016/S0925-2312(98)00030-7.

Konstantinidis, G., Drinkwater, B.W. & Wilcox, P.D. 2006. The temperature stability of guided wave structural health monitoring systems. *Smart Materials and Structures*. **15** (4): 967–976. DOI: 10.1088/0964-1726/15/4/010.

Koo, K.Y., Brownjohn, J.M.W., List, D.I. & Cole, R. 2013. Structural health monitoring of the Tamar suspension bridge. *Structural Control and Health Monitoring*. **20** (4): 609–625. DOI: 10.1002/stc.1481.

Kromanis, R. & Kripakaran, P. 2014. Predicting thermal response of bridges using regression models derived from measurement histories. *Computers & Structures*. **136**: 64–77. DOI: 10.1016/j.compstruc.2014.01.026.

Kromanis, R. & Kripakaran, P. 2016. SHM of bridges: characterising thermal response and detecting anomaly events using a temperature-based measurement interpretation approach. *Journal of Civil Structural Health Monitoring*. **6** (2): 237–254. DOI: 10.1007/s13349-016-0161-z.

Lämsä, V. & Raiko, T. 2010. Novelty detection by nonlinear factor analysis for structural health monitoring. In *2010 IEEE International Workshop on Machine Learning for Signal Processing*. 468–473. DOI: 10.1109/MLSP.2010.5588688.

Lanata, F. & Del Grosso, A. 2006. Damage detection and localization for continuous static monitoring of structures using a proper orthogonal decomposition of signals. *Smart Materials and Structures*. **15** (6): 1811–1829. DOI: 10.1088/0964-1726/15/6/036.

Lanata, F. & Posenato, D. 2007. A Multi-Algorithm Procedure for Damage Location and Quantification in the Field of Continuous Static Monitoring of Structures.

Key Engineering Materials. **347**: 89–94. DOI: 10.4028/www.scientific.net/KEM.347.89.

Lanata, F., Posenato, D. & Inaudi, D. 2007. Data Anomaly Identification in Complex Structures Using Model Free Data Statistical Analysis. In *The 3rd International Conference on Structural Health Monitoring of Intelligent Infrastructure Vancouver*. British Columbia, Canada.

Lange, N., Bishop, C.M. & Ripley, B.D. 1997. Neural Networks for Pattern Recognition. *Journal of the American Statistical Association*. **92** (440): 1642. DOI: 10.2307/2965437.

Laory, I. 2013. Model-Free Methodologies for Data-Interpretation during Continuous Monitoring of Structures. Thesis (PhD). EPFL. DOI: 10.5075/epfl-thesis-5518.

Laory, I., Trinh, T.N. & Smith, I.F.C. 2011. Evaluating two model-free data interpretation methods for measurements that are influenced by temperature. *Advanced Engineering Informatics*. **25** (3): 495–506. DOI: 10.1016/j.aei.2011.01.001.

Laory, I., Trinh, T.N., Posenato, D. & Smith, I.F.C. 2013. Combined Model-Free Data-Interpretation Methodologies for Damage Detection during Continuous Monitoring of Structures. *Journal of Computing in Civil Engineering*. **27** (6): 657–666. DOI: 10.1061/(ASCE)CP.1943-5487.0000289.

Li, J. & Hao, H. 2015. Damage detection of shear connectors under moving loads with relative displacement measurements. *Mechanical Systems and Signal Processing*. **60**–**61**: 124–150. DOI: 10.1016/j.ymssp.2014.09.014.

Li, H.-N., Ren, L., Jia, Z.-G., Yi, T.-H. & Li, D.-S. 2016. State-of-the-art in structural health monitoring of large and complex civil infrastructures. *Journal of Civil Structural Health Monitoring*. **6** (1): 3–16. DOI: 10.1007/s13349-015-0108-9.

Li, J., Hao, H., Fan, K. & Brownjohn, J. 2015. Development and application of a relative displacement sensor for structural health monitoring of composite bridges. *Structural Control and Health Monitoring*. **22** (4): 726–742. DOI: 10.1002/stc.1714.

Liang, Y.C., Lee, H.P., Lim, S.P., Lin, W.Z., Lee, K.H. & Wu, C.G. 2002. Proper

Orthogonal Decomposition and Its Applications } Part Ii : Model Reduction for Mems Dynamical Analysis. *Journal of Sound and Vibration*. **256** (November 2015). DOI: 10.1006/jsvi.5007.

Liang, Y.C., Lee, H.P., Lim, S.P., Lin, W.Z., Lee, K.H. & Ww, C.G. 2002. Proper orthogonal decomposition and its applications - Part I: Theory. *Journal of Sound and Vibration*. **252** (3): 527–544. DOI: 10.1006/jsvi.2001.4041.

Loh, C.-H., Huang, Y.-T., Hsueh, W., Chen, J.-D. & Lin, P.-Y. 2017. Visualization and Dimension Reduction of High Dimension Data for Structural Damage Detection. *Procedia Engineering*. **188**: 17–24. DOI: 10.1016/j.proeng.2017.04.452.

Lucas, J.-M., Berred, A. & Louis, C. 2003. Thermal actions on a steel box girder bridge. *Proceedings of the Institution of Civil Engineers - Structures and Buildings*. **156** (2): 175–182. DOI: 10.1680/stbu.2003.156.2.175.

MAIA, N.M.M., SILVA, J.M.M., ALMAS, E.A.M. & SAMPAIO, R.P.C. 2003. Damage Detection in Structures: From Mode Shape To Frequency Response Function Methods. *Mechanical Systems and Signal Processing*. **17** (3): 489–498. DOI: 10.1006/mssp.2002.1506.

Malere, J.P.P. & Santos, L.G. dos. 2013. Challenges for Costs and Benefits Evaluation of IVHM Systems. *SAE International Journal of Aerospace*. **6** (2): 2013-01-2183. DOI: 10.4271/2013-01-2183.

Manevitz, L.M., Yousef, M., Cristianini, N., Shawe-Taylor, J. & Williamson, B. 2001. One-Class SVMs for Document Classification. *Journal of Machine Learning Research*. **2**: 139–154. DOI: 10.1162/15324430260185574.

Marefat, M.S., Ghahremani-Gargary, E. & Ataei, S. 2004. Load test of a plain concrete arch railway bridge of 20-m span. *Construction and Building Materials*. **18** (9): 661–667. DOI: 10.1016/j.conbuildmat.2004.04.025.

Markou, M. & Singh, S. 2003. Novelty detection: A review - Part 2:: Neural network based approaches. *Signal Processing*. **83** (12): 2499–2521. DOI: 10.1016/j.sigpro.2003.07.019.

McBain, J. & Timusk, M. 2011. Feature extraction for novelty detection as applied

to fault detection in machinery. *Pattern Recognition Letters*. **32** (7): 1054–1061. DOI: 10.1016/j.patrec.2011.01.019.

Medeiros, R., Vandepitte, D. & Tita, V. 2018. Structural health monitoring for impact damaged composite: a new methodology based on a combination of techniques. *Structural Health Monitoring*. **17** (2): 185–200. DOI: 10.1177/1475921716688442.

Mojtahedi, A., Lotfollahi Yaghin, M.A., Ettefagh, M.M., Hassanzadeh, Y. & Fujikubo, M. 2013. Detection of nonlinearity effects in structural integrity monitoring methods for offshore jacket-type structures based on principal component analysis. *Marine Structures*. **33**: 100–119. DOI: 10.1016/j.marstruc.2013.04.007.

Mokhtari, S., Mehdawi, N., Park, S.-H., Sallam, A.M., Chopra, M., Reddi, L.N. & Yun, H.-B. 2014. Monitoring Proximity Tunneling Effects Using Blind Source Separation Technique. In *Wicks A. (eds) Structural Health Monitoring, Volume 5. Conference Proceedings of the Society for Experimental Mechanics Series*. Springer, Cham. DOI: 10.1007/978-3-319-04570-2_12.

Mokios, K.N., Sidiropoulos, N.D. & Potamianos, A. 2006. Blind Speech Separation Using Parafac Analysis and Integer Least Squares. In *2006 IEEE International Conference on Acoustics Speed and Signal Processing Proceedings*. V. 5. IEEE. V-73-V-76. DOI: 10.1109/ICASSP.2006.1661215.

Moorty, S. & Roeder, C.W. 1992. Temperature-Dependent Bridge Movements. *Journal of Structural Engineering*. **118** (4): 1090–1105. DOI: 10.1061/(ASCE)0733-9445(1992)118:4(1090).

Moser, P. & Moaveni, B. 2011. Environmental effects on the identified natural frequencies of the Dowling Hall Footbridge. *Mechanical Systems and Signal Processing*. **25** (7): 2336–2357. DOI: 10.1016/j.ymssp.2011.03.005.

Moya, M.., Koch, M.. & Hostetler, L.. 1993. One-class classifier networks for target recognition applications. *NASA STI/Recon Technical Report N*.

Mujica, L., Rodellar, J., Fernández, A. & Güemes, A. 2011. Q-statistic and T2-statistic PCA-based measures for damage assessment in structures. *Structural Health Monitoring: An International Journal*. **10** (5): 539–553. DOI: 10.1177/1475921710388972.

Mujica, L.E., Ruiz, M., Pozo, F., Rodellar, J. & Güemes, A. 2014. A structural damage detection indicator based on principal component analysis and statistical hypothesis testing. *Smart Materials and Structures*. **23** (2): 025014. DOI: 10.1088/0964-1726/23/2/025014.

National Instruments. 2009. *NI 9949 Accessory User Guide*. Available: http://www.ni.com/pdf/manuals/372278b.pdf.

National Instruments. 2015. *Datasheet NI 9237*. Available: http://www.ni.com/pdf/manuals/374186a_02.pdf.

Nazarko, P. & Ziemianski, L. 2016. Damage detection in aluminum and composite elements using neural networks for Lamb waves signal processing. *Engineering Failure Analysis*. **69**: 97–107. DOI: 10.1016/j.engfailanal.2016.07.001.

Nazarko, P. & Ziemiański, L. 2011. Application of artificial neural networks in the damage identification of structural elements. *Computer Assisted Mechanics and Engineering Sciences*. **18** (3): 175–189.

Nguyen, V.H., Schommer, S., Maas, S. & Zürbes, A. 2016. Static load testing with temperature compensation for structural health monitoring of bridges. *Engineering Structures*. **127**: 700–718. DOI: 10.1016/j.engstruct.2016.09.018.

Ni, Y., Xia, H., Wong, K. & Ko, J. 2011. In-service condition assessment of bridge deck using long-term monitoring data of strain response. *Journal of Bridge Engineering*. **17** (December): 876–885. DOI: 10.1061/(ASCE)BE.1943-5592.0000321.

Ni, Y.Q., Hua, X.G., Fan, K.Q. & Ko, J.M. 2005. Correlating modal properties with temperature using long-term monitoring data and support vector machine technique. *Engineering Structures*. **27** (12 SPEC. ISS.): 1762–1773. DOI: 10.1016/j.engstruct.2005.02.020.

Ni, Y.Q., Hua, X.G., Wong, K.Y. & Ko, J.M. 2007. Assessment of Bridge Expansion Joints Using Long-Term Displacement and Temperature Measurement. *Journal of Performance of Constructed Facilities*. **21** (2): 143–151. DOI: 10.1061/(ASCE)0887-3828(2007)21:2(143).

OBrien, E.J., Malekjafarian, A. & González, A. 2017. Application of empirical mode decomposition to drive-by bridge damage detection. *European Journal of Mechanics - A/Solids*. **61**: 151–163. DOI: 10.1016/j.euromechsol.2016.09.009.

Ozden Caglayan, B., Ozakgul, K. & Tezer, O. 2012. Assessment of a concrete arch bridge using static and dynamic load tests. *Structural Engineering and Mechanics*. **41** (1): 83–94. DOI: 10.12989/sem.2012.41.1.083.

Peeters, B. & De Roeck, G. 2001. One-year monitoring of the Z24-Bridge: environmental effects versus damage events. *Earthquake Engineering & Structural Dynamics*. **30** (2): 149–171. DOI: 10.1002/1096-9845(200102)30:2<149::AID-EQE1>3.0.CO;2-Z.

Pimentel, M.A.F., Clifton, D.A., Clifton, L. & Tarassenko, L. 2014. A review of novelty detection. *Signal Processing*. **99**: 215–249. DOI: 10.1016/j.sigpro.2013.12.026.

Poncelet, F., Kerschen, G., Golinval, J.-C. & Verhelst, D. 2007. Output-only modal analysis using blind source separation techniques. *Mechanical Systems and Signal Processing*. **21** (6): 2335–2358. DOI: 10.1016/j.ymssp.2006.12.005.

Posenato, D., Lanata, F., Inaudi, D. & Smith, I.F.C. 2008. Model-free data interpretation for continuous monitoring of complex structures. *Advanced Engineering Informatics*. **22** (1): 135–144. DOI: 10.1016/j.aei.2007.02.002.

Posenato, D., Kripakaran, P., Inaudi, D. & Smith, I.F.C. 2010. Methodologies for model-free data interpretation of civil engineering structures. *Computers & Structures*. **88** (7–8): 467–482. DOI: 10.1016/j.compstruc.2010.01.001.

Qiu, L., Yuan, S. & Boller, C. 2017. An adaptive guided wave-Gaussian mixture model for damage monitoring under time-varying conditions: Validation in a full-scale aircraft fatigue test. *Structural Health Monitoring*. **16** (5): 501–517. DOI: 10.1177/1475921717692571.

Roan, M.J., Erling, J.G. & Sibul, L.H. 2002. A new, non-lineara, adaptive, blinde source separation approach to gear tooth failure detection and analysis. *Mechanical Systems and Signal Processing*. **16** (5): 719–740. DOI: 10.1006/mssp.2002.1504.

RS Components. n.d. *RS thermocouple No . 621-2170*. Available: https://docs-emea.rs-online.com/webdocs/157a/0900766b8157a829.pdf.

Rytter, A. 1993. Vibrational Based Inspection of Civil Engineering Structures. DOI: 10.1016/j.jsv.2016.06.047.

Sadhu, A., Narasimhan, S. & Antoni, J. 2017. A review of output-only structural mode identification literature employing blind source separation methods. *Mechanical Systems and Signal Processing*. **94**: 415–431. DOI: 10.1016/j.ymssp.2017.03.001.

Saduf, M.A.W. 2013. Comparative Study of Back Propagation Learning Algorithms for Neural Networks. *International Journal of Advanced Research in Computer Science and Software Engineering*. **3** (12): 1151–1156. Available: https://www.ijarcsse.com/docs/papers/Volume_3/12_December2013/V3I12-0376.pdf.

Sazonov, E. & Klinkhachorn, P. 2005. Optimal spatial sampling interval for damage detection by curvature or strain energy mode shapes. *Journal of Sound and Vibration*. **285** (4–5): 783–801. DOI: 10.1016/j.jsv.2004.08.021.

Schölkopf, B., Platt, J.C., Shawe-Taylor, J., Smola, A.J. & Williamson, R.C. 2001. Estimating the Support of a High-Dimensional Distribution. *Neural Computation*. **13** (7): 1443–1471. DOI: 10.1162/089976601750264965.

Seppänen, J., Turunen, J., Koivisto, M. & Haarla, L. 2015. Measurement based analysis of electromechanical modes with Second Order Blind Identification. *Electric Power Systems Research*. **121**: 67–76. DOI: 10.1016/j.epsr.2014.11.023.

Shyu, M.-L., Chen, S.-C., Sarinnapakorn, K. & Chang, L. 2003. *A Novel Anomaly Detection Scheme Based on Principal Component Classifier*. Available: https://users.cs.fiu.edu/~chens/docs/ICDM03_WS.pdf.

Sibi, P., Jones, S. & Siddarth, P. 2013. Analysis of different activation functions using back propagation neural networks. *Journal of theoretical and applied Information Technology*. **47** (3): 1264–1268.

Sohn, H. 2007. Effects of environmental and operational variability on structural health monitoring. *Philosophical Transactions of the Royal Society A: Mathematical,*

Physical and Engineering Sciences. **365** (1851): 539–560. DOI: 10.1098/rsta.2006.1935.

Sohn, H., Worden, K. & Farrar, C.R. 2002. Statistical Damage Classification Under Changing Environmental and Operational Conditions. *Journal of Intelligent Material Systems and Structures*. **13** (9): 561–574. DOI: 10.1106/104538902030904.

Sohn, H., Farrar, C.R., Hemez, F.M., Shunk, D.D., Stinemates, D.W., Nadler, B.R. & Czarnecki, J.J. 2003. *A review of structural health monitoring literature: 1996--2001*.

Stone, J. V. 2001. Blind Source Separation Using Temporal Predictability. *Neural Computation*. **13** (7): 1559–1574. DOI: 10.1162/089976601750265009.

Su, J.Z., Xia, Y., Zhu, L.D., Zhu, H.P. & Ni, Y.Q. 2017. Typhoon- and temperature-induced quasi-static responses of a supertall structure. *Engineering Structures*. **143**: 91–100. DOI: 10.1016/j.engstruct.2017.04.007.

Sun, J., Chen, D., Li, C. & Yan, H. 2018. Integration of scheduled structural health monitoring with airline maintenance program based on risk analysis. *Proceedings of the Institution of Mechanical Engineers, Part O: Journal of Risk and Reliability*. **232** (1): 92–104. DOI: 10.1177/1748006X17742777.

Tan, Z.X., Thambiratnam, D.P., Chan, T.H.T. & Abdul Razak, H. 2017. Detecting damage in steel beams using modal strain energy based damage index and Artificial Neural Network. *Engineering Failure Analysis*. **79** (May): 253–262. DOI: 10.1016/j.engfailanal.2017.04.035.

Timusk, M., Lipsett, M. & Mechefske, C.K. 2008. Fault detection using transient machine signals. *Mechanical Systems and Signal Processing*. **22** (7): 1724–1749. DOI: 10.1016/j.ymssp.2008.01.013.

Toivola, J., Prada, M.A. & Hollmén, J. 2010. Novelty detection in projected spaces for structural health monitoring. In *Lecture Notes in Computer Science (including subseries Lecture Notes in Artificial Intelligence and Lecture Notes in Bioinformatics)*. V. 6065 LNCS. 208–219. DOI: 10.1007/978-3-642-13062-5_20.

Tokyo Sokki Kenkyujo. n.d. *Foil Strain Gauges*. Available:

http://www.tml.jp/e/product/strain_gauge/gauge_list/f_list.html.

Tong, L., Soon, V.C., Huang, Y.F. & Liu, R. 1990. AMUSE: a new blind identification algorithm. In *IEEE International Symposium on Circuits and Systems*. IEEE. 1784–1787. DOI: 10.1109/ISCAS.1990.111981.

Tong, M., Tham, L.G., Au, F.T.K. & Lee, P.K.K. 2001. Numerical modelling for temperature distribution in steel bridges. *Computers & Structures*. **79** (6): 583–593. DOI: 10.1016/S0045-7949(00)00161-9.

Tsogka, C., Daskalakis, E., Comanducci, G. & Ubertini, F. 2017. The Stretching Method for Vibration-Based Structural Health Monitoring of Civil Structures. *Computer-Aided Civil and Infrastructure Engineering*. **32** (4): 288–303. DOI: 10.1111/mice.12255.

Tuong Vinh Ho & Rouat, J. 1998. Novelty detection based on relaxation time of a network of integrate-and-fire neurons. In *1998 IEEE International Joint Conference on Neural Networks Proceedings. IEEE World Congress on Computational Intelligence (Cat. No.98CH36227)*. V. 2. IEEE. 1524–1529. DOI: 10.1109/IJCNN.1998.686003.

Ubertini, F., Comanducci, G., Cavalagli, N., Laura Pisello, A., Luigi Materazzi, A. & Cotana, F. 2017. Environmental effects on natural frequencies of the San Pietro bell tower in Perugia, Italy, and their removal for structural performance assessment. *Mechanical Systems and Signal Processing*. **82**: 307–322. DOI: 10.1016/j.ymssp.2016.05.025.

Valinejadshoubi, M., Bagchi, A. & Moselhi, O. 2016. Structural Health Monitoring of Buildings and Infrastructure. *International Journal of Civil and Engineering and Technology*. **10** (6): 731–738. DOI: 10.5281/zenodo.1124679.

Vapnik, V. 2013. The Nature Of Statistical Learning Theory. *Springer science & business media*.

Vishay Precision Group. 2014. Linear Displacement Sensors - HS50. 12–14. Available: http://www.vishaypg.com/docs/11350/hs-series.pdf.

Westgate, R.J. 2012. Environmental Effects on a Suspension Bridge's

Performance. Thesis (PhD). The University of Sheffield. Available: http://etheses.whiterose.ac.uk/id/eprint/2884.

Wong, K.-Y. 2007. Design of a structural health monitoring system for long-span bridges. *Structure and Infrastructure Engineering*. **3** (2): 169–185. DOI: 10.1080/15732470600591117.

Wood, M.G. 1992. Damage analysis of bridge structures using vibrational techniques. Thesis (PhD). University of Aston in Birmingham. Available: http://publications.aston.ac.uk/11832/1/Wood_Michael_G_1992.pdf.

Worden, K. & Dulieu-Barton, J.M. 2004. An Overview of Intelligent Fault Detection in Systems and Structures. *Structural Health Monitoring*. **3** (1): 85–98. DOI: 10.1177/1475921704041866.

Wu, Z. & Huang, N.E. 2009. Ensemble empirical mode decomposition: a noise-assisted data analysis method. *Advances in Adaptive Data Analysis*. **01** (01): 1–41. DOI: 10.1142/S1793536909000047.

Xia, Y., Chen, B., Zhou, X. & Xu, Y. 2013. Field monitoring and numerical analysis of Tsing Ma Suspension Bridge temperature behavior. *Structural Control and Health Monitoring*. **20** (4): 560–575. DOI: 10.1002/stc.515.

Xu, Y.L. & Xia, Y. 2012. *Structural health monitoring of long-span suspension bridges*. London: Spon Press.

Xu, Y.L., Chen, B., Ng, C.L., Wong, K.Y. & Chan, W.Y. 2010. Monitoring temperature effect on a long suspension bridge. *Structural Control and Health Monitoring*. **17** (6): 632–653. DOI: 10.1002/stc.340.

Yan, A.-M., Kerschen, G., De Boe, P. & Golinval, J.-C. 2005a. Structural damage diagnosis under varying environmental conditions—part II: local PCA for non-linear cases. *Mechanical Systems and Signal Processing*. **19** (4): 865–880. DOI: 10.1016/j.ymssp.2004.12.003.

Yan, A.-M., Kerschen, G., De Boe, P. & Golinval, J.-C. 2005b. Structural damage diagnosis under varying environmental conditions—Part I: A linear analysis. *Mechanical Systems and Signal Processing*. **19** (4): 847–864. DOI:

10.1016/j.ymssp.2004.12.002.

Yang, Y. & Nagarajaiah, S. 2013. Time-Frequency Blind Source Separation Using Independent Component Analysis for Output-Only Modal Identification of Highly Damped Structures. *Journal of Structural Engineering*. **139** (10): 1780–1793. DOI: 10.1061/(ASCE)ST.1943-541X.0000621.

Yang, Y. & Nagarajaiah, S. 2014. Structural damage identification via a combination of blind feature extraction and sparse representation classification. *Mechanical Systems and Signal Processing*. **45** (1): 1–23. DOI: 10.1016/j.ymssp.2013.09.009.

Yang, Y. & Nagarajaiah, S. 2015. Output-only modal identification by compressed sensing: Non-uniform low-rate random sampling. *Mechanical Systems and Signal Processing*. **56**: 15–34. DOI: 10.1016/j.ymssp.2014.10.015.

Yang, C., Liu, Y. & Sun, Y. 2016. Damage Detection of Bridges Considering Environmental Temperature Effect by Using Cluster Analysis. *Procedia Engineering*. **161**: 577–582. DOI: 10.1016/j.proeng.2016.08.695.

Yang, D.-H., Yi, T.-H., Li, H.-N. & Zhang, Y.-F. 2018. Monitoring and analysis of thermal effect on tower displacement in cable-stayed bridge. *Measurement*. **115** (October 2017): 249–257. DOI: 10.1016/j.measurement.2017.10.036.

Yang, J.N., Lei, Y., Lin, S. & Huang, N. 2004. Hilbert-Huang Based Approach for Structural Damage Detection. *Journal of Engineering Mechanics*. **130** (1): 85–95. DOI: 10.1061/(ASCE)0733-9399(2004)130:1(85).

Yang, Y.-B., Lin, C.W. & Yau, J.D. 2004. Extracting bridge frequencies from the dynamic response of a passing vehicle. *Journal of Sound and Vibration*. **272** (3–5): 471–493. DOI: 10.1016/S0022-460X(03)00378-X.

Yang, Y., Nagarajaiah, S., Li, H. & Zhou, P. 2016. Real-Time Output-Only Identification of Time-Varying Cable Tension from Accelerations via Complexity Pursuit. *Journal of Structural Engineering (United States)*. **142** (1): 1–10. DOI: 10.1061/(ASCE)ST.1943-541X.0001337.

Yarnold, M.T. 2013. Temperature-based structural identification and health

monitoring for long span bridge. Thesis (PhD). Drexel University.

Yarnold, M.T. & Moon, F.L. 2015. Temperature-based structural health monitoring baseline for long-span bridges. *Engineering Structures*. **86**: 157–167. DOI: 10.1016/j.engstruct.2014.12.042.

Yarnold, M., Moon, F., Dubbs, N. & Aktan, A. 2012. Evaluation of a long-span steel tied arch bridge using temperature-based structural identification. 2397–2403. DOI: 10.1201/b12352-361.

Yarnold, M.T., Moon, F.L. & Emin Aktan, A. 2015. Temperature-Based Structural Identification of Long-Span Bridges. *Journal of Structural Engineering*. **141** (11): 04015027. DOI: 10.1061/(ASCE)ST.1943-541X.0001270.

Yuen, K.V. & Ortiz, G.A. 2017. Outlier detection and robust regression for correlated data. *Computer Methods in Applied Mechanics and Engineering*. **313**: 632–646. DOI: 10.1016/j.cma.2016.10.004.

Zang, C., Friswell, M.I. & Imregun, M. 2004. Structural Damage Detection using Independent Component Analysis. *Structural Health Monitoring: An International Journal*. **3** (1): 69–83. DOI: 10.1177/1475921704041876.

Zhao, X. 2015. New Methods for Structural Health Monitoring and Damage Localization. Thesis (PhD). University of Sheffield. Available: http://dx.doi.org/10.1016/j.proeng.2017.09.472.

Zhou, L., Xia, Y., Brownjohn, J.M.W. & Koo, K.Y. 2016. Temperature Analysis of a Long-Span Suspension Bridge Based on Field Monitoring and Numerical Simulation. *Journal of Bridge Engineering*. **21** (1): 04015027. DOI: 10.1061/(ASCE)BE.1943-5592.0000786.

Zhu, Y., Jesus, A. & Laory, I. 2017. Thermal Effect Identification and Bridge Damage Disclosure by using Blind Source Separation Method. In *Structural Health Monitoring*. 527–534. DOI: 10.12783/shm2017/13907.

Zuk, W. 1965. Thermal behavior of composite bridges - Insulated and uninsulated. In *Highway Research Record*. San Francisco, CA: Highway Research Board. 231–253. Available: https://trid.trb.org/view/105274.